Universitat Autònoma de Barcelona

Unraveling CK2 inhibition and temozolomide contribution to therapy response in preclinical GL261 glioblastoma: immune system implications and magnetic resonance based nosological imaging

Lucía Villamañán de Santiago

Universitat Autònoma de Barcelona

Department of Biochemistry and Molecular Biology

Unraveling CK2 inhibition and temozolomide contribution to therapy response in preclinical GL261 glioblastoma: immune system implications and magnetic resonance based nosological imaging

Lucía Villamañán de Santiago

Ph. D. Thesis

2018

Dissertation presented by

Lucía Villamañán de Santiago

Submitted for the Degree of PhD of Biochemistry, Molecular Biology and Biomedicine at the

Autonomous University of Barcelona

of the doctoral program of

Biochemistry, Molecular Biology and Biomedicine

of the department of

Biochemistry and Molecular Biology

supervised by

Ph. D. Ana Paula Candiota, Ph. D. María Plana and Ph. D. Emilio Itarte

Signatures of the directors

_____ _____

Ph. D. Ana Paula Candiota Ph. D. María Plana

Signature of the tutor

_____

Prof Emilio Itarte

Signature of the PhD thesis author

_____

Lucía Villamañán de Santiago

Cerdanyola del Vallés, 18th of December 2018

Table of contents

Index of figures

Index of tables

List of abbreviations

ALL	Acute Lymphocytic Leukemia
Akt	Protein Kinase B
ANOVA	Analysis of variances
APC	Antigen presenting cell
APS	Ammonium persulfate
Asp	Aspartic acid
ATP	Adenosine- 5'- triphosphate
Bad	Bcl-2-associated death promoter
BBB	Blood Brain Barrier
BSA	Bovine serum albumin
BDTP	Below Detection Threshold Period
CAR	Chimeric antigen receptor
CD	Cluster of differentiation
Cdk	Cyclin-dependent kinases
Cho	Choline
CI	Combination index
CK2	Protein Kinase CK2
CL	Contralateral Brain
CNS	Central nervous system
CPA	Cyclophosphamide
Cre	Creatine
CRT	Calreticulin
CTL	Cytotoxic T lymphocyte
CTLA-4	T-lymphocyte antigen 4
CX-4945	5-(3-chlorophenylamino)benzo(c)(2,6)naphthyridine-8-carboxylic acid
DAMP	Damage-associated molecular patterns
DC	Dendritic cell
Dm	Median effect dose
DMAT	2-Dimethylamino-4,5,6,7-tetrabromo-1H-benzimidazole
DMPM	Dynamic MRSI processing Module
DMSO	Dimethyl sulfoxide
Doxo	Doxorubicin
DRB	5,6-dichloro-1-(β-ribofuranosyl)benzimidazole
DTT	Dithiothreitol

Dx	Affected fraction at x concentration
EC_{50}	Half maximal effective concentration
EDTA	Ethylenediaminetetraacetic acid
EGFR	Epidermal growth factor receptor
ELISA	Enzyme-linked immunosorbent assay
EP	Exponential phase
ER	Endoplasmic reticulum
ETL	Echo Time Length
fa	Affected fraction
FASTMAP	Fast Automatic Shimming Technique by Mapping Along Projections
FBS	Fetal bovine serum
FOV	Field of View
FSC	Forward scatter
fu	Unaffected fraction
GB	Glioblastoma
GEM	Genetically engineered mice
GL261	Glioma 261
Glu	Glutamic acid
GTP	Guanosine-5'-triphosphate
Gy	Gray
HMGB	High Mobility Group Box 1
HPLC	High Performance Liquid Chromatography
HR	High response
HSP	Heat Shock Protein
IC_{50}	Half maximal inhibitory concentration
ICD	Immunogenic cell damage
IMS	Immune Enhanced Metronomic Schedule
IFN	Interferon
IG	Immunoglobulin
IL	Interleukin
IP	Intraperitoneal
IR	Intermediate Response
IT	Interslice thickness
kDa	kilodalton

KS	Kolmogorov-Smirnov
Lac	Lactate
LR	Low response
m	Hill-type coefficient
MeA	Methylated adenine
MeG	Methylated guanine
MGMT	O6-methylguanine-DNA methyltransferase
MHC	Major histocompatibility complex
ML	Mobile lipids
MM	Mobile macromolecules
MMR	Mismatch Repair System
MS	Mass spectrometry
MRI	Magnetic resonance imaging
MRS	Magnetic resonance spectroscopy
MRSI	Magnetic resonance spectroscopic imaging
MTD	Maximum tolerated dose
MTIC	Methyl-triazeno imidazole carboxamide
MTX	Matrix size
mTOR	Mammalian target of rapamycin
MTT	3-(4,5-dimethylthiazol-2-yl)-2,5-diphenyltetrazolium bromide
NA	Number of acquisitions
NAA	N-acetylaspartate
NF-κB	Kappa-light-chain-enhancer of activated B cells
NK	Natural killer
NMF	Non-negative matrix factorization
NMR	Nuclear Magnetic Resonance
NS	Number of scans
OS	Overall survival
p21	Cyclin-dependent kinase inhibitor 1
PBS	Phosphate-buffered saline
PC	Pharmacokinetics
PCP	Postconfluent phase
PDK-1	3'-phosphoinositide-dependent kinase- 1
PD	Pharmacodynamics

PFS	Progression Free Survival
PI	Propidium Iodide
p.i.	Postimplantation
PI3K	Phosphoinositide 3-kinase
Pim	Proviral integration Moloney virus
PP2A	Protein phosphatase 2
ppm	Parts per million
PR	Pattern recognition
PRESS	Point-Resolved Spectroscopy
PUFA	Polyunsaturated fatty acids
PVDF	Polyvinylidene fluoride
RAGE	Receptor for advanced glycation end-products
ROI	Region of interest
ROS	Reactive oxygen species
RT	Radiotherapy
SDS-PAGE	Sodium Dodecyl Sulfate Polyacrylamide Gel Electrophoresis
Ser	Serine
SSC	Side scatter
ST	Slice thickness
SW	Sweep width
T2w	T2 weighted MRI
TAT	Total acquisition time
TBS	Tris Buffered Saline
TBB	4,5,6,7-Tetrabromobenzotriazole
TBI	4,5,6,7-tetrabromo-1H-benzimidazole
TDB	1-(β-D-2'-deoxyribofuranosyl)-4,5,6,7-tetrabromo-1H-benzimidazole
TE	Echo Time
TE (eff)	Effective Echo Time
TEMED	Tetrametiletilendiamine
Thr	Threonine
TLR	Toll like receptor
TMZ	Temozolomide
TR	Relaxation Time
Treg	Regulatory T cells

TTBS	Tween Tris Buffered Saline
TV	Tumor volume
UPR	Unfolded protein response
UT	Untreated
VAPOR	Variable Power and Optimized Relaxation Delay
VOI	Volume of interest
wt	Wild type

1 Introduction

1.1 Brain tumors

Tumors of the central nervous system (CNS) comprise less than 2% of all cancer cases diagnosed each year worldwide, although their prognosis is very poor, accounting for a high mortality rate [1]. Among CNS tumors, brain tumors are a common designation for tumors arising in the intracranial regions, that could be either benign or malignant (Figure 1A). Brain tumors could be either primary tumors, originated in the brain, or secondary tumors, with a metastatic origin resulting from cancers primarily located in other organs [2] such as lungs or colon. The incidence of brain tumors in Spain is 9.2 cases per 100,000 population [1], while the incidence rates worldwide are shown in Figure 1B. According to Rouse et al [3], brain tumors are one of the types leading to highest number of years of life lost (20 years in average), which is a measure of how much a patient's life is likely to be shortened by his or her cancer.

Primary brain tumors are designated according to their originating cell type. Gliomas, which arise from glial cells, are the most prevalent brain tumor type, and can account for ca. 31% of all primary brain tumors [4]. According to their malignancy, gliomas are classified into 4 different grades. Grade IV gliomas, also called glioblastomas (GB), are the most aggressive form of gliomas, characterized by mitotically active lesions, with a high vascular proliferation, necrotic areas and a rapid pre and postoperative evolution of the disease [2].

1.2 Glioblastoma treatment

Glioblastoma is the most prevalent malignant primary brain tumor in adults [2] with a median survival below 18 months even after aggressive treatment [5]. The standard treatment for GB nowadays is maximal surgical resection followed by ionizing radiation treatment and chemotherapy with the alkylating agent Temozolomide (TMZ) (see section 1.2.3 for details). Other therapies are being tested (see section 1.2.4) but nowadays there is no reported cure for GB. Improvements in follow-up and patient management are urgently needed to improve patient's outcome (section 1.5 for more details).

1.2.1 Surgery

Whenever possible, maximal surgical resection is the first step in therapy for GB, provided that eloquent brain areas are not affected. The main goal of this procedure is to remove as much tumor mass as possible without compromising the neurological functions of the patient. Fluorescence-guided surgery using 5-aminolevulinic acid is often used for a better visualization of the tumor tissue, improving the possibility of achieving a complete tumor resection [6]. Despite these improvements, the diffuse tumor distributions and the highly infiltrative pattern displayed by GB commonly restricts complete surgical resection and even if this is possible, the

disseminated tumor cells across the brain will proliferate and give rise to new tumor masses. For these reasons, surgery must be accompanied by adjuvant and postoperative radio and chemotherapy.

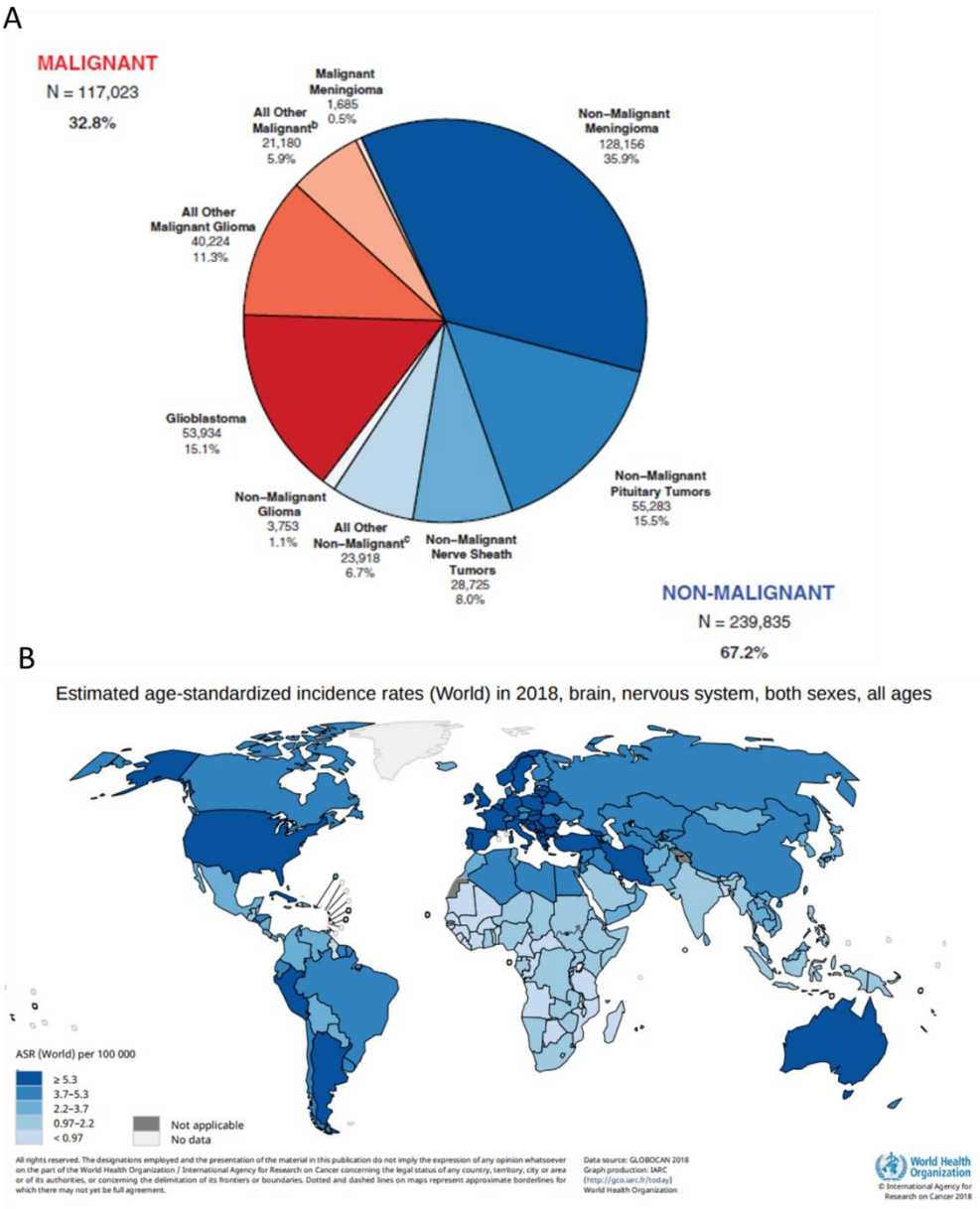

Figure 1: CNS tumors classification and incidence.
A) Distribution of Primary Brain and CNS Tumors by Behavior (n = 356,858) in the United States from 2008-2012, CBTRUS Statistical Report: NPCR and SEER, 2008-2012. The overall average incidence rate for 2008-2012 in the United States for all primary brain and CNS tumors are 21.97 per 100,000 population [7]. B) Worldwide incidence of malignant brain tumors in 2018 ASR (Age Standardized Rate) (Global Cancer observatory http://gco.iarc.fr/).

1.2.2 Radiotherapy

Radiotherapy (RT) consists of the administration of ionizing radiation either directly to the location of the tumor or at a systemic level with the use of radioactive drugs. The main goal of RT is to kill tumor cells, while leaving normal cells intact and sometimes, non-invasive methods

such as Magnetic Resonance Spectroscopy Imaging (MRSI) (section 1.5) can be used to help and plan irradiation. RT has been shown to not only be efficient killing tumor cells but also to trigger immunogenic signals [8, 9] (see section 1.3.3.1 for a comprehensive description of immunogenic signals) and even improve patient's survival (ca. 4 months described in [10]. However, even when applying the best tolerated RT dose, GB will relapse and kill the patient.

1.2.3 Chemotherapy for GB treatment – TMZ

Chemotherapy is defined as the use of anti-cancer drugs, usually cytotoxic, either with a curative intent or to prolong patient's life. The alkylating agent Temozolomide (TMZ) is the standard chemotherapeutic treatment for GB nowadays [5], based on the "European Organisation for Research and Treatment of Cancer" (EORTC) Brain Tumor and Radiotherapy Groups and the National Cancer Institute of Canada (NCIC) Clinical Trials Group protocols. TMZ is a small (194Da) lipophilic molecule, orally bioavailable and capable to penetrate the blood brain barrier, achieving effective concentrations in the cerebrospinal fluid and in the brain parenchyma [11].

1.2.3.1 TMZ mechanism of action

TMZ is a prodrug which is stable at acidic pH value and labile above pH 7, with a plasma half-life of 1.8 hours at pH 7.4 [11]. Thus, TMZ is absorbed intact and is further hydrolyzed to its active form, methyl-triazeno imidazole carboxamide (MTIC) (Figure 2). MTIC is immediately converted into 5-aminoimidazole-4-carboxamide (AIC) and the electrophilic alkylating methyldiazonium cation that transfers a methyl group to DNA. Differences between intracellular and extracellular pH in brain tumors favors TMZ activation inside cells. The pH inside tumor cells decreases due to the high glycolytic activity and, in order to counteract the intracellular enhanced acidification, tumor cells increase the extracellular pH by ion channel related mechanisms. The fact that normoxic brain tumor cells possess a more alkaline pH compared with the surrounding healthy tissue ultimately favors prodrug activation preferentially within tumor tissue [12]. The active species methyldiazonium cation preferentially methylates DNA at N7 positions of guanine in guanine rich regions (N7-MeG; 70%), but also methylates N3 adenine (N3-MeA; 9%) and O6 guanine residues (O6-MeG; 6%) [12]. Although being the least frequent lesion, O6-meG adducts are the responsible for the cytotoxic effect triggered by TMZ.

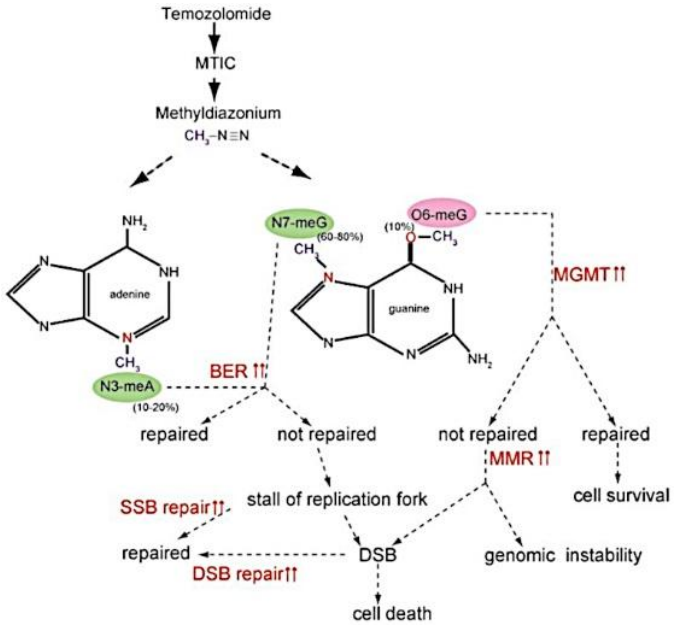

Figure 2: *Pathway for Temozolomide activation, resulting metabolites and activated DNA repair pathways* [14]. *MGMT: O6-methylguanine DNA methyltransferase. BER: base excision repair. SSB: single strand break. DSB: double strand break. MMR: mismatch repair.*

The O6-methylguanine-DNA methyltransferase (MGMT) repairs the O6-meG DNA adducts by transferring the methyl group to its own cysteine residue. MGMT is a suicide enzyme since it is degraded after repairing the DNA lesion. During DNA replication, when this enzyme is missing or low expressed and this lesion is not reverted, the O6-MeG mispairs with thymidine instead of cytosine, triggering the activation of the DNA mismatch repair system (MMR) [14].

The MMR only excises the thymidine residue of the 'daughter' strand, but the O6-MeG of the template strand is not repaired or removed. Thus, the cycle of insertion and excision of thymidine provoke multiple DNA strand breaks, leading to replication fork collapse and subsequent G2/M cycle arrest in the second cell cycle following treatment [14]. Therefore, tumors with low MGMT expression and a functional MMR should be more sensitive to TMZ action [16].

1.2.3.2 Effect of TMZ in GB cells

TMZ was historically thought to trigger a cytotoxic effect in GB cells and tumors [17, 18]. However, its effect has proven to vary among different cell lines. For example, TMZ has been described to produce apoptotic-related signs in the human B lymphoblastoid MMR proficient TK6 cell line: hypodiploid DNA content, cell shrinkage, peripheral cytoplasmic vacuole formation and chromatin concentration. However, in MMR deficient cell line MT1 no signs of apoptotic death were shown after TMZ treatment [15]. These findings suggest that TMZ can trigger a cytotoxic effect on cells with certain characteristics, such as MGMT low expression or a MMR proficient profile. On the other hand, TMZ has been described to trigger CRT exposure

[20] and HMGB-1 release [21] in a GL26 glioma model. Both are recognized DAMPs (see section 1.2.1) which could elicit immune system attraction to the damage location, changing the simplistic paradigm claiming that the whole therapeutic effect would be exclusively due to massive cell death due to DNA lesions and cell cycle arrest.

1.2.4 Treatment pitfalls and second line alternatives

After GB surgery, the standard treatment protocol in humans consists of a daily dose of TMZ at 75 mg/m^2 for 6 weeks combined with RT in 30 fractions of 2 Gy. After this treatment, six additional maintenance cycles of TMZ are administered in a therapy schedule of 5 days of a 28-day cycle at 150-200 mg/m^2 standard treatment. The median overall survival (OS) for patients receiving this treatment is 14.6 months [5]. Moreover, although some evidence suggests that administration of more than 6 cycles of TMZ may benefit patient's OS, this has not been yet confirmed in a randomized clinical trial [22]. One of the main problems associated with TMZ treatment is the development of resistance mechanisms, being the most accepted one due to MGMT overexpression (details in section 1.2.3.1). A dose-dense schedule of TMZ was designed by authors in [23], hypothesizing that longer TMZ exposure would deplete MGMT levels. In this treatment schedule, the six adjuvant cycles of TMZ were of 21 consecutive days of treatment, instead of 5 days, in a 28-day cycle at 75-100 mg/m^2. However, neither the progression free survival (PFS) nor the OS were increased in comparison with the standard treatment. Several and severe side effects are described for GB treatment with TMZ. Among them, fatigue and vomiting and serious blood cells alterations, such as severe neutropenia, thrombocytopenia, leukopenia and anemia [18], highlighting the impairment of the patient's immune system produced by these therapies.

Classical second line and novel alternatives/targets reaching clinical trials

Once patients stop responding to TMZ, second line alternatives such as interstitial chemotherapy with implantable carmustine wafels (Gliadel) or antiangiogenic therapies such as Bevacizumab [24] can be used, but their benefits in overall survival are unclear. Other therapeutic approaches, already approved for cancer treatment, are being tested for glioblastoma, either alone or in combination with standard chemotherapy. For example, immune checkpoint inhibitors as anti-PDI (Nivolumab [25], approved for melanoma, lung and kidney cancer treatment) reached phase III studies for recurrent glioblastoma[1]. In addition, novel compounds with different targets were studied and reached clinical trials, such as enzastaurin or temsirolimus. Enzastaurin is a potent inhibitor of protein kinase C-beta which

[1] https://clinicaltrials.gov/ct2/show/NCT02017717, still active

also inhibits angiogenesis [26] which reached phase III studies[2] or the mammalian target of rapamycin (mTOR) inhibitor temsirolimus [27], approved for kidney cancer and which reached phase I/II studies for glioblastoma, either alone or in combination with other therapeutic strategies[3]. Different approaches as tumor treating fields (electric fields alternating at a frequency of 200 kHz on patient's head, selectively blocking tumor cell division during mitosis) plus TMZ have shown some improvement in survival in comparison with TMZ alone [28] with a very large increase in treatment cost. In summary, unfortunately, the available results until now show no or only modest improvement in OS, confirming the complex landscape in GB treatment. It is worth mentioning that most clinical trials are focused in recurrent glioblastoma, which indeed contributes to making the therapeutic challenge more complex. Reviews about different approaches in clinical trials and the actual perspective can be found in [29, 30].

Despite all efforts made to improve GB outcome, the fact is that no effective therapeutic strategies have been found and the standard treatments did not quite improve outcome since 2005. Moreover, small patient cohort, tumors and patients' heterogeneity, the lack of appropriate controls and the numerous undesired side effects triggered by these treatments impair the development of better therapeutic solutions. The lack of effective therapies for GB highlights the urgent need of a change of paradigm in the treatment design, specially taking into account that the newly developed schedules are not novel, but based in the classical assumption that the best dose of administration is the maximum tolerated dose (MTD) [31], which may be highly toxic for the immune system of the patient.

1.3 Immune system role in response to therapy: the key for therapeutic success

Historically, as previously said, chemotherapy regimens have been applied at maximum tolerated doses (MTD) with considerable rest periods between therapy cycles, which can lead to regrowth and resistance development [32]. This was based in the assumption that the main focus of the therapy should be as much “cell killing” as possible, but the deleterious effects over the host immune system forced to alternate periods of administration with large interleave periods. Nowadays, this is changing and several aspects of the immune system participation in therapy response are being considered: not only the type and dose of drugs used, but also its timing of administration and respecting/enhancing the host immune system.

[2] https://clinicaltrials.gov/ct2/show/NCT00295815, completed with non-satisfactory results [264]

[3] https://clinicaltrials.gov/ct2/show/NCT00316849, still active

1.3.1 The Cancer Immunity Cycle

The destruction of tumor cells by the immune system occurs after a series of sequential events that are repeating in cycles, that will be referred to in the Thesis as the Cancer Immunity Cycle [33]. This cycle is a multi-step challenge (Figure 3) where antigen-presenting cells (APCs) have a relevant role in initiating the defense against cancer. Cell damage due to therapy is produced and APCs mature due to the recognition and engulfment of tumor antigens as well as signaling received from proinflammatory signals, such as cytokines. After maturation, APCs migrate to the lymphatic nodes. Once in the lymph nodes, APCs present tumor antigens to naïve CD4+ and CD8+ T cells in a process called cross-priming, causing the maturation of these cells to effector T cells. This T cell priming is followed by T cell expansion and differentiation (days 2-5 of the cycle). Then, effector T cells migrate to the tumor niche and, together with the innate immune cells, destroy antigen-expressing tumor cells. This process can occur either directly or through interaction with macrophages [34], which can represent percentages as high as 30% of the abnormal mass [35] in different polarization stages: M1 (anti-tumor) or M2 (pro-tumor) [36].

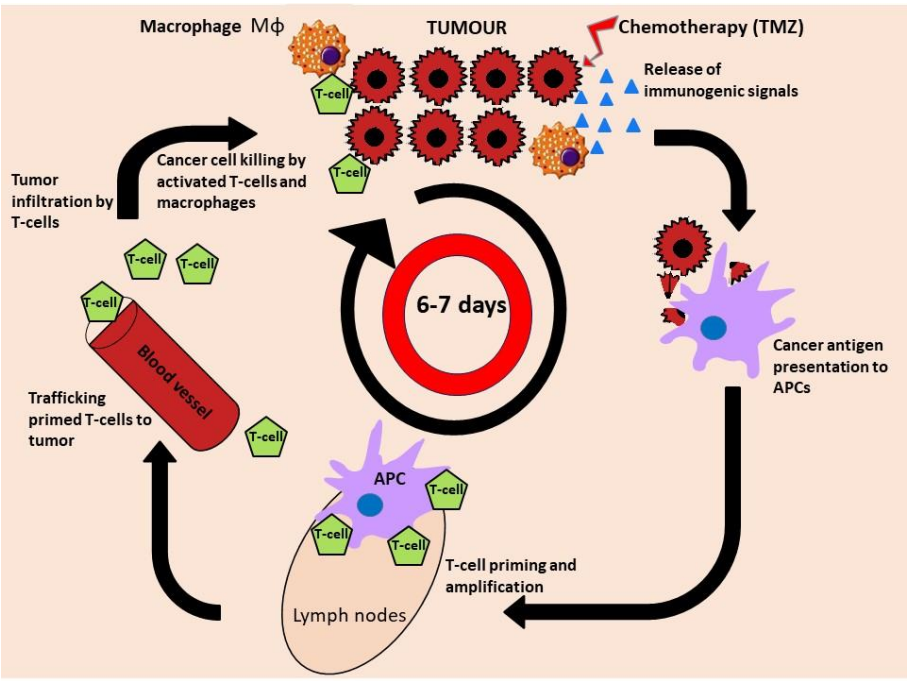

Figure 3: Scheme for Cancer Immunity Cycle after a chemotherapeutic dose.
Modified from Arias N et al [37]*; see also* [33]*: 1) Tumor cells damaged by therapy produce, expose and/or release signals that attract antigen presenting cells (APCs) and Macrophages. This may lead to recognition of compromised tumor cells and migration of APCs towards draining lymph nodes (LNs). 2) APCs present captured antigens to naive T cells within LNs. This leads to T cell expansion and generation of effectors. 3) Activated effector T cells infiltrate the tumor microenvironment where they may recognize and kill tumor cells, either directly or through M1-polarised macrophages. 4) Killing of the target cancer cells by T cells and M1 macrophages releases additional tumor-derived antigens (step 1 again) in subsequent turns of the cycle.*

Two major signals are involved in the activation or inhibition of the T-cell response: the primary signal occurs when antigens are presented to the T-cell receptor, while a secondary signal determines the T-cell response [38]. This may be exploited by tumor cells to evade immune detection. Signaling can be being either co-stimulatory or co-inhibitory of T-cell response (such as cytotoxic T-lymphocyte-associated antigen 4 (CTLA4), and programmed death-1). Still, GB tumors can counteract immune response through participation of regulatory T cells (T_{reg}) which actively suppress cytotoxic responses [39] or generation of myeloid derived suppressor cells [40] generating an immunosuppressive condition. Accordingly, in order to improve effective cancer therapy, a complete understanding of the dynamic immune environment within GB must be achieved. Moreover, in order to allow immune response to be established, adequate timing of cytotoxic/cytostatic therapeutic agent administration is crucial [41].

1.3.3 Immunotherapeutic strategies

Only about 30% of GB patients survive 2 years after being diagnosed, with the current therapeutic strategies [42], and there is urgent need to seek for leading edge therapies. One of the most relevant strategies investigated for cancer treatment worldwide in the last decade is immunotherapy, taking into account the cycle described in Figure 3.

Immunotherapy can be broadly defined as any treatment capable of stimulating the immune system to fight against an infection or a disease [43]. One relevant hallmark of cancer cells is the ability to escape immunosurveillance. Cancer cells have the ability to induce immunosuppression, by keeping a constant inflammatory milieu which leads to immunotolerance [44]. In this sense, immunotherapy aims to activate the immune system against the tumoral cells and block immunotolerance development.

The first immune-based treatment for cancer was developed by William B. Coley already in the 19th century, when he established a correlation between concomitant infections and the remission of malignant neoplasias [45]. However, this important advance in the oncologic clinical practice was doomed due to the lack of a scientific explanation for those results.

In the 50s of the 20th century, the first cancer vaccine, consisting in a tumor lysate was administered to gynecologic cancer patients [46]. Later, in the 1970s, recombinant interferon alpha was used to treat chronic myeloid leukemia [47]. Despite these limited steps occurred along the 20th century, the idea that the immune system could be key for cancer therapy success was still not fully understood or accepted, mainly due to lack of conclusive successful results.

Immunotherapies based either on ***immune checkpoints*** and ***vaccination*** [48], ***adoptive cell transfer*** [49] or based in ***metronomic therapy*** schedules have been shown to help to enhance the host immune system participation in response to therapy [50]. To elicit host immune system activation during metronomic therapy, it is relevant that therapeutic agents could trigger immunogenic cell damage (ICD) (see section 1.2.1.3 below).

Accordingly, along the last decade, some promising immunotherapies are being tested to treat human cancer. For example, the inhibition of the T-lymphocyte antigen 4 (CTLA-4), a critical immune checkpoint, is being used to treat metastatic melanoma [51]. Moreover, the adoptive cell transfer based on chimeric antigen receptor (CAR) T cells is a strategy on rise, such as CAR T cells targeted to CD19 antigen to treat acute lymphocytic leukemia (ALL) [52] and dendritic cell vaccines were used to treat prostate cancer [53]. However, these strategies are not free of limitations, because tumor cells are still able to develop immune escape mechanisms. In addition, undesired side effects [54, 55], mainly related with excessive activation of immune system, and the long-term impact of these treatments in patient's life is still unclear.

A less exploited immunotherapeutic strategy is the enhancement of host immune system elicitation and attraction to the tumor environment for an effective response to therapy. For this, it is relevant that therapeutic agents could produce the so-called immunogenic cell damage, which will be key in immune system attraction.

1.3.3.1 Immunogenic cell death/damage

In addition to the previously described immunotherapeutic treatments based on vaccination or immune checkpoints targeting, several chemotherapeutic drugs and/or drug schedules have been described to induce immunogenic cell death [56]. In fact, although several authors refer to "immunogenic cell death" in their work, tumor cells do not need to completely die to attract immune system elements and it would be more comprehensive to talk about immunogenic cell damage (ICD) rather than death. The ICD is a non-tolerogenic form of cell damage able to trigger an effective immune response against the tumor cells through the activation of both innate and adaptive immunity elements in the host. This indicates that if the suitable combination of damage-associated molecular patterns (DAMPs) is produced/exposed/released, tumor eradication will be performed by the host immune system rather than by direct killing of all tumor cells by chemotherapeutic drugs.

Damage-associated molecular patterns

The previously described "immunogenic drugs" lead tumor cells to expose or release certain molecules known as damage-associated molecular patterns (DAMPs) which are able to interact

with immune system cells and trigger an effective antitumor immune response. Danger signals or DAMPs have physiological, mostly non-immunogenic related, roles inside the cells. Once they are secreted or exposed, the immunomodulatory activities are triggered. DAMPs, together with cancer cell antigens cause the maturation of antigen presenting cells (APCs), which ultimately "cross-prime" and activate anti-tumorigenic CD4+/CD8+ T-cell immunity [57] (Figure 4, see also section 1.3.1).

The exposure and release of DAMPs are mediated by the combined action of endoplasmic reticulum (ER) stress and reactive oxygen species (ROS) production. This joint action activates danger signaling pathways that help to traffic DAMPs to the extracellular space by mechanisms that remain unclear at present. It is not surprising that these two requisites elicit ICD, since ER stress homeostasis controls the protein folding and secretory machinery while ROS production is an important mechanism related with an increase in immunogenicity [58]. The endoplasmic reticulum (ER) is an organelle involved in the synthesis, folding and post-translational modifications of a large number of proteins. When ER stress occurs, normally by an accumulation of unfolded and misfolded proteins, a complex signaling pathway called the unfolded protein response (UPR) is activated. To restore ER homeostasis, UPR temporary halts the translation of big proteins, while increasing the overall production of chaperones to help protein folding. If ER stress becomes severe, UPR turns to a pro-death pathway and the cell undergoes apoptosis [59].

The oxidative modification of molecules has been shown to increase immunogenicity and enable danger signaling [58]. ER stress and ROS production have been described to be indispensable to elicit ICD, although the mechanisms remain elusive [60].

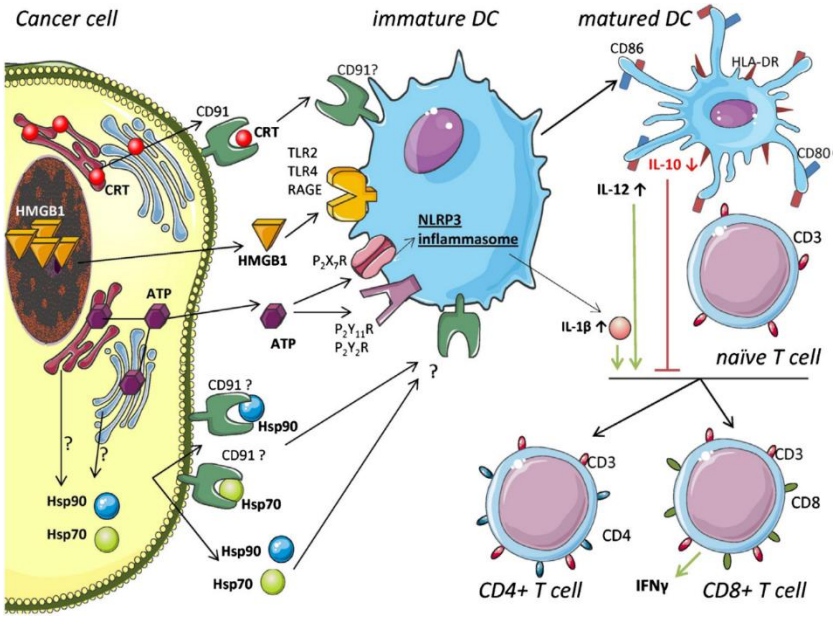

Figure 4: Schematic representation of immunogenic cell damage (ICD) in cancer cells. *Cancer cells undergoing ICD emit DAMPs: surface exposed (ecto-) CRT, secreted ATP, surface exposed HSP90 or HSP70 and passively released HMGB1, HSP70 or HSP90* [61]

The main DAMPS described in literature are summarized below:

1. Calreticulin

Calreticulin (CRT) is a highly conserved Ca^{2+}-binding protein. In the ER, CRT functions as a chaperone and regulates Ca^{2+} homeostasis and signaling. Along its physiological functions, CRT helps in the proper assembly of the Major Histocompatibility Complex (MHC) class I molecules and in antigen loading. Outside the ER, CRT also regulates nuclear transport, cell proliferation and migration [62, 63].

CRT exposure is described as one of the first events in the ICD cascade, in pre and early apoptotic stages. Its exposure is thought to be an active process mediated by a secretory pathway [64]. Once exposed, CRT is a potent "eat-me" signal recognized by Cluster of Differentiation (CD) 91, a receptor present in dendritic cells (DCs, which are antigen-presenting cells) [65]. This recognition facilitates the engulfment of the CRT-exposing tumor cell by DCs, which leads to tumor antigen presentation and tumor-specific cytotoxic T lymphocyte (CTL) responses (see also section 1.3.1). Moreover, CRT can be a potent inducer of activation and maturation of B cells and macrophages [65]. CRT has been also described to facilitate engulfment by phagocytes, since it possesses homologues of prominent phagocytosis motifs (NPxY and KGE) [66].

2. ATP release

Extracellular nucleotides have emerged as important regulators of inflammatory and immune responses. In particular, extracellular release of ATP has been described to activate eosinophils and stimulate the proliferation of T lymphocytes by Ca^{2+} mobilization mechanisms, membrane

polarization and upregulation of CD11b [67]. Extracellular ATP is also a well-known “find-me” signal released from apoptotic cells and released ATP was described to bind to P_2Y, P_2X and P_2Z receptors of macrophages, DCs, neutrophils and tumor cells [68–70].

When ATP binds the P_2 family receptors, it causes the activation of the NLRP3 inflammasome, activating the secretion of interleukin (IL)-1β. The IL-1β secretion, together with antigen presentation, are required for the CD8+ T cell polarization for interferon (IFN)-γ production and ultimately for the immune response against tumors[71]. According to this, extracellular ATP has been described to trigger DCs maturation, augmenting DCs' capacity to promote naïve T cells proliferation [72].

3. High Mobility Group Box 1

The High Mobility Group Box 1 (HMGB1) is usually located in the nucleus, where it acts as a DNA-binding transcription factor. HMGB1 can be actively secreted by macrophages, DCs and natural killer (NK) cells or it can be also passively released by necrotic cells, acting as a pro-inflammatory cytokine [73]. HMGB1 binds to Toll-Like receptor (TLR)-2, TLR-4 and receptor for advanced glycation end-products (RAGE) [74] leading to nuclear factor kappa-light-chain-enhancer of activated B cells (NF-κB) activation [75].

During ICD, passively-released HMGB1 from necrotic tumor cells has been shown to bind TLR-4 on DCs, stimulating the production of proinflammatory cytokines and assisting in proper antigen presentation [76].

4. Other DAMPs

The first three mentioned DAMPs are the most relevant and widely described, but other molecules have been also reported to contribute to ICD. For example, genomic DNA has been described to provoke TLR9 and NACHT, LRR and PYD domains-containing protein 3-mediated innate immune response and DC maturation. Also, the heat-shock protein (HSP)70 and 90 are involved in the recruitment of immune cells, DC maturation and T-cell based antitumor immunity. Finally, uric acid crystals can induce DC maturation and neutrophil recruitment [61, 77–80].

1.3.1.4 Types of ICD inducers

The ER is a key organelle responsible for proper protein synthesis and folding. When ER homeostasis is disrupted, it leads to an accumulation of unfolded and misfolded proteins. In response to this ER stress, cells activate certain defense pathways called unfolded protein response (UPR), which increase ER volume, ER-associated chaperones expression and attenuate global protein translation. When ER stress is too severe, UPR engages signaling

pathways culminating into immunogenic cell death [81]. Moreover, ER stress inducers have been shown to sensitize tumor cells to certain chemotherapeutic drugs [82]. Some of the therapeutic strategies classically described to be immunogenic cell death inducers are doxorubicin, mitoxantrone and γ-irradiation. Depending on the administration scheme, several drugs can induce ICD, although they are not known as classical inducers, for example TMZ [20]. Classical ICD inducers can be classified into two major groups, type I and type II. ***Type I inducers*** target cytosolic proteins, plasma membrane channels or DNA-replication proteins, but not directly the ER. They induce ICD-danger signaling through collateral ER stress effects. Some examples of type I inducers are anthracyclines, such as doxorubicin, or radiotherapy and cyclophosphamide (CPA). On the other hand, ***Type II inducers*** selectively target the ER, inducing both cell death and ICD-associated immunogenicity in an ER-focused manner. They are more effective in inducing ICD than type I inducers. Some examples are photodynamic therapy and coxsackievirus B3 [61].

Having in mind that DAMPs produced by cellular damage initiate and mediate in the host immune response, having a fully active immune system is a key point. Still, it should not be neglected that damage produced by therapeutic agents is usually nonspecific and non-selective and immune system cells can be also damaged: if this is the case, even with a massive DAMPs production, no or little effective immune response will be triggered against the target tumor. For example, if T-cell amplification and proliferation were to be impaired, this would compromise the outcome of the immune response and in consequence, of the therapeutic strategy. This has lead to the development of different therapeutic strategies, such as metronomic administration (see below).

1.3.1.5 Metronomic treatment: adjusting timing

As opposed to MTD schemes, metronomic chemotherapy was defined as the frequent and equally spaced administration of the minimum biological effective dose, significantly below the MTD, of chemotherapeutic drugs without long rest periods [83]. Along this Thesis, our group has tested another modality of metronomic administration, in which the chemotherapeutic drug is administered every 6 days, as described by other authors [84]. This is effective in enhancing antitumoral immune responses, leading to tumor regression and avoiding tumor regrowth. These authors [84] used an every 6 days schedule for CPA, showing potent antitumor response in preclinical subcutaneous GL261 GB growing in C57BL/6j mice. As soon as after 2 therapy cycles, an increase in tumor-associated NK cells, DCs and macrophages was observed, followed by an increase in the innate response (i.e. increase of CD4+ helper T cells and CD8+ cytotoxic T effector cells but not of T_{regs}). These observations suggest that this

administration schedule activates the adaptive immune response against the tumor which induced specific long-term T-cell tumor memory. This administration schedule also proved useful with TMZ (see also section 4.3.3) alone, and also in combination with other therapeutic agents [85]. In order to avoid confusion with the original "metronomic schedule" meaning in which the 6-7 day interval was not contemplated, our group coined a new expression: **the "Immune-enhancing Metronomic Schedule" (IMS)**. Conceptually similar approaches have been also used in clinical studies for GB, such as the study with the alkylating agent Fotemustine, although only with a restricted number of cycles being administered [86].

1.4 Preclinical models to investigate human glioblastoma

Clinical trials performed in GB patients have several limitations that prevent proper evaluation of novel therapy agents or combinations that could lead to improvements in therapy outcome and overall survival. First, the heterogeneity among patients' conditions, disease progression and therapy response are a challenge in these experimental sets. In addition, small cohort sizes and ethical restrictions such as the obvious absence of a control, non-administered group or the intermediate histopathological validation also hamper a full evaluation and reaching conclusions. In this sense, preclinical approaches allow us to investigate the evolution of control groups, to perform repeated explorations and to euthanize animals for molecular or pathological validation purposes. For these reasons, preclinical models are essential and useful tools to investigate novel drugs and new therapeutic schedules.

Taking into account the relevance of the immune system in the response to therapy, we should consider that the chosen preclinical model must recapitulate as close as possible the human disease including immune system features and influence [87]. Tumor environment is also relevant, and ectopic, subcutaneous models were described to provide over-optimistic therapy response results with respect to orthotopic, intracerebral models [88]. Useful data can be generated from diverse models, especially regarding treatment and resistance to therapy, also opening up the possibility of exploring combinations of treatments. A brief explanation of the main preclinical models suitable for brain tumors response to therapy evaluation will be provided below. Most of the currently available models are murine, and the mouse genome has a high level of similarity to humans and is well characterized [89], although more recent studies suggest some degree of transcriptional regulation divergence between human and mice genome [90]. Murine brain tumor models can be either spontaneous (Genetically engineered mouse models), or transplantable, generated through injection of cell or tissue samples.

Transplantable models

The most commonly used preclinical models for GB research are generated by external cell or tumor implantation into healthy mice. Depending on the site of implantation, animal models can be classified as ectopic or orthotopic (Figure 5). **Ectopic tumors** are generated in a different site from where disease naturally occurs, normally subcutaneously (mice flank). This strategy allows an easy tumor generation and monitoring. However, the lack of a proper tumor microenvironment may not recapitulate relevant characteristics crucial for therapy outcome, like cerebral parenchyma infiltration, one of the most important characteristics implicated in tumor recurrence, the most common cause of GB treatment failure [87]. On the other hand, *i*n **orthotopic tumors**, the site of implantation is the same where the disease naturally occurs, in our case, the brain. This helps mimicking the infiltrative nature of GB and its tumor microenvironment, although not in such reliable manner as in Genetic Engineered mice (GEM), in which the spontaneous appearance mimics better tumor progression. Non-invasive techniques, such as Magnetic Resonance Imaging (MRI) or Magnetic Resonance Spectroscopy (MRS) are needed to follow up disease progression, as opposed to caliper methods, which can be used to monitor ectopic tumors. Cells/tissues implanted could have the same species origin (syngeneic/isogeneic, depending on genetic background) or a different origin (the so-called xenografts).

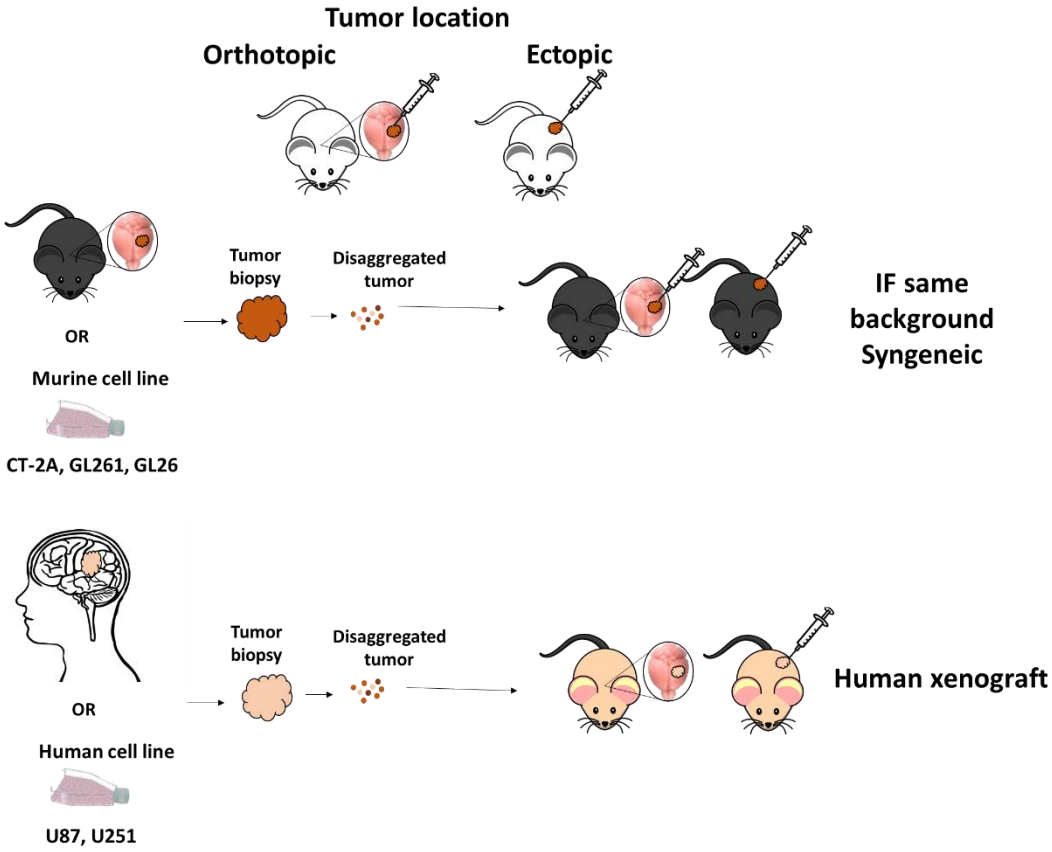

Figure 5: Glioma preclinical models.
Regarding their location, mice models can be classified in orthotopic, if the tumor is injected in the equivalent organ where the tumor was originated, or ectopic, if the tumor is injected in a different site, being in general subcutaneous. By its origin, preclinical mouse models can be syngeneic, meaning that the cells or tissue implanted originated in a mouse with the same genetic background. In this case, immunocompetent mice can be used for tumor generation. If the tumor cells are of human (or any non-mouse) origin, immunocompromised mouse strains are needed and these models are called xenografts.

A. ***Xenograft models:*** For xenograft models generation, tumor cells from different species (in general humans in case of brain tumors, also called PDX, patient-derived xenografts) are implanted in immunocompromised mice. There are different grades of immunocompromised mice [91], consequently they do not recapitulate the role of the host immune system. Evenso, they are widely used in cancer therapy research. The United States National Cancer Institute guidelines from drug screening for anticancer therapies require testing human tumors xenotransplanted into immunocompromised mice, since it should allow the assessment of the therapeutic effect of the studied drug over those specific tumor cells [92]. However, this requirement hampers the study of the role of the host immune system in cancer treatment, which has been proven to be crucial for therapeutic success [93], and should not be neglected.

B. ***Syngeneic/Isogeneic models:*** The syngeneic mice models are generated by the implantation of tumor cells from the same genetic background of the host mice, ensuring a

very low or inexistent basal immune response against the implanted tumor cells. These models allow working with immunocompetent animals, being suitable to study the full role of the immune system in therapy response [94].

Genetically Engineered Mouse models (GEM)

The GEM models mimic better the invasiveness, angiogenesis and tumor microenvironment of human GB in comparison with transplantable models. These models bear certain genetic alterations such as EGFR overexpression or ink4a/arf deletion [87], that provoke the spontaneous appearance of tumors throughout animal's life. However, one of the handicaps of this type of model is the time required for tumor development and low penetrance in comparison with the transplantable model (unpublished data from our group with 5 GEM colonies). Finally, high heterogeneity from groups prevents suitable therapy studies.

1.4.1 GL261 model

The GL261 mice model is a transplantable, orthotopic and syngeneic GB model generated by the stereotactic injection of the murine glioma cell line GL261 into C57BL/6j mice. It mimics the characteristic infiltrative pattern and aggressiveness of GB and its high penetrance and reproducibility allow the formation of homogeneous tumor-bearing mice groups, ideal for therapy-response evaluation. Moreover, the immune system of the GL261 mice is intact [95] which allows the assessment of its participation and relevance in therapy response. This model was generated first in the early 40's [96] and it would probably belong to the "venerable" tumor classes [97] where no or few immunological effects are expected against the tumor when inoculating these cells in immunocompetent mice. This model has been largely used as an *in vivo* model for GB characterization and therapy evaluation, being one of the most common immunocompetent preclinical models used for GB research, in our group [37, 98–100] and other researcher groups worldwide [101–104]. Regarding the GL261 cell line, not much is known about its molecular characteristics. Still, it has been described that GL261 cells carry point mutations in K-ras and p53 genes and they express basal MHCI, but not MHCII [95]. Considering its advantages and disadvantages, and the relevant background of our group with the GL261 model, it was chosen for the work developed in this thesis.

1.5 Targeted therapies as novel glioblastoma therapeutic strategies

Several proteins have been described to be over expressed in GB which would lead to an increased activation of pro-survival, anti-angiogenic or pro invasion pathways enhancing GB growth and invasiveness [105–107]. Inhibition of protein kinases by small molecular weight inhibitors is being evaluated for treatment of several types of cancer. Some of these inhibitors

have been tested in clinical trials for GB in combination with standard therapeutic agents. Examples are the Endothelial Growth Factor Receptor inhibitor erlotinib[4] (a tyrosine kinase inhibitor), or the Platelet-Derived Growth Factor inhibitor imatinib mesylate[5] (a tyrosine kinase inhibitor commercialized as Gleevec® for acute lymphocytic leukemia, and was also tested for GB in the past years). More recently, the multikinase inhibitor regorafenib (inhibitor of some tyrosine kinases and several mutant oncogenic kinases) is producing satisfactory results in relapsing glioblastoma[6].

Protein Kinase CK2 and proviral integration Moloney virus (Pim)-1 are two serine-threonine kinases over expressed in several types of cancer that are related with pro survival and anti-apoptotic pathways [108, 109] and this non-mutagenic therapies were exploited in this thesis for preclinical GB treatment as it was proven useful in previous work [110, 111]. Both CK2 and Pim-1 inhibitors are being evaluated to treat several types of cancer at preclinical and clinical levels (see section 1.4.3).

1.5.1 Protein kinase CK2

Protein kinase CK2 is a serine threonine kinase, ubiquitously expressed and constitutively active. CK2 is a pleiotropic kinase that has a very large number of substrates [112] and therefore it is involved in many cellular processes, such as cell cycle, gene expression, protein synthesis and metabolism [108]. CK2 is implicated in the regulation of multiple signaling pathways, mostly related with survival, proliferation and development which are involved in oncogenesis [113]. Some examples are the Phosphoinositide 3-kinase (PI3K)/Protein Kinase B(Akt) pathway [114], which promotes survival and growth in response to extracellular signals, the Wnt/β-catenin pathway, which is involved in cellular migration and proliferation during embryonic development [115] or NFκβ signaling, which plays a role in DNA transcription, cytokine production and cellular survival [116]. CK2 has the ability to phosphorylate serine or threonine residues located close to acidic amino acids. The minimal consensus sequence established for phosphorylation by CK2 is serine(Ser)/threonine(Thr)-Xaa-Xaa-Acidic, where the acidic residue may be glutamic acid (Glu), aspartic acid (Asp), phospho(p)Ser or pTyrosine [117].

1.5.1.1 CK2 subunits

CK2 is a tetramer, consisting of two catalytic subunits (2α/αα'/2α') and two regulatory subunits (2β) (Figure 6) and uses either Adenosine-5'-triphosphate (ATP) or Guanosine-5'-triphosphate

[4] https://clinicaltrials.gov/ct2/show/NCT00039494
[5] https://clinicaltrials.gov/ct2/show/NCT00290771
[6] https://clinicaltrials.gov/ct2/show/NCT02926222

(GTP) as phosphate donor. Depending on the protein substrate, CK2 activity can be enhanced or decreased upon binding of the catalytic subunit to a dimer of CK2β, because some protein substrates are exclusively phosphorylated by the free catalytic CK2 subunits α and α' [118] while others are phosphorylated by tetrameric CK2, also called holoenzyme [119].

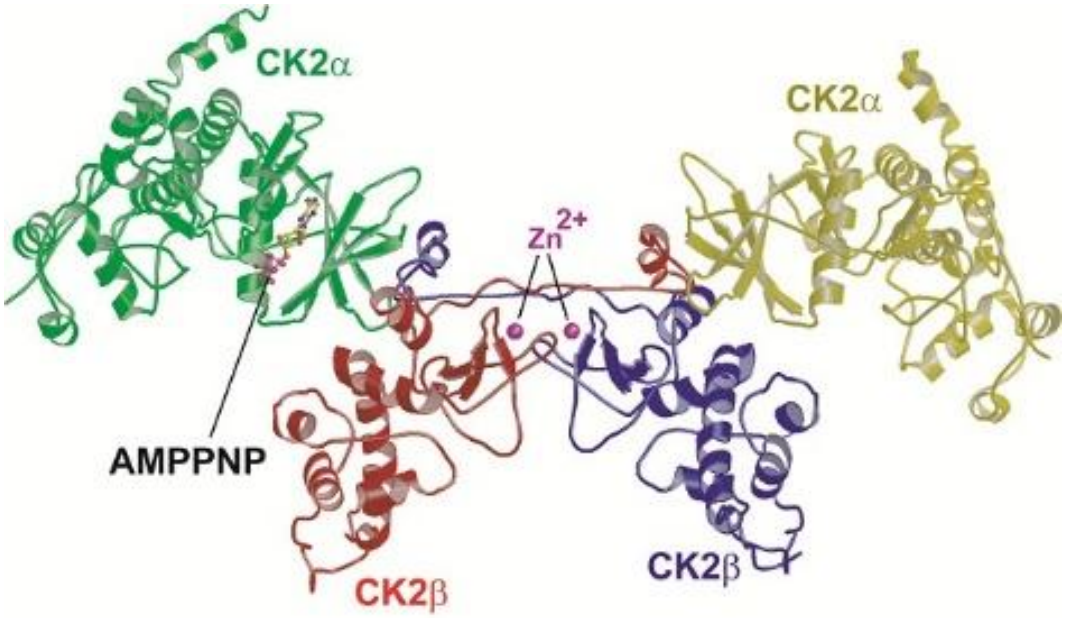

Figure 6: Tridimensional structure of tetrameric CK2.
The catalytic CK2α subunits are shown in green and yelow, while one of the regulatory CK2β subunits are shown in red and purple.AMPPNP states for nonhydrolyzable ATP analogue adenosine 5«-[β,γ-imido]triphosphate, which is located in the ATP binding site of one of the CK2α subunits [120].

The two isozymic forms of the catalytic subunit of CK2 are encoded by two different genes and exhibit extensive similarity within their catalytic domains but have completely unrelated C-terminal sequences [121]. Mice lacking CK2α show embryonic lethality, with structural defects in heart and neural tube [122]. In contrast, homozygous null CK2α' -/- mice are viable, but the males are sterile due to abnormal spermatogenesis [123]. Moreover, CK2α is ubiquitously expressed in every tissue [124], whereas high concentrations of CK2α' are found exclusively in brain and testes [125], suggesting discrete functions of the isoforms. For example, CK2α' has been described to induce the degradation of Breast Cancer Metastasis Suppressor 1 in non-small cell lung cancer, correlating with metastases increase [126]. Also, CK2α' may inhibit caspase-dependent apoptosis by specifically phosphorylating pro-caspase 3 in a inhibitory position within the caspase motif, which blocks caspase-3 cleavage by both caspases-8 and -9 [127]. On the other hand, peptidyl-prolyl cis-trans isomerase NIMA-interacting 1 [128], Protein phosphatase 2 (PP2A) [121, 129], HSP90 [130] and CK2 interacting protein 1 [131] bind to CK2α

but not no CK2α'[121, 128–132]. These facts provide further evidence to support that CK2α and CK2α' play independent roles in the cellular functions of CK2.

1.5.1.2 CK2 regulation

Little is known about the regulation of CK2 expression and activity. To date, CK2 is thought to be constitutively activated [113]. Regarding its expression, some reports state that CK2 itself may regulate CK2 expression. For instance, CK2α was found to form a complex with the CK2β gene promoter, suggesting that CK2α may regulate CK2β transcription [133]. Moreover, it was described that the inhibition of CK2 activity produces a decrease in CK2α and CK2β transcription, indicating that CK2 activity is needed for transcriptional regulation of CK2 subunits [134].

1.5.1.3 CK2 and cell cycle

CK2 is known to play a critical role in promoting cellular proliferation and several evidences suggest that CK2 could be related to cell cycle progression and cellular senescence. For instance, in *Saccaromyces cerevisae* CK2 is essential during G1/S and G2/M transitions [135]. CK2 activity increases in quiescent fibroblast after serum stimulation [136, 137], suggesting that CK2 plays an important role in the G0/G1 transition. Also, CK2α' mRNA expression is induced by serum treatment in mouse fibroblasts, correlating with an increase in CK2 activity [138]. CK2 activity and CK2α expression decrease in both replicative and H_2O_2-induced senescence human fetal lung diploid fibroblast cells [139] and CK2α' silencing induces the senescence phenotype also in this cell line [140].

Cyclins and cell cycle

The family of D-type cyclins (D1, D2, and D3) regulates the G1/S-phase transition (Figure 7). D cyclins bind and activate cyclin-dependent kinases (Cdk4 and Cdk6) to phosphorylate the retinoblastoma protein and through titration of the Cdk inhibitors cyclin-dependent kinase inhibitor 1 (p21) and cyclin-dependent kinase inhibitor 1B, the cyclin D–Cdk4/6 complexes activate cyclin E/Cdk2 [141]. More specifically, cyclin D1 expression varies along cell cycle and these variations are essential for maintaining proliferation. Cyclin D1 levels must be high during G1 phase for a cell to initiate DNA synthesis, but then must be suppressed during S phase to allow an efficient DNA synthesis. If the cell should continue proliferating, cyclin D1 levels must be induced once again during G2 phase. On the contrary, if cyclin D1 expression remains low during G2 phase the cell becomes quiescent after mitosis [142]. Therefore cyclin D1 is frequently used as a proliferative marker, for example, to study the effects of different treatments in proliferation [143, 144]. In summary, cyclin D1 expression is higher in proliferating cells and decrease when cells enter in G0/G1 phase.

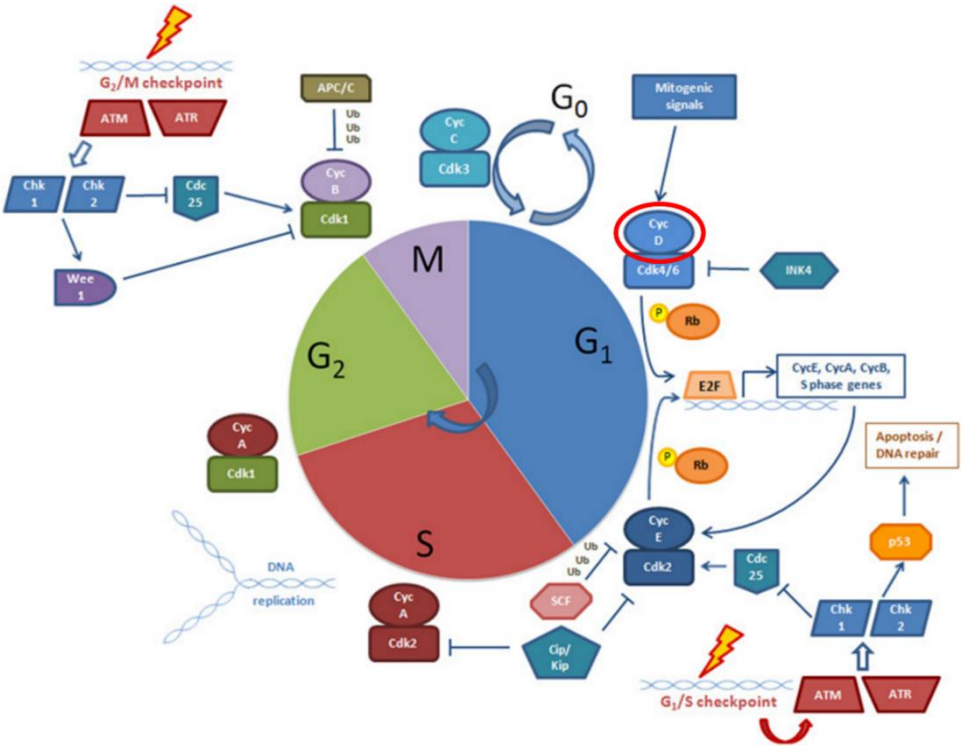

Figure 7: An overview of cell cycle progression and checkpoint regulation.
Cell cycle progression is driven by the periodic oscillation of Cdk/cyclin activities. Cdk3/cyclin C regulates cell cycle re-entry from the quiescent state. Upon mitogenic stimulation, cyclin D is upregulated to drive E2F-dependent transcription of cyclin E, cyclin A, cyclin B and genes required for S phase progression and DNA synthesis. The INK4 and Cip/Kip families of Cdk inhibitors restrain Cdk/cyclin activities. The SCF and APC/C-mediated ubiquitination of cyclins provides an additional means to control the cyclical activities of the Cdks. The DNA damage checkpoints safeguard the genomic integrity of a cell at the G1/S and G2/M boundaries [145].

1.5.1.4 CK2 and cancer

CK2 is over expressed in rapidly proliferating tissues and in human tumors, when compared to the corresponding non-neoplastic tissues. This was observed in neoplastic tissues of colorectal and breast carcinomas [146] and squamous cell carcinomas [147, 148] which is in agreement with its described role in several oncogenic pathways.

In particular, CK2α has been observed to be upregulated in GB human biopsies. Deletion of the regulatory subunit CK2β was observed only in 7% of GB biopsies. In the case of CK2α', only sporadic gene dosage gains were observed [149]. CK2α expression was found to be upregulated in GL261 GB tumor compared to wild type brain parenchyma [150], suggesting that CK2α should be the main target along CK2 subunits for GB treatment (see also section 1.5.1.1).

Abnormal high levels of CK2 activity in cancer cells create an anti-apoptotic environment and downregulation of CK2 activity in such affected cells restores apoptosis, thus suggesting a druggable target [151]. Different molecules have been identified as CK2 inhibitors [152], with

several of them having an anti-proliferative effect toward different tumor cells lines, as for example the human breast cancer cell line MCF-7 and the human leukemic lymphoblasts CCRF-CEM [153] (Figure 8).

1.5.2 Pim

Pim-1 is a serine threonine kinase, constitutively active, which induces cell cycle progression and inhibits apoptosis. Two isoforms of this protein have been described, Pim1S, the short of isoform of 33 kilodaltons (kDa), which is mainly located in the nucleus but can be also found in the cytoplasm and the long isoform, Pim1L, of 44kDa that is found only in the cytoplasm. It is known as an oncogenic protein, since its overexpression induces lymphomas in mice [109]. Some of its targets are related with increased proliferation and cell death inhibition, such as the cell cycle activating phosphatases Cdc25A and C, the cell cycle inhibitor p21 or the pro-apoptotic molecules Bcl-2, associated cell promoter (Bad) and Forkhead box O3a [154–158]. Also, the epidermal growth factor receptor (EGFR) is known to induce Pim-1 expression and some downstream effectors of Pim-1 are the pro-survival molecule Akt and the cell cycle activator c-myc [159, 160].

Thus, Pim-1 can be a novel therapeutic target for cancer treatment and more specifically could be a good target candidate for GB treatment, since EGFR, c-myc and Akt are often upregulated in GB. Moreover, no Pim-1 expression was detected in normal glial tissue, whereas a high Pim-1 expression was found in GB samples, highlighting the oncogenic role of Pim-1 in this type of cancer as described in [111]. According to these same authors [111], the preclinical model used in their work, the GL261 GB murine model, could be a good candidate to evaluate the effect of Pim-1 inhibition. GL261 cells shows high EGFR phosphorylation, an overexpression of c-myc and Akt and express HSP90, which is necessary for Pim-1 stabilization.

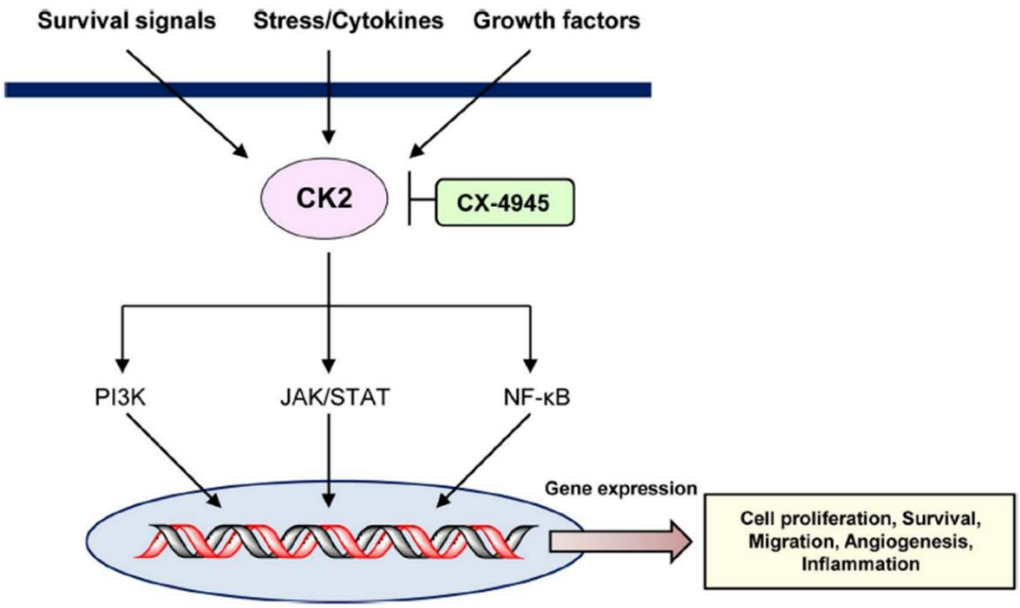

Figure 8: Pathways affected by CK2 inhibition.
Figure modified from [161].

1.5.3 Kinases Inhibition: CK2 or dual CK2-Pim

The first inhibitor described for CK2 was the nucleoside 5,6-dichloro-1-(β-ribofuranosyl)benzimidazole (DRB) in 1986 [162]. At the beginning of the 21st century, more potent CK2 inhibitors were developed taking DRB structure as a model, replacing the chlorine atoms with bromines and deleting the sugar moiety. The more relevant ones were the tetrabromo derivatives 4,5,6,7-Tetrabromobenzotriazole (TBB) [163] and 2-Dimethylamino-4,5,6,7-tetrabromo-1H-benzimidazole (DMAT)[164] (Figure 9). However, these compounds were found to inhibit other kinases (e.g. Dual Specificity Tyrosine Phosphorylation-regulated Kinase 1a, Glycogen Synthase Kinase β or Homeodomain Interacting Protein Kinase 2 [165]) as much as CK2 itself, lacking specificity.

Tetra-halogenated compounds (e.g. 4,5,6,7-tetrabromo- and 4,5,6,7-tetraiodo-1H-benzimidazoles) reveal distinct affinities towards the two isoforms of the catalytic CK2 subunit: CK2α' may be up to 6 times more sensitive (i.e. lower inhibitory constant) to those compounds than CK2α [166]. In this sense, these inhibitors could be useful to clarify the distinct functions of the different CK2 catalytic subunits. Furthermore, some efforts are being directed towards the development of specific inhibitors of CK2α and CK2α' [167].

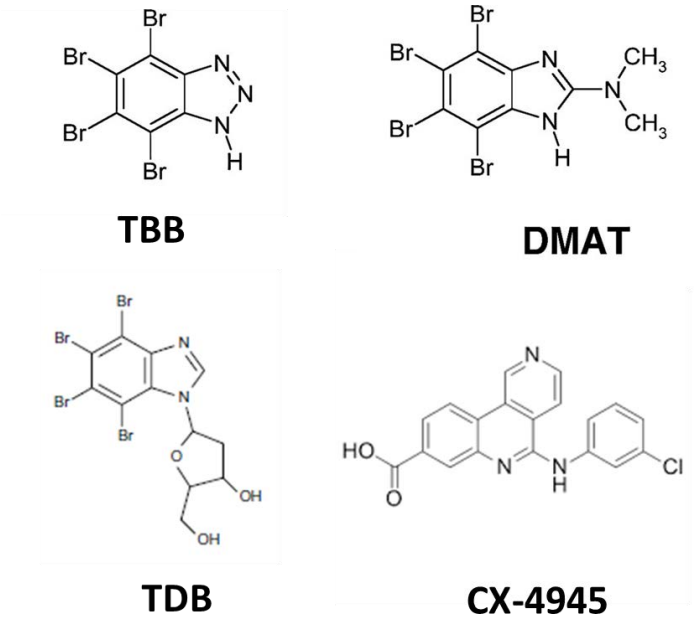

Figure 9: Molecular structure of the most relevant CK2 inhibitors
TBB, DMAT and TDB are tetrahalogenated compounds whereas CX-4945 is a derivative from quinoline [166].

1.5.3.1 CX-4945: CK2 inhibition

The 5-(3-Chloroanilino)-benzo[c][2,6]naphthyridine-8-carboxylic acid (CX-4945) is a CK2α small molecule inhibitor which acts as an ATP binding site competitive inhibitor. CX-4945 has been shown to inhibit the PI3K/Akt pathway *in vitro* in various cancer cell lines, such as the human squamous cell carcinoma UM-SCC [168], the human breast cancer cell line BT-474 or the human pancreatic cell line BXPC-3 [169, 170]. *In vitro*, CX-4945 treatment reduces cell adhesion and decreases integrin expression. It inhibits Janus kinases (JAK)/signal transduction and activator of transcription (STAT) proteins, in addition to inhibit the NFκβ pathways and PI3K/Akt signaling. Since STAT-3 has been implicated in the resistance of GB to TMZ [171], its inhibition would highlight the potential of CX-4945 in GB therapy. . Furthermore, CX-4945 has been shown to effectively inhibit CK2 and to reduce viability *in vitro* in the GL261 cell line [85].

CX-4945 proved useful in treatment of preclinical xenograft models of GB [110] and prostate cancer [172]. It was also able to reduce IL-6 levels, an interleukin that contributes to tumor invasiveness, *in vivo* in an inflammatory breast cancer xenograft model [173]. In addition to the above described results, a pharmacokinetic study showed that CX-4945 exhibits a long half-life in blood and high oral bioavailability [169], pointing to it being a good candidate for GB therapy.

CX-4945 has been evaluated in several clinical trials for human cancer although not all of them presented updated results. Phase I dose-escalation studies were performed to evaluate CX-4945 safety in refractory multiple myeloma[7] and in advanced solid tumors[8]. Inhibition of Akt

[7] https://clinicaltrials.gov/ct2/show/NCT01199718

and p21 pathways was shown in peripheral blood mononuclear cells along with a decrease in the number of circulating tumor cells. Also, in a high percentage of patients, IL-6 and IL-8 levels were decreased after CX-4945 treatment [174]. This compound is currently being evaluated in an active clinical trial addressed to patients with cholangiocarcinoma for assessing its added value in combination with Gemcitabine and Cisplatin[9]. In our group, CX-4945 showed to have relevant effects over GL261 cell viability, decreasing CK2 activity in both cultured cells and established tumors, although only discrete effects were observed in overall survival of tumor-bearing mice. However, it was proven to have significant effects when combined with TMZ in metronomic (IMS) administration schedules [85].

1.5.3.2 TDB: Dual CK2 and Pim1 inhibitor

The 1-(β-D-2'-deoxyribofuranosyl)-4,5,6,7-tetrabromo-1H-benzimidazole (TDB) is a dual ATP-competitive CK2 and Pim-1 inhibitor whose half-maximal inhibitory concentration (IC_{50})[10] values for both CK2 and Pim-1 (32 nM and 86 nM respectively) are one order of magnitude lower compared to the values obtained for others structurally related compounds, as DRB or 4,5,6,7-tetrabromo-1H-benzimidazole (TBI). And even in comparison with more potent CK2 inhibitors such as CX-4945 (IC_{50} 1-2 nM), TDB is much more effective in inducing cell death and producing a more long-lasting effect in CK2 inhibition [175, 176]. Together with its potency as a CK2 and Pim-1 inhibitor, TDB is selective, cell-permeable and have a stronger effect in cancer cells compared to normal cells, postulating this compound as a very promising therapeutic drug for cancer treatment [175]. Also, a Pim-1 inhibitor (3-Cyano-4-phenyl-6-(3-bromo-6-hydroxy)phenyl-2(1H)-pyridone) was proved to decrease tumor volume in GL261 tumor-bearing mice [111] and one PIM inhibitor (SGI-1776) has been evaluated in a clinical trial for prostate cancer and Non Hodgkin's lymphoma[11], although it was soon withdrawn. The joint CK2 and Pim-1 inhibition would be expected to enhance the therapeutic effect in GL261 cells and GL261 tumor bearing mice, possibly having a synergistic effect in the inhibition of survival and anti-apoptotic pathways. Still, we would expect successful combination of kinase inhibition and standard therapies as TMZ.

1.5.4 CK2 and Pim1 activity measurement

Interestingly, it was described that CK2 directly phosphorylates Akt1 and 2 in the Ser129 site, which fulfills the consensus sequence for CK2 (Ser-Xaa-Xaa-Glu/Asp) and has acidic residues at positions +3, +4, +6 and -2 with respect to Ser. The Ser129 residue is located in the linker

[8] https://clinicaltrials.gov/ct2/show/NCT00891280

[9] https://clinicaltrials.gov/ct2/show/NCT02128282

[10] IC_{50} values are used to measure the potency of a substance in inhibiting a specific biochemical function.

[11] https://clinicaltrials.gov/ct2/show/NCT00848601

region between the pleckstrin homology and the catalytic domains. CK2 phosphorylation of this site produces the hyperactivation of Akt [177]. The knowledge of this specific target of CK2 allows researchers to evaluate CK2 activity by assessing the phosphorylation status of the Ser129 site of Akt. Akt is known to have two main activation sites: Thr308, located in the activation loop, which is described to be phosphorylated by 3'-phosphoinositide-dependent kinase- 1 (PDK-1) [123] and Ser473, which is found in the hydrophobic domain outside the catalytic domain and is phosphorylated by mTOR2 [124]. Neither Thr308, nor Ser473 display the consensus required for CK2 phosphorylation but still, phosphorylation of Ser 129 by CK2 produces Akt activation [177] (Figure 10).

Regarding Pim1, it is known to phosphorylate the pro-apoptotic protein Bcl-2-associated death promoter (Bad) at Ser112 [154] (Figure 10), although it is not the only kinase phosphorylating at this site. Akt [180] and cyclin adenosine monophosphate-dependent protein kinase also phosphorylate Bad at Ser112 [181]).

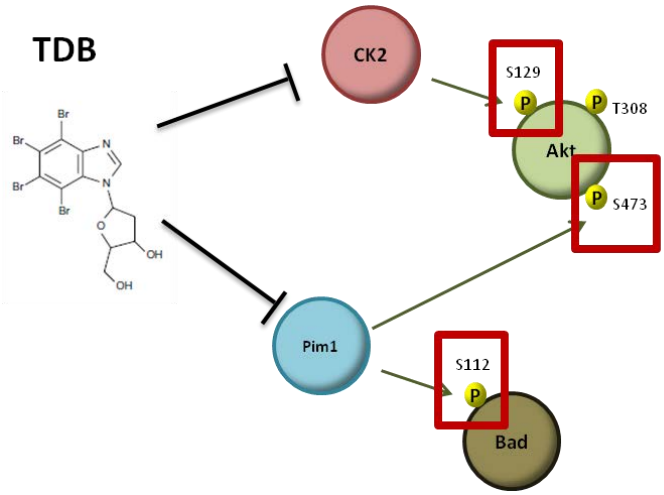

Figure 10: Target validation for CK2 and Pim-1 inhibition through assessment of specific substrates

1.6 Non-invasive techniques for diagnosis and follow-up progression in GB: Magnetic Resonance

Non-invasive techniques are essential for GB diagnosis and follow-up. Among them, the most used non-invasive technique for brain-related pathologies is nuclear magnetic resonance. Magnetic resonance techniques are based in radiofrequency (RF) energy absorption by tissues which is a harmless, non-ionizing radiation, being this a clear advantage compared to other imaging, non-invasive techniques which use ionizing radiation frequencies, such as positron-emission tomography, X-rays or computed tomography. An exhaustive description of the physical phenomena behind nuclear magnetic resonance techniques is beyond the scope of

this thesis and can be found in classical references such as [182]. Regarding brain tumor diagnosis and therapy response assessment, it is mostly based on proton (^{1}H) nuclei resonance, and the information obtained could be either anatomical (magnetic resonance imaging, MRI) or metabolomic (magnetic resonance spectroscopy, MRS). With MRI it is possible to obtain high quality images of the brain, as well as the size, shape and location of tumors. Therefore, MRI is a very useful tool at the time of diagnosis, before surgery and also for therapy response assessment and follow up of disease progression. In fact, the protocols for clinical brain tumor patient therapy response assessment and follow-up are based mostly in MRI parameters, such as the RANO criteria [183]. On the other hand, magnetic resonance spectroscopy (MRS) provides information about the biochemical environment of a given region of interest and can be acquired in two modalities: single volume or multi-volume (see section 1.5.3). Magnetic resonance techniques are available in most hospitals and clinical imaging centers, especially MRI and MRS and a standard MRI/MRS exploration can be carried out in a reasonable time frame depending on the chosen acquisition sequences (ca 20-30 min). This section will underline the main aspects related to MR techniques that could be relevant for proper understanding of results obtained in this Thesis and their discussion.

1.6.1 Magnetic Resonance Imaging (MRI)

MRI is widely used applied for brain tumors diagnosis and follow up providing images with outstanding anatomical detail and accurate information about the size, location and morphology of brain tumors and it is based on signal measured from naturally present ^{1}H nuclei. The intrinsic contrast registered in MRI is determined by three parameters: in addition to the concentration of hydrogen nuclei, proton density, the longitudinal (T1) and transversal (T2) relaxation times of mobile protons are also responsible for this basal contrast level. Mobile protons basically mean fat and water protons. The parameters chosen in acquisition sequences are relevant to “weigh” images, i.e. parameters as repetition time (TR) and echo time (TE) can be tuned to weigh images in order to highlight differences in T1 or T2 of mobile protons (Figure 11).

Still, the intrinsic tissue contrast can be enhanced through the use of exogenous contrast agents, which are usually based in Gadolinium [184] and act by shortening the relaxation time of water protons. In brain tumour acquisitions, they are usually applied for assessment of the blood-brain barrier (BBB) integrity, because they are unable to cross intact BBB. However, contrast-enhanced acquisitions were not used in this thesis and, accordingly, no detailed subsections will be devoted to exogenous contrast agents.

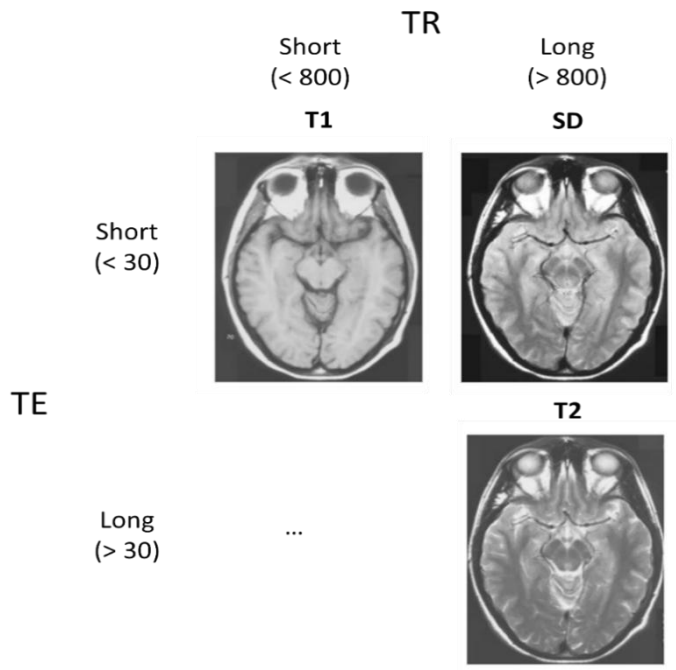

Figure 11: Human brain images obtained by MRI with different combinations of TR and TE.
SD states for spin density or proton density and --- represent poor image contrast with not enough signal to noise ratio (SNR)[12] *and/or bad contrast between tissue types.*

1.6.2 Magnetic Resonance Spectroscopy (MRS)

The MRS can provide insight into the biochemical properties of tissues *in vivo* in a non-invasive manner, making it possible to study their evolution over time under certain circumstances, for example, to follow up the metabolic changes observed in a tumor subjected to treatment. It is usually based in signals from ^{1}H mobile protons, (^{13}C and ^{31}P applications are also available, although more restricted to the research environment). MRS provides information about the relative abundance of several low molecular weight metabolites, lipids and macromolecules having mobile protons in the millimolar range concentration. Due to the difference in concentration range of orders of magnitude, the large signal arising from water protons should be suppressed before observing low molecular weight metabolites. The resonance frequency of a particular nucleus, also called chemical shift, is dependent on its chemical environment and, accordingly, it allows us to distinguish signals arising from different metabolites. The spectral pattern may change among different tissue types, classes of tumors or the same tumor subjected to different conditions (e.g. therapeutic agent administration). Magnetic resonance spectroscopy can be acquired in either single voxel modality, in which a region of interest (usually cubic) is studied, or multivoxel (multivolume, or Magnetic Resonance Spectroscopic Imaging, MRSI) which combines the metabolic and spatial information, allowing the study of metabolic differences across tumor/brain regions. However, the interpretation of

[12] Source: https://slideplayer.com/slide/4262652

MRS(I) data is not straightforward for clinicians because it is not in a regular image format. In this sense, the use of postprocessing methods for automated data evaluation may be helpful (see section 1.5.3.1, pattern recognition).

Major ^{1}H-NMR detectable compounds of mouse normal brain tissue and GL261 GB tumors *in vivo*

The spectral metabolic pattern contains multitude of signals from a large list of metabolites but the resolution achieved in *in vivo* acquisition does not allow the individual identification of all of them, i.e. there is a considerable overlapping. The difference between the metabolic pattern found in normal brain and in GB tumors is well known and characterized. Figure 12 shows a C57BL/6j wild type (wt) normal brain single voxel spectra in comparison with a GL261 GB tumor.

Among the main signals observed in mice brain spectra, lactate (Lac) appears at 1.3 and 4.10 ppm, an end product of anaerobic glycolysis that is usually present in the healthy mouse brain at low concentrations. In tumor tissue, Lac may be increased due to hypoxic conditions of the tumor milieu and or the glycolysis-based tumor metabolism [185]. Choline-containing-metabolites (Cho) are also increased in GB tumors compared to normal brain as a result of an abnormal Cho metabolism, usually related to increased cell membrane turnover due to high proliferation rate. Creatine (Cre) is involved in energy metabolism and it is described to decrease in tumoral tissue compared to normal brain parenchyma. N-acetylaspartate (NAA) resonates at 2.01 ppm and it is the major signal found in normal brain spectrum. NAA indicates neuronal functional integrity and, accordingly, is found essentially reduced in brain tumor spectra, although its signal *in vivo* can have also contribution of other N-acetyl containing compounds. Mobile lipids (ML) and macromolecules (MM) are observed in different spectral regions at ca. 0.9, 1.3-1.4, 2-0 and 2.6 ppm and are increased in tumor masses due to the presence of hypoxia and necrotic events in these areas. Still, large ML signals can appear due to 'voxel contamination' with lipids from subcutaneous tissue near scalp. Other contributions are glutamine plus glutamate (Glx 2.10-2.40 and 3.8 ppm) and myo-inositol and glycine (Ins + Gly, both observed at 3.55 ppm, at the echo time 14ms used for acquisition). Comprehensive reviews of brain MRS and detailed explanation of the observed metabolites can be found in [186, 187]. Other minority compounds that can appear in specific situations such as response to therapy may be also mentioned here. Polyunsaturated fatty acids resonances (i.e. the PUFA resonances at ca. 2.8 ppm) are primarily constituents of cellmembranes which are essentially MR-undetectable in normal brain conditions. However, it has been observed that PUFA levels increase in brain tumors after therapy in preclinical glioma, which was described to be related

to cell apoptosis. This increase in PUFA levels have also been observed in our group in GL261 tumor bearing mice after TMZ treatment [188].

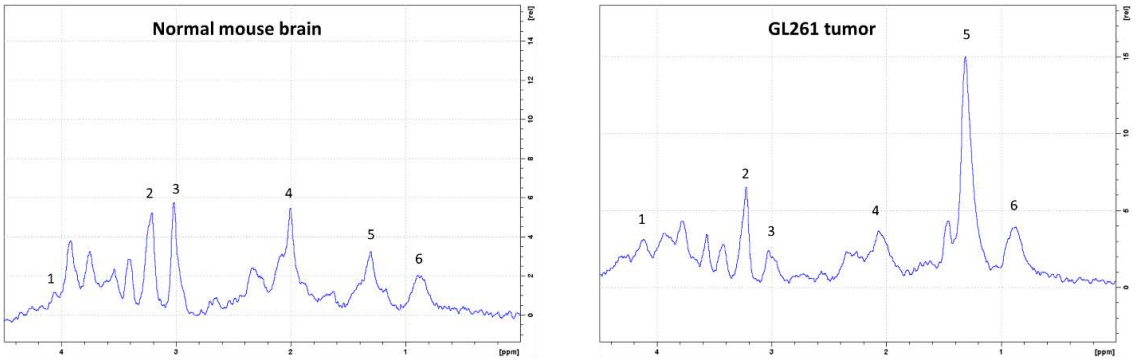

Number	Metabolite	Resonance Frequency (ppm)
1	Lactate (Lac)	4.10
2	Choline-containing compounds (Cho)	3.21
3	Creatine (Cre)	3.03
4	N-acetyl-aspartate (NAA) and N-acetyl (NAc) group containnig compounds	2.02
5	Mobile lipids (ML) 1.3 + Lactate (Lac)	1.3
6	Mobile lipids (ML) 0.9 + Mobile Macromolecules (MM)	0.9

Figure 12: Normal brain and GL261 GB tumor spectra from mouse brain.
Single Voxel (2.5x2.5x2.5mm^3) MRS (12ms TE) results from left: a wt C57BL/6j mouse brain parenchyma and right: a GL261 tumor the C57BL/6J mouse C1202 (CXXXX being a unique identifier for tumor-bearing animals in our group). The main pattern differences between the two spectra are numbered and labeled in the table below. For each metabolite the chemical shift displacement in parts per million (ppm) is indicated [37] .

1.6.3 Magnetic Resonance Spectroscopy Imaging (MRSI)

A combination of metabolomics and spatial information can be achieved with MRSI acquisitions in which a grid of spectra are superimposed to different anatomical locations, making it possible to gather metabolic information from different regions of the studied tissue (Figure 13). Therefore, MRSI can be a powerful tool to monitor the metabolic heterogeneity of brain tumors in clinical and also preclinical settings [98, 189] and may be a valuable approach to complement MRI information in assessing therapy response. However, the processing and postprocessing of MRSI data is complex and require different software tools to ensure proper handling. In addition, proper interpretation of spectra would require relevant biochemistry background, which could not be feasible in the clinical pipeline.

The MRSI information can be processed to be shown in an “image-like” output: for example, metabolite maps can be generated, such as the ones in [190]. However, although this may result useful in clear discriminations as tumor vs normal, more subtle changes will probably

take place when different questions are addressed to the system (e.g. control tumors vs tumors responding to therapy). In this case, probably several metabolites are changing at once, and/or suffering only small changes, that could be extremely difficult to detect with current quantifications or single metabolite maps. Then, the rich information contained in MRSI data is the ideal candidate for the application of pattern recognition techniques, which consider changes occurring in the whole pattern instead of analyzing a single or few metabolites.

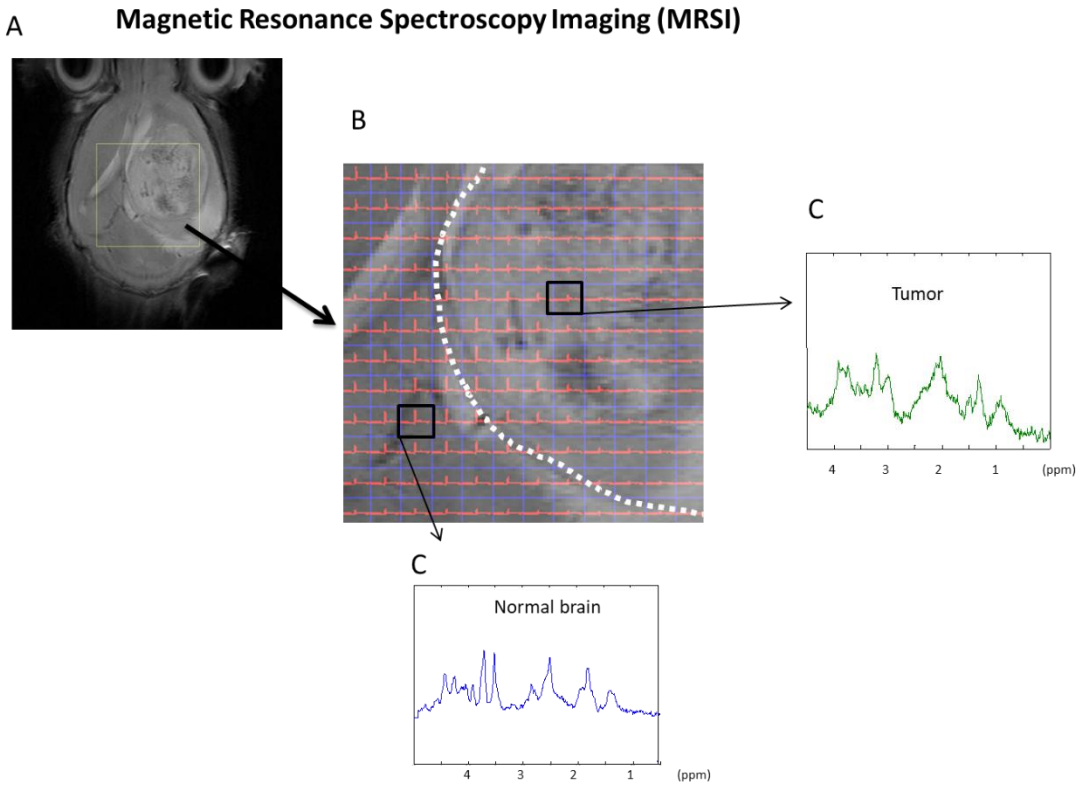

Figure 13: Examples of representative spectra obtained in a 12x12 MRSI grid from GL261 tumor-bearing mice.
A) Axial T2W weighted MRI showing the volume of interest (VOI) from tumor-bearing mouse C1181, enlarged in "B". B) MRSI grid acquired from VOI shown in "A" with a 12x12-grid size. The boundaries of the tumor mass are marked with a white discontinuous line. C) Individual spectra from short echo time (14ms) MRSI grid acquired from tumoral and normal-appearing brain zones showing 0.5-4.5 ppm range.

1.6.4 Pattern recognition techniques for metabolomics analysis

Pattern recognition (PR) techniques aim to recognize and classify data, as such MR spectral date vectors, detecting meaningful and key features characteristic from different groups, through automated decision-making processes. There are three major classification strategies used in PR: supervised, unsupervised and semi-supervised classification with relevant differences in the development of the mathematical models for classification.

In the supervised PR methods, a "training set" of known classes is used to develop the classification model. Once the system is trained with this previous knowledge, the classifier can be applied to a different set of cases ("test set"). As opposed, in the unsupervised classification, no previous class assignation is performed for initial cases, which are grouped based on their similarities. Non-negative matrix factorization (NMF) [190] is an example of unsupervised PR technique in which each class is represented by a "paradigmatic spectral pattern" also called "source". The source extraction technique assumes that individual voxels may be contributed by a mixture of heterogeneous patterns and the contribution of each source is calculated. Finally, the semi-supervised method which was the approach used in this thesis and described in [98] for noninvasive therapy response studies, uses both labelled and unlabeled data for training and proposes, in order to benefit from class membership, prior knowledge to guide the source extraction.

Color-coding the metabolomics information: generation of nosological images

Once the system is properly trained and evaluated, new cases can be analyzed and the contribution of each source to the individual voxels in MRSI grid is calculated in order to assign each acquired voxel to one of the predetermined classes. The paradigmatic spectrum or source with the highest contribution to a given voxel is chosen as the "winning source" and the voxel is colored accordingly. As a result, we obtain color-coded maps called nosological images (Figure 14), providing a visual representation of the results and a **surrogate imaging biomarker** for therapy response. In the case of the therapy response assessment, depending on the spectral pattern mostly contributing to a given voxel pattern, color could be blue for normal brain parenchyma, red for pattern of actively proliferating, non-responding tumor and green for responding tumors.

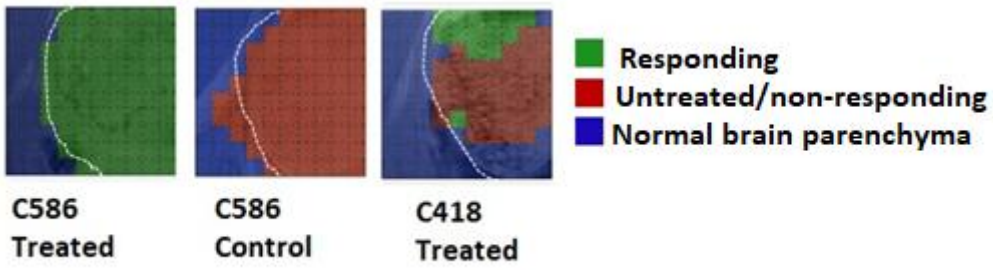

Figure 14: Examples of nosological images obtained with the semi-supervised source extraction in control and TMZ-treated GL261 GB tumor-bearing mice.
Adapted from [98].

A spectrum is classified as “undetermined” when the system is unable to associate it with confidence to any of the predetermined classes and in this case, it is shown in black. This semi-supervised approach has been used within our group for noninvasive assessment of therapy response, mostly with TMZ and showing correlation with Ki67 proliferation index [37, 98] although it also proved useful for assessment of CPA treatment [191]. Accordingly, this PR strategy was used to follow-up GL261 tumor-bearing treated mice analyzed with multislice MRSI during this thesis (chapter 4.3).

2 General objectives

The general objective of this thesis is the improvement of preclinical glioblastoma therapy and non-invasive response assessment through different sub-objectives:

1. To advance and unravel relevant aspects of CK2 inhibition in preclinical GL261 therapy, including standard and novel CK2 inhibitors with therapeutic potential for *in vivo* work
2. To gain more insight regarding the potential of therapeutic agents such as CX-4945 (CK2 inhibitor) and TMZ, either alone or in combination, to trigger immunogenic cell damage, *in vitro*
3. To apply semi-supervised pattern recognition techniques for noninvasive therapy response follow-up in GL261 tumor-bearing mice treated with IMS metronomic TMZ administration

3 Materials and methods

3.1 *In vitro* studies with GL261 cells

3.1.1. GL261 cells culture

GL261 mouse glioma cells were obtained from the Tumor Bank Repository at the National Cancer Institute (Frederick/MD, USA). These cells have been used in our group for some time already [188, 192–194] due to the high penetrance, reproducibility and reliability in generating glioblastomas when implanted into C57BL/6j mice. GL261 cells were grown in 75cm^2 culture flasks (Sartstedt) with RPMI-1640 culture medium supplemented with 2.0 g/L of sodium bicarbonate, 0.285 g/L glutamine, 1% penicillin-streptomycin (all from Sigma-Aldrich) and 10% fetal bovine serum (FBS) (Reactiva). Cells were incubated at 37 ^{o}C in a 5% CO_2 and 95% humidity (Incubator HERAcell, 150i, Thermo Scientific). For cell subculturing, medium was aspirated with a vacuum pump and cells were washed with phosphate-buffered saline (PBS) in order to completely remove the medium, since the remaining FBS could inactivate trypsin. Then, 2ml of trypsin-EDTA (Sigma-Aldrich) were added to detach the cells. After a 3 min incubation, cells were resuspended in RPMI medium. Then, cells were centrifuged and supernatant discarded. Finally, the appropriate number of cells were seeded in a new culture flask. Cells were cultured until passage 25, when they were discarded and a new aliquot was thawed in order to avoid possible undesired new mutations and ensure consistent tumor development and behaviour.

3.1.2 Cell growth curve

For the growth curve of GL261 cells, 5x10^5 cells were seeded in 75 cm^2 flasks (Sarstedt) and counted with the TC10 counter from Bio-Rad every day from day 1 to 11 post-seeding (n=3 to 6 for each day). Sample analyses were done based in a Trypan blue exclusion assay: 20 µl of the cell suspension was added to 20 µl of Trypan Blue (Sigma), a 10 µl aliquot of the mixture was loaded into the cell counting slide (Bio-Rad) and counted with the TC10 cell counter (Bio-Rad).

3.1.3 Cell treatments

The GL261 cells were treated with the following therapeutic agents: temozolomide, CX-4945, TDB and Doxorubicin. The concentrations and time of treatment varied along the experiments and depended on the question being addressed (details will be provided in the respective chapters/sections). The GL261 cells (3,500-500,000, depending on the test) were seeded in well plates (6, 24 or 96 wells) or in dishes (60mm) (both from Sarstedt) and treatment took

place during 8-72h. After that, viability was assessed through different methods such as Trypan blue exclusion, MTT or propidium iodide. See 3.1.4 for specific methods of viability assessment.

3.1.4 Cell viability assays

A) Trypan blue exclusion assay

GL261 cells were seeded in a 24-well plate, 32,000 cells per well. After 24h, medium was removed and new medium with the desired treatment was added. After the established time of treatment, medium was collected and cells were washed with PBS and trypsinized (0.5 ml of trypsin). After 3 min, cells were resuspended with 1 ml of RPMI medium and, together with the cellular supernatant previously collected, centrifuged for 5 min at 900 x g. Supernatant was discarded and cells were resuspended in 1 ml of PBS. Then, 20µl of the cell suspension was added to 20 µl of Trypan Blue (Sigma) and a 10 µl aliquot of the mixture was loaded into the cell counting slide (Bio-Rad) and counted with the TC10 cell counter (Bio-Rad). Live cells were the ones excluding Trypan Blue.

B) MTT proliferation assay

Reduction of tetrazolium salts is a widely accepted method to determine cell proliferation and viability. The 3-(4,5-dimethylthiazol-2-yl)-2,5-diphenyltetrazolium bromide (MTT) assay is based on the ability of the mitochondrial dehydrogenases (Succinate dehydrogenase) of living cells to reduce rings of MTT to purple formazan crystals, allowing its accumulation inside healthy cells. To solubilize the crystals, dimethyl sulfoxide (DMSO) was added after MTT incubation. Using a spectrophotometer it is possible to determine the quantity of formazan formed, which will be proportional to the number of living cells.

Procedure:

Fifty microliters of a cell suspension of 70,000 cells were seeded in each well. Wells located in the edge of the plate received only culture medium, in order to minimize evaporation of the inner wells. After 24h, 50 µl of medium with the desired drug or vehicle treatment were added to each well. After the appropriate time of treatment, 50 µl of MTT dissolved in PBS at 1 mg/ml were added to each well and incubated for 1h at 37 ^{o}C in the dark. Plate was read at 595 nm with the Victor3 Multilabel Counter.

C) Flow cytometry analysis with propidium iodide

Propidium iodide (PI, Sigma) was used to stain dead cells since it cannot cross through intact cellular membranes but may freely enter cells with damaged plasma membrane. Upon entering dead cells, propidium iodide intercalates into double-stranded DNA or double-stranded RNA. GL261 cells were seeded in a 24-well plate at 32,000 cells per well and were grown and collected as described in section 3.1.1. Cells were washed in PBS, centrifuged at 300 x g and the supernatant was discarded. Then, cells were resuspended in 200 µl buffer containing PBS + 2% Bovine Serum Albumin (BSA) + 1 µg/ml of PI dissolved in PBS. Each sample was analyzed using Cytometer FACSCalibur (Becton Dickinson) for 30 seconds at medium speed. After the analysis, values were plot as size (forward scatter, FSC) vs. granularity (SSC, side scatter) and size (FSC, forward scatter) vs FL-2 channel intensity. Cell distribution was assessed and positive PI cells were considered dead disregarding the intensity of the detected signal.

3.1.4.1 *In vitro* drug effectiveness parameters calculation from cell viability results

IC_{50}/EC_{50} calculation

The IC_{50} states for half-maximal inhibitory concentration, being commonly used to measure the potency of a substance in pharmacological research. The IC_{50} is a parameter used for drugs capable of diminishing cellular viability, which corresponds to the concentration needed to decrease the viability of the control conditions by half.

The half-maximal effective concentration (EC_{50}) is the concentration of drug that induces an effect, in this case decrease of cellular viability, halfway between the baseline and maximum effect after a chosen exposure time. In other words, it is the concentration where 50% of the drug's maximal effect is observed. For example, if the maximum effect observed of a drug is to reduce the viability down to 30% of control value, the EC_{50} will be the concentration necessary to reduce the viability down to 65%, which is halfway between 100% and 30% (Figure 15). Both IC_{50} and EC_{50} parameters were calculated with the GraphPad Prism software with results from cell viability (for example, MTT assay) as input.

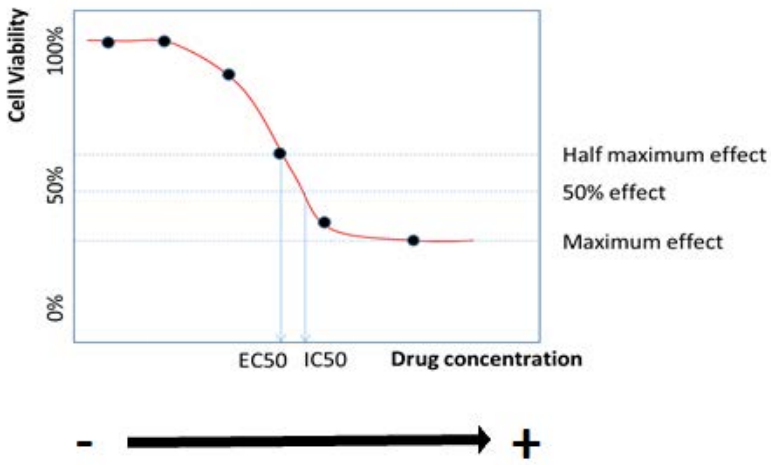

Figure 15: Differences between IC50 and EC50 shown in an example of a dose-dependent curve.

Assessment of synergy or antagonism with Chou-Talalay method

This quantitative method was used to determine the combined effect of two drugs and was performed as described in [195]. The dose-effect data of each drug separately and the combination of both are used to establish a factor named combination index (CI, see below) that will determine if both drugs have a synergistic (CI < 1), additive (CI = 1) or antagonistic effect (CI > 1). The input for calculations of CI was cell viability data calculated by MTT assay. The relationship between drug concentration and reduced cellular viability is represented in dose-effect curves. This method uses the terminology of unaffected fraction (fu) for the fraction of cells that survive after treatment and affected fraction (fa) for the cells that are missing when comparing untreated and treated cells, affected by the treatment. The survival fraction of cells is used to obtain the *median effect dose* and *Hill-type coefficient* for each condition, which are further used to calculate CI for determining synergism, addition or antagonism in the combined treatment. Annex I shows an example of extended calculation with experimental values.

3.1.5 Protein extraction and quantitation

3.1.5.1 Protein extraction of GL261 cellular suspensions

For western blot analysis of exponential phase (EP) and postconfluent phase (PCP) cells, 75 cm^2 flasks were used for cell culture (see also section 3.1.1 and 3.1.2). After 6 (EP) or 9 (PCP) days of culture, cells were collected and washed twice with 10 ml of PBS. For target validation experiments in TDB treated cells, GL261 cells were cultured in 60 mm dish (Sarstedt) and, after the chosen time of treatment, cells were collected and washed twice with 1ml of PBS.

Next, cells were incubated for 10 minutes on ice with 1 ml of cold lysis buffer which contained 50 mM Tris-HCl pH 7.4, 150 mM NaCl, 1 % triton-X-100, 1 mM Dithiothreitol (DTT), 1 mM phenylmethylsulfonylfluoride (PMSF), 1 mM Ethylenediaminetetraacetic acid (EDTA), 25 mM NaF, 0.2 mM Na_2VO_3, 2 mM PPi, 1 µg/mL protease inhibitors (leupeptin, benzamidin, aprotinin, pepstatin). After this incubation, samples were centrifuged at 13,000 x g for 15 min at 4 °C. Then, supernatant was collected and samples stored at -20 °C.

3.1.5.2 Protein extraction of GL261 tissue samples

To obtain tissue extracts, samples of GL261 tumors excised from tumor-bearing euthanized mice were weighted and 200 µl of cold lysis buffer added per each 50 mg of tissue. Lysis buffer for tissue samples contained 50 mM Tris-HCl pH 7.7, 150 mM NaCl, 15 mM $MgCl_2$, 0.4 mM EDTA, 0.5 mM DTT, 100 µg/ml of leupeptin, aprotinin and benzamidin and 2 mM of PMSF. Then, samples were sonicated until complete tissue disaggregation. After that, 0.5% of Triton X-100 was added. Then, samples were incubated on ice for 15 min and centrifuged at 13,000 x g for 20min at 4 °C. Finally, supernatant was collected and samples stored at -20 °C.

3.1.5.3 Bradford assay for protein quantification

The protein content of each sample was quantified with Bradford assay (Bio-Rad) in a 96 well plate, following manufacturer's instructions. A calibration curve was performed with BSA concentration ranging from 0.4 to 3.6 µg/µl. Plate was read at 595 nm with the Victor3 Multilabel Counter.

3.1.6 Western blot analysis

3.1.6.1 Polyacrilamide gel electrophoresis

Sodium Dodecyl Sulfate Polyacrilamide Gel Electrophoresis (SDS-PAGE) was used for separating proteins based on their molecular weight under denaturing conditions. The Mini Protean system from Bio-Rad was used to perform SDS-PAGE.

Gel preparation, sample loading and electrophoresis

Two glasses of 10 x7 cm and 1.5 mm thickness were used for gel preparation. The stacking gel had a constant concentration of acrylamide (3.5%) whereas the acrylamide concentration of the running gel in our case was of 12% which is suitable for analysis of proteins of 10 to 70 kDa, such as CK2α (37 kDa) or CK2β (25 kDa) analysed in this thesis.

Composition of the running gel at 12% acrylamide: 3 ml acrylamide (Acryl-bis acryl 30%, NZY-tech), 1.9 ml buffer B (Tris-HCl 1M, 0.4% SDS, pH 8.8), 2.6 ml deonized H_2O miliQ, 10 µl

tetrametiletilendiamine (TEMED) and 100 µl Ammonium persulfate (APS). Composition of stacking gel: 0.7 ml acrylamide, 1.5 ml of buffer C (Tris-HCl 0.5M, 0.4% SDS, pH 6.8), 3.8 ml H_2O miliQ, 10 µl of TEMED and 100 µl of APS.

Protein extracts (section 3.1.5) were diluted in Laemmli buffer 5X (350 mM Tris, 10% SDS, 50% glycerol, 0.0125% bromophenol blue, 0.5% β-mercaptoethanol) and boiled at 100 °C for 5 min, vortexed and spin-down. Samples (25-30 µl) corresponding to 25 µg of protein were loaded into the gel wells and NZY-Tech protein marker was used as a molecular weight marker. Electrophoresis was set at constant amperage, 30-35 mA per gel, until the sample forehead arrived to the bottom of the gel.

Electrotransfer of proteins and membrane blocking

Proteins from the gel electrophoresis were transferred onto Polyvinylidene fluoride (PVDF) membranes (Millipore) using Mini Trans-Blot® Electrophoretic Transfer Cell from Bio-Rad. Before transfer, PVDF membrane was activated by incubation in methanol (Sigma) for 15 seconds at room temperature. The transfer cassette was assembled following manufacturer's instructions and protein transference was done at a constant voltage of 100V for 1h. Then, membrane was washed with deionized H_2O and blocked with methanol for 15 seconds, air dried and incubated for 15 min in 5% milk powder in Tris Buffered Saline (TBS) buffer (50 mM Tris-HCl, 150 mM NaCl, pH 7.4) at room temperature.

Immunodetection

After blocking, membranes were washed three times with TTBS (TBS buffer containing 0.1% Tween-20). Membranes were incubated overnight at 4 °C with the primary antibodies (see Table 1 for details on sources, origin and dilution) diluted in TTBS 1X with 5% BSA and 0.02% sodium azide. Following incubation, membranes were washed three times with TTBS and incubated with the secondary antibody (Immunoglobulin (Ig)G Goat Anti-Rabbit/Mouse IgG (h+L)- Horseradish Peroxidase conjugate, Bio-Rad) diluted in TTBS + 5% milk powder for 1h. Then, membranes were washed again three times with TTBS. The signal was developed with Clarity™ Western ECL Blotting Substrates from Bio-Rad. Images were scanned with Chemidoc MP Image System and quantified with the ImageJ software.

In Table 1, the complete list of primary antibodies is shown. Two homemade antibodies were used in this thesis; anti-CK2 α antibody, which was produced in rabbit against the sequence of the human protein at C-terminus [376–391] made in Padova's University and anti-CK2β (clone P3β) made in the Autonomous University of Barcelona.

Target	Protein size (kDa)	Trading house/Origin	Reference number	Dilution	Producer Host
CK2α	45	Homemade (Morgana)	-	1:500	Rabbit
CK2α'	37-38	Benthyl	A300-199A	1:2000	Rabbit
CK2β	25	Home made	-	1:5000	Rabbit
β-Tubulin	50	Cell signaling	2146	1:1000	Rabbit
Cyclin D1	37	Santa Cruz	sc-753	1:1000	Rabbit
pAkt s129	55	Abcam	ab133458	1:1000	Rabbit
pAkt S473	60	Cell Signaling	D9E	1:1000	Rabbit
Total Akt	60	Cell signaling	9272s	1:1000	Rabbit
pBad S112	23	Cell signaling	40A9	1:500	Rabbit
Pim-1	33	Santa Cruz Biotechnology	Sc-13513	1:500	Mouse

Table 1: List of primary antibodies used for western blot analysis.

3.1.7. CK2 activity assay

Cell and tissue lysates (obtained as in [85]) were assayed for CK2 activity without any previous immunoprecipitation and/or purification steps. For a standard assay, 2, 4 or 6 µg of protein lysates were incubated at 30 °C for 30 min in a total volume of 20 µl, in the presence of 50 mM Tris–HCl pH 7.5, 100 mM MgCl2, 100 mM NaCl, 20 mM ATP and $^{[33P]}$ATP (specific radioactivity 2000-3000 cpm/pmol), and 0.1 mM CK2-tide (RRRADDSDDDDD), which is a specific CK2 substrate peptide [196]. After incubation, reactions were stopped by spotting the whole volume on phosphocellulose filters (2 x 2 cm squares), then, filters were washed three times in 0.5% (v/v) phosphoric acid (200 ml, in a beaker on a magnetic stirrer, 5 min for each washing) and counted in scintillation fluid.

3.1.8. DAMPs release/exposure assessment

DAMPs release or exposure were evaluated in GL261 cells untreated and treated with CX-4945, TMZ or the combination of both drugs. Drug concentrations and times of treatment varied depending on the DAMP analysed.

3.1.8.1 Enzyme-Linked Immunosorbent Assay (ELISA) for HMGB1 detection

The HMGB1 content was measured in the cellular supernatant with the HMGB1 ELISA kit from IBL international, which have HMGB1 antibody-coated wells. The cellular supernatant of treated and control cells cultured in 60 mm dishes were collected (see section 3.1.3) after 48h of treatment and the protein content was concentrated using Pierce™ Protein Concentrator PES Tubes 10K from Thermo Fisher. Then, total protein content was measured by Bradford assay (see section 3.1.5) in order to standardize the amount of protein loaded on each well and the ELISA assay was performed according to manufacturer's instructions.

3.1.8.2. Immunofluorescence for CRT detection

The CRT exposure in the membrane of treated and control GL261 cells was observed with Immunofluorescence. Cells were seeded in MatTek Glass Bottom Disher. Twenty-four hours later, culture medium was replaced by medium containing the appropriate treatment. After 24h of treatment, cells were washed twice with 0.5 ml of PBS and fixed with paraformaldehyde pH 7.4 at 2% for 10 min. Then, cells were washed twice with 2 ml of ice-cold PBS and cells were incubated with 2 ml of blocking buffer (3% BSA in PBS) for 30 min. After that, cells were incubated overnight with the primary anti-calreticulin antibody from Abcam (ab2907) at 1:100 dilution and 4 °C.

The next day, cells were washed 3 times with 2 ml of PBS for 5 min and incubated with secondary antibody (goat anti-rabbit IgG H&L, alexa fluor 488 from Abcam, ab150077) at 1:1000 dilution at room temperature in the dark. Cells were washed again three times for 5 min with 2 ml of PBS. Then, cells were incubated with Hoechst 33342 and Cell Mask Deep Red Membrane staining for nuclei and cellular membranes respectively, at 1:100 dilution for 5 min. Cells were washed with 2 ml PBS again and samples were prepared for confocal microscopy visualization with mounting buffer. A confocal microscope Leica SP5, equipped with 8 excitation lines and six detection channels was used for image acquisition with the objective PL APO 40x/1.25-0.75 in oil immersion. The acquired images were visualized and analysed using Image J software.

3.1.8.3. Bioluminescent assay for ATP measurement

Extracellular and intracellular ATP content was measured using the ATP Bioluminescent Assay Kit from Sigma-Aldrich ("FLAA" sigma kit), based on the ability of the luciferase enzyme to produce light using the substrate luciferin and ATP. These measurements were performed either in cellular supernatants (from control and treated cells) and also in collected lysed cells, allowing assessment of extracellular and intracellular ATP. These assays were performed after 12, 18 and 24h treatment.

Extracellular ATP

For these measurements, in order to avoid ATP degradation by the ATPases present in the FBS culture medium, specific culture medium with inactivated FBS was used. The FBS was inactivated by incubation for 2h at 65 °C as described in [197]. Cells were seeded in 24- well plates at 32,000 cells per well in culture medium with non-inactivated FBS. After 24h, medium was removed and new culture medium with inactivated FBS and the chosen treatment was added. To assess ATP degradation in presence of non-inactivated FBS, the supernatant of cells growing in medium with non-inactivated FBS was also analyzed as an additional control. Once

the time of treatment was finished, 150µl of cellular supernatant were collected and centrifuged at 900 x g for 2 min in order to remove any floating cells. Then, 100µl of supernatant of each sample were loaded in a 96 well plate special for luminescence assays. The plate was introduced in the Victor3 Multilabel Counter and 100 µl of the ATP mix containing luciferin and luciferase were added with the help of an automatic injection system. Immediately after this addition, the generated light was measured during 10 seconds.

Intracellular ATP

For intracellular ATP measurement, cells were washed with PBS, trypsinized and centrifuged. Then, supernatant was removed and pelleted cells, resuspended in 1ml of Tris Borate buffer 40 mM pH 9.2 and incubated at 95 °C for 10 min to lyse them. Then, samples were incubated for 30 seconds on ice and centrifuged at 13,000 x g at 4 °C for 5 min. An aliquot of 100 µl of the cell lysate was used for ATP measurement. With the luminescence assay, an estimation of the ATP content *per well* was estimated. As different treatments may cause a decrease in total cell number for each well, ATP content was calculated *per cell* in order to take these differences into account. To achieve this, the number of cells after each treatment was calculated from Trypan blue and MTT viability assays and cellular volume was estimated as ca. 1.2 pl, by comparison with the volume of the C6 glioma cells in postconfluent phase [198].

3.2. *In vivo* studies: GL261 mice

Animal models used in this thesis were C57BL/6j female wild type (wt) mice weighting 18-24 g and aged 12-16 weeks, which were obtained from Charles River Laboratories (Charles River Laboratories Internacional, l'Abresle, France) and housed in the animal facility (*Servei d'Estabulari,* https://estabulari.uab.cat/ *)* of the *Universitat Autònoma de Barcelona*.

All animal experiments were conducted according to experimental protocols, previously approved by the local ethics committee (*Comissió d'Ètica en l'Experimentació Animal i Humana, https://www.uab.cat/etica-recerca/)* according to regional and state legislations (protocol CEEAH-3665). The supervision protocol applied by the animal facility staff in order to assess mice welfare parameters in GL261 tumor-bearing animals is shown in Annex II. The final score obtained in this assessment was determinant for decision regarding euthanization and halting of the experimental protocol if needed due to humanitary reasons. Each mouse evaluated was given a unique alphanumerical identifier. Identifier CXXXX belong to mice bearing GL261 tumors. In order to distinguish animals from the same cage, unique ear notch combinations were made with an ear punch device.

3.2.1 GL261 tumor generation

For GL261 GB generation, analgesia (Metacam, Böhringer Ingelheim at 1 mg/kg) was administered subcutaneously to each animal 15 minutes prior to anaesthesia and 24 and 48h after surgery. Animals were anesthetized with a mixture of ketamine (Parke-Davis SL, Madrid) at 80 mg/kg and xylazine (Carlier, Barcelona, Spain) at 10mg/kg administered intraperitoneally. Once anesthetized, the head area was shaved and animals were immobilized in a stereotactic holder (Kopf Instruments, Tujunga/CA, USA). The incision site was sterilized and a 1 cm incision was made exposing the scull. Then, a 1mm hole was drilled 0.1 mm posterior to the Bregma and 2.32 mm to the right from the midline using a microdrill (Fine Science Tools, Heidelberg, Germany). A 26G Hamilton syringe (Reno/NV, USA), positioned on a digital push-pull microinjector (Harvard Apparatus, Holliston/MA, USA) was then used for injection of 4 µl of RPMI medium containing 100,000 GL261 cells (obtained as in 3.1.1) at a depth of 3.35 mm from the skull surface at a rate of 2 µl/min. Once the injection was completed, the syringe was left untouched for 2 additional minutes before its removal to prevent the cells from leaking outside the scull. Then, the Hamilton syringe was gently and slowly taken out and the scission site closed with suture silk 6.0 (Braun, Barcelona, Spain). The animal was left in a warm environment to recover from anaesthesia.

3.2.2 Tissue preservation

GL261 mice were euthanized by cervical dislocation either for cellular/molecular validation or due to symptoms of suffering according to score and criteria shown in Annex II. Brain samples (tumor, contralateral) or other organs of interest like the spleen were excised and stored in liquid nitrogen for further western blot analysis. Tumor samples were obtained through dissection and separated from contralateral normal brain parenchyma. These tissues were resected after visual inspection of the whole brain and tumor, avoiding as much as possible the crossed contamination of tissues.

3.2.3 Therapy administration to GL261 mice

TMZ (Sigma-Aldrich, Madrid, Spain) was dissolved in 10% DMSO in saline solution (0.9% NaCl) and was administered by oral gavage at a dose of 60 mg/kg every six days from day 11 post implantation. The maximum cumulative dose administered was 480 mg/kg, which states for a total of 8 therapy cycles. This dose was established in [191] as the highest safe TMZ dose not causing lymphoma to treated mice.

TDB was dissolved in 10% DMSO in saline solution (0.9% NaCl) and it was administered either by oral gavage or by intraperitoneal injection at either 253.8 mg/kg or 507.6 mg/kg split into two doses one in the morning and one in the afternoon for 3 consecutive days for target validation purposes. To analyze the amount of TDB in blood, a single dose of TDB was administered, either by oral gavage or intraperitoneal injection, at 253.8 mg/kg.

3.2.4 *In vivo* MRI/MRS/MRSI

MR studies were carried out at the joint NMR facility of the *Universitat Autonòma de Barcelona* and CIBER-BBN (*Cerdanyola del Vallès*, Spain) Unit 25 of the ICTS NANOBIOSIS (www.nanbiosis.es) with a 7T horizontal magnet (Biospec 70/30, Bruker Biospin, Ettlingen, Germany) equipped with actively shielded gradients (B-GA12 gradient coil inserted into a B-GA20S gradient system) and a quadrature receive surface coil, actively decoupled from a volume resonator with 72 mm inner diameter. Mice were placed in the scanner bed and anesthetized with 0.5-2% isoflurane in O_2, keeping the respiratory frequency at 60-80 breaths/min. Breathing and body temperature was constantly monitored (SA Instruments, Inc., New York, USA).

3.2.4.1 MRI studies

MRI acquisitions were performed in GL261 tumor-bearing mice for tumor detection and volume measurement. The GL261 mice were screened by acquiring high resolution coronal T2-weighted (T2w) images using a Rapid Acquisition with Relaxation Enhancement (RARE) sequence to detect brain tumor presence and to monitor its evolution stage. The acquisition parameters were as follows: repetition time (TR)/effective echo time (TE_{eff}) = 4200/36 ms; echo train length (ETL) = 8; field of view (FOV) = 19.2 × 19.2 mm; matrix size (MTX) = 256 × 256 (75 × 75 µm/pixel); number of slices (NS) = 10; slice thickness (ST) = 0.5 mm; inter-ST = 0.1 mm; number of averages (NA) = 4; total acquisition time (TAT) = 6 min and 43 s. MRI data were acquired and processed on a Linux computer using ParaVision 5.1 software (Bruker BioSpin GmbH, Ettlingen, Germany).

3.2.4.2 Multislice MRSI acquisitions

The MRSI acquisitions were performed following a multi-slice, 3D like acquisition protocol optimized in our group [37] for gathering metabolic information across the whole tumor volume. Consecutive 14 ms echo time (TE) MRSI grids with Point-RESolved Spectroscopy (PRESS) localization were acquired individually across the tumor, using as a reference T2w high resolution MRI slices as references. The first upper grid (Grid 1) had a matrix size of 10 × 10. Then, Grid 2 was acquired 1 mm below Grid 1 with a matrix size of 12 × 12. Grid 3 was

acquired 1 mm below Grid 2, with a matrix size of 12 × 12. Finally, if tumor volume was not completely covered with 3 grids, a last Grid 4 was acquired 1mm below Grid 3 with a matrix size of 10 × 10 (Figure 16). In order to ensure quality of the acquired data, shimming was performed individually for each MRSI grid. MRSI grids were spatially located such that the volume of interest (VOI) included most of the tumoral mass as well as normal/peritumoral brain parenchyma.

Acquisition parameters for all grids were: FOV, 17.6 mm × 17.6 mm; VOI in Grids 1 and 4 was 5.5 mm × 5.5 mm × 1.0 mm. VOI in Grids 2 and 3 was 6.6 mm × 6.6 mm × 1.0 mm. ST, 1 mm; TR, 2500 ms; Sweep Width (SW), 4006.41 Hz; NA, 512; TAT, 21 min 30 s. Water suppression was performed with Variable Power and Optimized Relaxation Delay (VAPOR), using a 300 Hz bandwidth. Linear and second order shims were automatically adjusted with Fast Automatic Shimming Technique by Mapping Along Projections (FASTMAP) in a 5.8 mm × 5.8 mm × 5.8 mm volume which contained the VOI region. Six saturation slices (ST, 10 mm; sech-shaped pulses: 1.0 ms/20250 Hz) were positioned around the VOI to minimize outer volume contamination in the signals obtained. Total acquisition time for a typical MRI/MRSI 4 grids full protocol was about 3.5 h. In general, multislice MRSI studies were only performed in tumors presenting volume larger than $20mm^3$, since from our group experience, smaller volumes cannot be segmented in a confident way with our semi-supervised analysis approach [191]. If the measured tumor volume was below $20mm^3$, only MRI studies were performed to follow up tumor volume.

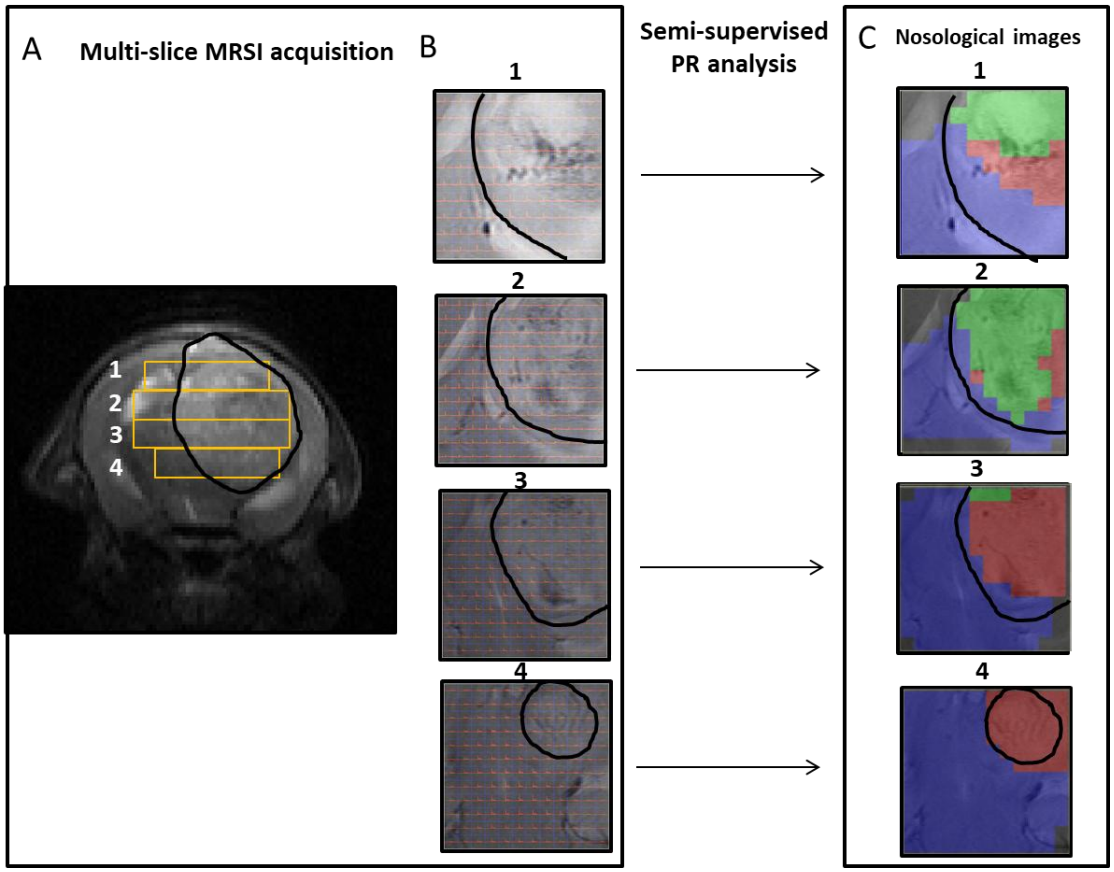

Figure 16: Spatial location of multislice MRSI grids within the mice brain and the obtained nosological images.
A) Coronal T2 weighed MRI for tumor-bearing mouse C1263 with positioning of the four MRSI grids. B) Enlarged view of MRSI grids shown in the axial orientation. C) Nosological images obtained after semisupervised PR analysis (see section 1.5.4). Black lines mark tumor boundaries.

3.2.4.3 MRI and MRSI Processing and Post Processing

Volume calculation

Manual segmentation of abnormal brain masses in T2w images was performed and tumor volumes were calculated from T2w high resolution axial images using the following equation:

$$TV\ (mm^3) = [(AS1 \times ST) + [(AS2 + (\ldots) + AS10) \times (ST + IT)]] \times 0.075^2 \qquad \text{(Equation 1)}$$

Where TV is the tumor volume, AS is the number of pixels contained in the region of interest delimited by the tumor boundaries in each slice of the MRI sequence, ST is the slice thickness (0.5 mm), IT the inter-slice thickness (0.1 mm) and 0.075^2 mm^2 is the individual pixel surface area. The tumor area was calculated from pixels in each slice, using an automated system for generating regions of interest (ROIs) available in the ParaVision 5.1 software (Bruker BioSpin, Ettlingen, Germany). The inter-slice volume was not registered and it was estimated adding the inter-slice thickness (IT) to the corresponding slice thickness in Equation 1.

MRSI post-processing and pattern recognition (PR) strategies

Data were initially pre-processed at the MR workstation with Para Vision 5.1, and then post-processed with 3D Interactive Chemical Shift Imaging (3DiCSI) software package version 1.9.17 (Courtesy of Truman Brown, Ph.D., Columbia University, New York, NY, USA) for line broadening adjustment (Lorentzian filter, 4 Hz), zero-order phase correction and exporting the data in ASCII format. Dynamic MRSI processing Module (DMPM), running over Mat Lab 2013b (The Math Works Inc., Natick, MA, USA) was used to align all spectra within each MRSI matrix (using the choline containing compounds signal as reference, 3.21 ppm). No baseline correction was performed in these spectra. The 0–4.5 ppm region of each spectrum in the MRSI matrix was individually normalized to unit length and the normalized matrix was exported in ASCII format which was the input for PR analysis. The semi-supervised source extraction approach was then applied for the extraction of meaningful source signals from the MRSI investigated tumors. From the biochemical viewpoint, the source extraction technique to classify MRS data assumes that in each voxel there is a mixture of heterogeneous tissues and its metabolites from which the contribution of each source can be obtained. This semi-supervised approach was previously described by our group [98] and it is based on constrained non-negative matrix factorization (cNMF) for initial source extraction. This allows the classification of each acquired voxel into normal brain parenchyma, actively proliferating tumor and tumor responding to treatment and calculation of nosological maps representing the spatial response to treatment. Green color is used when the GB responding to treatment source contributes the most, blue for normal brain parenchyma, red for actively proliferating GB and black for undetermined tissue.

Tumor Responding Index (TRI) Calculations

In order to measure the overall response level from a given tumor using the obtained nosological images, an arbitrary parameter named Tumor Responding Index (TRI), described in [37], was calculated (Equation 2).

$$TRI = \frac{Tumor\ responding\ pixels}{Total\ tumor\ pixels}\ x\ 100 \qquad \text{(Equation 2)}$$

The TRI value corresponds to the percentage of green (responding) pixels over the total tumor pixels. It was calculated as follows: first, tumor silhouette was outlined and all the pixels within the tumor region were counted, including blue, red, green and black. Then, only green (responding) pixels were counted and procedure repeated for each slice. With the overall values for the whole tumor, the percentage of responding pixels was calculated for all

recorded grids. Then, cases were categorized according to the classes established in [37], taking into account both TRI percentage and volumetric data from MRI measurements. **High response**, presenting TRI > 65%, tumor volume reduction regarding the previous measurement (partial response or stable disease according to RECIST criteria [199]) and green pixels observed in at least two consecutive MRSI grids. **Intermediate response**, with TRI ranging 35–65%, tumor size unchanged, reduced or not growing more than 20% (stable disease according to RECIST criteria) and green pixels must be present in at least two consecutive MRSI grids. **Low response**, with TRI < 35% and tumor size increasing more than 20%.

3.3 Statistical analyses

The Shapiro-Wilk or Kolmogorov-Smirnov tests were performed for assessment of sample distribution. Levene's test was used for assessing variance homogeneity. For groups following normal distribution, parametric tests were used for the analysis (Student's t test). For groups following a non-normal distribution, nonparametric tests were performed (Mann-Whitney U test). *The ATP measurement* required different approaches following advice from the Statistical Facility (*Servei d'Estadística UAB,* http://sct.uab.cat/estadistica/*).* Data were transformed with a natural logarithm calculation, due to the large variance difference among groups. After transformation, sample distribution was assessed with Kolmogorov-Smirnov (KS) test and variance homogeneity assessed with Levene's test. Analysis of Variance (ANOVA) test was applied with Tukey's post-hoc correction for multiple comparisons. Survival analyses of GL261 mice were compared with Log Rank (Mantel-Cox) Test using GraphPad Prism software.

4. Results

4.1 Unraveling aspects of CK2 inhibition contribution to therapy response in preclinical GL261 glioblastoma

The promising results with CK2 inhibition in GL261 cells *in vitro*, reaching 20% of cellular viability [85], in addition to satisfactory results described by other groups working with preclinical tumors [110] lead us to hypothesize and expect an excellent performance of CK2 inhibitors for *in vivo* work. Specifically CX-4945, already at clinical trial level, was expected to improve outcome in our preclinical GB models. However, the performance of CX-4945 as a single agent showed discrete results far from the expected [85], driving us to explore different aspects of CK2 inhibition to better understand *in vivo* performance such as differential subunits expression or dual inhibition CK2-Pim1, which also presented outstanding results in GL261 cultured cells.

4.1.1 On the differential expression of Protein Kinase CK2 depending on proliferative status of GL261 cultured cells: possible relevance of CK2α' content for glioblastoma therapy

Specific goals: to analyze the relative protein content of α, α' and β CK2 subunits in exponentially growing (EP, exponential phase) and partially growth arrested (PCP, postconfluent phase) GL261 cells in culture and also in GL261 established tumors, which could help to understand expression changes related to the proliferative status of cells and differential susceptibility to inhibition. In order to assess the proliferation status of cells in the different growth curve phases, cyclin D1 expression was also analysed. Furthermore, overall CK2 activity was checked through the phosphorylation status of the CK2-specific site Ser129 of Akt 1 in GL261 cells. This work is currently under review in the Pathology & Oncology Research Journal.

4.1.1.1 GL261 growth curve: CK2 content and activity in EP and PCP GL261 cells

The GL261 growth curve showed the expected phases (Figure 17A), corresponding to initial phase (IP) (days 1 to 3), exponential phase (EP) (days 4 to 7) and postconfluent phase (PCP) (days 8 to 11). CK2 content and activity were assessed in IP, EP and PCP GL261 cells at days 3, 6 and 9 of the growth curve, respectively.

Cyclin D1 content was analyzed in GL261 cells (both EP and PCP) and GL261 tumors (Figure 17B and C, Table 2) showing a significant ($p<0.05$) 7.1-fold decrease during the PCP phase compared to the EP. GL261 tumors presented an intermediate content between EP and PCP cells (Figure 17D and E).The content of different CK2 subunits is shown in Figure 18A and

Figure 18B. CK2α' content decreases (1.42-fold) during the postconfluent phase compared to the exponential phase ($p<0.05$). On the other hand, CK2α and β protein content remained essentially unchanged, although a differential trend was observed (slightly higher values in PCP in comparison with EP, with tendency for signification ($0.05\leq p\leq 0.1$) for CK2α). Furthermore, CK2α, α' and β content were also assessed in IP cells and no differences were found between IP and EP cells ($p>0.05$, results not shown). In addition to expression levels, CK2 activity was indirectly assessed by Western blot (Figure 18C and D, Table 2). The pAkt Ser129 content decreases during the postconfluent phase (3.8 fold decrease, $p<0.05$), which would agree with CK2 activity diminishing in less proliferative cells.

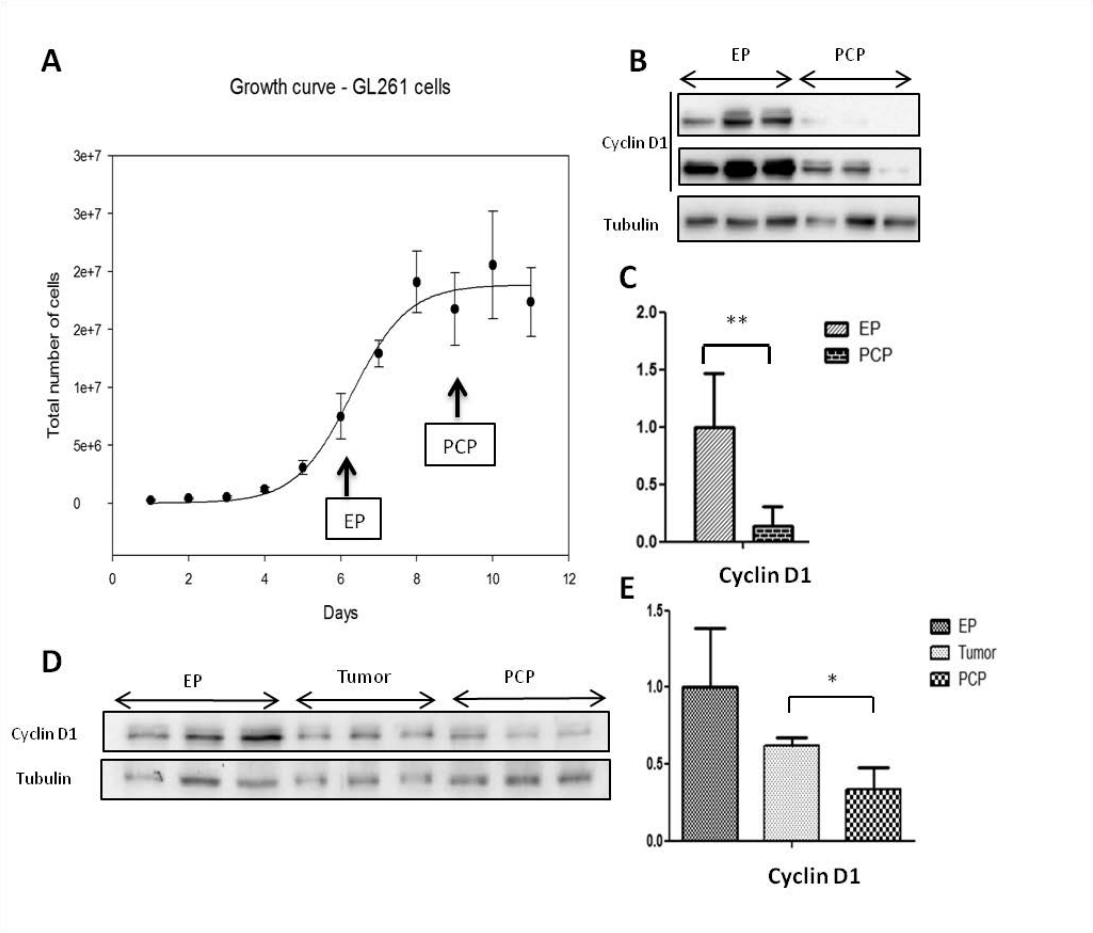

Figure 17: GL261 cells growth curve and proliferative status along growth phases.
*(A) Growth curve carried out with n=3 to 6, depending on the time point evaluated, showing mean ±SD for each time point. (B) Western blot for EP and PCP GL261 protein extracts (n=3 for each condition is shown) in which Cyclin D1 and Tubulin expression were analyzed. The lower lane for Cyclin D1 shows a more exposed image to visualize better cyclin D1 expression in PCP cells. (C) Comparative quantification of Cyclin D1 normalized with tubulin expression (n=13 for each group). (D) Cyclin D1 content in EP and PCP cells and in GL261 tumors (n=3 for each condition is shown). (E) Comparative quantification of Cyclin D1 normalized with tubulin expression (n=3 for GL261 cultured cells and GL261 tumors). *=p<0.05, **=p<0.01.*

	EP	PCP	p- value
CK2α'	1.00 ± 0.21	0.54 ± 0.26	3.75E-05**
CK2α	0.81 ± 0.42	1.00 ± 0.26	0.091
CK2β	0.77 ± 0.39	1.00 ± 0.34	0.233
Cyclin D1	1.00 ± 0.46	0.14 ± 0.16	2.31E-06**
pAkt Ser129/total Akt	1.00 ± 0.42	0.26 ± 0.27	1.87E-05**
CK2α'/ CK2α	1.56 ± 0.76	0.6 ± 0.29	0.0006**
CK2α'/CK2β	1.48 ± 0.72	0.67 ± 0.44	0.004**
CK2α/CK2β	1.16 ± 0.64	1.15 ± 0.59	0.97

Table 2: Comparative analysis of CK2 content and activity and Cyclin D1 expression in GL261 cells

Analysis of CK2 α', α and β and Cyclin D1 expression and pAkt S129 phosphorylation/ total Akt ratio in different growth phases of cultured GL261 cells, as well as ratios of different subunits. EP= exponential phase, PCP= postconfluent phase. Mean ± SD is shown, and experiments were performed with n=13. **=p<0.01. The value of 1 was attributed to the highest one in EP/PCP comparison.

4.1.1.2 Assessment of CK2 content in GL261 tumors

The content of CK2 subunits (α', α and β) in GL261 tumors was assessed and compared with EP and PCP GL261 cells (Figure 18). Values found are summarized in Table 3, with higher expression of all subunits in EP in comparison with PCP and GL261 tumors, whereas the difference between tumors and PCP cells varied depending on the subunit studied. Nevertheless, no significant differences were found for CK2α or CK2β expression when comparing the three different conditions. Regarding CK2α' expression, tumors presented an intermediate value between EP cells and PCP cells ($p<0.05$ for both comparisons).

4.1.1.3 Unbalanced CK2 expression

In order to assess the possible unbalance in expression of CK2 subunits, ratios were calculated for the different conditions studied. Regarding CK2α'/α and CK2α'/β ratios, these were found 2.6 and 2.2 fold lower, respectively, in PCP cells in comparison with EP cells, whereas no significant differences were found for CK2α/β (Table 3).

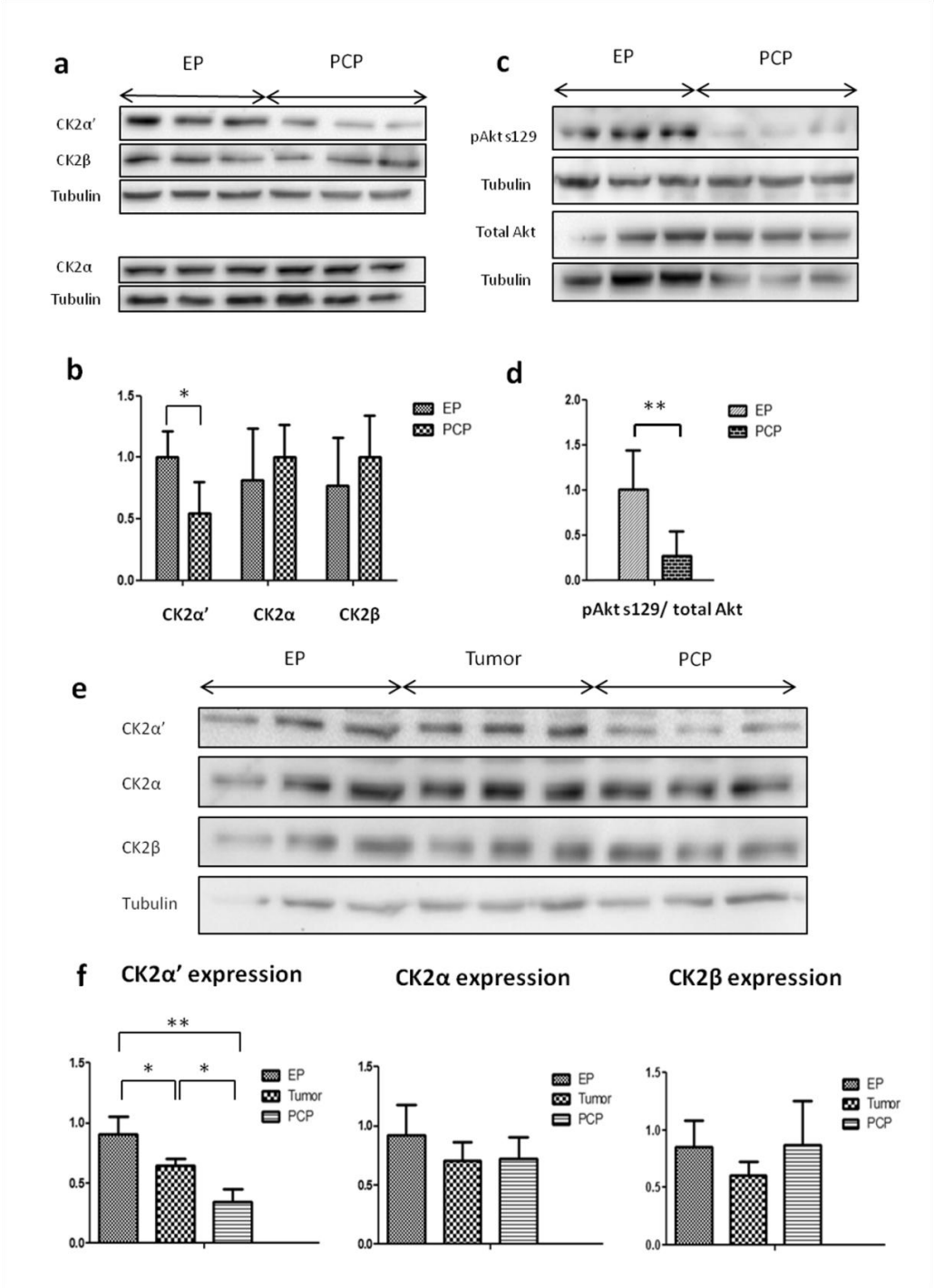

Figure 18: CK2 content and CK2 activity in EP and PCP GL261 cells and in GL261 tumors.
*(A) Western blot analysis of GL261 cell protein extracts. (B) Comparative quantification of CK2α', α and β content normalized with Tubulin content in EP and PCP cells (n=13 for each group). The CK2α' levels were found 1.42 fold lower in PCP cells in comparison with EP ones (**=p<0.01), whereas the CK2α and CK2β contents remained constant in both phases. (C) Western blot for EP and PCP GL261 cell protein extracts in which total Akt, Tubulin content and Akt s129 phosphorylation status were analysed. (D) Comparative quantification of pAkt s129/total Akt ratio normalized with tubulin content in which a 3.8 fold decrease is seen in PCP cells (n=13 for each group). **=p<0.01. (E) Western blot for EP and PCP GL261 cells and GL261 tumor protein extracts in which CK2α, α' and β content was analysed. F) Comparative quanitification of the CK2 subunits content in EP, tumor and PCP cells normalized with tubulin (n=3 for each condition). *=p<0.05 and **=p<0.01 according to Student's t-test.*

				p value		
	EP	Tumor	PCP	EP-Tumor	EP-PCP	Tumor-PCP
CK2α'	0.90 ± 0.15	0.65 ± 0.06	0.35 ± 0.1	0.048*	0.006*	0.011*
CK2α	0.92 ± 0.26	0.70 ± 0.16	0.72 ± 0.18	0.274	0.327	0.910
CK2β	0.85 ± 0.23	0.61 ± 0.12	0.87 ± 0.38	0.200	0.952	0.400
Cyclin D1	1±0.39	0.62±0.05	0.33±0.14	0.23	0.049*	0.029*
CK2α'/ CK2α	1.01 ± 0.14	0.95 ± 0.21	0.48 ± 0.09	0.726	0.006**	0.006**
CK2α'/CK2β	1.08 ± 0.14	1.08 ± 0.11	0.43 ± 0.17	1.000	0.007**	0.007**
CK2α/CK2β	1.08 ± 0.08	1.16 ± 0.02	0.88 ± 0.2	0.544	0.174	0.174

Table 3: Comparative analysis of CK2α, α' and β and Cyclin D1 content in GL261 tumors.
Analysis of CK2α', α and β and Cyclin D1 content, as well as the ratios of different subunits for GL261 tumors. Ratios were obtained for each individual sample (not from division of average values). EP= exponential phase, PCP= postconfluent phase. Mean ± SD is shown, experiments were performed with n=3. Please refer to Materials and Methods section 3.1.6 for details about quantitation.*=p<0.05, **=p<0.01.

This decrease in CK2α', which is not fully compensated by the increase in CK2α, changes the proportion between catalytic and regulatory subunits. In tumors, the ratios calculated suggested higher similarity with EP cells and, accordingly, no significant differences were found between EP cells and GL261 tumors (Table 3). On the other hand, CK2α'/α and CK2α'/β ratios were significantly higher in GL261 tumors compared to PCP cells, underlining the CK2α' downregulation in PCP cells, whereas no differences were found in CK2α/CK2β ratio.

4.1.1.4 Discussion

CK2 is known to promote proliferation and inhibit apoptosis [200], being involved in cell cycle regulation and senescence. CK2 plays an important role in cell division [201] and mitosis [202], being essential for G2/M transition in early embryo mitosis [203]. In this study, we have observed decreased CK2 activity in GL261 postconfluent cells compared to exponential cells (Figure 18), which would agree with the decrease in CK2 activity in quiescent cells.

The asymmetric expression of CK2 subunits has been described by some authors [204] who reported that a higher CK2α/CK2β ratio correlates with expression of epithelial-to-mesenchymal transition markers in breast cancer samples. Ratios obtained for these authors (ca. 1.4, see [204] for details on calculations) were comparable to ratios calculated in this

chapter for EP cells and GL261 tumors (1.08 ± 0.08 and 1.16 ± 0.02 respectively), being lower for PCP cells (0.46 ± 0.22).

However, the novel part of this thesis chapter is related to CK2α' expression levels in the GL261 cell line. Results reported here show, for the first time and to our knowledge, that CK2α' is specifically downregulated in postconfluent, slowly proliferating GL261 cells. This agrees with Pinna's and Oliviero's work [138], in which an induction of CK2α' expression was observed during G0/G1 transition in fibroblasts, suggesting a differential expression in senescent and proliferating fibroblasts [138] and with Bae's work, reporting reduced CK2α' expression in senescent fibroblasts [205]. Taken together, these findings suggest that CK2α' content could be proposed as a proliferation marker for GL261 cells. However, it is still unclear whether CK2α' itself plays specific roles in quiescent GL261 cells, or whether there is a direct relationship between CK2 activity decrease and CK2α' content decrease in PCP cells of this murine cell line. One hypothesis could be that the holoenzyme containing CK2α' would be able to phosphorylate Akt1 in S129 better than the one containing CK2α, or that phosphatase activity, such as protein phosphatase 2A, was higher in PCP cells [206]. We have also observed that CK2α' content in GL261 tumors reached an intermediate value between EP and PCP GL261 cells, probably due to the heterogeneous nature of GL261 tumors, composed by both highly proliferating and slowly proliferating cells [190] (similar to EP and PCP, respectively). The environment and growth regulatory conditions in each growth phase could present similarities with a different tumor region. The EP cells would be similar to the peripheral tumor cells: ample access to nutrients and oxygen and, accordingly, a very high proliferative rate. On the other hand, the PCP cells would resemble more cells in the inner part of the tumor, where growth factors, nutrients and oxygen may become limiting, decreasing the proliferation rate and where cell death-related phenomena may be also taking place. This is in agreement with results reported by [190], in which the same GL261 tumor can present regions with different Ki67% values ranging from 40-80%, with higher values on the highly proliferative periphery, reflecting the mixed contribution that may be taking place also in the investigated GL261 tumors in this work.

As CK2α' has been described to inhibit caspase 3 cleavage [127], we could hypothesize that higher levels of this subunit could make GL261 cells less prone to apoptotic death, although this protective effect can be also mitigated by CK2β, which has been shown to attenuate CK2α'-mediated phosphorylation of caspase 3 [127]. If we accept that GL261 tumors are composed by cells with mixed proliferative characteristics, these results point that cells with high CK2α' levels could benefit from a protective effect against apoptotic death triggered by

treatment, and this could lead to resistance to such treatment. Moreover, differences between the expression and activity of CK2 catalytic subunits may become relevant to improve therapeutic success, since CK2α' has been described to be more sensitive to some CK2 inhibitors than CK2α [165] and efforts are being made to develop CK2α and CK2α' specific inhibitors [167]. Still, further work will be needed to clarify whether the susceptibility to CK2 inhibitors is actually different according to GL261 cell proliferative status. Data presented here suggest that whenever CK2α' selective inhibitors were available, it may be relevant to evaluate them in GL261 GB bearing mice. In this respect, a word of caution should be raised if such a treatment becomes available: immune system participation in response to therapy, which cannot be simulated with *in vitro* assays, could be affected if an inappropriate schedule of administration is applied [85], reverting the expected beneficial effect.

4.1.1.5 Conclusions

- CK2α' showed remarkable differences in its content along the cell growth phases in GL261 cultured cells, being higher in EP in comparison to PCP cells, whereas GL261 tumors presented an intermediate content value. This could allow us to suggest that in this tumour model, CK2α' could act as a proliferation marker. CK2α and CK2β content, on the other hand, did not present significant changes along different growth phases or in comparison with GL261 tumours.
- CK2 measured activity was much higher in EP (highly proliferating cells) in comparison with PCP (slowly proliferating, quiescent cells), although it is still unclear if the events of the decrease in CK2 activity and the decrease of CK2α' content are directly related. In addition, unbalanced content of CK2 subunits was detected, i.e. the decrease of CK2α' content is not fully compensated by CK2α increase which indicates change in the balance of catalytic and regulatory subunits.
- GL261 tumours presented results supporting a mixed contribution of highly proliferating and slowly proliferating cells. Selective CK2α' inhibitors, whenever available, could be useful for targeting cells actively proliferating, provided a suitable schedule of administration is used.

4.1.2 TDB emerging as a potential non-mutagenic therapy approach for preclinical GL261 glioblastoma: dual CK2 and Pim1 inhibition

The 1-(β-D-2'-deoxyribofuranosyl)-4,5,6,7-tetrabromo-1H-benzimidazole (TDB) is a dual inhibitor of CK2 and Pim-1 kinases with high efficiency and remarkable selectivity [207] that has been shown to produce a very potent effect on cellular viability in different cell lines [175]. This suggests TDB as a promising candidate for cancer treatment. In addition, preliminary results from our group [85] showed outstanding results over GL261 cell viability *in vitro,* which may point to another non-mutagenic targeted therapy for our preclinical GB model. .

Specific objectives: To confirm and expand the results obtained *in vitro* with the GL261 cultured cells, getting more insight about TDB efficacy and adequate targeting. To perform a preliminary pharmacokinetics profile and to proceed with evaluation of TDB in GL261 tumor-bearing mice treatment.

A summary of different concentrations, doses and conditions used for TDB potential evaluation alone and in combined experiments is summarized below (Table 4) in order to provide the information at a glance.

***In vitro* studies**			
	Concentration (μM)	**Duration of treatment (h)**	
Viability Assays			
MTT	1.25-80	72	
Trypan Blue	5-30	24-72	
Target Validation			
Level of phosphorylated substrates	1.25-40	8-24	
CK2 activity	2.5-40	24	
Combined Treatment			
TDB concentration	5-30	72	
TMZ concentration	250-1000		
***In vivo* Studies**			
	Dose (mg/kg/day)	**Doses**	**Analysis time after last dose (h)**
Target Validation			
Oral	253.8-507.6	3	24
Intraperitoneal	253.8	3	24
TDB bloodstream level			
Oral	253.8	1	0.5, 1 and 2
Intraperitoneal	253.8	1	0.75

Table 4: Summary of conditions used for in vitro and in vivo TDB studies

4.1.2.1. In vitro results with GL261 cells

TDB effects over cell viability

The effect of TDB on GL261 cellular viability *in vitro* was assessed by MTT assay after 72h of treatment at concentrations ranging from 1.25 to 80 μM (Figure 19A). TDB presented a

prominent effect and the calculated EC_{50} and IC_{50} (both values were coincident for these cells was 13.14 µM, clearly lower than other kinase inhibitors such as TBB, apigenin and CX-4945 tested in [85]. We also wondered whether TDB produced mostly cytostatic or cytotoxic effect on GL261 cells. In order to answer this question, TDB-treated cells were harvested after 24, 48 and 72 hours of treatment, stained with Trypan Blue and counted (Figure 19B). The percentage of dead cells (Trypan blue positive) increased with TDB concentration. At the 15 µM concentration, the closest to the calculated IC_{50} (13.14 µM), the TDB effect seemed to be mainly cytostatic, since the number of living cells was reduced and there was no significant increase in dead cell counting (in fact, there was a significant reduction). On the other hand, at 30µM concentration, TDB seemed to already produce a cytotoxic effect since 57 ± 30% of GL261 cells were Trypan blue positive after 48h of treatment and 82 ± 14% after 72h. Accordingly, this suggests that the local TDB concentration would determine the main effect taking place: low concentrations (5 - 15 µM) would produce mostly cytostatic effect while with higher concentrations (≥30 µM) a more pronounced cytotoxic effect would be triggered.

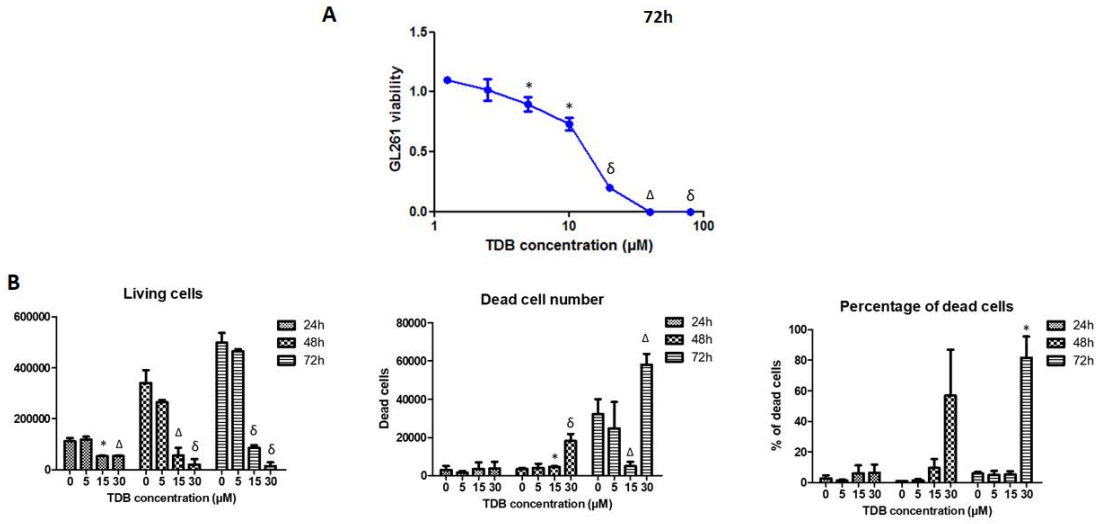

Figure 19: Dose-dependent GL261 cell viability after TDB treatment and assessment of cell death induction at different treatment times

*A) TDB concentrations were 1.25, 2.5, 5, 10, 20, 40 and 80 µM. The value 1 (100% viability) evaluated with MTT assay was assigned to control cells treated with vehicle (DMSO ranging from 0.0025 to 0.16%, since every concentration has its own vehicle control). Experiments were performed with n=4 and mean ± SD values are shown. B) Total living and dead cells number and percentage of dead cells evaluated by Trypan Blue exclusion assay after TDB treatment (n=3 for every condition). *= p<0.05, Δ=p<0.01 and ϑ=p<0.001 indicate statistical significance according to Student's t-test comparing treated and control cells.*

TDB target validation *in vitro* for CK2 inhibition

As a dual CK2-Pim1 inhibitor, both activities were assessed after treatment of GL261 cultured cells at concentrations ranging from 1.25 to 40 µM during 8 and 24 hours.

CK2 activity: the CK2 inhibition level was evaluated in TDB-treated cells through two different methods: the analysis of the phosphorylation status of the CK2-specific site Ser129 of Akt1 and measurement of CK2 activity using a peptide specific for CK2.

Phosphorylation of CK2 specific substrates: Results showed that TDB inhibited Akt Ser129 phosphorylation in a dose-dependent manner (Figure 20A,C). The phosphorylation of Akt Ser129 was significantly lower in TDB treated cells at 5 and 10 µM ($p<0.01$) and at 20 and 40 µM ($p<0.001$), after 8 and 24h of treatment. The pAkt S129 phosphorylation was significantly reduced after treatment with concentrations equal or higher than 5µM, reaching a maximum of 5 fold decrease at 20 and 40 µM. In this case, the period of treatment does not seem determinant and results obtained after 24h of treatment were not significantly different from results obtained at 8h. Additionally, the phosphorylation status of Akt Ser473, phosphorylated by mTORC2 [179] see Figure 10 from section 1.5.3), was also evaluated in TDB-treated cells (, because it had been described that both CK2 and Pim-1 inhibition can lead to an indirect decrease in Akt Ser473 phosphorylation [169, 179]. A decrease in the phosphorylation at this target can be observed at high concentrations after 8 and 24 hours of treatment (Figure 20B, C). Significant differences were found in pAkt Ser473 in TDB-treated cells at 20 and 40 µM compared to untreated cells ($p<0.001$). Only the two highest concentrations (20 and 40 µM) produced a noticeable reduction in pAkt S473 and, as for Akt Ser129, no significant differences were observed among 8 and 24h, so these quantifications were grouped for further analyses.

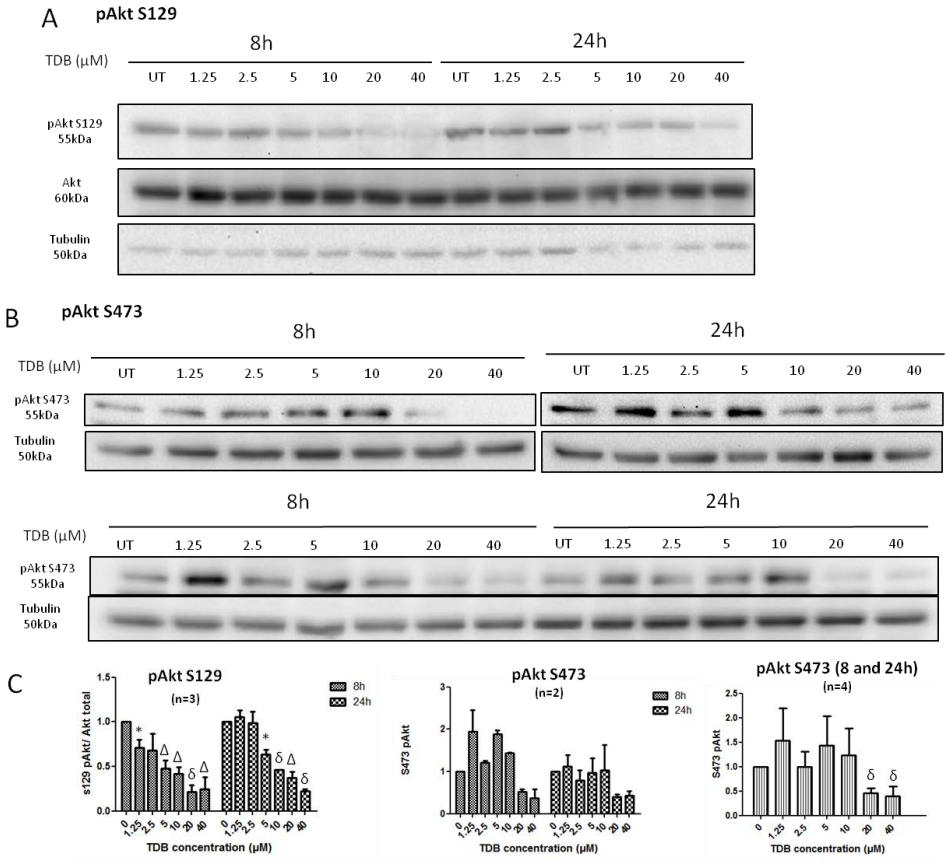

Figure 20: CK2 inhibition evaluated with specific substrates in TDB-treated GL261 cells
*UT and TDB treated cells at 1.25, 2.5, 5, 10, 20 and 40 µM for 8 and 24h were analyzed by Western blot. The value 1 was assigned to control cells treated with vehicle (DMSO). Blots were quantified and normalized by Tubulin expression. A) Phosphorylation status of Akt1 Ser129 assessment. Akt was analyzed in order to calculate the pAkt/total Akt ratio and tubulin was analyzed as loading control. B) Phosphorylation status of Akt Ser473 was assessed, two experiments are shown. Tubulin was analyzed as loading control. C) Quantification of pAkt Ser129 (n=3 different experiments) and pAkt Ser473 (n=2 experiments). For Ser473 two graphs are shown: the first showing 8 and 24h separately and the second with joint results for 8 and 24h to allow for statistical analysis. According to Student's t test *=p<0.05, Δ=p<0.01 and δ=p<0.001 in comparison with untreated cells.*

CK2 activity was analyzed in GL261 cells treated with concentrations of TDB ranging 2.5 - 40 µM and in control, non-treated cells after 24h of treatment (Figure 21). The CK2 activity is strongly inhibited by TDB even at the lowest concentration studied (2.5 µM) in which 40% of activity was detected, compared to untreated cells. At the highest concentration studied (40 µM), CK2 activity is lower than 20%, compared to untreated cells.

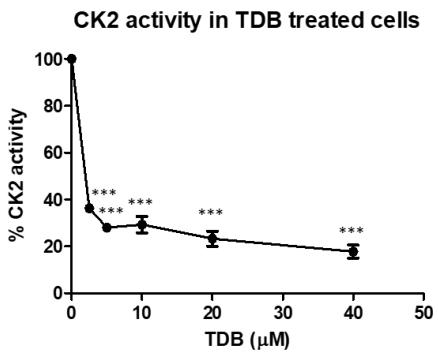

Figure 21: CK2 activity in TDB-treated GL261 cells
*CK2 activity measured on a CK2-specific synthetic peptide in lysates from GL261 cells treated with 2.5, 5, 10, 20 and 40 μM of TDB for 24h (n=4 for each condition). ***= p< 0.001 for Student's t-test for the comparison of control (100% initial value) and treated groups.*

From these results, we can observe that TDB have a strong effect inhibiting CK2 activity in GL261 treated cells. The direct measurement of CK2 activity showed a much stronger CK2 inhibition compared to the effect on pAkt S129 phosphorylation. Although both methods measure CK2 activity in a specific manner, the measurement of CK2 target pAkt S129 is an indirect indicator of CK2 inhibition, being less sensitive to changes in CK2 activity than the activity assay. Still, it should be taken into account that although the decrease on pAkt S129 is an actual indicator of the decrease in the phosphorylating activity of CK2, we cannot rule out that this pathway could be compensated *in vitro* by other kinases, and results misinterpreted. In conclusion, both methods are complementary and reflect the inhibitory effect of TDB in this case.

Pim-1 activity: the CK2 inhibition level was evaluated in TDB-treated GL261 cells through Pim-1 specific substrate Bad Ser112.

Work described by others [111] report that only the long form of Pim1 (Pim1L) is expressed in the GL261 cell line and data reported by them suggest a low content of Pim1. Accordingly, Pim1 presence was first evaluated in GL261 cells (Figure 22A,C). In addition, Pim-1 inhibition was evaluated in TDB-treated cells through the analysis of the phosphorylation status of the Pim-1 specific substrate Bad Ser112. However, due to the low expression of Pim-1 we did not really expect a decrease in pBad Ser112. Indeed, after 8 and 24 hours of treatment, no significant differences were found for pBad (Figure 22B,C) in comparison with untreated cells (8 and 24h data were grouped for this analysis). From the obtained results, it is unclear whether Pim-1 was inhibited or not. From one side we do not observe any decrease in pBad Ser112 phosphorylation in TDB treated cells, but on the other hand, Pim1 expression is weak in our cell line, as already suggested by data in [111]. Even if Pim-1 is inhibited, it is unlikely that any effect could be observed in GL261 cells viability, due to the low basal expression of Pim-1.

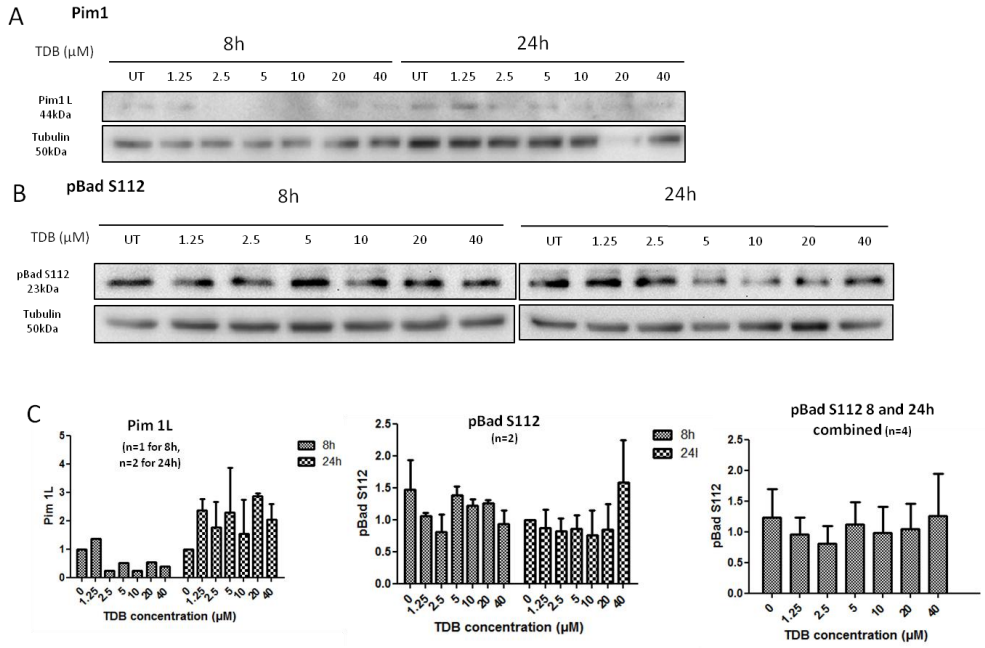

Figure 22: Pim-1 expression and inhibition in TDB-treated GL261 cells.
Untreated (UT) cells and TDB treated cells at 1.25, 2.5, 5, 10, 20 and 40μM for 8 and 24h were analyzed by Western blot. Blots were quantified and normalized by Tubulin content. A) Pim1 content. Only a low content of the long form of Pim1 was detected. B) Evaluation of the Phosphorylation status of Bad Ser112. Tubulin was analyzed as loading control. C) Quantification of the blots is shown. No significant differences were found for pBad Ser112 (results 8 and 24h of treatment were grouped for increasing "n"). Pim1 content 8h of treatment n=1 and 24h of treatment n=2. pBad S112 8h n=2 and 24h n=2. pBad all times of treatment (8+24h) n=4.

Evaluation of the *in vitro* TDB+TMZ combined treatment

The standard chemotherapeutic treatment used currently for clinical GB is TMZ [5], which also produced improved survival in preclinical GB in an adapted administration schedule [37, 188]. Moreover, the combination of TMZ and the CK2 inhibitor CX-4945 produced synergistic effect both *in vitro* and *in vivo* [85], provided an immune cycle respectful administration protocol was used for *in vivo* administration. Therefore, it was of interest to check whether the combination of TDB and TMZ could be also useful for GL261 cell treatment.

GL261 cells were treated with increasing concentrations of TDB and TMZ for 72h and the cellular viability was assessed by MTT (Figure 23A). Then, results were analyzed by the Chou-Talalay method [195] in order to determine whether the effect of the combined treatment were synergistic, additive or antagonistic. For every pair of concentrations, the combination index obtained was higher than 1, suggesting that the combined effect of TMZ and TDB is antagonistic. One possible explanation for this antagonist may be that TDB produces a more potent effect in highly proliferating cells and since TMZ slows down the proliferation rate of the cells, then TDB would produce a weaker effect on them

Dose effect curve, Median effect plots and CI calculation

The relationship between drug concentration and reduced cellular viability is shown in the dose effect curves (Figure 23A) for TDB, TMZ and TDB+TMZ after 72h treatment. As it can be observed, the combined treatment seems to work slightly better in low drug concentrations, but the joint performance is not better at higher drug concentrations (> 20µM of TDB and > 1mM TMZ).

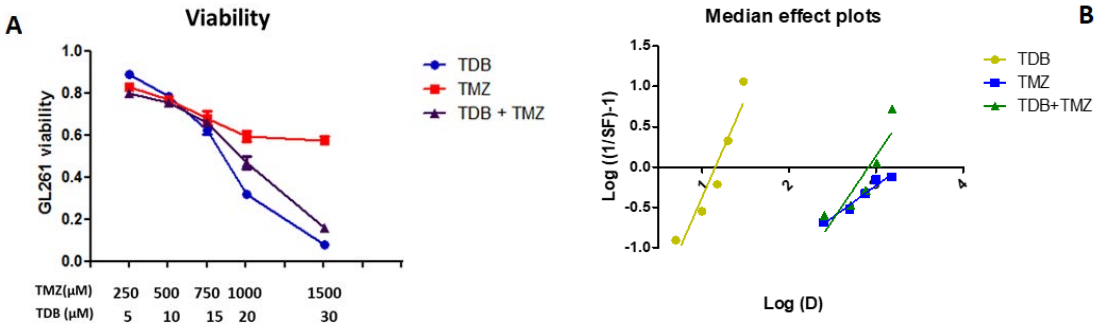

Figure 23: A) Dose-dependent GL261 cell viability and B) median effect plots from Chou-Talalay method for TDB, TMZ and the combined TDB+TMZ treatment

For cell viability experiments (A), TDB concentrations were 5, 10, 15, 20 and 30 µM and TMZ concentrations 250, 500, 750, 1000 and 1500 µM. The value 1 (100% viability) was assigned to control cells treated with vehicle. Experiments were performed with n=4 and mean ± SD values are shown. For median effect plots (B), the slope of each line (m) is Hill coefficient and the intersection with the x-axis is Dm, the dose necessary to obtain a Fu (surviving fraction) of 0.5. 'SF' states for survival fraction of cells (see Annex I for details on calculations)

The median effect plots (Figure 23B) of TMZ, TDB and the combination of both were performed in order to obtain the parameters **"m"** (median effect dose) and **"D_m"** (Hill-type coefficient). To determine if the combined effect of TDB and TMZ in GL261 is synergistic, antagonistic or just additive, it is necessary to calculate the CI for a certain value of x (i.e. for a certain fraction of affected cell). In this case the value x = 0.47 was used, corresponding to the fraction of unaffected cells obtained in the treatment with 1 mM TMZ + 20 µM TDB. Finally, the CI was calculated according to the method explained in Annex I and values found are shown in Table 5 below. The ratio P/Q ([TMZ]/[TDB]) for this study was 50:1 and the CI calculated for every concentration is higher than 1 accordingly, these results point that the combined effect of TMZ and TDB in GL261 cultured cells would be antagonistic for every studied concentration.

From these results, it is unclear whether treatment *in vivo* would succeed since *in vitro* an antagonistic effect has been demonstrated and could also take place *in vivo*. However, the *in vivo* environment is not completely mimicked in an *in vitro* experiment and some elements such as the immune system are lacking. Accordingly we still considered that a single and combined approach *in vivo* could be tested. In order to decide if it was appropriated to

proceed with an *in vivo* study with GL261 GB tumor-bearing animals, the *in vivo* target validation in single dose TDB-administered animals was needed.

TDB (μM)	TMZ (μM)	f_a	CI	Result
5	250	0.2	2.59	Antagonism
10	500	0.25	2.45	Antagonism
15	750	0.34	2.26	Antagonism
20	1000	0.53	1.96	Antagonism
30	1500	0.84	1.5	Antagonism

Table 5: TDB and TMZ concentration, fraction of affected cells and combination index for the joint TMZ+TDB treatment

The individual doses for TDB and TMZ and the fa resulting for the combined treatment are indicated. The combination index for every set of concentrations is higher than 1, indicating that, in every case, the effect of the combination is antagonistic.

4.1.2.2 In silico results

An *in vivo* longitudinal experiment was only sensible if TDB was able to reach the bloodstream and tumors after reasonable dosage administration, and exert its effects accordingly. Being it a novel drug, and as opposed to CX-4945, pharmacokinetic data was still missing and few data related to this were known for TDB. Before embarking in *in vivo* experiments, we tried a bioinformatics approach in order to get some predictions about absorption, expected effects/targets and toxicological potential.

Bioinformatics approach for TDB pharmacokinetics (PK) and pharmacodynamics (PD): what should we expect?

These approaches were attempted following advice from Dr. Jordi Llorens from the Department of Physiological Sciences, Faculty of Medicine and Health Sciences, *Universitat de Barcelona*, who suggested the use of bioinformatics tools in order to predict TDB bioavailability and expected effects on and off target in addition to CK2 and PIM-1.

The following bioinformatics tools were used:

- SwissADME (http://www.swissadme.ch/) [208]
- Marvin Sketch v. 17.11.0
- GUSAR (General Unrestricted Structure-Activity Relationship) v.2011.1 (http://www.pharmaexpert.ru/GUSAR/)
- Pass and PharmaExpert (http://www.way2drug.com/)

Several parameters have been estimated, such as partitioning calculations (oil/water and hydrophilic-lipophilic balance), estimation of druggabitlity, bioavailability score, predicted targets and toxicity. The most relevant /interesting results will be commented and shown here.

Partitioning coefficient, solubility, HLB

Regarding the partitioning coefficient, it measures whether a chemical substance is mostly hydrophilic or hydrophobic and it is useful in estimating the distribution of drugs within the body [209]. For a drug to be orally absorbed, it normally must first pass through lipid bilayers in the intestinal epithelium being hydrophobic enough to partition into the lipid bilayer, but not too hydrophobic, allowing its further distribution towards blood. Taking into account the chemical structure of TDB (Figure 9, Section 1.5.3) and the pH value of mouse stomach (between 3 and 4 depending on the feeding state, [210]), the prevailing microspecies are shown in Figure 24. It is a general consensus that the absorption of uncharged forms is more efficient [210] and the protonated form B tends to reduced lipophilicity, thus limiting passive absorption across biomembranes.

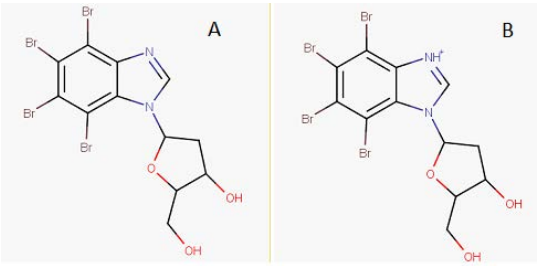

Figure 24: TDB predicted microspecies in the pH range 3-4
Estimated ranges of each species were A: 5.8 to 38.1% and B: 94.2 to 61.9 (ranges values at pH 3 and 4 respectively). Protonated form B is expected to present lower absorption rate in comparison with deprotonated A.

We were also able to estimate the hydrophilic/lipophilic balance (HLB) for TDB. This parameter was based on identifying characteristic regions in the molecule, and the value estimated for TDB pointed to a borderline behavior situated between values of hydrophobic and water-dispersible agents. This was corroborated by the water solubility estimation, in which TDB was categorized as low solubility. All the above-mentioned estimations were performed with MarvinSketch v. 17.11.0 and from that, we would expect that TDB would be at least partially absorbed in oral administration.

Bioavailability

The bioavailability was calculated with swissADME based on the method described in [211] which takes into account different characteristics of the molecules to predict druggability and bioavailability. It is based on data available from drug databases (see Figure 25) and values obtained for TDB pointed to a druggable compound (except by a slight exceeding in the ideal molecular weight: upper expected limit of druggable compounds set at 500 according to the Lipinski "rule of 5" [212]), with a probability of more than 50% of getting a bioavailability above 10% of the administered dose. Still, further calculations predict that TDB has probability for BBB crossing.

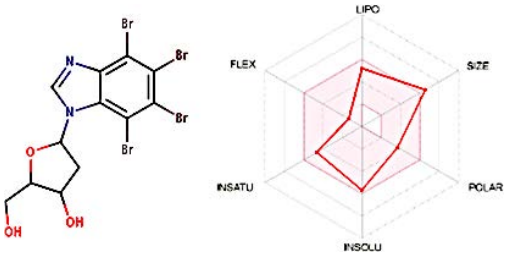

Figure 25: TDB chemical structure and the "bioavailability radar" result from swissADME
Six physicochemical properties are taken into account: lipophilicity (LIPO), size (SIZE), polarity (POLAR), solubility (INSOLU), flexibility (FLEX) and saturation (INSATU). The pink area within the 3D cubedefines the radar plot of the molecule, which must fall entirely inside the radar plot cube to be considered drug-like.

Expected targeting

The swissADME bioinformatics tool also allowed us to inspect for possible additional targets (shown in Figure 26) in addition to the described CK2 and PIM-1 inhibition, which was estimated through comparison with similar compounds and following procedures described in [233].

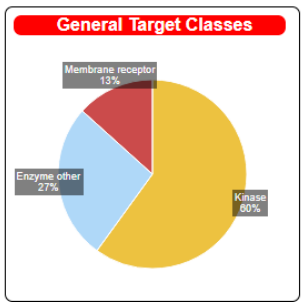

Target	Target Class
Casein kinase II subunit alpha' *(by homology)*	Ser_Thr Kinase
Casein kinase II subunit alpha	Ser_Thr Kinase
Dual specificity tyrosine-phosphorylation-regulated kinase 1A *(by homology)*	Ser_Thr_Tyr Kinase
Casein kinase II subunit alpha 3 *(by homology)*	Ser_Thr Kinase

Figure 26: Distribution of general target classes estimated for TDB in mice and their probability.
The table on the right shows only the targets with probability equal or higher than 40%.

As expected, TDB activity is predicted to be mostly related to kinases, being CK2 the first predicted one although it does not seem to be specific for a single catalytic subunit. Other targets are also expected, although with slightly lower probability, such as cyclins and thymidine kinase (ranging 32-36% probability), being this activity high in proliferating cells and peaking during the S-phase of the cell cycle [145], being very low in resting cells. This is in agreement with data obtained using Pass & Pharma Expert tools: high probability of thymidine kinase inhibition, which could cause DNA synthesis halt and cytostasis. It is worth noting that although with a lower probability, according to Pass & Pharma Expert results, TDB could also impair the enzyme adenosine deaminase, involved in the development and maintenance of the immune system [213]. An unexpected result was that PIM-1 was not considered among the possible targets of TDB with the available informatics tools, although it could be also due to the lack of PIM-1 inhibitors in the comparison database used.

Toxicological potential

Regarding acute toxicity expected in rodents, it was estimated with the General Unrestricted Structure-Activity Relationship (GUSAR) tool. The model available in GUSAR is based in

information from rats through taking into account data from similar compounds using different administration routes. A very good tolerability is expected in oral route for TDB (LD50[13] of 7,190 mg/kg) and indeed the minimal MTD calculated by us [85] was of 2,160 mg/Kg. This is not a real MTD: due to solubility constraints, it was not possible to administer higher doses and, accordingly, the real MTD should be higher. The expected LD50 for intraperitoneal administration is around 2,000mg/kg, and both (oral and intraperitoneal) are below the administered doses given in section 4.1.2.3 of this chapter. TDB is classified as nontoxic in general although the fragment analysis performed by swissADME based in the implementation described in [214] alerts for the halogenated ring (bromine) which is part of the TDB structure. However, bromine toxicity is lighter than other heavier halogens as fluorine and chlorine.

Altogether, these results seemed to point that TDB should be absorbed, at least a small percentage of the administered dose, which should be confirmed with suitable techniques such as high performance liquid chromatography (HPLC) of serum of administered mice (see section 4.1.2.3, HPLC subsection). Accordingly, if TDB reached the organs/tumor in considerable amounts and it was functional, a decrease of local CK2 activity should be seen.

4.1.2.3 In vivo results

TDB target validation *in vivo.*

Assessment of TDB arrival into the tumor after oral/ intraperitoneal administration

Oral administration of 253.8 mg/Kg: A first attempt of functional validation was performed to check whether TDB would trigger an effect on CK2 activity after oral administration in mice. This was done through the assessment of the phosphorylation status of the CK2 specific target Akt S129 and activation site of Akt 473 of different mice tissues.

Six tumor-bearing mice were used (generated as described in section 3.2.1). At day 11 post implantation, n=3 mice were treated with TDB vehicle (saline solution with 10% of DMSO) and n=3 were treated with TDB (oral administration) at 253.8 mg/Kg, which is the equivalent molar dose calculated from CX-4945 administration in [85]. The administration was performed for 3 consecutive days, split into two administrations each day (126.9 mg/Kg for each administration). Finally, 24 hours after the last dose, the animals were euthanized and tumor, contralateral (CL) brain, cerebellum, spleen and small intestine were collected and stored in liquid nitrogen. Protein was extracted from tissues of control (untreated, UT) and TDB-treated animals as described in section 3.1.5. Then, pAkt Ser129 and pAkt Ser473 levels were analyzed

[13] The value of LD_{50} for a substance is the dose required to kill half the members of a tested population after a specified test duration

by Western blot in these tissues (Figure 27). It is worth mentioning that pBad Ser112 analysis was not performed since we did not observe any inhibitory effect *in vitro* (See section 4.1.2.1).

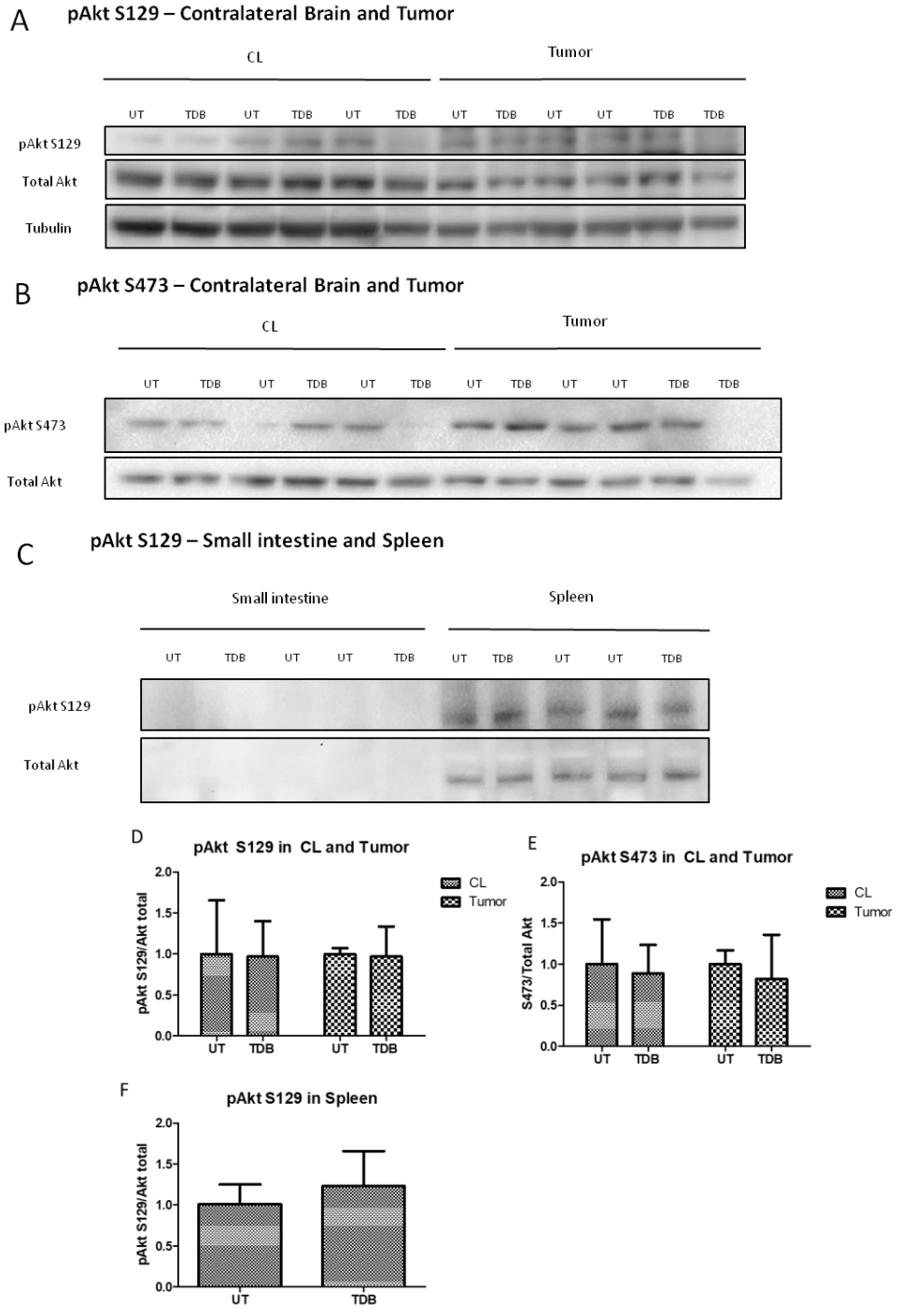

Figure 27: CK2 target validation in UT and TDB-treated GL261 tumor-bearing mice (oral gavage administration, 253.8 mg/kg)

A) Akt Ser129 phosphorylation assessed by Western blot in CL brain and tumor of UT and TDB treated mice. Total Akt and Tubulin were analyzed as controls. B) Akt Ser473 phosphorylation assessed in CL brain and tumor of UT and TDB-treated mice. C) pAkt Ser129 phosphorylation analyzed in small intestine and spleen. D, E and F) Blot quantification from A, B and C. Mean ± SD is shown. No significant differences were found between UT and TDB treated tissue according to Student's t- test. No quantification was performed with small intestine results since no signal was detected.

Tumor and CL brain results: pAkt Ser129 phosphorylation levels were analyzed in vehicle (UT) and TDB-treated mice (Figure 27A). No significant differences were observed in the pAkt Ser129 levels. These results suggest that either TDB did not reach mice brain or it was not fully functional once reaching brain tumors. The phosphorylation level of Akt Ser473 was also assessed in CL brain and tumor (Figure 27B). In this case, a decrease (ca 20%) in the average values of phosphorylation levels was observed in TDB-treated mice, but due to the high variability of the results within groups, no significant differences were found.

Small intestine and spleen results: small intestine samples were analysed to check for local CK2 inhibition, which could be detected in the gastrointestinal tract and it could also be useful in case TDB was poorly absorbed (no tumor/brain effects) and had only local action in small intestine cells. On the other hand, spleen results could provide insight about the potential TDB impact in the immune system. In the small intestine samples, neither Akt nor pAkt signals were detected, while in spleen no differences were found between pAkt Ser129 in vehicle and TDB treated mice (Figure 27C), suggesting that either TDB was not able to reach the blood stream, or we were not able to detect CK2 inhibition with this approach.

Since these results were inconclusive, a second step was performed including two experimental modifications focused into two possible explanations for this lack of noticeable CK2 inhibition and to overcome possible problems related to TDB absorption.

a) Possible problem: TDB absorption rate could be far below the predicted with *in silico* models, and the administered dosage was not enough to secure CK2 inhibition *in vivo*. Solution: doubling TDB dose administered by oral gavage (507.6 mg/kg) in 3 animals, secured by the high MTD calculated dose found for this compound when using oral gavage (2,160 mg/kg [215]). After 24h of the last administration, animals were euthanized and samples collected and frozen.
b) Possible problem: the low solubility of high TDB dosages does not allow improvement of oral absorption without changing the administration route or formulation. Solution: try intraperitoneal injection (253.8 mg/Kg) in 3 mice for 3 consecutive days. Additionally, 3 animals were administered with vehicle. As for the oral gavage group, animals were euthanized, samples collected and frozen 24h after the last administration.

Mice body weight evolution in UT and TDB-treated mice both by oral gavage and intraperitoneal injection was monitored, since it is one of the recommendations of the

Laboratory Animal Science Association (LASA) in drug dose selection [216]. Both groups (oral and IP administered) of TDB-treated mice lost weight compared to mice receiving intraperitoneal administration of vehicle (9.3% of weight loss in mice with oral administration and 10.8% of decrease for the intraperitoneal administration group; the vehicle treated groups did not show any weight loss). These results suggest that TDB administration in this experimental design triggered mild undesirable side effects.

Regarding to pAkt Ser129 in tumor, a strong signal was detected both for treated and untreated mice (which is an uncommon finding for this phosphorylation site). No differences were observed between UT and treated animals (Figure 28A,B), suggesting that either CK2 was not inhibited or pAkt S129 content is not a good biomarker to assess TDB target validation *in vivo,* maybe due to other local compensatory effects. Phosphorylation of GSK3β, a downstream effector of Akt signalling, was also analysed. In this case, we would expect a decrease in GSK3β phosphorylation as a result of CK2 inhibition. No significant differences were found between treated and UT groups although a decreasing trend is observed in TDB-treated animals (0.76 ± 0.29 for oral TDB administration and 0.75 ± 0.18 for intraperitoneal administration compared to 1 ± 0.32 in UT animals (Figure 28)). In the case of pAkt Ser473, results were inconclusive: most of the detected bands presented a very faint signal except one mouse, administered with intraperitoneal TDB, and no significant differences were found.

These results based in the effects on CK2 targets were not conclusive and did not allow to confirm that TDB reached tumors. Our *in silico* estimations suggested that enough TDB could arrive in enough local concentration to trigger the expected effects[14]. However, no noticeable effect was detected and, accordingly, the relevant question to address was to check whether TDB was actually reaching the blood stream after oral or IP administration.

[14] On each dose, we have administered either 126.9mg/kg (253.8 split in two doses) or 253.8 mg/kg (507.6 mg/kg split in two doses). If we assume the estimations made by Swissadme, considering that 10% of TDB arrived to the blood stream and assuming a blood volume of 1.1ml, the estimated concentration of TDB in blood would be 419.6 µM (253.8 mg/kg dose) or 838.2 µM (507.6mg/kg dose), which is 5 to 700 fold higher than the range of concentrations used *in vitro* (ranging from 1.25 to 80 µM).

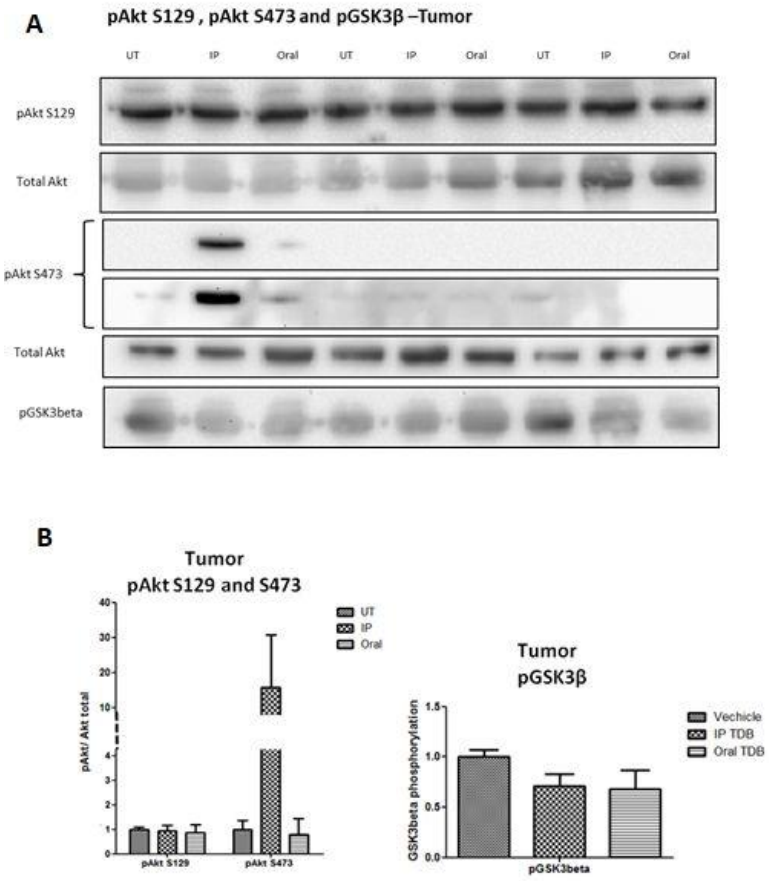

Figure 28: Assessment of CK2 inhibition in oral/intraperitoneal TDB administered mice

A) Phosphorylation levels of Akt Ser129, Ser473 and GSK3β in UT and treated mice. Total Akt was analyzed as control. pAkt Ser473 is shown twice, the second with an increased exposure time allowing observation of extremely faint bands at the expense of saturation. B) Quantification for pAkt Ser129 and Ser473 and pGSK3β for tumor samples. No significant differences were found (n=3 mice were analyzed per group).

Assessment of TDB concentration reaching the blood stream after oral / intraperitoneal administration

NMR approach

A preliminary attempt using high resolution Nuclear Magnetic Resonance (NMR) was performed using serum of C57BL/6j mice after TDB administration (126.9 mg/kg were administered once and blood was collected 1 h after the administration). No signal was found in mice serum, and taking into account estimations of bioavailability (419.6 μM) TDB concentration in the bloodstream should reach enough concentration to be detected, but we cannot discard that absorption rate had been far below the predicted. However, it is also true that standard TDB (at 14 mM) only could be detected once it was dissolved in DMSO 100% (see acquired spectra in Annex III). The lack of signals in TDB-administered mice serum would be most probably due to its hydrophobicity producing either binding to serum macromolecules or precipitation, causing line broadening and hampering detection by this technique.

HPLC approach

A High Performance Liquid Chromatography with ultraviolet visible absorption protocol was designed to analyze serum samples of TDB-administered C57BL/6j mice due to its highest sensitivity. This was the approach used for similar studies [217] and it was found suitable for this assessment. Twelve wt C57BL/6j mice were used for this study. TDB was administered

either by oral gavage (n=9 mice) or intraperitoneal injection (n=3 mice) at 126.9 mg/kg dosage. In the case of oral gavage, mice blood was collected by cardiac puncture 30min, 1 and 2h after TDB administration whereas for IP administration, blood was collected after 45 min. From each mouse, 700-900µl of blood was collected and serum was obtained through ice incubation of blood samples (15 min) followed by centrifugation at 1,500 x g for 15 min. Serum samples were analyzed by HPLC at the Chemical Analysis Facility (*Servei d'Anàlisi Química* at UAB http://sct.uab.cat/saq). The analysis was performed in a chromatograph 1200 with diode array detector from Agilent Technologies and a Chromatographic Colum Xterra MS C18 3.5µm, 2.1x50mm (Waters) and mobile phases used were water and methanol in variable proportions. Figure 29A shows TDB detection at 270 nm after 11.9 min in a serum sample with TDB added, for control purposes. The detected area is proportional to the amount of TDB.

A hypothetical 100% bioavailability situation with TDB would produce a detection of 2115 mg/L (ppm) of TDB in serum, which corresponds to 3.84mM, but previous *in silico* and *in vivo* data did not point in this direction. TDB was indeed found in all analyzed samples, although with relevant value dispersion (Figure 29B): for oral administration, the detected concentrations were 13.9 ± 11.8 µM, 19.2 ± 21.1 µM and 21.2 ± 15.5 µM for samples collected after 30 min, 1h and 2h respectively. For intraperitoneal administration, the value was 8.8 ± 5.1 µM in samples collected 45 min after administration. Then, the concentration found in the serum samples ranged from 6.7 to 23.8 ppm, which would correspond to 1.22 to 43.2 µM, pointing to a very low bioavailability (only 0.06 - 2% of the administered dose reached bloodstream) for TDB. *In vitro* results showed that concentrations as low as 2.5 µM of TDB were able to inhibit CK2 and 5 µM decreased GL261 cell viability so even exhibiting low bioavailability, TDB could have potential *in vivo*. Furthermore, crossing the BBB is not an issue with GB tumor-bearing animals, since GL261 GBs have compromised BBB [194]. However, as observed in Figure 27 and Figure 28, no significant changes were detected in expression levels of phosphorylated Akt 129, 473 or GSK3β. Having this in mind, and since TDB was proven to reach the bloodstream, a direct CK2 activity assay with specific substrates was performed with tissue samples of TDB treated mice treated twice a day (253.8 mg/kg daily) for 3 days and euthanized 24h after the last administration.

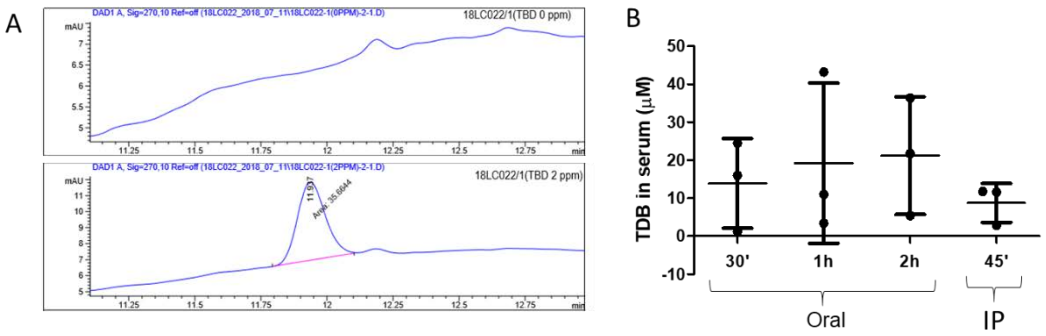

Figure 29: HPLC profile in TDB calibration curve and TDB concentration found in serum of administered mice

A) Examples of HPLC profiles performed for calibration purposes and protocol optimization. Mice serum profile is shown before (top) and after (bottom) TDB addition (2 ppm (mg/L)). B) TDB concentration found in serum of TDB-administered mice (oral gavage and IP administration).

CK2 activity assays in TDB treated mice

Target validation involving direct CK2 activity assays were performed in cerebellum instead of contralateral, since in some cases contralateral tissue were too small to be analyzed. Tumor samples of GL261 GB tumor-bearing mice, both UT and TDB-treated, treated for 3 days at 253.8 mg/kg of TDB per day were also evaluated. Samples were collected 24h after the last TDB administration. This would be more specific than the previous methods used for detecting CK2 inhibition and would not be interfered by local compensatory mechanisms. However, no significant differences were found in CK2 activity comparing UT and TDB-treated mice (Figure 30). This could mean that TDB was not fully able to reach the tumor, or at least not in enough concentration to produce relevant decrease in CK2 activity in a similar way that was observed in *in vitro* studies.

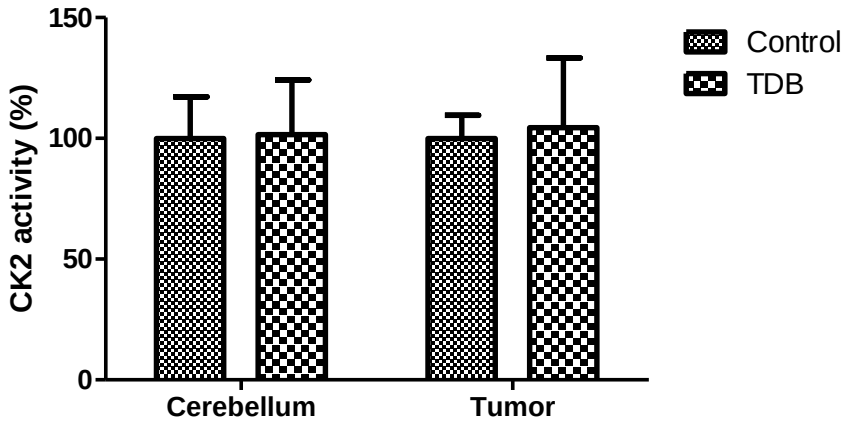

Figure 30: CK2 activity in cerebellum and tumor samples of UT and TDB-treated tumor-bearing mice

No differences were found in CK2 activity between control and TDB treated mice, according to Student's T test (n=10-16 for each group).

At this point and despite all efforts made in this direction, it became clear that there is still a long way to go until TDB can be adequately evaluated *in vivo*. An HPLC analysis of extracted tumor sample of TDB-administered mice may be helpful in future work to fully elucidate TDB presence and quantitation reaching GL261 tumors, but a change in its formulation seemed to be mandatory to improve tumor arrival which was beyond the objectives of this thesis and the expertise of the group in pharmacological development.

4.4.6 Discussion

TDB was a promising dual CK2-PIM1 inhibitor described to trigger potent effect in cell viability in cell lines such as CEM (human T lymphoblastoid cells) and HeLa (human cervical cancer cells), with DC50 values around 2-3 μM [175]. On the other hand, CK2 and PIM1 inhibitors such as CX-4945 for CK2 [110] and TCS for PIM-1 [111] had proven to be useful as single agents in preclinical GB. Our hypothesis was that TDB could be a potential good candidate for GL261 GB treatment, alone and/or in combination with TMZ.

In vitro results

Preliminary results in GL261 cultured cells showed indeed a good performance, showing the lowest EC_{50} among the investigated compounds for CK2 inhibition (8.1 μM), in agreement with low DC_{50} values reported by developers (ca. 2.5 μM for HeLa and human T lymphoblastoid cells) [175]. Further studies in this Thesis showed that this effect was mainly cytostatic at the lower range of concentrations and became cytotoxic when higher concentrations were used (80% of cell death at 30 μM of TDB, Figure 19). Regarding early drug discovery, TDB would fit in the "focused screening" category (see [218]) for compounds previously identified as hitting specific classes of targets (e.g. kinases), which enables robust testing and comparison with similar structures and compounds *in vitro*.

The assessment of effects triggered by the combined TDB+TMZ treatment in GL261 cells pointed to an antagonistic action in comparison with single effects (Table 5), which could be due to a 'protective' effect from TMZ in front of TDB action. However, it is possible that further investigation in right intervals or shifts in administration time would result in beneficial effects when using the therapeutic combinations. Nonetheless, the disappointing results with the *in vivo* administrations of TDB (see below) discouraged us to put effort in further experiments with the combined treatment.

TDB target validation *in vitro* was fully successful for pAkt Ser129, which has proven to be a good reporter for dose-dependent CK2 inhibition for GL261 cells treated with TDB (Figure 20),

as already described in [175]. Furthermore, the inhibition of CK2 was observed in TDB treated cells by measuring directly CK2 activity with a specific peptide on these cells (Figure 21). Comparing the results from the CK2 activity assay and the phosphorylation status of pAkt S129, we could observe that the method that measures directly CK2 activity is much more sensitive to detect CK2 inhibition. Still, the analysis of the phosphorylation of the CK2 specific target indicates that CK2 inhibition is producing noticeable effects in the signaling machinery of the cell. Regarding Pim-1 inhibition, and since Pim-1 basal expression is very low in the GL261 cell line, it was not straightforward to check for differences in pBad Ser112, as it was done in [175] for human T lymphoblastoid cells. Also, pAkt Ser473 was analyzed, as an indirect biomarker for both Pim and CK2 inhibition (Figure 20B). Although we did not find a dose-dependent inhibition, a drop in the phosphorylation of this site was found at the highest concentrations of TDB used in the experiments. Due to the lack of a confident target validation *in vitro* for Pim-1 inhibition, Pim-1 activity assays with TDB treated cells would be needed to confirm the inhibition.

In silico results

Different bioinformatic tools (section 4.1.2.2) were used in order to predict TDB targeting, bioavailability and toxicity. TDB was identified as a "druggable" substance (Figure 25) and, as expected, it was predicted to act mostly inhibiting kinases, more specifically CK2 (Figure 26), but not Pim-1, although it could be due to the lack of Pim-1 inhibitor structures for comparison in the database of the aforementioned tools. Still, the prediction of thymidine kinase inhibition should not be neglected in the overall effect of TDB in proliferating cells.

The estimated distribution coefficient, log D (ratio of the sum of the concentrations of all forms of the compound (ionized plus un-ionized) in aqueous and lipophilic phases) at pH 7.4 was ca. 3.67, slightly above the recommended value described in [218] (0-3), and also above the recommended value for BBB penetration (around 2), although GL261 GB had compromised BBB [194] and drugs like TDB should be able to reach tumor milieu. Still, we considered that even if the bioavailability was somewhat restricted, it could be compensated by its extreme effectiveness in cell viability reduction at low concentrations, and it was worth trying *in vivo* work. We should also take into account that *in silico* simulations are often based in comparisons not always valid due to the lack of enough similar structures for comparison. Finally, the predicted toxicology was favorable with high predicted LD50 (ca 2,000 mg/kg), in line with the minimal estimated MTD calculated by us in [85].

In vivo results

In vivo results showed that only a small amount of TDB (0.06 - 2% of the administered dose) was able to reach the bloodstream as determined by HPLC at different time points after administration, both by oral gavage or intraperitoneal administration, below from the predicted from SwissADME but in line with was predicted according to [218]. Still, although a low toxicity was expected from the *in silico* predictions and calculated MTD, mice with oral (507.6mg/kg) and intraperitoneal (253.8mg/kg) TDB administration presented body weight losses in comparison with vehicle-administered mice. This suggests that TDB can exert undesired side effects, probably depending on the absorption rate, which can be variable due to the low solubility of this compound.

In general, it is described that drugs fail in the progress towards preclinical/clinical settings for two main reasons: either they do not work and/or they are not safe. The *in vitro* tests are useful to unravel the signaling and biochemical mechanisms beyond drug action, but they are far from simulating the real situation in tumors *in vivo*. Some examples are absence of extracellular matrix and blood vessel elements, impossibility of simulation of gradients of oxygen tension, extracellular pH, nutrients, catabolites, and absence of drug penetration barriers [219]. In addition, solubility and permeability are crucial for a compound to become a drug. Deficiency in one or other parameter can be overcome in formulation but a compound lacking both properties is unlikely to become a drug, no matter the efficacy it has shown in preliminary *in vitro* screenings. Further studies would be needed to better clarify how it can be improved in case of TDB and it is clear that there is much work to be done and probably the involvement of other groups with pharmacological expertise would be needed. It was beyond the scope of this thesis to improve TDB profile as a drug, and next steps were planned with CX-4945 for CK2 inhibition, since this compound is very well characterized and its pharmacokinetics and pharmacodynamics profile were already known. Accordingly, it was chosen to proceed with the study of CK2 inhibition details in GL261 tumors (Table 6).

	Current results		Future experiments
Target validation	GL261 cells	GL261 tumors	
pAkt S129	✓	✗	Improvement of TDB formulation
pAkt S473	✓	✗	
pBad S112	✗	✗	
TDB detecion in serum by NMR		✗	
TDB detection in serum by HPLC-MS		✓	
CK2 activity measurement	✓	✗	

Table 6: Approaches performed in this thesis and future experiments needed to gain more insight regarding TDB potential in GL261 GB treatment

4.4.7 Conclusions

- TDB is a potent CK2-Pim-1 dual inhibitor *in vitro*, showing low IC_{50} in GL261 cells (13.14 µM, 72h treatment). Its effect is mostly cytostatic at low concentrations (5 and 15 µM) and cytotoxic at 30 µM. This was confirmed through assessment of targets such as pAkt Ser129 and Ser473 and also direct CK2 activity measurement. On the other hand, Pim1 expression in GL261 cells is very low and Pim1 target validation through pBad Ser 112 *in vitro* was not successful. Pim1 activity assays should be performed instead for this purpose.
- TMZ and TDB produce an antagonistic effect when added together to GL261 cells, as opposed to what was observed with CX-4945 (chapter 4.2). This suggests that further investigation would be needed to refine administration schedule of both compounds
- TDB has been absorbed both by oral and IP administrations, although its bioavailability was poor (only between 0.05-2% of the administered dose). The low solubility observed and also the low partition coefficient predicted suggest that even though a potent effect is shown in cultured cells *in vitro*, structural and formulation changes would be needed to ensure that TDB could be effective *in vivo*. The assessment of phosphorylation of Akt Ser129 and Ser473 in GL261 tumors *in vivo* revealed no changes between untreated and treated mice, as well as direct assays of CK2 activity.
- Determining differences between the *in vitro* and *in vivo* environment should be taken into account when evaluating new druggable compounds for preclinical GB. Desirable characteristics regarding solubility, partitioning coefficient and safety must be considered when choosing suitable candidates for preclinical evaluation. At this moment, we decided that TDB was not a suitable compound to proceed with further studies until improvement

in its bioavailability and arrival to tumor with target validation was improved, even though *in vitro* results were excellent.

4.2 What is behind treatment success. Exploring the potential of immunogenic signals triggered by TMZ, CX-4945 and TMZ+CX-4945 in GL261 cultured cells.

Specific goals: gain more insight about the single and combined treatment of TMZ and CX-4945 (CK2 inhibitor) in GL261 cultured cells, having in mind the satisfactory results obtained with *in vivo* treatment in GL261 tumor-bearing mice. To characterize their cytotoxic/cytostatic effect and production/release of immunogenic cell damage signals *in vitro*. This should help to better understand and explain the basis of the combined treatment opening the door for future optimization.

Furthermore, the combined Immuno-Enhanced Metronomic Schedule treatment (every 6 days as described by others [84, 93] and by us [85, 191]) of TMZ and CX-4945 has demonstrated better survival rates compared to single TMZ metronomic treatment [85] (54.7 ± 11.9 days in the combined treatment vs 38.7 ± 2.7 days in the TMZ single treatment). On the other hand, the metronomic administration of CX-4945 itself only produced a discrete, although significant, survival improvement (untreated control: 22.5 ± 1.2 days and CX-4945: 24.5 ± 2 days, Figure 31). This proved that a synergistic combined action of TMZ and CX-4945 was taking place, provided the IMS treatment protocol was followed, producing better results than each therapeutic agent in single administration. We wondered whether these two drugs were able to produce additive/complementary immunogenic cell death or damage (see section 1.2.3.1 of introduction), which would trigger host immune system elicitation and, ultimately, improve outcome of treated animals. For that, *in vitro* studies were performed with GL261 cultured cells and release/exposure of DAMPs was assessed, as well as their potential of inducing cell death.

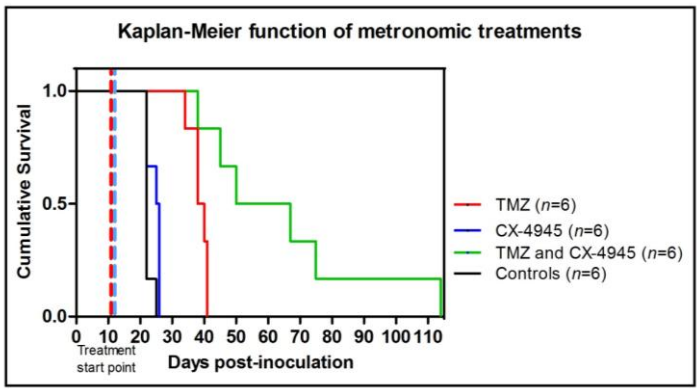

Figure 31: Kaplan-Meier survival curve of GL261 GB tumor-bearing mice treated with different therapeutic approaches in metronomic schedule (every 6 days)
Survival Kaplan-Meier curve for metronomic CX-4945 treated mice (n=6, blue line) metronomic TMZ treated mice (n=6, red line) CX-4945 and TMZ metronomic treated mice (n=6 green line) and control mice (n=6 black line). From [85].

The following Table 7 summarizes the different experimental conditions applied to the assessment of viability, synergism, cytotoxic potential and DAMPs release/exposure.

	MTT	**Trypan Blue**	**PI**	**CRT exposure**		**ATP release**		**HMGB1 release**	
Therapeutic agent	*Conc. range (µM)*			*Conc. (µM)*	*Time (h)*	*Conc. (µM)*	*Time (h)*	*Conc. (µM)*	*Time (h)*
TMZ	31-4000	500-4000	500-4000	2000	24	2000	12-18-24	2000	48
CX-4945	12.5-2000	25-100	33-150	25	24	100	12-18-24	100	48
TMZ + CX-4945	250-1500 16-100		250-1500 16-100	2000 25	24	2000 100	12-18-24	2000 100	48
Doxo				50	24			50	48

Table 7: Summary of the experimental conditions (concentration and time range) used for DAMPs release assessment and cytotoxic potential

4.2.1. TMZ effect in GL261 cultured cells

TMZ is an alkylating agent and the current standard chemotherapeutic for GB treatment. Although this agent is widely used in the clinical pipeline, and its mechanism of action is known, its overall effect on cells has not been fully understood yet and can be complex.

Cellular viability was evaluated after 24, 48 and 72h of TMZ treatment (at concentrations ranging 15-8000 µM) by MTT viability assay (Figure 32A). Even at high TMZ concentrations (in the milimolar range, up to 4mM) the maximum viability reduction was of 50%, in agreement with results previously described by us in [85]. Significant differences in viability were found at 2 and 4 mM after 24h of treatment (25-30% viability reduction compared to vehicle treated cells). After 48h of treatment, the cellular viability was significantly diminished at 0.5, 1, 2 and 4 mM. The calculated IC_{50} according to MTT results from four independent experiments was 5.57 mM after 72h of treatment, whereas the EC_{50} was 1.72 mM (see Section 3.1.4 for details). This value is indeed higher than what we have found in [85], although the method used for viability estimation was not the same and the number-range of overall concentrations measured was also modified, which can influence the EC50 estimation, according to [220].

According to MTT results and the obtained IC_{50}, GL261 cells display a behavior extremely resistant to TMZ treatment. However, MTT is not totally accurate since it is based only in the activity of one mitochondrial enzyme which is suggestive but not always indicative, of cell death [221].

To elucidate whether TMZ produces cytostatic or cytotoxic effect in GL261 cells, TMZ-treated cells during 24, 48 and 72 hours at concentrations 0.5, 2 and 4 mM were stained with Trypan Blue and counted (Figure 32B). The number of living cells significantly decreased after 48 and 72h of treatment at every concentration analyzed (0.5, 2 and 4 mM) whereas no significant changes were found in the dead cell counting, except at 2 mM when the number of dead cells was significantly lower compared to control cells. This result may be due to the spontaneous cell death occurring in the control cells, whose total cell number is much higher than the number of treated cells. Taking this into account, the absolute number of dead cells in the control may be higher in comparison with the treated cells. Due to the relevant differences in total and living cell counting in the different conditions studied, the absolute number of dead cells may not be the best parameter to elucidate if a drug is producing cytotoxic effect. The percentage of dead cells can be more useful for that, since it relates the number of dead cells and the number of total cells. After 48h, the percentage of dead cells at 2 and 4mM increase from 3 to 8% and after 72h. the percentage of dead cells at 4mM reached values as high as 27%. This may indicate that TMZ has indeed some cytotoxic effect at 4mM. However, we should also take into account that the concentration values that would be reached after *in vivo* administration (250 μM, according to [222], also in agreement with the range described in [223]) is much lower than 4 mM .

TMZ-treated cells were also stained with propidium iodide (PI) and analyzed by flow cytometry after 72h of treatment at 0.5, 1, 1.5 and 2 mM (Figure 32C). A decrease in living cells was found at 1, 1.5 and 2 mM. The percentage of dead cells increased from 6 to 10 % in cells treated at 0.5 mM. Although this difference is statistically significant, it may not be enough to characterize TMZ as a cytotoxic agent.

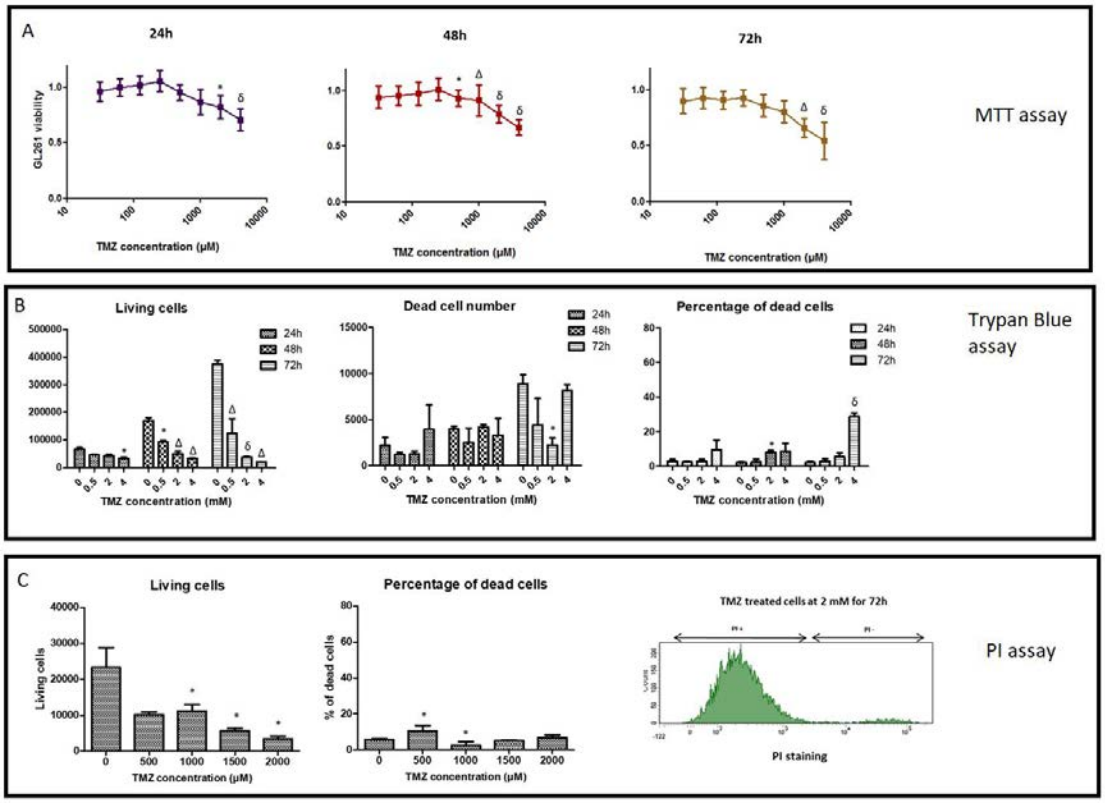

Figure 32: Summary of cell viability/cell death assessment in TMZ-treated GL261 cells
*A) Time course GL261 viability after TMZ treatment evaluated by MTT assay. TMZ concentrations ranged from 31 to 4000 µM (n=8 for every condition after 24 and 48h and n=12 for 72h). B) Total living and dead cells number and percentage of dead cells evaluated by Trypan Blue exclusion assay after TMZ treatment (n=2-3 for every condition). C) Living cells and percentage of PI positive cells (dead cells) evaluated by flow cytometry after 72h of TMZ treatment (n=3 for every condition). Histogram shows PI staining in TMZ treated cells. For all instances, mean ± SD are shown. More details about flow cytometry analysis in section 3.1 4 *, Δ and ð indicate statistical significance according to Student's t-test comparing treated and control cells.*

Surprisingly, the calculated IC_{50} according to Trypan Blue and Flow Cytometry results after 72h of treatment was much lower than the IC_{50} calculated with MTT assay (see summary in Table 8), being 254 µM for calculation with Trypan Blue values and 572 µM for calculation with Flow Cytometry values. Trypan Blue and PI evaluate the ability of active staining extrusion requiring energy, or cell membrane integrity, which are more reliable signs than assuming that the malfunction of a mitochondrial enzyme such as MTT is unequivocal sign of cell viability although it can be true in most situations. However, a small range of different concentrations was used to calculate IC_{50} in Trypan Blue and Flow Cytometry analysis, and also the lowest concentration used (0.5 mM) already produces a big effect on cellular viability (more than 50% of decrease in the case of flow cytometry), leading to a lack of "low-effect" measured values, which can influence in these estimations [220]. These two facts could ultimately lead to some inaccuracy in the estimation of this parameter.

These results taking together suggest that TMZ has a cytostatic rather than cytotoxic effect in GL261 cells *in vitro* at concentrations relevant for *in vivo* at relevant therapeutic used (ca. 250μM). The discrepant results obtained with MTT in comparison with Trypan Blue and Flow Cytometry lead us to deduce that MTT may not be the best choice for calculating quantitative parameters such as $IC_{50.}$ However, MTT assay allows high throughput analysis in a short time frame, being useful to perform preliminary screenings for rough estimations of drug effect.

	TMZ		
IC50 (μM)	**MTT**	**Trypan Blue**	**Flow Cytometry**
24h		319.7	
48h		504	
72h	5570	254	572
EC50 (μM)			
24h		805.7	
48h		569.6	
72h	1720	263.9	-*

Table 8. Summary of IC_{50} and EC_{50} calculated values for TMZ
**It was not possible to calculate EC_{50} with Flow Cytometry results due to the lack of enough concentrations. Still, the most used value to evaluate the potency of a drug is IC_{50} rather than $EC_{50.}$ The parameters obtained by MTT assay are much higher than the obtained by the other techniques, suggesting that MTT assay may not be reliable enough for these estimations. Values calculated with GraphPad Prism software.*

4.2.2 CX-4945 effect in GL261 cells

CX-4945 is an ATP-competitive inhibitor of CK2 that is currently being evaluated in clinical trials for cancer treatment (see section 1.4.3). CX-4945 has been shown to inhibit pro-survival pathways and to decrease cell migration and invasiveness in different GB cell lines [110]. Moreover, is ableto significantly increase GL261 tumor bearing mice survival when combined with TMZ in a metronomic schedule and was also proven to decrease GL261 cultured cells viability [85].

Indeed, CX-4945 significantly reduced GL261 cell viability in this Thesis after 72h of treatment according to MTT assay (Figure 33A) down to 0% viability. Having in mind discrepancies between MTT and other assays such as Trypan Blue or PI, the same approach used for TMZ was applied. CX-4945-treated GL261 cells were collected and Trypan Blue assay performed (Figure 33B). The number of living cells decreased significantly after 24h of treatment and this effect in living cell reduction was higher at larger times of treatment. No differences were found for total dead cell countings. Regarding the percentage of Trypan-blue positive cells, it was significantly higher after 48h of treatment at the highest concentration studied (100 μM), reaching an average value of 27% of dead cells. After 72h of treatment the percentage of dead cells was 21% at 50μM and 50% at 100 μM, although in the latest the difference in the

percentage of dead cells is not significant compared to untreated cells due to high dispersion of the results.

To support Trypan Blue exclusion assay results, flow cytometry analysis was also performed with cells incubated with the vital dye PI. After 72h of treatment, the number of living cells was significantly reduced (Figure 33C) and the average percentage of dead cells was 19, 26 and 32% at 50, 100 and 150 µM respectively (non-significant at 100 µM due to values dispersion). The graphical representation of PI positive and negative cells is shown in Figure 33C.

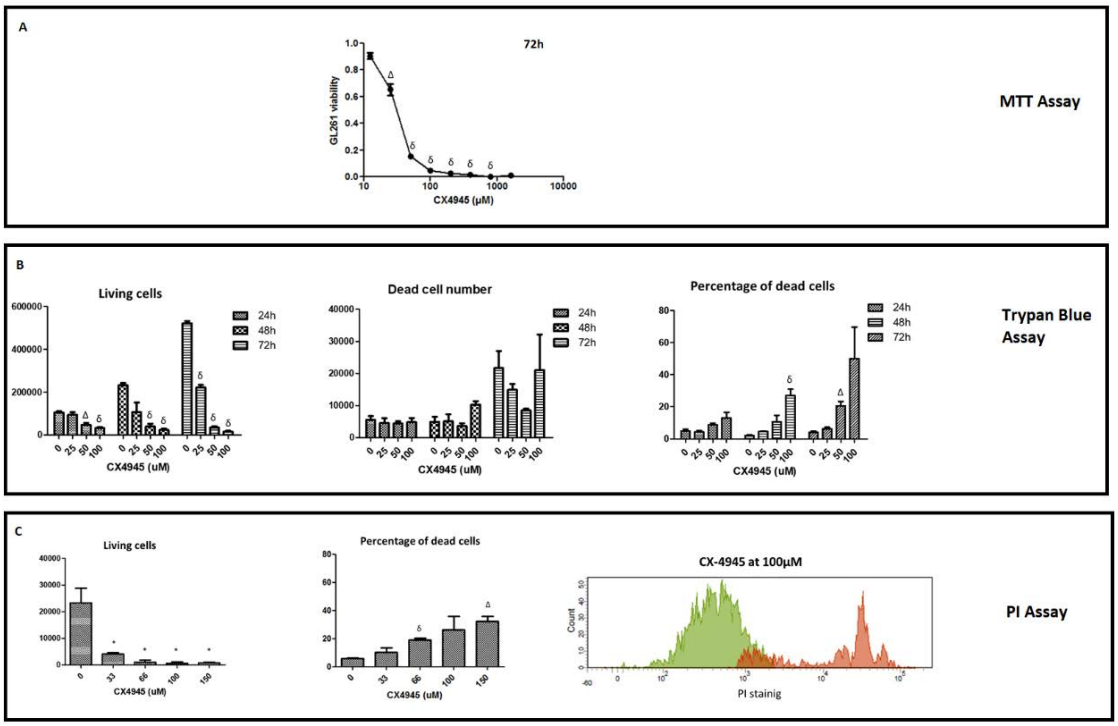

Figure 33: Summary of cell viability/cell death assessment in CX-4945-treated GL261 cells
*A) GL261 viability after 72h of CX-4945 treatment assessed by MTT. CX-4945 concentrations ranged from 12.5 to 2000 µM (n=4 for every condition). B) Total living and dead cells number and percentage of dead cells evaluated by Trypan Blue exclusion assay after CX-4945 treatment (n=3 for every condition). C) Living cells and percentage of PI positive cells evaluated by flow cytometry after 72h of CX-4945 treatment (n=3 for every condition). Histogram shows PI staining in CX-4945 treated cells. Living cells (PI negative) are represented in the green population while the red population stands for dead and membrane-compromised cells (PI positive). More details about flow cytometry analysis can be found in section 3.1.4. For all instances, mean ± SD are shown. * (p<0.05), Δ(p<0.01) and δ (p<0.001) indicate statistical significance according to Student's t-test comparing treated and control cells.*

Regarding the IC_{50} and EC_{50} values (Table 9), they also vary with the different techniques employed, although in this case, the variability was much smaller, as opposed to what was observed with TMZ results. The EC_{50} value is higher (33 µM) than the IC_{50} (20 µM) probably because even the lower concentration assayed (12.5 µM) already showed viability decrease to 90% of control value, so the viability range used for EC50 estimation did not start in 100%. This

would mean that EC_{50} would be set at 45% (halfway between 90 and 0), which is a lower viability than the 50% used for IC_{50} estimation.

CX-4945			
IC50 (µM)	**MTT**	**Trypan Blue**	**Flow Cytometry**
24h		147	
48h		23	
72h	20	23	7
EC50 (µM)			
24h		37	
48h		22	
72h	33	23	20

Table 9. Summary of IC_{50} and EC_{50} calculated values for CX-4945

Results show that CX-4945 produces mainly a cytostatic effect reducing the number of living cells but, unlike TMZ, cytotoxic effect is also clearly observed when high concentrations and longer treatment times are employed (Figure 33). If we compare the hypothetical concentration of CX-4945 *in vivo* after oral administration as performed in [85], taking into account the pharmacokinetic parameters of absorption calculated in [217], the plasma concentration of CX-4945 would be 6.16 mM, much above than concentrations used for the *in vitro* experiments. We also need to take into consideration that the amount reaching the tumor could be much lower than the one found in plasma. Still, we could hypothesize that, at the concentration reaching the GL261 tumor, there be with a high probability a cytotoxic one (> 100 µM, 60 times lower than the predicted concentration in plasma). Therefore, CX-4945 should produce a cytotoxic effect in the tumor cells, perhaps responsible for the synergistic effect shown when treating the GL261 mice in combination with TMZ in a metronomic schedule.

4.2.3. CX-4945 and TMZ combined effect *in vitro*

In previous work from our group, the combined CX-4945 + TMZ showed better results than single agent treatment both *in vitro* by MTT assay (combined treatment diminished viability 4.5 fold in comparison with CX alone (3 fold) and TMZ alone (1.7 fold) [85]. In the same work, we showed that *in vivo* treatment of GL261 tumor-bearing mice with concomitant TMZ and CX-4945 in a IMS protocol (every 6 days) increased significantly mice survival time (from 39 ± 3 days p.i. in TMZ-treated mice and 24.5 ± 2 days in CX-4945 treated mice to 55 ± 12 days in TMZ+CX-4945 treated mice). In order to check the nature of the combined effect of these two drugs *in vitro,* the Chou-Talalay method was applied [195].

4.2.3.1 MTT viability assay and synergy assessment

GL261 cells were treated with increasing concentrations of CX-4945 and TMZ for 72h (Figure 22A) and cellular viability was assessed by MTT. Then, results were analyzed by the Chou-Talalay method in order to determine whether the effect of the combined treatment were synergistic, additive or antagonistic.

The relationship between drug concentration and reduced cellular viability is shown in the dose-effect curves (Figure 34A) for CX-4945, TMZ and CX-4945+TMZ treatments, in which the combined performance is clearly better than single effects. The median effect plots (Figure 34B) for TMZ, CX-4945 and the combination of both drugs were plotted in order to obtain the parameters **"m"** (median effect dose) and **"D_m"** (Hill-type coefficient, see Annex I for details in calculation). These values were used to calculate the combination index (Table 10), which determined the type of effect of the combined treatment (synergistic, additive or antagonistic).

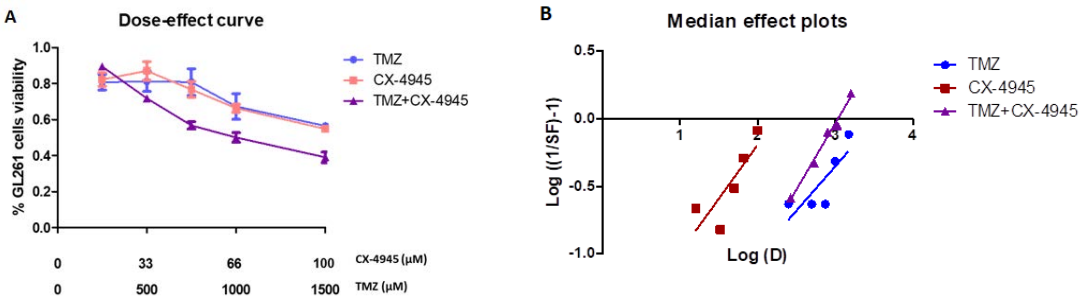

Figure 34: A) Dose-dependent GL261 cell viability and B) median effect plots for CX-4945, TMZ and the combined CX-4945+TMZ treatment

CX-4945 concentrations were 16, 33, 50, 66 and 100 µM and TMZ concentrations 250, 500, 750, 1000 and 1500 µM. The value 1 (100% viability) was assigned to control cells treated with vehicle. Experiments were performed with n=4 and mean ± SD values are shown. The slope of each line (m) is Hill coefficient and the intersection with the x-axis is Dm, the dose necessary to obtain a Fu (surviving fraction) of 0.5.

The combination index was calculated for every set of concentrations according to [195]. Table 10 shows that, depending on the concentration, the effect of the drug combination can be either synergistic, additive or antagonistic.

CX-4945 (µM)	TMZ (µM)	f_a	CI	Result
16	250	0.21	1.42	Antagonism
33	500	0.32	1.09	Addition
50	750	0.44	0.88	Synergy
66	1000	0.47	0.83	Synergy
100	1500	0.61	0.67	Synergy

Table 10. CX-4945 and TMZ concentration, fraction of affected cells and combination index for the joint CX-4945 +TMZ treatment

The individual doses for CX-4945 and TMZ are also indicated. The nature of the combined effect varied according to the concentrations used, with synergy being predominant at highest concentration values.

For the lowest concentrations, the combined effect is antagonistic, since the CI is higher than 1 (1.42). Still, we need to take into account that the viability reduction at the lowest concentrations assayed is very small for all conditions. Moreover, for 500 µM of TMZ and 33 µM of CX-4945, there is an additive effect, since CI is close to 1 (1.09). Regarding the higher concentrations studied the combined effect is synergistic, since CI is in every case lower than 1 (0.88, 0.83 and 0.67). This agrees with our own *in vitro* results reported in [85], although with slightly different combination of concentrations (CX-4945 ranging 30-50 µM and TMZ ranging 1000-1500 µM).

4.2.3.2. Assessment of cytotoxic/cytostatic effects

Flow cytometry with PI-stained cells treated with TMZ, CX-4945 and the combination of both was performed in order to assess the cytostatic and/or cytotoxic potential of the combined treatment compared to individual treatments. The living cell counting was very similar when comparing CX-4945 treated cells and cells treated with the combination TMZ+CX-4945 (maximum difference was 5.2% of living cells, non-significant). The percentage of dead cells was 26.6% ± 9.9 for CX-4945 at 100 µM and 29.6% ± 1.6 for the combination of both at the same concentration of CX-4945 combined with 1.5 mM of TMZ, suggesting a discrete, non-significant synergistic effect of these treatments (Figure 35A), as already suggested by the calculated CI.

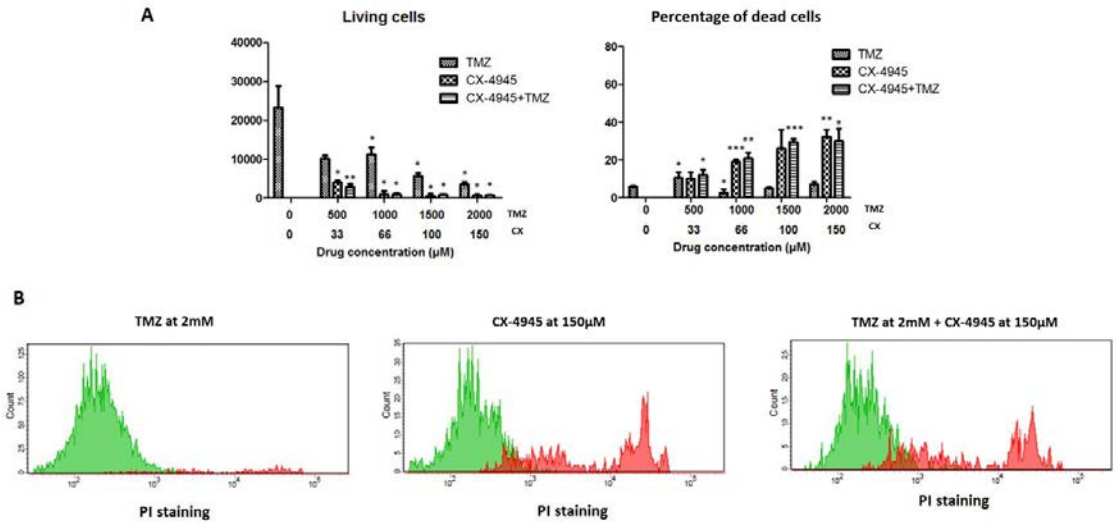

Figure 35: Assessment of cytotoxic/cytostatic effect in GL261 cells treated with TMZ, CX-4945 and the combination of CX-4945 and TMZ.

*A) Living cells and percentage of dead cells after CX-4945, TMZ and CX-4945+TMZ treatments after 72h at 0.5, 1, 1.5 and 2mM of TMZ and 33, 66, 100 and 150 µM of CX-4945 stained with PI and analyzed by flow cytometry (n=3 for each condition). B) Histogram showing the distribution of PI staining. Living cells (PI negative) are represent ted in green population while red population stands for dead and membrane-compromised cells (PI positive). More details about flow cytometry analysis can be found in section 3.1.4. For all instances, mean ± SD are shown. * = p < 0.05, ***

*= p < 0.01 and *** = p < 0.001 indicate statistical significance according to Student's t-test comparing treated and control cells.*

4.2.4 Immunogenic cell death/damage signs triggered in GL261 cells *in vitro* under TMZ and CX-4945 treatment (single and combined treatment)

The capability of CX-4945, TMZ and TMZ+CX-4945 to produce immunogenic cell death/damage and trigger the exposure or release of immunogenic signals was assessed *in vitro*. This would help to explain the beneficial results obtained with metronomic treatments in GL261 tumor-bearing mice and to better understand the combined effects *in vivo*. Several immunogenic death signals are responsible for triggering an antitumor immune response [66]. Among them, the three most important and agreed ones are Calreticulin exposure, ATP secretion and HMGB1 release.

4.2.4.1 Calreticulin exposure

CRT is a chaperone normally localized in the ER. CRT is exposed early in the ICD cascade, in the pre and early apoptotic stages, acting as a potent "eat-me" signal [57]. CRT exposure was analyzed by confocal microscopy in untreated and TMZ (2mM), CX-4945 (25µM) and CX-4945+TMZ (2mM + 25µM) treated GL261 cells after 24h of treatment. Doxorubicin (Doxo) treated cells have been described to trigger CRT exposure [63] and therefore, Doxo-treated cells were used as a positive control. The CRT exposed in the plasmatic membrane of cells has been described to assemble itself in clusters in order to facilitate the binding to the APCs receptor CD91 [63]. In a first step, CRT would be transported by the ER Golgi transport [58] towards the plasma membrane, being first organized in a linear shape along the membrane and later it gets organized in the form of clusters or foci (Figure 36, white brackets and arrows).

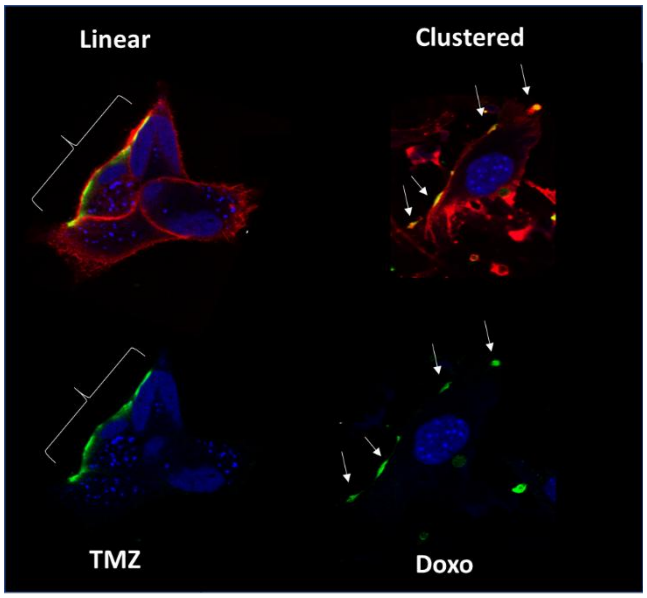

Figure 36: CRT exposure in cell membrane of GL261 cells upon treatment

Example of CRT exposure in different conformations. In the upper part, membranes are shown in red, nuclei in blue and CRT in green (or yellow due to the overlay with membrane). In the lower part, only the nuclei (blue) and CRT (green) are shown. In the left side, Doxo treated cells (50 µM, 24h of treatment) show a linear conformation of CRT exposure (green). In the right, TMZ treated cells (2mM, 24h of treatment) show a clustered CRT exposure. In the case of TMZ treated cells, nuclei were stained with Hoechst dye. For Doxo-treated cells, blue staining corresponds to the autofluorescence of the Doxo itself, since Doxo prevents the union of Hoechst to the nuclear structures. White brackets and arrows point to lineal or clustered CRT, respectively

In order to quantify the results obtained with confocal fluorescence microscopy, cells with no CRT signal in the membrane were considered negative (i.e. no exposure). On the other hand, positive cells were classified either as linear or clustered exposed CRT. The results from the quantification of total positive, linear and clustered exposed of CRT are shown in Figure 37. It is worth mentioning that a large dispersion was observed in the number of CRT exposed cells in Doxo and TMZ treated samples, as it can be seen in the boxplots of Figure 37 and values did not follow a normal distribution. Accordingly, non-parametric tests were used to compared UT cells with the rest of the groups. The UT cells showed only a small percentage of CRT exposing cells (7.9 ± 13.5% in average for total CRT) which was considered as the basal CRT exposure of the GL261 cell line. Doxo-treated cells showed a higher percentage of CRT-exposing cells (ca. 4-fold change, 30.6 ±32.4% of cells) although the dispersion of values prevent to reach statistical significance. Thus, Doxo-treated cells were confirmed to be a suitable positive control for this experiment.

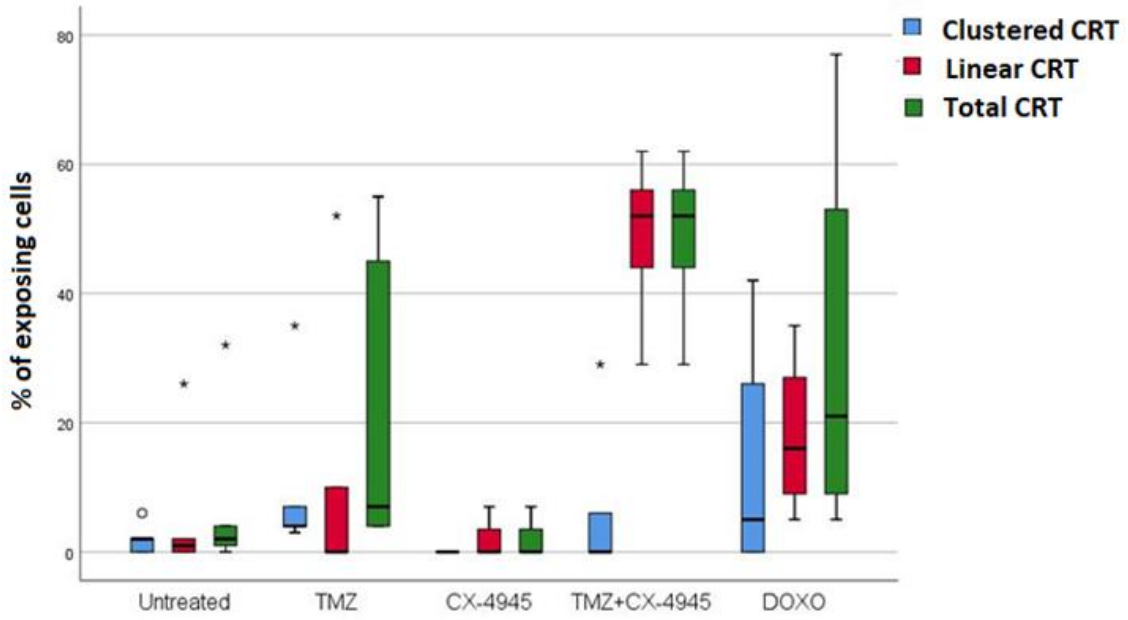

Figure 37: Boxplots for quantitation of total, linear and clustered CRT-exposing GL261 cells upon treatment

The percentage of positive cells is shown (n=3-5 for each condition). All measurements were performed after 24h of treatment. The doses used were 2 mM for TMZ, 25 µM for CX-4945 and 50 µM for Doxo .The limits of the box represent quartiles 1 (Q1) and 3 (Q3) of the distribution, the central line corresponds to the median (quartile 2). Whiskers symbolize the maximum and minimum values in each distribution that are not above or below 1.5 times the interquartile range (IQR), which obtained by difference of Q3 and Q1. Outliers whenever present are marked with "o" (1.5 times IQR < value < 3.0 times IQR) or "" (values higher than 3.0 times IQR, extreme outliers).*

Regarding TMZ-treated cells, a higher percentage of clustered CRT positive cells was found in comparison with UT with tendency to significance in the clustered form (p=0.056), suggesting that TMZ may indeed trigger CRT translocation to the membrane and the subsequent formation of clusters also *in vivo*. Moreover, CX-4945 single treatment only triggered CRT exposure in a small fraction of treated cells and it was not significantly different from the basal expression measured in untreated cells (average values even lower than UT cells). The combined CX-4945+TMZ treatment significantly improved the percentage of CRT-exposing cells in comparison with single treatments, especially in the linear form (20-fold change in comparison with CX-4945 alone and ca. 4-fold change in comparison with TMZ alone). Regarding the clustered form, the combined treatment outperforms the treatment with CX-4945 alone (increasing from 0 to 7.0% exposing cells in average), but shows a slight decrease in comparison with TMZ-treated cells which presented an average value of 10.6% exposing cells. Representative images from confocal microscopy obtained with the different treatments are shown in Figure 38. In these representative images, we can observe that Doxo-treated cells

showed mostly linear exposure of CRT, whereas TMZ-positive cells expose CRT preferentially in clusters. The CX-4945+TMZ treated cells also expose linear CRT in their surface.

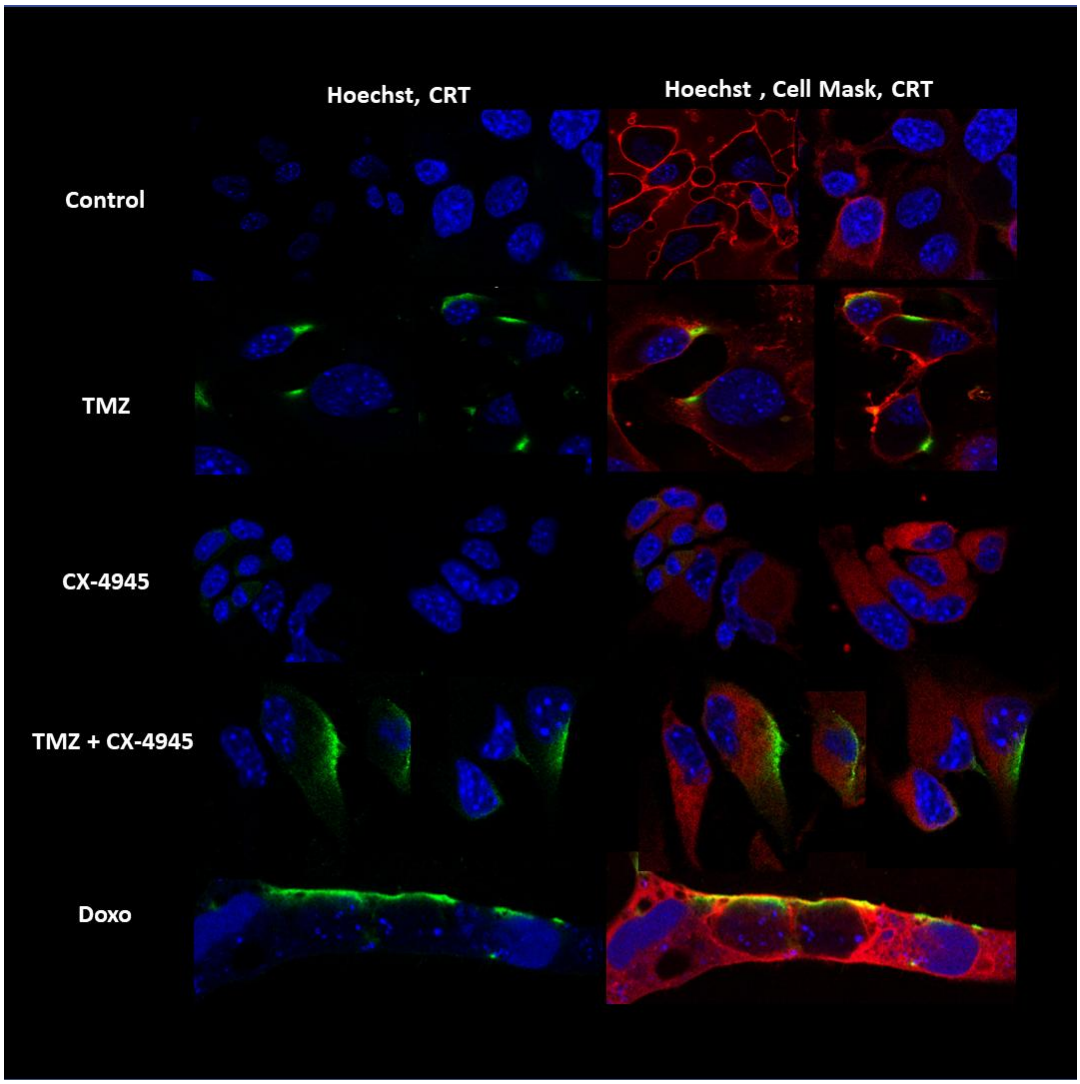

Figure 38: Representative images of immunofluorescence of TMZ and Doxo-treated GL261 cells exposing CRT

Immunofluorescence staining for all conditions. Nuclei were stained with Hoechst (except for Doxo treated cells which prevented Hoechst staining; instead, autofluorescence of Doxo is shown in blue) and membrane with Cell Mask Deep Red. In the left side, nuclei (blue) and CRT (green) are shown. In the right, membranes are shown in red, nuclei in blue and CRT in green (also yellow due to the overlay with membrane). All treatments were performed for 24h: TMZ (2 mM), CX-4945 (25 µM), TMZ+CX-4945 (2 mM, 25 µM) and Doxo (50 µM).

4.2.4.2 ATP release

Released ATP has been shown to stimulate the immune response as a short-range "find-me" signal and as a proinflammatory molecule by binding to P_2Y_2, P_2X_7 and P_2 receptors found in dendritic cells (DCs) and monocytes [68]. In order to find optimal conditions in which treated cells may release ATP, the experimental design performed in [197] was used to assess ATP release in TMZ (2 mM), CX-4945 (100 µM) or CX-4945+TMZ (100 µM and 2 mM) treated cells. First, the viability of treated cells was assessed after short treatment periods. The aim of this

first experiment was to establish the dose and time of treatment in which 50% of cellular viability was achieved when compared to untreated cells to work in similar conditions as described in [197].

Cellular viability assessment after short times of drug treatment

Cellular viability of GL261 cultured cells was assessed after 4, 8, 12 and 18h of CX-4945 treatment as in [197]. Viability after 24h treatment was also analyzed in order to get a time point suitable for comparison with CRT analysis and Trypan Blue assays. Since TMZ needs a longer time to decrease cellular viability (Figure 35), it was added 24 hours before CX-4945 treatment in the combined experiment. Therefore, viability was assessed after a total of 28, 32, 36, 42 and 48h of TMZ treatment.

Three different concentrations of CX-4945 (100, 200 and 300 μM) were used in these experiments. TMZ concentration used was 2mM, to be consistent with CRT exposure studies and also because at this concentration TMZ showed effects over cellular viability (after 48h of treatment TMZ significantly diminishes total living cells counting, Figure 35B).

GL261 cell viability after TMZ, CX-4945 and CX-4945+TMZ treatments is shown in Figure 39. The shorter periods of treatment (4 and 8h) were discarded because only small effects (around 5% of decrease) were observed in cell viability. The concentration of 100μM for CX-4945 was chosen because suitable viability decrease (50%) was achieved after 18h of treatment both in single and combined treatment. In summary, the experimental conditions chosen for ATP release analysis were 12, 18 and 24h of CX-4945 treatment at 100 μM.

Assessment of ATP release after TMZ, CX-4945 and TMZ+CX-4945 treatment

ATP content in the supernatant was measured with a luciferin-luciferase based assay. The procedure is explained in detail in the 3.1.8.3. section. Results show that CX-4945 and CX-4945+TMZ treated cells released much higher amounts of ATP compared to UT and TMZ-treated cells (Figure 40A).

For CX-4945 and the combined CX-4945+TMZ treatment, all studied time periods presented an increase in ATP release which was significant ($p<0.05$) for all time points. However, the maximum difference in ATP release in comparison to UT cells was found at 12h treatment (ATP was found 37-fold higher for single CX-4945 treatment and ca 12-fold higher for the combined treatment) Lower results obtained with the combined treatment suggest that the combination with TMZ caused a 3-fold decrease in the overall ATP released although it was still significantly higher than UT cells. On the other hand, treatment with TMZ alone indeed decreased the

amount of released ATP (0.32 for UT vs 0.17nM for TMZ) although it was non-significant, with p>0.3 at all time points studied. This could be due to the production of a different immunogenic signal associated to ATP consumption or interference with the ATP release system in GL261 cells.

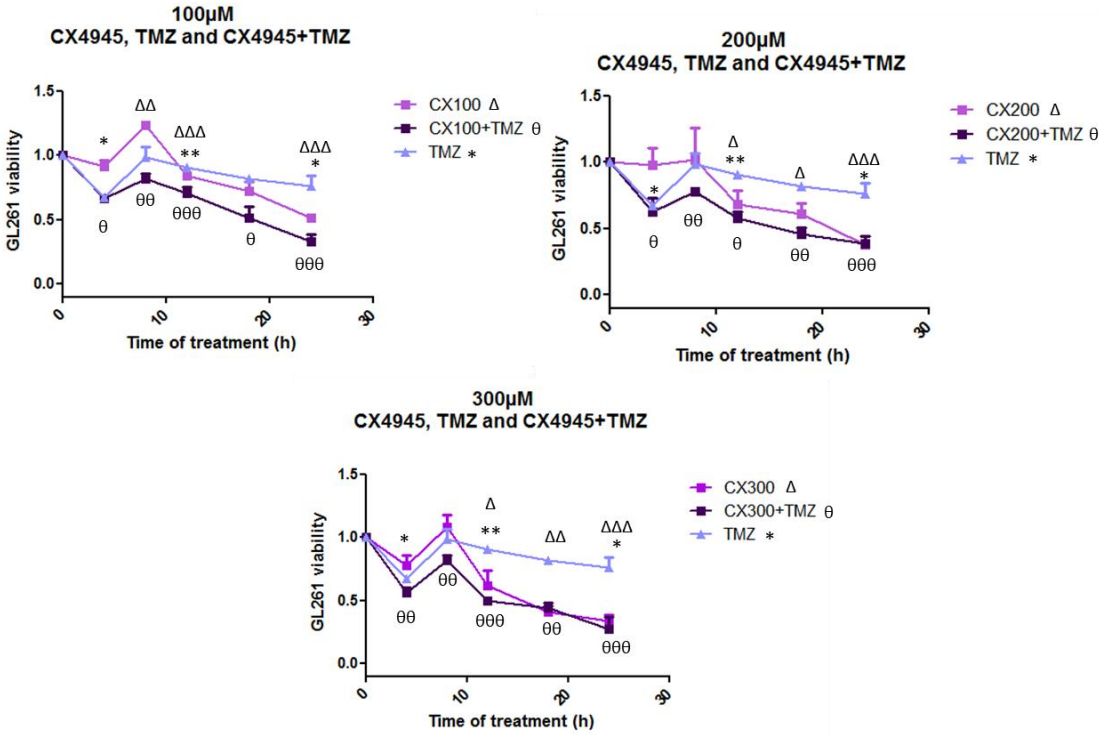

Figure 39: GL261 viability with TMZ, CX-4945 and the combined treatment at short time periods.
*A) GL261 cells treated with CX-4945 at 100, 200 and 300μM for 4, 8, 12, 18 and 24h. TMZ was added at 2mM concentration for CX-4945+TMZ treated cells, TMZ at 2mM was added 24h before CX-4945, so the total time of TMZ treatment was 28, 32, 36, 42 and 48h. *, Δ and ϑ indicate statistical significance according to Student's t-test comparing treated and untreated (UT), control cells. One symbol indicates p<0.05, two p<0.01 and three p<0.001.*

In addition, intracellular ATP was also measured and the estimated amount of ATP per cell is shown in Figure 29B. No significant differences were found among different treatments, suggesting that the evaluated treatments did not produce noticeable changes in the intracellular ATP content, but only in the amount of released ATP.

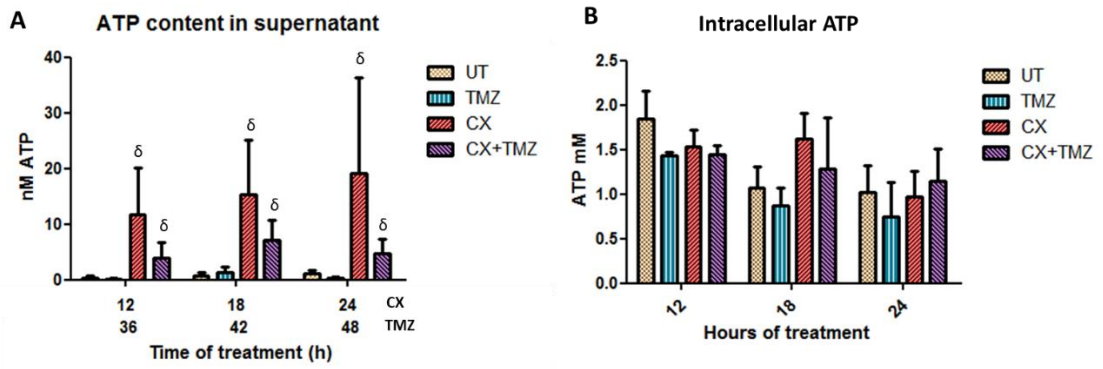

Figure 40: Supernatant release and intracellular ATP quantification in GL261 treated cells
CX-4945 (100 µM), TMZ (2mM) and CX-4945+TMZ (100µM, 2mM) treated cells were evaluated. A) Supernatant content of released ATP. Mean ± SD are shown for n=6 for every condition. δ states for p<0.001 according to ANOVA test with Tukey's post-hoc comparisons with TMZ and UT cells. Single CX-4945 and joint CX-4945+TMZ treatment did not present significant differences between them. B) Intracellular ATP measured in GL261 treated cells. (n=3). Mean ± SD is shown, no significant differences were found.

These results demonstrate that CX-4945 treatment triggers a relevant ATP release in GL261 cells at every time point studied. The average of released ATP increases along time in GL261 cells under single CX-4945 treatment: starting from the value measured after 12h, a 23% increase is seen at 18h of treatment and a 38% increase at 24h. Meanwhile, in the combined treatment, released ATP is 46% higher after 18h of treatment compared to 12h of treatment but decreases with respect to earlier time points after 24h of treatment.

Cytotoxicity assessment after short treatment periods and its relationship with ATP release

ATP is thought to be released either by active mechanisms in pre/ early apoptotic cells or by passive release in necrotic cells. We wondered whether ATP detected after treatments was being released by living or membrane-compromised cells, and to elucidate it, treated cells were incubated with PI and analyzed by flow cytometry in the same conditions mentioned in the previous section (Figure 41).

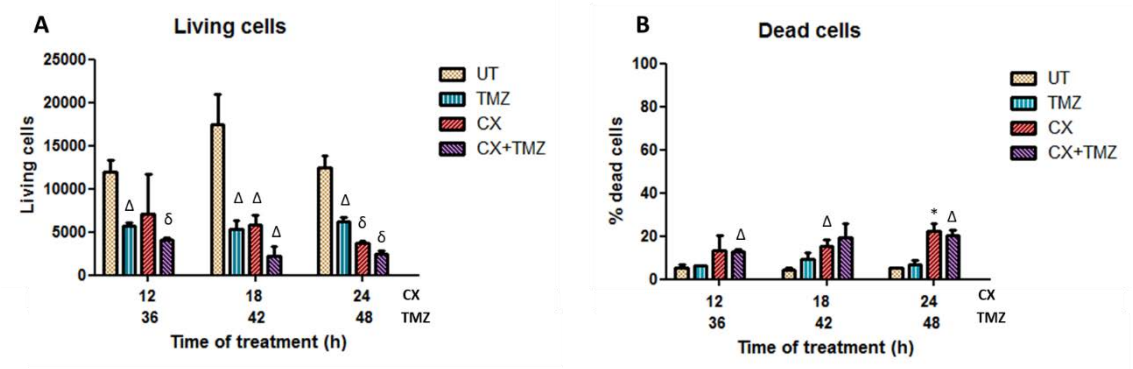

Figure 41: Cytotoxicity assessment after short treatment time periods in GL261 cells
*A) Living cells after CX, TMZ and CX+TMZ treatments, stained with PI and analyzed by flow cytometry. (n=3 for each condition). B) Percentage of dead cells after the indicated treatments. For all instances, mean ± SD are shown. *, Δ and ϑ indicate statistical significance (p<0.05) according Student's t-test comparing treated and control cells.*

As previously stated, the maximum amount of ATP released, in comparison with UT cells, was observed after 24h of CX-4945 treatment. The flow cytometry results after 24h of CX-4945 and CX-4945+TMZ treatments show a percentage of dead cells of 22.3 and 20.5% respectively, indicating that most of the remaining cells were still alive. Therefore, ATP might be probably released to the extracellular space by living cells through an active mechanism.

However, having in mind the results obtained *in vivo* with CX-4945 treatment in GL261 GB tumor-bearing mice, it becomes clear that released ATP cannot be the only (neither the major) determinant immunogenic signal triggered in GL261 because CX-4945 produced only a small (although significant) improvement in overall survival of tumor-bearing mice [85].

4.2.4.3 HMGB1 release

HMGB1 is known to be passively released by necrotic cells and be in charge of immune system activation against damaged cells. It is though that necrotic, membrane compromised cells, freely release the HMGB1 content of the nucleus into the extracellular medium. Accordingly, HMGB1 release was assessed in TMZ, CX-4945 and CX-4945+TMZ treated cells after 48h treatment. The time of treatment is longer in this case, since HMGB1 is released by dead cells and it is not until this time point that dead cells are detected in large amounts according to our results (see Figure 33 and Figure 35). Doxo-treated cells were used as positive control since Doxo is known to trigger HMGB1 release [224].

Results show that only Doxo-treated cells release more HMGB1 in comparison with UT cells (Figure 42) (33.3 ± 12.8 vs 81.7 ± 22.2 ng/ml, p<0.05). Moreover, CX-4945 treatment seems to somehow impair the release of HMGB1, since the HMGB1 concentrations obtained for CX-4945 and CX-4945+TMZ treatments are significantly lower than the obtained for UT cells.

Value found were 3.9 ± 5.4 ng/ml for CX-4945 alone and 1.1 ± 1.9 ng/ml for CX-4945+TMZ ($p<0.05$ compared to UT cells, but no significant differences were found comparing CX-4945 solo treatment with the TMZ combination (

Figure 42).

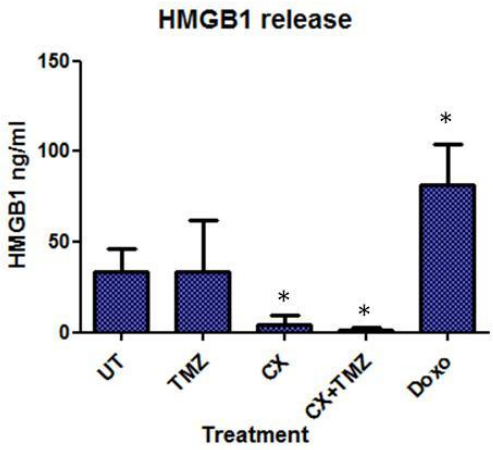

Figure 42: HMGB1 content in supernatant of control and treated GL261 cells
HMGB1 content was analyzed by ELISA. (n=3 for each condition). Cells were treated for 48h at 2mM TMZ, 100µM CX-4945 and 50µM Doxo.
** indicates significance (p<0.05) according to Student's t-test*

4.2.5 Discussion

4.2.5.1 In vitro TMZ effect in GL261 cells

In this chapter, TMZ effects regarding the decrease in total living cells counting and in the induction of cell death in the GL261 cell line were systematically analyzed. Although TMZ is the standard chemotherapeutic treatment for GB in the clinical pipeline, there is no clear consensus about the molecular mechanisms underlying its antitumoral effect. For instance, TMZ is described as a cytotoxic agent triggering different modalities of cell death, such as autophagy or apoptosis [17, 225]. On the other hand, a main cytostatic effect has been described for TMZ in high MGMT expressing GB cell lines, which are more resistant to TMZ effect [226]. In our experimental conditions, TMZ has demonstrated a cytostatic rather than cytotoxic effect in the GL261 cell line (Figure 32), confirmed by Trypan Blue assays and flow cytometry with PI stained cells. The maximum percentage of dead cells found was 29 ± 2.3 %% after 72h of treatment and at a concentration of 4 mM (Figure 32B). These results indicate that GL261 cells behave as TMZ death resistant cells, although its MGMT status is still unclear. Moreover, authors reporting TMZ-resistant GB cell lines [227] found IC_{50} values for TMZ in the same range (ca 454-871 µM vs 254-572 µM in this thesis) and percentage of apoptotic cells (2.4% after 24h of TMZ treatment at 800 µM vs 2.5% after 24h of TMZ at 500 µM in this thesis).

The MTT is a tetrazolium-based viability assay which measures the reduction of MTT (3-(4,5-dimethylthiazol-2-yl)-2,5-diphenyltetrazolium bromide) by the mitochondrial complex II/succinate dehydrogenase [228]. This assay is inexpensive, fast, easy and requires a small number of cells, being suitable for high throughput rough preliminary screenings. However, it is not free from over or underestimations of the cellular viability due to factors different from cellular viability such as inhibition of mitochondrial functions [221] which do not necessarily imply cell death. In this sense, although Trypan Blue is a more expensive and time-consuming method, its results are thought to be more accurate and reliable regarding living and dead cell number estimation. Moreover, flow cytometry of PI stained cells can also be a reliable method for these estimations.

In this chapter, inconsistent results regarding EC_{50}/IC_{50} have been found for TMZ treated cells when its viability was measured by MTT (IC_{50} 5.57 mM) compared to results obtained with Trypan Blue and Flow Cytometry (IC_{50} of 254 µM and 572 µM respectively after 72h of treatment). Since MTT results can be in some occasions inaccurate the parameters obtained using Trypan Blue and Flow Cytometry results were considered as the most reliable. The difference in the IC_{50} obtained by Trypan Blue and Flow cytometry may be due to the lack of a concentration lower than 500 µM in the protocol used. Indeed, IC_{50} would be more suitable for direct comparison of agents having such different range of effects in viability. Thus, the results obtained in this chapter agree with results published by other authors in the GL261 cell line, with IC_{50} values ranging between 100 and 500 µM [225, 229].

4.2.5.2 CX-4945 effect in vitro

The CK2 inhibitor CX-4945 is a potent drug that decreases significantly the living cell counting in GL261 treated cells (Figure 33). As expected, low IC_{50} values were obtained, one order of magnitude lower than TMZ (see Table 9 and Table 8 respectively). For CX-4945 treatment, the IC_{50} calculated with MTT and Trypan Blue results after 72h of treatment was similar, around 20 µM in both cases. However, the IC_{50} calculated with flow cytometry data was lower (6.8 µM). Still, these differences can be attributed to the lack of lower drug range concentrations in the flow cytometry analysis.

Regarding the cytotoxic potential of this inhibitor in GL261 cells, the percentage of dead cells found was 26.9 ± 7% after 48h and 50 ± 34 % after 72h of treatment (Figure 33). These results agree with authors in [230], in which a similar percentage of dead cells was found in different acute lymphoblastic leukemia cell lines, showing the cytotoxic potential of CX-4945 in these

cells. In our case, results suggest that indeed CX-4945 may have a cytotoxic effect on GL261 cells at the concentrations studied, especially the highest ones.

4.2.5.3 Combined effect of TMZ and CX

TMZ and CX-4945 had been described by us to produce a synergistic effect *in vitro* and *in vivo* both in the GL261 cell line and with GL261 established tumors [85]. However, a systematic analysis and quantitation of this effect was still missing and it was addressed in this thesis. Accordingly, the combined effect of these drugs was analyzed by the Chou-Talalay method, an approach described to be useful for this purpose [195] and it was demonstrated that, at the highest concentrations studied, CX-4945 and TMZ indeed exert a synergistic effect on GL261 cell viability.

CX-4945 inhibits the PI3K/Akt pathway, among others, through the inhibition of CK2 [110]. On the other hand, TMZ administration has been described to hyperactivate the PI3K/Akt pathway as a stress-related response [226]. Accordingly, TMZ was described to produce a synergistic effect when used in combination with PI3K/Akt/mTOR inhibitors, increasing the survival of xenograft mice with pituitary adenomas [231]. Since CK2 inhibition has been described to also inhibit PI3K/Akt pathway [114], CX-4945 could compensate the hyperactivation of PI3K/Akt pathway triggered by TMZ. Therefore, one of the possible explanations for this synergistic effect of both drugs *in vitro* could be the compensatory effect on the PI3K/Akt signaling, although further confirmation would be needed to clarify and complete this information.

4.2.5.4 ICD signals

Previous results from our group in GL261 GB tumor treatment showed that the use of a regularly spaced, every 6 day metronomic administration (the IMS, see section 1.3.1.5) of therapy resulted in improved survival of tumor-bearing mice ([85], Figure 31), especially for TMZ and the combination TMZ+CX-4945. The IMS for TMZ administration demonstrated improved survival in comparison with the previously described TMZ non-metronomic treatment used by us ([98, 188] and unpublished data), although without significance (39 ± 3 days, n=6 vs 34 ± 12 days, n=38, respectively). These results confirmed that TMZ was an effective drug for GL261 GB treatment, even better when an immune cycle respectful cycle was applied, and that CX-4945 could enhance the effect of TMZ when administered in combination (55 ± 12 days overall survival). However, only small improvement in mice survival was appreciated in single metronomic administration of CX-4945 (24 ± 2 days vs 22 ± 1 days for control mice), in disagreement with *in vitro* results in this chapter (Figure 32 and Figure 33).

For example, CX-4945 proved to have a much more potent effect *in vitro* in GL261 cultured cells (IC_{50} of 20 μM) than TMZ (IC_{50} 254 μM).

Yet it is true that these drugs presented synergistic effects when combined *in vitro*, it does not fully explain the results obtained *in vivo* with the combined treatment, especially having in mind the poor results obtained with the non-metronomic approaches, in which the addition of CX-4945 reverted the beneficial effects of TMZ (17.8 ± 2.8 days for mice treated with TMZ+CX-4945 vs. 19.8 ± 1.5 days for control mice, [85]). These findings suggest that something different than the direct tumor cell killing is leading to an increasing survival in TMZ and TMZ+CX-4945 treated mice studied in [85].

In this line of thought, Wu et al [84] reported that the alkylating agent CPA can induce the host immune system recruitment through immunogenic death of tumor cells, when administered in an every 6-day cycle. The cells of the host immune system may be attracted through the exposure and emission of DAMPs and after that, tumor cell killing would take place as described in section 1.2.1. The improved outcome of the combined treatment when the schedule switched to IMS, even when administering *lower* overall doses of therapeutic agents, lead us to hypothesize that host immune system recruitment could be taking place. Accordingly, we wanted to evaluate the exposure and emission of DAMPs in TMZ, CX-4945 and TMZ+CX-4945 GL261 treated cells *in vitro*, in order better explain the results obtained *in vivo* in [85].

Calreticulin

CRT exposure is one of the most widely characterized "eat-me" signals which elicit the host immune system. CRT binds to the receptor CD91 found in dendritic cells and macrophages, enabling the processing of tumor antigens [58]. Authors in [20] have demonstrated that TMZ at 100, 200 and 400 μM can trigger CRT exposure in GL26 cells glioma plasma membrane, observed through flow cytometry analysis. In our experimental conditions, TMZ-treated GL261 cells (2mM) triggered CRT exposure mainly organized in clusters (Figure 36). This cluster configuration of CRT has already been described by other authors [232, 233]. On the other hand, GL261 cells upon CX-4945 single treatment (25 μM) do not present significant differences in CRT exposure in comparison with controls. However, cells treated with the combined treatment (25 μM CX-4945 + 2mM TMZ) do expose CRT in their surface (Figure 36), even in a higher percentage of cells in comparison with single TMZ treatment (Figure 37). This would agree with the results obtained *in vivo* [85], although a further confirmation with the

same approach in GL261 GB tumor samples of treated animals would be needed for fully validating the in vitro findings.

Moreover, CX-4945 has been described in several publications to trigger ER stress in various types of cells such as T-cell lymphoblastic leukemia and retinal pigment epithelial cells [230, 234]. This ER stress could help enhance the immunogenic cell death mechanisms, although CRT exposure was not detected in the conditions investigated by us, which could contribute to the synergistic effect of TMZ and CX-4945 treatment *in vivo* in GL261 GB tumor-bearing mice (Figure 31).

ATP

ATP release is one of the main immunogenic signals required to elicit the host immune system. The presence of ATP in the tumor microenvironment stimulates the purinergic receptors P_2Y_2 and P_2X_7 receptors on DCs and macrophages, stimulating the recognition of antigens, the phagocytosis of tumor cells and the differentiation of CD8+ T cells [71]. In this thesis, and for the first time to its author´s knowledge, CX-4945 treatment was shown to produce a massive release of ATP after treatment. After 12h of treatment, CX-4945 treated cells release in average, 37 times more ATP than control cells (11.7 vs 0.32 nM). In addition, it was also shown that in the combined administration of TMZ and CX-4945, TMZ does not prevent ATP release, although the final amount of released ATP (3.9 nM) is lower than the observed with CX-4945 single treatment. Even so, the amount of ATP released by TMZ+CX-4945 treated cells is still up to 9-fold higher than UT cells, highlighting the boosting effect of CX-4945 to induce antitumoral immunogenicity. Since ATP release is one of the most important "find-me " signals that attract immune cells to the tumor site, this study postulates CX-4945 as a pro-immunogenic drug when combined with a *per se* immune stimulating drug, as TMZ [85].

ATP plays a role in the immunogenic cell death/damage when its accompanied by other immunogenic signals, such as CRT or HMGB1 but when ATP it is the only immunogenic signal triggered, it could have an opposed immunosuppressive and even protumorigenic effect [235]. This could explain why CX-4945 single treatment in GL261 tumor-bearing mice did not improve their survival. In contrast, the synergistic effect seen in the CX-4945+TMZ combined treatment would indicate that the extracellular release of ATP enhances the anti-tumoral immune response when combined with a *per se* immunogenic treatment, such as TMZ (Figure 31). Still, the work of Zheng et al [110] showed an increased survival in xenograft mice triggered by CX-4945 treatment, this may be due a non-immunogenic related effect of CX-4945 since it was shown in immunocompromised mice, or, alternatively, an effect mediated by innate immune

system cells, i.e. natural killer and macrophages, some of them increased in immunocompromised mice [91].

Furthermore, ATP has been described to be either passively released by necrotic cells [58] or in an active way via lysosomal exocytosis by autophagy-dependent mechanisms [236]. Flow cytometry results (Figure 41) show that CX-4945 and TMZ+CX-4945 treated cells which released ATP may be probably living, PI negative cells, indicating that ATP release may happen by active mechanisms that could be related to autophagic cell death. Accordingly, with this proposal CX-4945 treated cells were described by others to undergo autophagic cell death [170].

HMGB1

Passive release of HMGB1 from necrotic tumor cells is one of the hallmarks of ICD [66]. In our experimental conditions, neither TMZ nor CX-4945 treated cells showed enhanced HMGB1 release in the studied conditions. In fact, HMGB1 release was significantly lower in CX-4945 treated cells. This makes sense since CX-4945 has been described to produce autophagic, but not necrotic, cell death [170]. Moreover, released HMGB1 has been described to induce both pro- and anti-tumorigenic activities, depending on the redox state of HMGB1 [66]. In our study, only total HMGB1 content was analyzed in the supernatant, and this approach did not provide information on HMGB1 redox state, which could be relevant to tackle in future work.

4.2.5.5 Timing in therapy administration: when are immunogenic signals produced?

Although our results of ICD signals were obtained only for *in vitro* conditions, we could hypothesize that similar situations are produced *in vivo*. In this sense, it is fair to assume that the beneficial effects in overall survival of tumor-bearing mice with IMS-administered TMZ were at least partly due to the immunogenic action triggered by CRT exposure. The antitumoral response was further enhanced with the immunoattractive action of the ATP released triggered by CX-4945 in the joint therapeutic treatment. Finally, ATP release alone does not seem to be sufficient to trigger an effective antitumoral immune response (Figure 43).

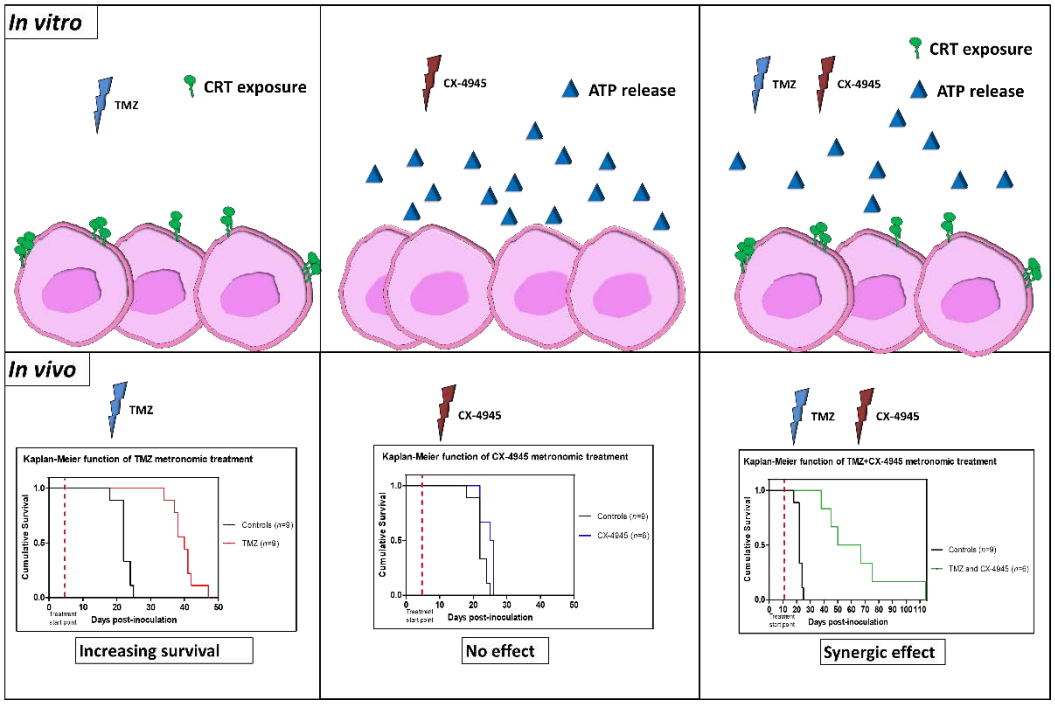

Figure 43: Comparison between in vitro emitted DAMPs and in vivo survival of GL261 tumor-bearing mice under TMZ, CX-4945 and TMZ+CX-4945 combined treatment

However, there are differences between the *in vivo* therapy administrations that are not straightforward to emulate in vitro and could have an influence in the extrapolation of results. In the in vitro treatment, the whole amount of added therapeutic agents are constantly in contact with all available tumor cells. On the other hand, in the *in vivo* treatment, each agent has its own bioavailability and pharmacokinetics profile, (maximum peak of TMZ after 0.5h, half-life ca. 1h [223], and maximum peak for CX after 1.5h, half-life ca. 10h [217]). Also, differences in perfusion rates between tumor zones could have an influence in therapeutic agents' arrival. Finally, it is worth noting that the *in vivo* administration of the therapeutic agents was done at different hours for TMZ and CX-4945 (split into two doses): the first CX-4945 dose was performed at 8 am, TMZ was administered at 2 pm and the second CX-4945 dose at 8 pm. Accurate investigation of DAMPs produced at different (and short) times *in vivo* may be needed to check if the drug administration hours and timing could be further improved to maximize the immunogenic signals co-release/ exposure.

4.2.5.6 Final remark: could we noninvasive assess the immune system action within tumors?

Having in mind a) the relevance of the immune system participation in the response to therapy described in the introduction (section 1.2), b) the length of the immune system cycle in mice [237], c) the immunogenic potential of therapeutic agents used in this thesis and shown in this section and d) the improved survival observed in GL261 GB tumor-mice treated with the IMS-

immune system respectful schedule, it is sensible to expect that relevant molecular/cellular changes will take place every 6-7 days, after each therapeutic cycle. Previous longitudinal data from our group described in [37] support this hypothesis, in which an oscillatory behavior in the therapy response imaging biomarker (see also section 1.5.4) was observed. Still, work in [37] was performed with a non-optimal TMZ administration schedule and essentially centered in validation rather than in longitudinal observation. Our next step was to extend the application of the noninvasive assessment of therapy response in GL261 GB tumor-bearing mice under IMS (the immune system respectful schedule) therapy administration, in order to confirm the oscillatory behavior of the therapy response imaging biomarker, which should be reproducible to validate its consistency.

4.2.6 Conclusions

- TMZ has a predominant cytostatic effect, rather than cytotoxic, in the GL261 cell line in culture, even with high concentrations (i.e. 2mM) are used in *in vitro* treatment. These concentrations would well be above the blood concentrations achieved after a regular dose in preclinical or clinical patients. The modest in vitro effect of TMZ, in contrast with satisfactory results presented *in vivo,* suggests that other effects than the DNA alkylation potential are taking place *in vivo*. Those could be related to the immunogenic cell death triggered by TMZ.
- In our hands, the MTT method has proved less reliable than other methods for assessing cell death such as Trypan Blue or PI-stained cells analyzed with flow cytometry. Recalculation of IC_{50} values with Trypan blue and cytometry results as input, reconciled the calculated values in this work (254 µM for Trypan Blue and 517 µM for Flow Cytometry) with literature values described for the GL261 cell line (400 µM in [157]) which is in agreement with our results.
- CX-4945 was confirmed as an effective CK2 inhibitor in the GL261 cell line in culture with an IC_{50} of 23 µM after 72h treatment. In addition, CX-4945 proved to have a variable effect according to the concentration, with low range concentrations (25-33 µM) producing mostly a cytostatic effect and high range concentrations (ca 100 µM) presenting cytotoxic effect (35% of dead cells at 150 µM after 72h). However, its single administration *in vivo* to GL261 tumor-bearing mice produced only small improvements in survival.
- Regarding synergistic/antagonistic action of CX-4945 and TMZ calculated with in vitro results through the Chou-Talalay method, the effect of the combined treatment was variable according to the concentrations studied. Low range concentrations lead to an antagonistic behavior, whereas high range concentrations rendered a synergistic effect. However, it is worth remembering that these types of in vitro assays do not fully mimic the real

concentrations, residence time of drugs and immune system effects in *in vivo* tumors. A word of caution should be raised when interpreting drug combination results in vitro without preliminary data from *in vivo* preclinical studies.

- Regarding the DAMPs studied in this chapter: a) CRT exposure: TMZ-treated cells exposed CRT after 24h of treatment (23% of cells), mostly in the clustered form. Only 2% of CX-4945 treated cells did expose CRT whereas the 49% of CX+TMZ treated cells did expose CRT, meaning that CX-4945 did not impair CRT exposure but could even enhance this effect. b) ATP release: cells treated with CX-4945, either alone or in combination with TMZ released high amounts of ATP. TMZ alone did not trigger differential ATP release in comparison with untreated cells. c) HMGB1 release was not shown neither in TMZ, CX-4945 nor in CX-4945+TMZ treated cells. Indeed, CX-4945 treatment seemed to impair HMGB1 release.
- One important summary conclusion is that rather than assessing how many cancer cells drugs are able to kill, we should ask ourselves if drugs produce the right immunogenic signal combination in order to attract and enhance host immune system participation in cell killing. Still, along the same line of thought, we should avoid hitting patients with treatment during periods that could hamper immune system priming and amplification, which could produce a worse outcome, even with potent cancer cell killing agents.

4.3 Multi-slice MRSI-based volumetric analysis of therapy response assessment in metronomic (IMS) TMZ treatment of GL261 tumors *in vivo*

Specific goals: to confirm and expand previous results from our group regarding the noninvasive assessment of response to therapy through MRSI followed by pattern recognition techniques and nosological maps generation, resulting in surrogate imaging biomarkers of response. Previous results from our group suggested that changes observed in the MRSI spectral pattern features in tumor-bearing mice under therapy could be related to the local action of the host immune system, although those observations were based on a non-optimal TMZ administration schedule (non-metronomic). Provided that the previous chapter confirmed the potential of TMZ and CX-4945 for producing immunogenic cell death, probably followed by immune system elicitation, we should expect that our system would be able to observe these changes in an optimized administration schedule focused in enhancing immune system participation (IMS, Immune-Enhanced Metronomic Schedule, [85, 191]).

In section 1.5 of the introduction, the added value of metabolomic information in therapy response assessment was explained, as well as the development of an MR-based biomarker for therapy response in preclinical GL261 GB. This biomarker was based in pattern recognition analysis of MRSI data acquired and it will be used as the basis of the work developed in this section. MRSI signal provides rich metabolic information that can be automatically categorized by PR techniques allowing to generate nosological maps of therapy response. In the semi-supervised source analysis (see section 1.5.4), paradigmatic spectra (or source spectra) are extracted from a training, well characterized group, corresponding to (1) normal tissue, (2) responding, slow proliferating, tumors and (3) non-responding, actively proliferating, tumors. These sources are used for comparison when new data is analyzed, and the predominant component is calculated for each input. The results are then displayed in the form of nosological maps, color-coded maps which represents the spatial distribution of the classification. The final color of each voxel is determined by the main contribution to its pattern. Spectra with a major contribution of normal tissue pattern appear in blue, the active proliferating GB is shown in red, while spectra from tumor responding to treatment is shown in green and undetermined tissue is shown in black.

In this chapter, three GL261 GB tumor-bearing mice treated with TMZ using the IMS administration protocol described in [191] are presented. In the longitudinal studies

performed, mutislice MRSI explorations acquired every 2 days, followed by nosological imaging calculation obtained through semi-supervised source analysis were performed [37, 98].

In the aforementioned work with multi-slice MRSI exploration [37], the evolution of response to therapy was monitored in GL261-tumor bearing mice treated with TMZ in a 5+2+2 therapy schedule at 60mg/kg. This schedule consisted in TMZ administration during 5, 2 and 2 days interleaved with 3-day rest periods and was described in [98, 194], before switching to the IMS protocol. The aim of this chapter was to evaluate therapy response and tumor evolution by MRSI-based nosological images, in GL261 tumor-bearing mice treated with TMZ with the IMS protocol (every six days) at 60mg/kg and starting at day 11 p.i. (Figure 44). This administration schedule was described by others to trigger immune system activation in CPA-treated mice [84] and it was shown to produce longer survival times (38.7 ± 2.7 days, n=6) compared to control mice (22.5 ± 1.2 days, n=6) [85], tending to better results in comparison with 5-2-2 cycle (33.9 ± 11.7 days, n=38, [98] and unpublished results).

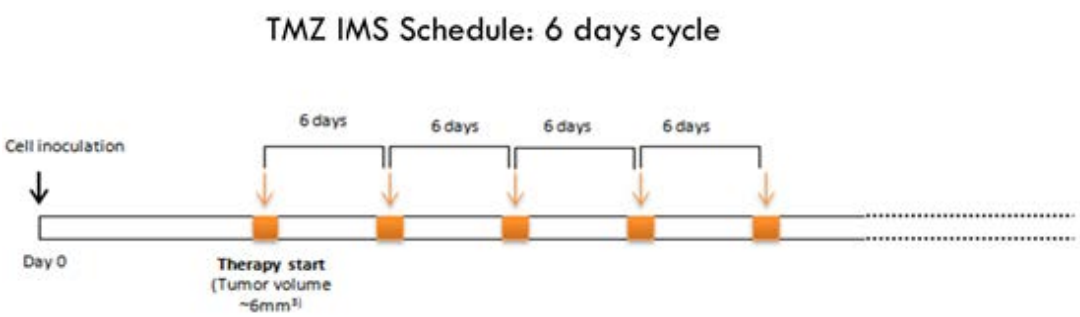

Figure 44: Immune-Enhanced Metronomic Schedule (IMS) used for GL261 GB therapy in mice.
TMZ therapy started at day 11 p.i. Number of cycles varied according to the response obtained, but was not higher than 8 (cumulative dose up to 480mg/kg), to avoid appearance of lymphomas as described in [191]

4.3.1. Monitoring of body weight and welfare parameters

The three mice studied were followed-up according to the supervision parameters for animal health status (Annex II) and weighted every two days. The score obtained in the supervision protocol determined endpoint for humanitarian reasons: at that point, animals in this series were euthanized due to welfare parameters. The Cxxxx notation corresponds to the internal research group unique mouse identifier code. In this case, the mice C1263, C1264 and C1270 were studied. As it can been seen in Figure 26, TMZ-treated mice maintained satisfactory body weight during TMZ administration except by case C1270 that slightly descended below the 20% weight reduction after the fifth cycle, when it was euthanized.

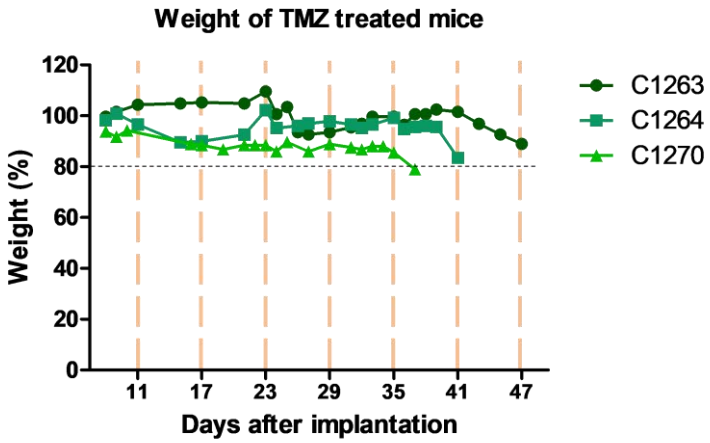

Figure 45: Body weight evolution of GL261 tumor-bearing mice during TMZ treatment with IMS protocol
Weight is expressed in %, assuming 100% for the weight at day 0; dashed horizontal black line indicates the 20% weight reduction point, below which animals must be euthanized due to welfare parameters. Dashed vertical yellow lines indicates the days of therapy administration.

4.3.2 Tumor volume evolution

The C57BL/6j mice were implanted with 10^5 cells of the glioma mouse line GL261 as described in the section 3.2.1. At days 7 and 11 p.i., high-resolution axial T2w MRI was acquired with the Bruker Biospec USR 70/30 (see section 3.2.4 for details) for tumoral volume assessment. The tumoral volumes were estimated by tracking the tumoral mass with Paravision 5.1 software (see section 3.2.4.3) and tumoral evolution for each individual mouse, as well as control mice evolution for comparison purposes, are shown in Figure 46. The tumor volume at therapy starting (day 11 p.i.) of the three mice investigated in this section was in average 6.0 ± 3.3 mm^3, similar to the average tumor volume of mice treated in [191] with metronomic TMZ at 60mg/kg, which was 6.0 ± 1.2 mm^3 at day 10 p.i. (p=0.97, no significant differences found between the tumor volume at the beginning of the therapy compared to previous results from the group).

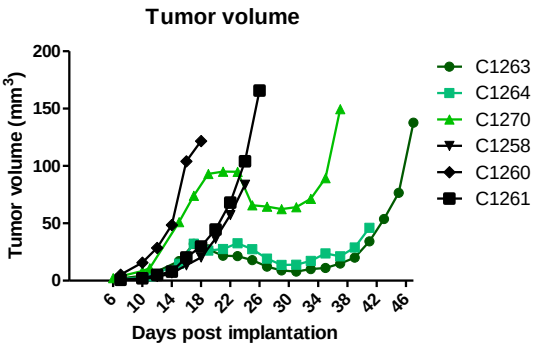

Figure 46: Tumor volume evolution for control, vehicle treated (n=3) and TMZ-treated GL261 tumor-bearing mice (n=3) (IMS protocol)
Tumor volumes were measured every 2 days starting at day 6 p.i.

4.3.3 Survival rate

In order to confirm that TMZ treatment with the IMS administration has a positive impact in the survival of GL261- bearing tumor mice, a Kaplan-Meier curve has been elaborated comparing the survival rate of control, vehicle treated (n=3) and TMZ-treated mice (n=3)

(Figure 38). The average survival rate for control mice was 22.5 ± 3.0 days whereas the TMZ-treated animals survived 42.0 ± 5.0 days ($p<0.05$ according to Log Rank (Mantel-Cox) Test), in line with results described in [85] in which IMS protocol for TMZ treatment overperformed the previously described 5-2-2 administration protocol [98].

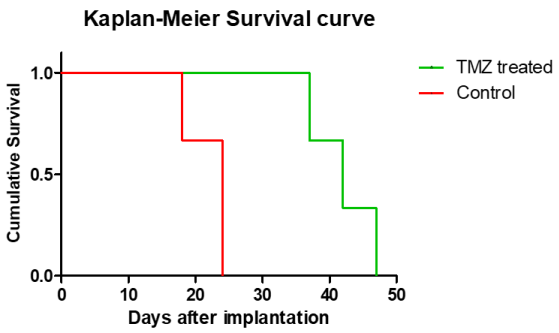

Figure 47: Kaplan-Meier survival curves for IMS TMZ-treated mice (n=3) and control mice (n=3).
Statistical differences were found between groups according to Log Rank test ($p<0.05$).

Furthermore, the average tumor volumes prior to treatment (at day 10 p.i.) were comparable between the control and TMZ-treated mice and no significant differences were found between groups ($p>0.05$). In few particular cases, the tumoral volume was not measured exactly at day 10 p.i., due to scanner schedule reasons. In these cases, the tumoral volume at day 10 p.i. was extrapolated using the tumoral volumes from prior and later days and the doubling time equation (Equation 3) from [100].

$$DT = \frac{(T_1 - T_0) \times ln2}{\ln(\frac{V_1}{V_0})} \qquad \text{(Equation 3)}$$

4.3.4 MRSI analysis: tumor responding index calculation along treatment

A longitudinal study was performed with the three TMZ-treated GL261 tumor-bearing mice (C1263, C1264 and C1270) and one control mouse (C1261) is also shown for comparison purposes. Mice were studied every two days by 3D like, multi-slice MRSI until endpoint in order to follow up metabolomic pattern changes along time and calculate the tumor responding index (TRI, see section 3.2.4.3 and [37]) at different longitudinal protocol time points. The starting of MRSI explorations was conditioned by the measured tumor volume. According to our experience and also data described by our group in [191], tumor volumes below 20 mm^3 are not properly segmented by MRSI, and this was the cut-off point to start MRSI acquisitions.

After TRI calculations, data were classified in arbitrary categories as described in section 3.2.4.3 and [37] according to the detected response level: high response cases (HR) and intermediate response cases (IR). Two out of three of the TMZ-treated cases analyzed were categorized as HR (C1264 at days 19 and 23 p.i. and C1270 at days 27, 29 and 33 p.i.), while the third case (C1263) was classified as an intermediate response (IR) case, although the maximum percentage of green tumor pixels was 63% at day 19 p.i. (close to the 65% boundary established to classify a case as HR). A more detailed description of each individual mouse evolution can be found below.

4.3.4.1. Case C1263

This tumor-bearing mouse was analyzed by T2w MRI and multi-slice MRSI from day 17 until day 47 p.i. when it was euthanized due to suffering symptoms and tumor mass effects (tumor volume at endpoint was 137.7 mm^3). A total of six TMZ cycles were administered with IMS protocol (every 6 days) from day 11 to day 41, right after the MRSI acquisition. In this case, the first cycle (time frame from 11 to 17 p.i.) was not monitored because MRI tumor volume measurements showed values not suitable for confident segmentation in nosological images generated from MRSI analysis (tumor volume below 20 mm^3). The next 5 cycles were monitored and TRI evolution is shown in Figure 48.

The tumor volume decreased from 32 mm^3 at day 17 p.i. until a minimum of 8 mm^3 at day 31 p.i. showing a behavior compatible with partial response according to adapted RECIST criteria [199], when it started increasing volume again and finally fully relapsed killing the mouse (Figure 48). In addition to tumor volume changes, Figure 48 show the evolution of TRI values along the follow-up period. According to the criteria stated in [37], this case should be classified as an intermediate response (IR) case, since the maximum TRI value analyzed was 63%, at day 29 p.i. As expected, data confirmed that TRI follows an oscillating pattern with limited length and which seem to be linked to therapy administration time points. In this sense, the first TRI maximum was detected at day 19 p.i. (8 days after the TMZ administration at day 11 p.i.), while the second TRI maximum was found at day 29 p.i. (6 day after the TMZ administration at day 23 p.i.), followed by a period below detection threshold, in which we cannot evaluate the TRI evolution due to the small size of the tumor (namely, day 31 to 37 p.i.). Finally, the last TRI increase is seen when tumor relapses from day 41 until day 45. It is worth noting that periodic cycling of TRI is seen during the period in which tumor is responding to therapy according to volume measurements (volume decrease or growth arrest, during days 19 to 31 p.i.).

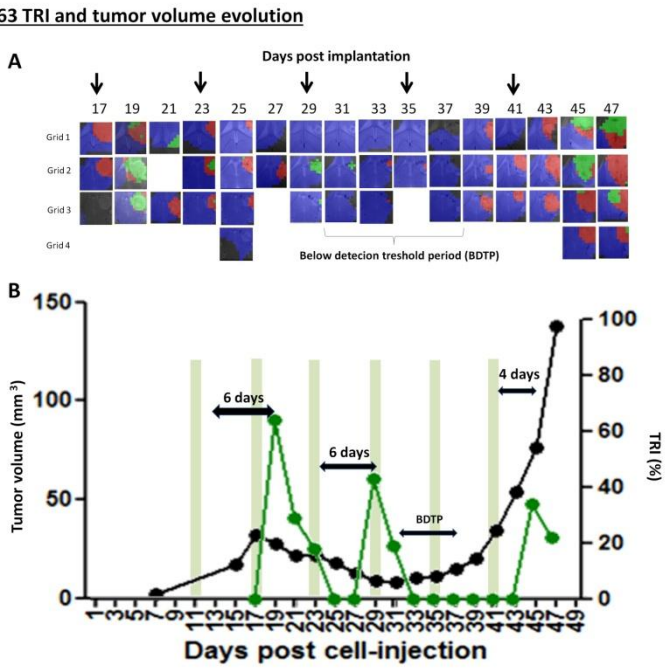

Figure 48: A) Nosological images and B) graphical representation of the tumor volume evolution for the tumor region in case C1263.
Tumor volume in mm^3 (black line, left axis) and the percentage of green, responding pixels (TRI) obtained taking into account total pixels counting (green line, right axis).

In A, chosen time points show the evolution of the nosological images in four rows of color-coded grids superimposed to the T2w-MRI for each slice. Vertical arrows indicate days of therapy administration. In B, green shaded columns indicate TMZ administration days. Two TRI peaks were observed with values of 64 and 43 % appearing 8 and 6 days respectively after TMZ administration. However, from days 34 to 43 it was not possible to evaluate TRI evolution because tumor volume was below the limit for confident MRSI segmentation, which we called below detection threshold period (BDTP). A last TRI increase is seen when the tumor is relapsing. It is worth nothing that during the response period, (classified as partial response according to adpated RECIST criteria), TRI peaks appear after TMZ administration time points with a frequency of 6.0 ±2.0 days.

This case was classified as partial response according to adapted RECIST criteria during the two TRI oscillating cycles (days 17 until 29 p.i.). During the below detection threshold period (days 33 till 37 p.i.), C1263 showed signs of progressive disease, since the tumor duplicated its size during this period. After day 39 p.i., tumor started to grow much faster, characterizing the relapse which caused animal death. A final TRI peak is seen during tumor relapse, at day 45 p.i., 4 days after the last given TMZ cycle.

Spectra acquired were of overall good quality and examples for case C1263 for chosen MRSI slices are shown below, also pointing to major metabolites present in spectra classified as normal brain parenchyma, actively proliferating tumor or responding tumor.

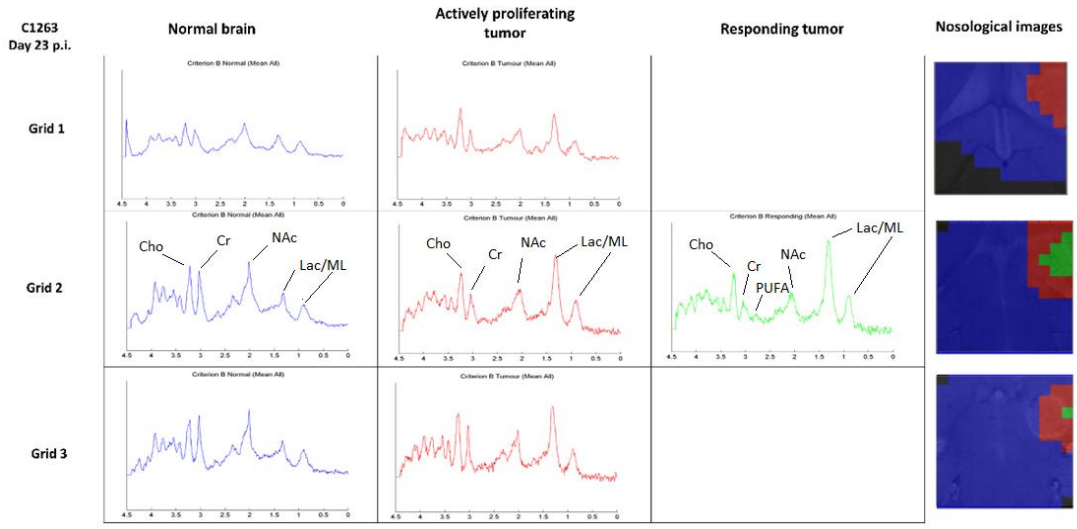

Figure 49: Examples of mean spectra calculated from chosen zones of nosological images classified as normal brain parenchyma, actively proliferating tumor and responding tumor in case C1263.

Normal brain is shown in blue (n=301 pixels), actively proliferating tumor in red (n=35) and responding tumor in green (n=9). Cho= choline, Cr= creatine, NAc= N-acetyl containing compounds, Lac= lactate, ML= mobile lipids. As expected, tumor zones present higher Cho/Cr and Cho/NAc ratio in comparison with normal brain parenchyma and higher Lac/ML signals. Still, responding zones present more noticeable 2.8 ppm signal, compatible with PUFA chemical shift.

One of the handicaps of this technique is that small sized tumors do not produce confident segmentation (e.g. at day 27 p.i. and days 33-37 p.i.) in which the tumor zone was mislabeled as normal brain parenchyma (blue) in 67-85% of the pixels (Figure 50).

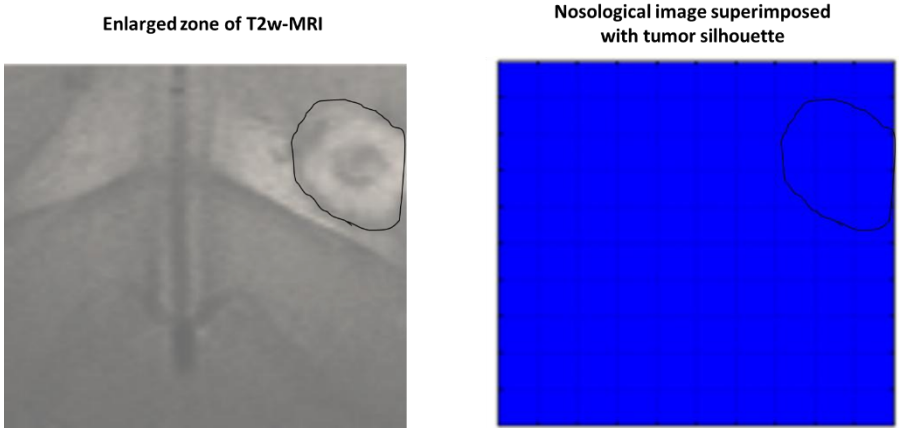

Figure 50: Example from the case 1263 in which the tumor was not recognized by the semisupervised system analysis due to its small size

Case C1263, (day 29 p.i., grid 1) showing one of the handicaps of the technique.
In the left side, the MRI image with the tumor surroundings in black. On the right, the nosological imaging mislabeled 'normal' blue over the tumor zone superimposed to the tumor silhouette

4.3.4.2 Case C1264

This tumor-bearing mouse was analyzed by T2w MRI and multi-slice MRSI from day 17 until day 41 p.i. At day 42 p.i. it was found dead in its cage although it did not meet any of the

endpoint criteria (weight loss not beyond 20%, no signs of suffering and tumor volume at day 41p.i. was 46.12 mm^3, which does not point to mass effect). A total of six TMZ cycles were administered with IMS protocol (every 6 days) from day 11 to day 41, right after MRSI acquisitions. As in the previous case, the first therapy cycle could not be MRSI-monitored due to its small value measured by T2w MRI, not enough for MRSI confident segmentation. The relationship between TRI and tumor volume evolution as well as the corresponding nosological images are shown in

Figure 51.

The oscillatory behavior of TRI was also present in this case with maximum values ranging 62-74%. The first TRI peak was observed after the second therapy cycle, at day 19 p.i. with subsequent peaks at days 23 and 29 p.i. (8, 6 and 6 days after TMZ administration points, respectively). It is also worth noting that two out of three TRI peaks corresponded to tumor volume decreases. Tumor volume measurements agree with stable disease (days 17 to 25) and partial response (days 27-33) and case was labeled as high response. From day 33 p.i. tumor started to regrow fast, being classified as progressive disease.

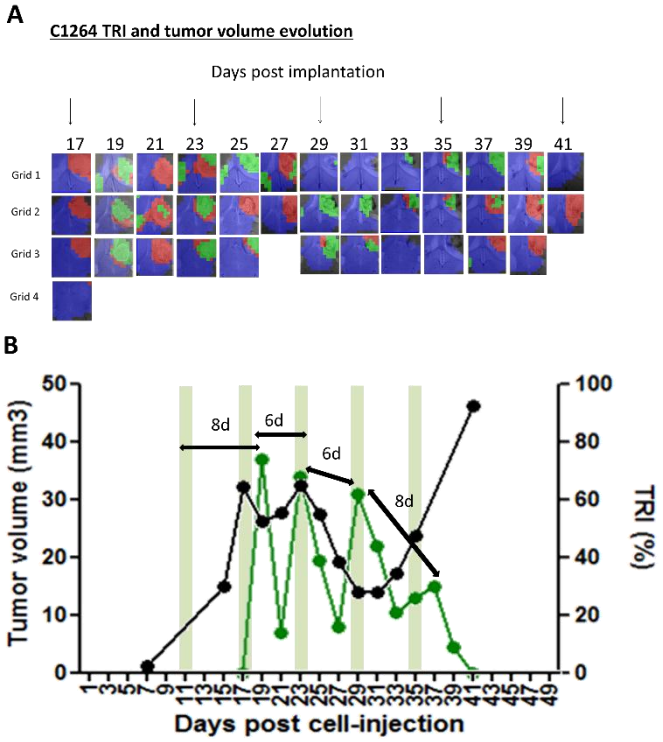

Figure 51: A) Nosological images and B) graphical representation of the tumor volume evolution for tumor area in case C1264. Tumor volume in mm^3 (black line, left axis) and the percentage of green, responding pixels obtained taking into account total pixels counting (green line, right axis)

In A, chosen time points show the evolution of the nosological images in four rows of color-coded grids superimposed to the T2w-MRI for each slice. Vertical arrows indicate days of therapy administration. In B, green

shaded columns indicate TMZ administration days. Three clear TRI peaks were observed during the transient response to therapy at days 19, 23 and 29 p.i.. TRI peaks (74, 62 and 62% respectively) occur after TMZ administration time points for a period of 7.0 ± 1.1 days. There is a final TRI increase (30%) during tumor regrowth-relapse.

4.3.4.3 Case C1270

This tumor-bearing mouse was analyzed by T2w MRI and multi-slice MRSI from day 15 until day 37 p.i., when it was euthanized due to welfare parameters with a tumor volume of 150 mm^3. A total of five TMZ cycles were administered with IMS protocol (every 6 days) from day 11 to day 35, right after MRSI acquisitions. In this case, the tumor volume was larger than in previous cases (range 60-90 mm^3 until relapsing point) and all five cycles could be monitored. Relationship between TRI and tumor volume as well as the corresponding nosological images are shown in Figure 52. Four TRI peaks were observed, three of them during transient response to therapy according to tumor volume measurements (days 17, 23, 29 and 33 p.i.) and appearing ca. 6 days after TMZ administration time points. Transient response took place after the third therapy cycle, as opposed to the previous cases, in which two cycles were enough to detect response, which probably explains the faster evolution and shorter survival of this mouse. During response, this case was classified as partial response according to adapted RECIST criteria (44% of tumor volume decrease), which in combination with high TRI values (average 67 ± 22 % in maximum points, achieving values of 90% at days 27 and 29 p.i.) allowed us to categorize this case as high response. However, after day 35, the tumor relapsed and started its fast regrowth.

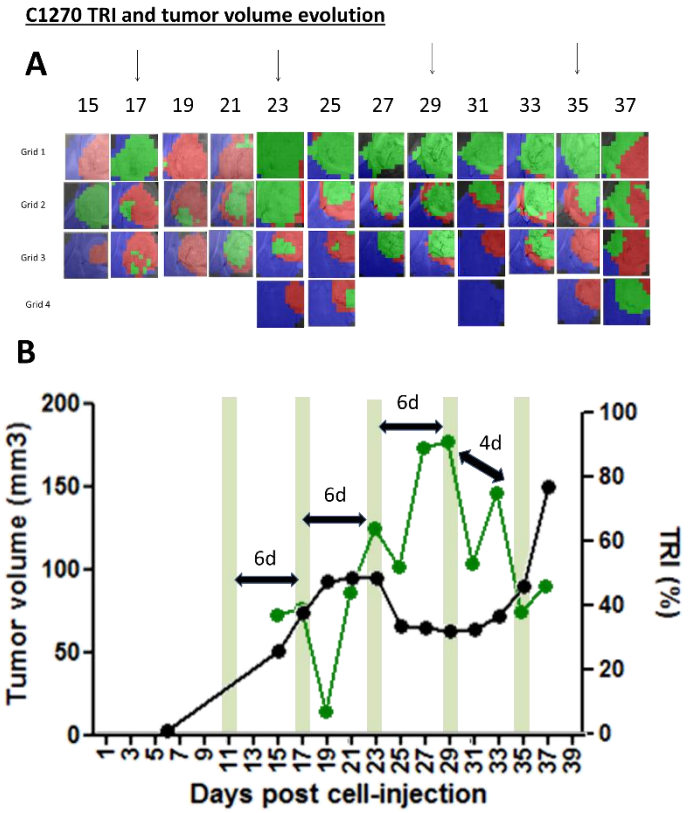

Figure 52: A) Nosological images and B) graphical representation of the tumor volume evolution for tumor area in case C1270. Tumor volume in mm^3 (black line, left axis) and the percentage of green, responding pixels obtained taking into account total pixels counting (green line, right axis)

In A, chosen time points show the evolution of the nosological images in four rows of color-coded grids superimposed to the T2w-MRI for each slice. Vertical arrows indicate days of therapy administration. In B, green shaded columns indicate TMZ administration days. Transient tumor response is only observed after the third therapy cycle in this case. Four TRI peaks were observed (at days 17, 23, 29 and 33 p.i.), three of them during the transient response to therapy. It is worth nothing that TRI peaks appear after *TMZ administration time points* with a frequency of *5.5 ± 1.0 days*.

4.3.4.4. Case 1261: Vehicle treated mouse

A control, vehicle treated mouse, was analyzed by T2w MRI and multi-slice MRSI every two days until euthanization to evaluate the TRI evolution of the mouse without treatment. The MRSI monitoring started at day 16 p.i. and finish at day 26 p.i., when the mouse had to be euthanized since the tumor volume was very big (165.73 mm^3). In Figure 53, the relationship between tumor volume and TRI is shown. As expected, tumor volume increased in an fast manner. Regarding TRI evolution, no oscillations are observed, only an increase with time: the more the tumor grows, the bigger is the TRI value. The fact that TRI increases in these cases may suggest that it is related to local changes that can also take place in a control subject but not enough, or not in a suitable timing, to eradicate tumor. For example, the presence of necrotic, non or low oxygenated areas that can cause cell death or the unspecific activation of the mouse immune system due to the high proliferation rate could cause metabolomic pattern changes similar to the ones produced in responding animals.

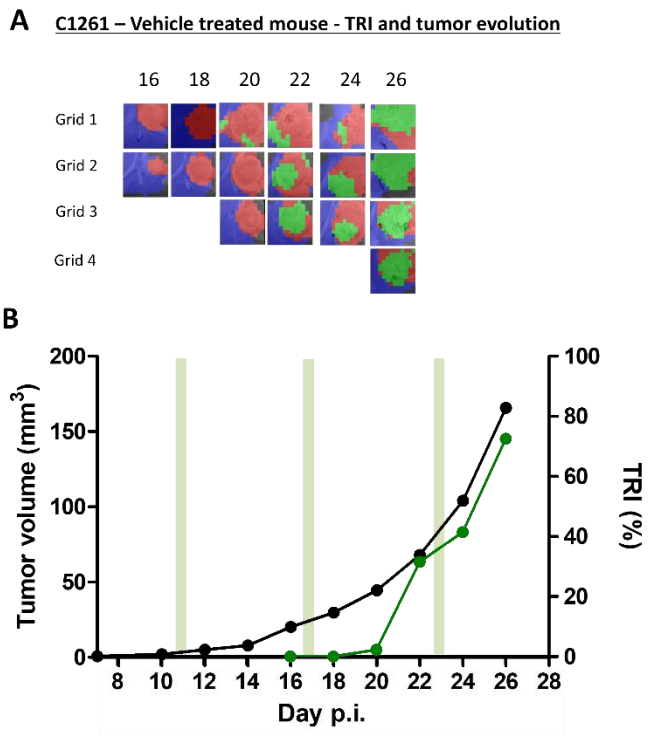

Figure 53: A) Nosological images and B) graphical representation of the tumor volume evolution for tumor area in the vehicle treated mouse C1261.
Tumor volume in mm^3 (black line, left axis) and the percentage of green, responding pixels obtained taking into account total pixels counting (green line, right axis)

In A, chosen time points show the evolution of the nosological images in four rows of color-coded grids superimposed to the T2w-MRI for each slice. Vertical arrows indicate days of vehicle administration. In B, green shaded columns indicate vehicle administration days. No TRI peaks or oscillation were observed, only a constant increase of TRI with tumor volume.

It is worth mentioning that the appearance of red pixels is more common at the periphery of the tumor (Figure 53, day 22 grids 2 and 3, day 24 grids 2 and 3 and day 26 grids 1, 3 and 4). The appearance of red pixels at the periphery of the tumor may underlie the fact that in these areas of the tumor, cells are proliferating fast, since the peripheral areas of the tumors are known to be well oxygenated and have wide access to nutrients.

4.3.5 Discussion

Three TMZ-treated tumor bearing mice and one control mouse were chosen to illustrate this section. Our group has a larger number of acquired cases and even cases of cured mice, but it was beyond the scope of this section to explore and explain all possible evolution types and specific details on each one. Results summarized here accomplish the goal of this section, which was to confirm the oscillating frequency of the response level detected in nosological images (TRI levels) due to changes in the metabolomic pattern. This was already shown in previous work with the standard 5-2-2 TMZ administration protocol and the multi-slice MRSI acquisition [37] and it was pending to confirm and validate in the IMS TMZ protocols of administration. Multi-slice MRSI acquisitions allowed us not only to detect TRI oscillations along the period of transient response to therapy, but also within the same tumor due to its

heterogeneity. The TMZ administration seems to be the responsible of “setting” cycles, since the period between therapy administration and appearance of a TRI peak is consistent along different cases, ranging 6-8 days in average during regular transient response periods, although in some last TRI peaks seen during tumor relapse, the time frame can be shorter (ca. 4 days). The average value for time distance recorded between TMZ administration and TRI peak appearance (being TRI peak average 71.4 ± 19% of all studied cases) is 6.2 ± 0.8 days.

Our working hypothesis, now supported by different experimental data from this thesis and other PhD thesis from our group, is that these TRI oscillations could be at least partially due to local metabolic changes resulting from immune system action within the tumor milieu. Our imaging biomarker was proven in previous work from our group [37, 98] to be correlated with the proliferation index Ki67, also reflecting changes related to the tumoral cells. However, it is known that up to 30% of the tumor mass area can be occupied by macrophages [35]. The MRSI acquisition is sampling the pattern of the whole studied zone, regardless if cells are from tumors or from the immune system, being logical to assume that local changes caused in the later should be also sampled by MRSI.

Results from TMZ-treated mice shown in this chapter (Cases C1263, C1264 and C1270) suggest that TMZ administration seems to “reset” the immune system cycle (see also Figure 3 in introduction, section 1.2.1), since TRI maximum peaks appear in average 6.2 ± 0.8 days after therapy administration (Figure 48, Figure 51,Figure 52). This value is in agreement with work published by our group with multi-slice MRSI acquisitions with a non-metronomic TMZ administration schedule (distance between TRI maxima, 6.3 ±1.3 days, n=4, [37]) and even with calculations approached with single-slice acquired cases (distance between TRI maxima, 6.2 ± 2.0 days, n=3 cases from [98]). This value is also in line with the length of immune cycle in mice brain, described to be of around 6 days [237]. Linking this finding with data presented in chapter 4.2, in which TMZ proved to trigger CRT exposure in GL261 cells in vitro, and taking into account that CRT is a potent immunogenic signal for immune system elicitation, we hypothesize that each TMZ cycle is triggering a new ‘turn’ of the immune cycle leading to an arrival of immune system cells within tumors ca. 6 days later, causing metabolomic pattern changes that are tackled by MRSI acquisitions followed by PR analysis and nosological imaging representation (scheme in Figure 54). This hypothesis is supported by histopathological findings, although obtained with non-optimal 5-2-2 TMZ cycles: TMZ-treated cases classified as high response reported in [37] presented a higher number of lymphocyte-like cells in tumor zone, and unpublished data from work in progress in our group showed significantly higher immunostaining for CD3 (lymphocytes presence) and Iba-1 (microglia/macrophages presence)

in tumor zones classified as “responding”, in comparison with control cases or “non-responding” areas.

Still, it is worth noting that TRI peak maxima are also accompanied, in some instances, by a reduction of the tumor volume characterizing either a partial response case (C1263 during the second and third TRI cycle, C1264 during the second TRI cycle and C1270 during the third therapy cycle) or stable disease (C1264 during the first TRI cycle). This reproducible behavior may underlie that high TRI is indicating an active anti-tumoral response triggered by the immunogenic potential of TMZ.

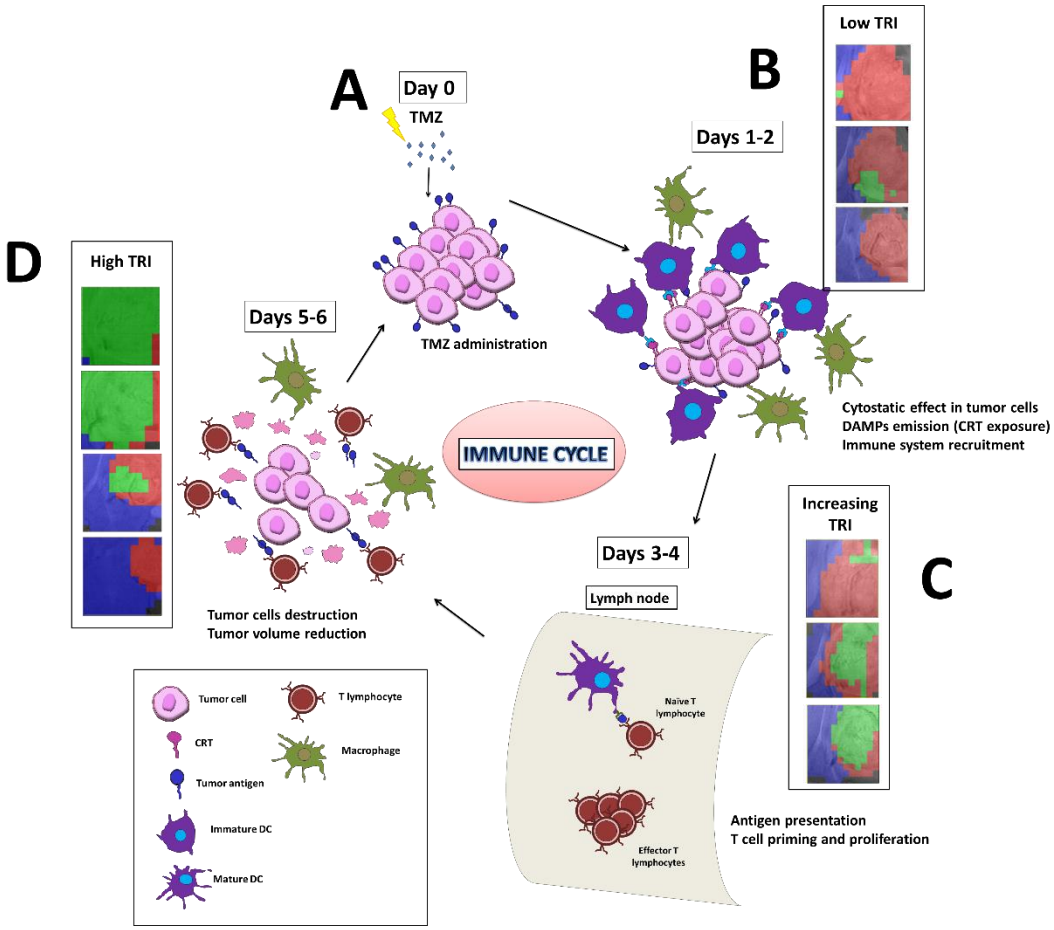

Figure 54: Hypothetic scheme of the cycle for immune response against a preclinical GB tumor after a therapy cycle and resulting nosological images using as example case C1270. The whole cycle is thought to last 6-7 days in mouse brain.

When treated with TMZ (A), tumor cells release and expose immunogenic signals, such as CRT (see 4.2.1) which attract DCs and macrophages to the tumor site. At this moment, the immune system is not active against these particular tumor cell clones and the nosological images correspond mostly to actively proliferating tumor. Due to TMZ action, proliferation of both tumor and immune cells is inhibited at this point, thus TRI is low (B). At days 3-4, DCs migrates to the lymph nodes and prime naïve CD8+ effector T cells, which start to proliferate. It is important that TMZ (or any antiproliferative agent) should not administered in this period because it would impair lymphocytes proliferation and hamper proper immune response. TRI may start increasing between day 4-6 (allowing for inter-subject variability) partially due to innate immune system action against tumor (C) [237]. *At days 5-6 of the cycle, effector T cells arrive at the tumor site and attack the tumor. In this period, we may observe a TRI peak and, in some instances, even reduction in tumor volume (D).*

Alkylating agents such as CPA and TMZ have been described to induce the immunogenic cell death of the tumor cells by activating the immune system through the exposure and emission of DAMPs, triggering the recruitment of the host immune system [20, 93, 238, 239] and this was indeed confirmed for TMZ in chapter 4.2, through increased exposure of CRT in GL261 treated cells *in vitro*. However, as relevant as eliciting the immune system is avoiding to impair its proper amplification. And here the Immuno-Enhanced Metronomic Schedule, IMS, gains importance. In the GL261 mouse model, TMZ produces a better survival rate when administered in a 6-day cycle [85] instead of in daily schedule of 5 consecutive days [240]. Alkylating agents, including TMZ, are known to induce side effects related to the immune system such as leukopenia and neutropenia, when administered daily [23]. If TMZ is administered in a continuous schedule, the anti-tumor immune cycle may be hampered due to the inhibition of the proliferation of immune cells, such as primed CD8+ T lymphocytes. On the other hand, in a metronomic administration schedule, TMZ would not interfere with the proliferation of immune cells, since the next TMZ dose is administered after the immune cycle of 6 days is completed. In addition to the beneficial effects related to immune system, this administration schedule also allows us to reduce the cumulative amount of administered TMZ and consequent development of tumors due to the mutagenic effects of TMZ, such as lymphomas. Still, if a translational protocol arrives to the clinical pipeline, the reduction of TMZ dosage should also reduce undesired side effects in patients.

The monitoring of TRI evolution could enable the design of personalized therapeutic schemes, adapting the TMZ therapy schedule in order to obtain an optimal anti-tumor effect. Once fully validated that the green pattern is associated with a productive action of host immune system against the tumor, its presence would mean that we may not apply a further TMZ cycle until TRI starts decreasing which would mean that a new, resistant clone of tumor cells is replacing cells killed by immune system action. The new TMZ administration would trigger a new turn in the immune system cycle and priming and amplification of lymphocytes would enable them to kill this new clone.

Results obtained in this study reinforce the idea of IMS TMZ as a good alternative for GB treatment. This hypothesis needs to be further validated by assessing the recruitment presence of the host immune system elements through histopathological validation during TRI maximum and minimum values, such as Iba-1 (microglia/activated macrophages), CD3 (T-lymphocytes) or FoxP3 (regulatory T lymphocytes), as well as specific markers for M1 and M2 macrophages (CD86, CD206 for M1 and M2 macrophages respectively). This would be of help

to understand better their potential contributions to the metabolomics pattern of responding and non- responding tumors.

It is worth mentioning that one of the most important limitations of this technique is related to tumor volume heterogeneity segmentation (lower limit ca. 20 mm^3), which hampers the proper evaluation of the tumor evolution by MRSI-based nosological images in small tumors, leading to lacking or incomplete information in cases with good response to treatment. Still, these results demonstrate how non-invasive methods based on PR analysis of MRSI acquisition can be applied in order to improve therapeutic success, making it possible to develop enhanced and personalized therapies based on metabolic information, which takes place before MRI volume-related changes.

Finally, if the relationship between TRI cycles and host immune system attraction for tumor fighting is fully confirmed, we should be also able to evaluate and quantify the response level in a combined treatment (e.g. synergistic TMZ + CX-4945), as well as to refine administration timing (see general discussion for insight of possible CK2 inhibitors effects in immune system cells). Our surrogate biomarker for therapy response, coded in nosological images from source-based analysis of acquired MRSI, was developed with TMZ-treated cases [98] and one of the fundamental questions was if it would be useful with other therapeutic agents. Indeed, it was also proven robust to detect tumor response in CPA-treated mice [191], suggesting that the changes sampled were not linked or restricted to TMZ, but were related to local changes taking place during different treatments, most probably related to immune system action against tumors which could be extremely valuable in tuning therapy administration to obtain the maximum effectiveness and improve outcome.

4.3.6 Conclusions

- TMZ administered in an IMS scheme (every 6 days) was confirmed to improve significantly GL261 tumor-bearing mice survival (42.0 ± 5.0 days vs 22.0 ± 3.5 days in control animals in the small cohort presented in this chapter), in agreement with work previously described by our group (38.7 ± 2.7 days vs 22.5 ± 1.2 days in control animals), outperforming also TMZ in the standard 5-2-2 scheme (33.9 ± 11.72) days.
- Nosological images generated from 3D like, multislice MRSI acquisitions were used for tumor responding index (TRI) calculation, which confirmed the presence of an oscillatory pattern. Maximum peaks appeared in average 6.2 ± 0.8 days after TMZ administration days. This period is in agreement with distance between TRI maxima previously detected by us with non-metronomic TMZ administration (oscillations with

6.3 ± 1.3 days frequency). This ca. 6 day period is also in agreement with the length of immune cycle activation in mice. The average TRI response level was higher with the IMS protocol 71.4 ± 19%. in comparison with levels described in [37], which were in average 51 ± 10.5%, considering high and intermediate response cases.

- TRI cycles with defined frequency took place mostly while GL261 tumors presented transient response to therapy ("partial response" or "stable disease" according to adapted RECIST criteria), suggesting an active response to therapy, until tumor started regrowing at 35 ± 3.5 days, finally leading to relapse.
- The oncological images generated through semi-supervised PR analysis of MRSI data confirmed their potential for noninvasive assessment of therapy response. The consistent periodicity of the detected changes in response level, in addition to results from chapter 4.2 regarding immunogenic signals production by TMZ and preliminary histopathological findings from our group support our hypothesis for those metabolomic pattern changes being due to immune system waves of activation causing tumor cell killing. Further histopathological validation, as well as high-resolution NMR investigation of the metabolomic changes in GL261 tumor samples are being currently performed and should help to better understand and characterize this phenomenon.

5. General discussion

5.1. GB therapy needs urgent improvement.

Glioblastoma (GB) is the most common and aggressive glial primary tumor with a survival average of 14–15 months, since the present therapeutic strategies available for GB are ineffective and tumor relapses [5]. New drugs and/or therapeutic schedules being investigated [22, 23, 25, 29] did not produce the expected results until this moment. Preclinical data showed, in addition, that the increase in the dose of mutagenic agents can lead to the development of other tumors, such as lymphomas [191], suggesting that the key for treatment improvement should lie either in non-mutagenic treatment strategies such as CK2 inhibition, or in improving the current administration schemes (e.g. using IMS) with standard chemotherapeutics, but avoiding dosage increases.

TMZ is the therapeutic treatment used for GB in the clinic. It is a mutagenic agent, not specific for tumor cells, which therefore can affect any proliferating cell, including the immune system cells, reflecting the main side effects described for this treatment. Results obtained in this thesis suggest that, at least for GL261 GB murine cells, TMZ acts as a cytostatic rather than cytotoxic agent, suggesting that its main beneficial effect in GL261 tumors should not be only related with direct cell killing. In the last years, cancer immunotherapy-related research has gained increased importance. In this respect, active immunotherapeutic strategies are being used [48, 51, 52, 241] but also chemotherapeutic agents administered in a schedule that respects the cycle of the antitumor immune response are being tried in preclinical models [93, 242–244] and even some conceptually similar approaches have been described for human patients [86] although only for a short time frame. At present, the clinical protocol involves daily administration of TMZ in the first treatment phase, which may not be respectful with the immune cycle and may be hampering effective anti-tumoral immune response. A change in the paradigm “the more, the better” is urgently needed and we need to see the “big picture” here: an immune - respectful therapeutic schedule needs to be implemented to improve outcome. Still, in addition to being respectful with immune system amplification cycles, a proper elicitation of the immune system is needed, with triggering of immunogenic cell death/damage. In this sense, TMZ proved to be a suitable agent for GL261 GB, triggering CRT exposure in vitro in cultured cells (section 4.2.1 for results, and also further discussion in section 5.4).

However, the mutagenic and non-specific action of TMZ could lead to the generation of secondary neoplasias, like lymphomas, even in an immune cycle respectful cycle if the

cumulative dose is high, as shown in [191]. In order to reduce as much as possible these effects, the combination with non-mutagenic therapies is therefore desirable. Among them, CK2 inhibitors could be a promising choice, and were shown to be synergistic with TMZ , as described in Section 4.2.3 and [85].

5.2. CK2 inhibition could be a candidate for GB therapy

CK2 is overexpressed in several types of cancer [146], including GB [149]. The inhibition of CK2 has been shown to inhibit several pro-survival signalling pathways such as PI3K/Akt [114], Wnt/β-catenin [115] or NFκβ [116].

Different CK2 inhibitors have been developed, and among them, one which was proven really promising was the ATP-competitive inhibitor CX-4945. Several studies have been successfully conducted with CX-4945 both *in vitro* with human cell lines from different types of cancer, including GB [168, 169] and *in vivo* with xenograft mice models from prostate cancer and GB [110]. This CK2 inhibitor even reached phase I and II clinical trials for cancer types such as myeloma[15] and it is now under current under study in combination with chemotherapy[16] (Gemcitabine) for cholangiocarcinoma. In addition, promising *in vitro* results with dual CK2/Pim-1 inhibitors could also be of interest for GB treatment. In this thesis, we used the immunocompetent GL261 GB model, which is widely used in preclinical studies for assessing standard and novel therapeutic approaches for GB for our group and other research groups worldwide [103, 188, 191, 193, 245]. Accordingly, in vitro experiments were performed with GL261 cells, the same line used for tumor generation.

In order to assess target effects of CK2 inhibitors in the GL261 model, CK2 activity and expression need to be evaluated. CK2 subunits expression and activity were analyzed in active proliferating, exponentially growing (EP) and in slow proliferating, postconfluent cells (PCP). Results showed that CK2α' is specifically downregulated in postconfluent, slowly proliferating GL261 cells. The differences between the expression of CK2 catalytic subunits (α and α') may be relevant for therapeutic success since CK2α and CK2α' specific inhibitors are being developed [167] and some CK2 inhibitors have a more potent effect over CK2α' subunits than in CK2α [165]. The availability of specific inhibitors could allow us to gain more specificity in treatment, differentially targeting cells in fast proliferation and quiescent cells, which would be relevant for GB treatment. This hypothesis may be addressed in the future if such specific inhibitors become available for *in vivo* work.

[15] https://clinicaltrials.gov/ct2/show/NCT00891280, https://clinicaltrials.gov/ct2/show/NCT01199718
[16] https://clinicaltrials.gov/ct2/show/NCT02128282

Two CK2 inhibitors have been evaluated in this Thesis for GB treatment: CX-4945 and TDB. CX-4945 has a well-defined pharmacokinetics profile [246], was – or is being – assessed in Phase I and II clinical trials, and it has been shown to have an anti-tumorigenic effect in GB xenografts growing in immunocompromised mice [110]. This beneficial effect observed in continuous administration to GB xenografts could be related to nude mice having increased NK cells content [91] to compensate for the lack of CTLs, and this NK cell activity against tumour xenografted cells being enhanced by CK2 inhibition such as described by [247].

On the other hand, results shown in this thesis and work from our group [85] with the GL261 immunocompetent model suggest that although CX-4945 is quite effective in vitro inhibiting GL261 cell viability, its effect *in vivo* is not beneficial at all if administered continuously, even reverting the beneficial effect from TMZ in joint treatments. As a generic antiproliferative, CX-4945 in a continuous administration would not only impair tumor cell proliferation, but also lymphocyte and macrophage proliferation, which could, at least partially, explain the poor results obtained in non-metronomic administration. The IMS administration produced only discrete improvement in tumor-bearing mice survival. Results obtained with IMS protocols (immune cycle respectful) and single CX-4945 administration described, for the first time to our knowledge, that CX-4945 treatment induce the release of a potent and well-known immunogenic signal, ATP (section 4.2.4.2), highlighting the immunogenic potential of CK2 inhibition, which was unknown until now. However, this single immunogenic signal could be insufficient to proper immune system elicitation.

This, in addition to some aspects described in the literature, should be further investigated in future work and can pave the way to a more sound application of CK2 inhibition as a therapeutic strategy for GB treatment, taking into account its effects and proper timing of application. For example, work described by [248] highlights CD163 (membrane scavenger receptor) which seems to signal through binding to CK2, increasing proliferation in glioma stem cells. Furthermore, CD163 seems to be a marker of M2-macrophages (protumoral phenotype, [249]) and in this sense, CK2 inhibition could even have a dual beneficial effect, over glioma stem cells and also over M2 macrophages with protumoral phenotype.

5.3. *In vitro* vs. *in vivo* tests in novel drugs: it is not always all what it seems

Novel therapeutic strategies are continuously being investigated, and GB is one of the examples of incurable conditions in which improvement is urgently needed. The first screenings, especially with large drug libraries, are done in vitro for a fast, achievable testing for selecting the best candidates. However, in vitro conditions are not able to fully mimic the *in*

vivo environment: the conventional cell monolayer cultures grown under unrealistic conditions regarding the physiology of real tissues. Factors such as tissue-specific architecture, mechanical/biochemical signals and cell-to-cell communication are not close to reality. Despite these drawbacks, monolayer cultures remain very attractive because of their simplicity and low cost. More realistic approaches such as 3D cultures are being studied (check for a review in [250]) but still, it is not straightforward to simulate the real *in vivo* situation and 3D culture approaches are not so widespread.

Moreover more authors have shown that the whole set of experiments (*in vitro* to preclinical *in vivo*) when investigating novel drugs in cancer [251, 252], performing *in vivo* experiments is more complex, more expensive, require higher amounts of drugs, more expertise, training and proper facilities, as well as authorization and toxicological preliminary tests than the *in vitro* part. Probably due to a combination of these reasons, the efficacy of some novel drugs is shown in vitro but *in vivo* information is lacking from many publications. Furthermore, the use of *in vivo* models that could produce overestimated results, such as subcutaneous murine tumor models, can also lead to failed clinical trials for some promising candidates found in preclinical studies.

Due to the challenge of simulating/modelling the immune system action of a living organism, some in vitro results provide us only part of the answer. In the case of TMZ, the results of the viability assays (showing a high IC_{50} estimation) could suggest a poor effect of the drug, at least in GL261 cells. However, the *in vivo* results showed a significant improvement in mice survival (Figure 31 and Figure 47). In chapter 4.2, we have analyzed the ability of different therapeutic agents to trigger ICD signals for immune system elicitation, showing that CRT exposure or ATP release could be the reasons behind the effects observed *in vivo* with these agents. In the future, *in situ in vivo* confirmation of the presence of these signals could fully validate these statements.

On the other hand, it is necessary to take into account than, even with a drug that displays a very potent effect in triggering cell death of cancer cells, if the administration schedule is not adequate and hampers immune system elicitation or action, the outcome will be unsatisfactory. The same situation can take place in drug combination studies. When assessing the synergistic or antagonistic action of two drugs *in vitro*, a word of caution should be raised because there are many factors *in vivo* that cannot be mimicked in cultured cells, for example differences in bioavailability, the ability of membrane crossing or dispersion coefficient and differences in half-life. In summary, before either reaching positive or negative conclusions

regarding drug action or combination looking only to *in vitro* data, studies with suitable preclinical models, such as immunocompetent models, should be considered.

The dual CK2 and Pim-1 inhibitor TDB has a very potent action in diminish cellular viability of GL261 cells in vitro (see section 4.1.2) but its poor and unclear pharmacokinetics profile prevented us to reach conclusions about its potential for GL261 GB treatment. At this point, we considered that until their properties of solubility/absorption were improved, it was not a good alternative to proceed with *in vivo* studies.

5.4. The participation of immune system in therapy response

The role of the immune system has been shown to be crucial to obtain a positive outcome in anticancer therapy [57, 243, 253–256]. In order to trigger the immune system action against the tumor, the exposure and/or release of the so-called DAMPs is crucial to signal immunogenic cell death/damage and elicit the immune system. The most relevant DAMPs described so far are CRT exposure [58, 63, 64] , ATP [67, 257] and HMGB1 [73, 75]. Still, many other DAMPs have been described such as HSP90 and HSP70 exposure and release, uric acid crystals and genomic DNA [77–80].

In preclinical GB models, the action of the immune system has been shown to be relevant for tumor regression and overall outcome. The combined action of TMZ with the adenovirus Delta 24-RGD has been shown to trigger a CD4+ and CD8+ dependent antitumor response in the GL261 model [225]. Moreover, the antitumoral immune response can be modulated through Magnetic Resonance image-guided focused ultrasound which is able to yield sub-ablative hyperthermia [258], in addition to several other examples cited along this thesis such as [103] and [84, 244].

The lack of early and robust, noninvasive image-based biomarkers for response to therapy GB hampers the proper follow-up and prevents early informed decisions about therapy switch or combination which could improve patient outcome and overall survival. Current procedures are based mostly in MRI and are not exempt of inaccuracy in some instances [259]. Still, some so-called “minimally invasive” approaches as liquid biopsy are being studied for brain tumor response follow-up [260] but there is still much room for improvement, and regarding the modality of cerebrospinal fluid collection, it is not exempt of risks. For this reason, a confident and early noninvasive MR-based biomarker which could reflect the effectiveness of a given therapy within the tumor milieu (for example, sampling in real time the immune system activity) would be relevant in the management of glioblastoma patients. MR-based approaches

are feasible in most hospital scanners and additional explorations could be easily incorporated in the follow-up pipeline if they are proven valuable in patient monitoring.

5.5. *In vivo* "imaging" of immune system participation in therapy response.

Provided that the suitable use of therapy strategies able to trigger ICD in an immune-friendly cycle can elicit immune system to fight tumor, it is relevant to have a non-invasive way to monitor these changes (see section 4.3). Data from our group suggest that the observed changes in the MRSI spectral pattern, unraveled through pattern recognition studies, could be related to immune system action and also have relationships with decrease in local proliferation measured by Ki67 [37, 98, 188].

If the changes observed in MRSI-based nosological images of response to therapy are fully validated to be related to immune system action within tumors, they could be used for personalization of therapy administration and early decision on second lines or therapy combination schedules if a lack of response is detected (for example, with reappearance of red, unresponsive pattern not followed by subsequent responding pattern increase). In addition, the rich information contained in MRI could also be integrated in pattern recognition studies, which is currently being explored for some authors [261], and it could be relevant because some imaging features such as oedema is being described as a sign of therapy success, particularly when immune system activation is involved [262, 263], a feature also observed in studies from our group in mice responding to IMS therapy [191].

Final conclusion:

The use of immune system respectful cycles for therapy administration (such as IMS), should improve outcome of GL261 GB treated mice due to proper immune system elicitation towards the tumor. For this, it is relevant to ensure that therapeutic agents are able to trigger ICD signaling and timing is carefully chosen, especially in joint therapy with more than one therapeutic agent: chemotherapy and non-mutagenic approaches such as CK2 inhibition. Finally, the ability of non-invasive, early monitoring of response to therapy through immune system-related changes, locally in the tumor tissue, should certainly improve mice outcome and could have a great translational interest in the future.

6. References

1. Ferlay J, Soerjomataram I, Dikshit R, Eser S, Mathers C, Rebelo M, Parkin DM, Forman D, Bray F (2015) Cancer incidence and mortality worldwide: Sources, methods and major patterns in GLOBOCAN 2012. Int J Cancer 136:E359–E386.

2. Louis DN, Perry A, Reifenberger G, Deimling A Von, Figarella D, Webster B, Hiroko KC, Wiestler OD, Kleihues P, Ellison DW (2016) The 2016 World Health Organization Classification of Tumors of the Central Nervous System : a summary. Acta Neuropathol 131:803–820.

3. Rouse C, Gittleman H, Ostrom QT, Kruchko C, Barnholtz-Sloan JS (2016) Years of potential life lost for brain and CNS tumors relative to other cancers in adults in the United States, 2010. Neuro Oncol 18:70–77.

4. Ostrom QT, Gittleman H, Stetson L, Virk SM, Barnholtz-Sloan JS (2015) Epidemiology of Gliomas. Springer, Cham, pp 1–14

5. Stupp R, Mason WP, van den Bent MJ, Weller M, Fisher B, Taphoorn MJB, Belanger K, Brandes AA, Marosi C, Bogdahn U, Curschmann J, Janzer RC, Ludwin SK, Gorlia T, Allgeier A, Lacombe D, Cairncross JG, Eisenhauer E, Mirimanoff RO, Groups EO for R and T of CBT and R, Group NCI of CCT (2005) Radiotherapy plus concomitant and adjuvant temozolomide for glioblastoma. N Engl J Med 352:987–996.

6. Hadjipanayis CG, Widhalm G, Stummer W (2015) What is the Surgical Benefit of Utilizing 5-Aminolevulinic Acid for Fluorescence-Guided Surgery of Malignant Gliomas? Neurosurgery 77:663–73.

7. Ostrom QT, Gittleman H, Fulop J, Liu M, Blanda R, Kromer C, Wolinsky Y, Kruchko C, Barnholtz-Sloan JS (2015) CBTRUS Statistical Report: Primary Brain and Central Nervous System Tumors Diagnosed in the United States in 2008-2012. Neuro Oncol 17:iv1-iv62.

8. Sologuren I, Rodríguez-Gallego C, Lara PC (2014) Immune effects of high dose radiation treatment: implications of ionizing radiation on the development of bystander and abscopal effects. Transl Cancer Res 3:18–31.

9. Weichselbaum RR, Liang H, Deng L, Fu Y-X (2017) Radiotherapy and immunotherapy: a beneficial liaison? Nat Rev Clin Oncol 14:365–379.

10. Barani IJ, Larson DA (2015) Radiation Therapy of Glioblastoma. Cancer Treat Res 163:49–73.

11. Tsang LLH, Farmer PB, Gescher A, Slack JA (1990) Characterisation of urinary metabolites of temozolomide in humans and mice and evaluation of their cytotoxicity. Cancer Chemother Pharmacol 26:429–436.

12. Honasoge A, Sontheimer H (2013) Involvement of tumor acidification in brain cancer pathophysiology. Front Physiol 4:316.

13. Denny BJ, Wheelhouse RT, Stevens MF, Tsang LL, Slack JA (1994) NMR and molecular modeling investigation of the mechanism of activation of the antitumor drug temozolomide and its interaction with DNA. Biochemistry 33:9045–51.

14. Yoshimoto K, Mizoguchi M, Hata N, Murata H, Hatae R, Amano T, Nakamizo A, Sasaki T (2012) Complex DNA repair pathways as possible therapeutic targets to overcome

temozolomide resistance in glioblastoma. Front Oncol 2:186.

15. Mojas N, Lopes M, Jiricny J (2007) Mismatch repair-dependent processing of methylation damage gives rise to persistent single-stranded gaps in newly replicated DNA. Genes Dev 21:3342–3355.

16. Perazzoli G, Prados J, Ortiz R, Caba O, Cabeza L, Berdasco M, Gónzalez B, Melguizo C (2015) Temozolomide Resistance in Glioblastoma Cell Lines: Implication of MGMT, MMR, P-Glycoprotein and CD133 Expression. PLoS One 10:e0140131.

17. Roos WP, Batista LFZ, Naumann SC, Wick W, Weller M, Menck CFM, Kaina B (2007) Apoptosis in malignant glioma cells triggered by the temozolomide-induced DNA lesion O6-methylguanine. Oncogene 26:186–197.

18. Kanzawa T, Germano IM, Komata T, Ito H, Kondo Y, Kondo S (2004) Role of autophagy in temozolomide-induced cytotoxicity for malignant glioma cells. Cell Death Differ 11:448–457.

19. D'Atri S, Tentori L, Lacal PM, Graziani G, Pagani E, Benincasa E, Zambruno G, Bonmassar E, Jiricny J (1998) Involvement of the mismatch repair system in temozolomide-induced apoptosis. Mol Pharmacol 54:334–41.

20. Kim T-G, Kim C-H, Park J-S, Park S-D, Kim CK, Chung D-S, Hong Y-K (2010) Immunological factors relating to the antitumor effect of temozolomide chemoimmunotherapy in a murine glioma model. Clin Vaccine Immunol 17:143–53.

21. Curtin JF, Liu N, Candolfi M, Xiong W, Assi H, Yagiz K, Edwards MR, Michelsen KS, Kroeger KM, Liu C, Muhammad AKMG, Clark MC, Arditi M, Comin-Anduix B, Ribas A, Lowenstein PR, Castro MG (2009) HMGB1 Mediates Endogenous TLR2 Activation and Brain Tumor Regression. PLoS Med 6:e1000010.

22. Darlix A, Baumann C, Lorgis V, Ghiringhelli F, Blonski M, Chauffert B, Zouaoui S, Pinelli C, Rech F, Beauchesne P, Taillandier L (2013) Prolonged administration of adjuvant temozolomide improves survival in adult patients with glioblastoma. Anticancer Res 33:3467–74.

23. Gilbert MR, Wang M, Aldape KD, Stupp R, Hegi ME, Jaeckle KA, Armstrong TS, Wefel JS, Won M, Blumenthal DT, Mahajan A, Schultz CJ, Erridge S, Baumert B, Hopkins KI, Tzuk-Shina T, Brown PD, Chakravarti A, Curran WJ, Mehta MP (2013) Dose-dense temozolomide for newly diagnosed glioblastoma: a randomized phase III clinical trial. J Clin Oncol 31:4085–91.

24. Chamberlain M, Rhun E, Taillibert S, Chamberlain MC (2015) The future of high-grade glioma: Where we are and where are we going. Surg Neurol Int 6:9.

25. Xue S, Hu M, Iyer V, Yu J (2017) Blocking the PD-1/PD-L1 pathway in glioma: a potential new treatment strategy. J Hematol Oncol 10:81.

26. Vanan MI, Eisenstat DD (2014) Management of high-grade gliomas in the pediatric patient: Past, present, and future. Neuro-oncology Pract 1:145–157.

27. Luchman HA, Stechishin ODM, Nguyen SA, Lun XQ, Cairncross JG, Weiss S (2014) Dual mTORC1/2 blockade inhibits glioblastoma brain tumor initiating cells in Vitro and in Vivo and synergizes with temozolomide to increase orthotopic xenograft survival. Clin Cancer Res 20:5756–5767.

28. Stupp R, Taillibert S, Kanner AA, Kesari S, Steinberg DM, Toms SA, Taylor LP, Lieberman F, Silvani A, Fink KL, Barnett GH, Zhu J-J, Henson JW, Engelhard HH, Chen TC, Tran DD, Sroubek J, Tran ND, Hottinger AF, Landolfi J, Desai R, Caroli M, Kew Y, Honnorat J, Idbaih A, Kirson ED, Weinberg U, Palti Y, Hegi ME, Ram Z (2015) Maintenance Therapy With Tumor-Treating Fields Plus Temozolomide vs Temozolomide Alone for Glioblastoma. JAMA 314:2535.

29. Abdul KU, Houweling M, Svensson F, Narayan RS, Cornelissen FMG, Küçükosmanoglu A, Metzakopian E, Watts C, Bailey D, Wurdinger T, Westerman BA (2018) WINDOW consortium: A path towards increased therapy efficacy against glioblastoma. Drug Resist Updat 40:17–24.

30. Alphandéry E (2018) Glioblastoma Treatments: An Account of Recent Industrial Developments. Front Pharmacol 9:879.

31. Scharovsky OG, Mainetti LE, Rozados VR (2009) Metronomic chemotherapy: changing the paradigm that more is better. Curr Oncol 16:7–15.

32. Casals E, Gusta MF, Cobaleda-Siles M, Garcia-Sanz A, Puntes VF (2017) Cancer resistance to treatment and antiresistance tools offered by multimodal multifunctional nanoparticles. Cancer Nanotechnol 8:7.

33. Chen DS, Mellman I (2013) Oncology Meets Immunology: The Cancer-Immunity Cycle. Immunity 39:1–10.

34. Haabeth OAW, Tveita AA, Fauskanger M, Schjesvold F, Lorvik KB, Hofgaard PO, Omholt H, Munthe LA, Dembic Z, Corthay A, Bogen B (2014) How Do CD4+ T Cells Detect and Eliminate Tumor Cells That Either Lack or Express MHC Class II Molecules? Front Immunol 5:174.

35. Glass R, Synowitz M (2014) CNS macrophages and peripheral myeloid cells in brain tumours. Acta Neuropathol 128:347–362.

36. Sica A, Mantovani A (2012) Macrophage plasticity and polarization: in vivo veritas. J Clin Invest 122:787–795.

37. Arias-Ramos N, Ferrer-Font L, Lope-Piedrafita S, Mocioiu V, Julià-Sapé M, Pumarola M, Arús C, Candiota A (2017) Metabolomics of Therapy Response in Preclinical Glioblastoma: A Multi-Slice MRSI-Based Volumetric Analysis for Noninvasive Assessment of Temozolomide Treatment. Metabolites 7:20.

38. Jackson C, Ruzevick J, Phallen J, Belcaid Z, Lim M (2011) Challenges in Immunotherapy Presented by the Glioblastoma Multiforme Microenvironment. Clin Dev Immunol 2011:1–20.

39. Humphries W, Wei J, Sampson JH, Heimberger AB (2010) The role of tregs in glioma-mediated immunosuppression: potential target for intervention. Neurosurg Clin N Am 21:125–37.

40. Domenis R, Cesselli D, Toffoletto B, Bourkoula E, Caponnetto F, Manini I, Beltrami AP, Ius T, Skrap M, Di Loreto C, Gri G (2017) Systemic T Cells Immunosuppression of Glioma Stem Cell-Derived Exosomes Is Mediated by Monocytic Myeloid-Derived Suppressor Cells. PLoS One 12:e0169932.

41. Gebremeskel S, Johnston B (2015) Concepts and mechanisms underlying chemotherapy

induced immunogenic cell death: impact on clinical studies and considerations for combined therapies. Oncotarget 6:41600–19.

42. Stupp R, Hegi ME, Mason WP, van den Bent MJ, Taphoorn MJ, Janzer RC, Ludwin SK, Allgeier A, Fisher B, Belanger K, Hau P, Brandes AA, Gijtenbeek J, Marosi C, Vecht CJ, Mokhtari K, Wesseling P, Villa S, Eisenhauer E, Gorlia T, Weller M, Lacombe D, Cairncross JG, Mirimanoff R-O, European Organisation for Research and Treatment of Cancer Brain Tumour and Radiation Oncology Groups, National Cancer Institute of Canada Clinical Trials Group (2009) Effects of radiotherapy with concomitant and adjuvant temozolomide versus radiotherapy alone on survival in glioblastoma in a randomised phase III study: 5-year analysis of the EORTC-NCIC trial. Lancet Oncol 10:459–466.

43. Galluzzi L, Vacchelli E, Bravo-San Pedro J-M, Buqué A, Senovilla L, Baracco EE, Bloy N, Castoldi F, Abastado J-P, Agostinis P, Apte RN, Aranda F, Ayyoub M, Beckhove P, Blay J-Y, Bracci L, Caignard A, Castelli C, Cavallo F, Celis E, Cerundolo V, Clayton A, Colombo MP, Coussens L, Dhodapkar M V, Eggermont AM, Fearon DT, Fridman WH, Fučíková J, Gabrilovich DI, Galon J, Garg A, Ghiringhelli F, Giaccone G, Gilboa E, Gnjatic S, Hoos A, Hosmalin A, Jäger D, Kalinski P, Kärre K, Kepp O, Kiessling R, Kirkwood JM, Klein E, Knuth A, Lewis CE, Liblau R, Lotze MT, Lugli E, Mach J-P, Mattei F, Mavilio D, Melero I, Melief CJ, Mittendorf EA, Moretta L, Odunsi A, Okada H, Palucka AK, Peter ME, Pienta KJ, Porgador A, Prendergast GC, Rabinovich GA, Restifo NP, Rizvi N, Sautès-Fridman C, Schreiber H, Seliger B, Shiku H, Silva-Santos B, Smyth MJ, Speiser DE, Spisek R, Srivastava PK, Talmadge JE, Tartour E, Van Der Burg SH, Van Den Eynde BJ, Vile R, Wagner H, Weber JS, Whiteside TL, Wolchok JD, Zitvogel L, Zou W, Kroemer G (2014) Classification of current anticancer immunotherapies. Oncotarget 5:12472–508.

44. Razavi S-M, Lee KE, Jin BE, Aujla PS, Gholamin S, Li G (2016) Immune Evasion Strategies of Glioblastoma. Front Surg 3:11.

45. Hoption Cann SA, van Netten JP, van Netten C (2003) Dr William Coley and tumour regression: a place in history or in the future. Postgrad Med J 79:672–80.

46. Graham JB, Graham RM (1959) The effect of vaccine on cancer patients. Surg Gynecol Obstet 109:131–8.

47. Talpaz M, McCredie KB, Mavligit GM, Gutterman JU (1983) Leukocyte interferon-induced myeloid cytoreduction in chronic myelogenous leukemia. Blood 62:689–92.

48. Ishikawa E, Yamamoto T, Matsumura A (2017) Prospect of Immunotherapy for Glioblastoma: Tumor Vaccine, Immune Checkpoint Inhibitors and Combination Therapy. Neurol Med Chir (Tokyo) 57:321–330.

49. Morgan RA, Johnson LA, Davis JL, Zheng Z, Woolard KD, Reap EA, Feldman SA, Chinnasamy N, Kuan C-T, Song H, Zhang W, Fine HA, Rosenberg SA (2012) Recognition of Glioma Stem Cells by Genetically Modified T Cells Targeting EGFRvIII and Development of Adoptive Cell Therapy for Glioma. Hum Gene Ther 23:1043–1053.

50. Wong ET, Timmons J, Callahan A, O'Loughlin L, Giarusso B, Alsop DC (2016) Phase I study of low-dose metronomic temozolomide for recurrent malignant gliomas. BMC Cancer 16:914.

51. Hodi FS, O'Day SJ, McDermott DF, Weber RW, Sosman JA, Haanen JB, Gonzalez R, Robert C, Schadendorf D, Hassel JC, Akerley W, van den Eertwegh AJM, Lutzky J, Lorigan P, Vaubel JM, Linette GP, Hogg D, Ottensmeier CH, Lebbé C, Peschel C, Quirt I, Clark JI, Wolchok JD,

Weber JS, Tian J, Yellin MJ, Nichol GM, Hoos A, Urba WJ (2010) Improved survival with ipilimumab in patients with metastatic melanoma. N Engl J Med 363:711–23.

52. Sadelain M, Brentjens R, Rivière I, Park J (2015) CD19 CAR Therapy for Acute Lymphoblastic Leukemia. Am Soc Clin Oncol Educ B 35:e360–e363.

53. Kantoff PW, Higano CS, Shore ND, Berger ER, Small EJ, Penson DF, Redfern CH, Ferrari AC, Dreicer R, Sims RB, Xu Y, Frohlich MW, Schellhammer PF, IMPACT Study Investigators (2010) Sipuleucel-T Immunotherapy for Castration-Resistant Prostate Cancer. N Engl J Med 363:411–422.

54. Michot JM, Bigenwald C, Champiat S, Collins M, Carbonnel F, Postel-Vinay S, Berdelou A, Varga A, Bahleda R, Hollebecque A, Massard C, Fuerea A, Ribrag V, Gazzah A, Armand JP, Amellal N, Angevin E, Noel N, Boutros C, Mateus C, Robert C, Soria JC, Marabelle A, Lambotte O (2016) Immune-related adverse events with immune checkpoint blockade: a comprehensive review. Eur J Cancer 54:139–148.

55. Bonifant CL, Jackson HJ, Brentjens RJ, Curran KJ (2016) Toxicity and management in CAR T-cell therapy. Mol Ther - Oncolytics 3:16011.

56. Kroemer G, Galluzzi L, Kepp O, Zitvogel L (2013) Immunogenic Cell Death in Cancer Therapy. Annu Rev Immunol 31:51–72.

57. Garg AD, Martin S, Golab J, Agostinis P (2014) Danger signalling during cancer cell death: origins, plasticity and regulation. Cell Death Differ 21:26–38.

58. Garg AD, Krysko D V, Verfaillie T, Kaczmarek A, Ferreira GB, Marysael T, Rubio N, Firczuk M, Mathieu C, Roebroek AJM, Annaert W, Golab J, Witte P De, Vandenabeele P, Agostinis P (2012) A novel pathway combining calreticulin exposure and ATP secretion in immunogenic cancer cell death. EMBO J 31:1062–1079.

59. Garg AD, Kaczmarek A, Krysko O, Vandenabeele P, Krysko D V., Agostinis P (2012) ER stress-induced inflammation: does it aid or impede disease progression? Trends Mol Med 18:589–598.

60. Garg AD, Martin S, Golab J, Agostinis P (2014) Danger signalling during cancer cell death: origins, plasticity and regulation. Cell Death Differ 21:26–38.

61. Dudek AM, Garg AD, Krysko D V., De Ruysscher D, Agostinis P (2013) Inducers of immunogenic cancer cell death. Cytokine Growth Factor Rev 24:319–333.

62. Gardai SJ, McPhillips KA, Frasch SC, Janssen WJ, Starefeldt A, Murphy-Ullrich JE, Bratton DL, Oldenborg P-A, Michalak M, Henson PM (2005) Cell-surface calreticulin initiates clearance of viable or apoptotic cells through trans-activation of LRP on the phagocyte. Cell 123:321–34.

63. Colangelo T, Polcaro G, Ziccardi P, Muccillo L, Galgani M, Pucci B, Milone MR, Budillon A, Santopaolo M, Mazzoccoli G (2016) The miR-27a-calreticulin axis affects drug-induced immunogenic cell death in human colorectal cancer cells. Nat Publ Gr 7:1–11.

64. Hong C, Qiu X, Li Y, Huang Q, Zhong Z, Zhang Y, Liu X, Sun L, Lv P, Gao X-M (2010) Functional Analysis of Recombinant Calreticulin Fragment 39-272: Implications for Immunobiological Activities of Calreticulin in Health and Disease. J Immunol 185:4561–4569.

65. Li Y, Zeng X, He L, Yuan H (2015) Dendritic cell activation and maturation induced by recombinant calreticulin fragment 39-272. Int J Clin Exp Med 8:7288–96.

66. Krysko D V, Garg AD, Kaczmarek A, Krysko O (2012) Immunogenic cell death and DAMPs in cancer therapy. Nat Rev Cancer 12:860–875.

67. Dichmann S, Idzko M, Zimpfer U, Hofmann C, Ferrari D, Luttmann W, Virchow C, Di Virgilio F, Norgauer J (2000) Adenosine triphosphate-induced oxygen radical production and CD11b up-regulation: Ca(++) mobilization and actin reorganization in human eosinophils. Blood 95:973–8.

68. Burnstock G (2013) Introduction to Purinergic Signalling in the Brain. Adv. Exp. Med. Biol. pp 1–12

69. Di Virgilio F, Sarti AC, Grassi F (2018) Modulation of innate and adaptive immunity by P2X ion channels. Curr Opin Immunol 52:51–59.

70. Faas MM, Sáez T, de Vos P (2017) Extracellular ATP and adenosine: The Yin and Yang in immune responses? Mol Aspects Med 55:9–19.

71. Ghiringhelli F, Apetoh L, Tesniere A, Aymeric L, Ma Y, Ortiz C, Vermaelen K, Panaretakis T, Mignot G, Ullrich E, Perfettini J-L, Schlemmer F, Tasdemir E, Uhl M, Génin P, Civas A, Ryffel B, Kanellopoulos J, Tschopp J, André F, Lidereau R, McLaughlin NM, Haynes NM, Smyth MJ, Kroemer G, Zitvogel L (2009) Activation of the NLRP3 inflammasome in dendritic cells induces IL-1β–dependent adaptive immunity against tumors. Nat Med 15:1170–1178.

72. la Sala A, Ferrari D, Corinti S, Cavani A, Di Virgilio F, Girolomoni G (2001) Extracellular ATP induces a distorted maturation of dendritic cells and inhibits their capacity to initiate Th1 responses. J Immunol 166:1611–7.

73. Lotze MT, Tracey KJ (2005) High-mobility group box 1 protein (HMGB1): nuclear weapon in the immune arsenal. Nat Rev Immunol 5:331–342.

74. Harris HE, Andersson U, Pisetsky DS (2012) HMGB1: A multifunctional alarmin driving autoimmune and inflammatory disease. Nat Rev Rheumatol 8:195–202.

75. Park JS, Svetkauskaite D, He Q, Kim J-Y, Strassheim D, Ishizaka A, Abraham E (2004) Involvement of toll-like receptors 2 and 4 in cellular activation by high mobility group box 1 protein. J Biol Chem 279:7370–7.

76. Apetoh L, Tesniere A, Obeid M, Ortiz C, Maiuri MC, Ullrich E, Saulnier P, Criollo A, Bourhis J, Andre F, Kroemer G, Zitvogel L (2007) Toll-like receptor 4 – dependent contribution of the immune system to anticancer chemotherapy and radiotherapy. 13:1050–1059.

77. Binder RJ, Vatner R, Srivastava P (2004) The heat-shock protein receptors: some answers and more questions. Tissue Antigens 64:442–451.

78. Shi Y, Evans JE, Rock KL (2003) Molecular identification of a danger signal that alerts the immune system to dying cells. Nature 425:516–21.

79. Garg AD, Vandenberk L, Fang S, Fasche T, Van Eygen S, Maes J, Van Woensel M, Koks C, Vanthillo N, Graf N, de Witte P, Van Gool S, Salven P, Agostinis P (2017) Pathogen response-like recruitment and activation of neutrophils by sterile immunogenic dying cells drives neutrophil-mediated residual cell killing. Cell Death Differ 24:832–843.

80. Vénéreau E, Ceriotti C, Bianchi ME (2015) DAMPs from Cell Death to New Life. Front Immunol 6:422.

81. Rufo N, Garg AD, Agostinis P (2017) The Unfolded Protein Response in Immunogenic Cell Death and Cancer Immunotherapy. Trends in Cancer 3:643–658.

82. Xipell E, Aragón T, Martínez-Velez N, Vera B, Idoate MA, Martínez-Irujo JJ, Garzón AG, Gonzalez-Huarriz M, Acanda AM, Jones C, Lang FF, Fueyo J, Gomez-Manzano C, Alonso MM (2016) Endoplasmic reticulum stress-inducing drugs sensitize glioma cells to temozolomide through downregulation of MGMT, MPG, and Rad51. Neuro Oncol 18:1109–19.

83. Hanahan D, Bergers G, Bergsland E (2000) Less is more, regularly: metronomic dosing of cytotoxic drugs can target tumor angiogenesis in mice. J Clin Invest 105:1045–7.

84. Wu J, Waxman DJ (2015) Metronomic cyclophosphamide eradicates large implanted GL261 gliomas by activating antitumor Cd8+ T-cell responses and immune memory. Oncoimmunology 4:e1005521.

85. Ferrer-font L, Villamañan L, Arias-ramos N, Vilardell J, Plana M, Ruzzene M, Pinna LA, Itarte E, Arús C, Candiota AP (2017) Targeting Protein Kinase CK2: Evaluating CX-4945 Potential for GL261 Glioblastoma Therapy in Immunocompetent Mice. Pharmaceuticals (Basel) 10:1–18.

86. Brandes AA, Tosoni A, Franceschi E, Blatt V, Santoro A, Faedi M, Amistà P, Gardiman M, Labianca R, Bianchini C, Ermani M, Reni M (2009) Fotemustine as second-line treatment for recurrent or progressive glioblastoma after concomitant and/or adjuvant temozolomide: a phase II trial of Gruppo Italiano Cooperativo di Neuro-Oncologia (GICNO). Cancer Chemother Pharmacol 64:769–775.

87. Kegelman TP, Hu B, Emdad L, Das SK, Sarkar D, Fisher PB (2014) In Vivo Modeling of Malignant Glioma. Adv. Cancer Res. pp 261–330

88. Antunes L, Angioi-Duprez KS, Bracard SR, Klein-Monhoven NA, Le Faou AE, Duprez AM, Plénat FM (2000) Analysis of Tissue Chimerism in Nude Mouse Brain and Abdominal Xenograft Models of Human Glioblastoma Multiforme: What Does It Tell Us About the Models and About Glioblastoma Biology and Therapy? J Histochem Cytochem 48:847–858.

89. Guenet JL (2005) The mouse genome. Genome Res 15:1729–1740.

90. Yue F, Cheng Y, Breschi A, Vierstra J, Wu W, Ryba T, Sandstrom R, Ma Z, Davis C, Pope BD, Shen Y, Pervouchine DD, Djebali S, Thurman RE, Kaul R, Rynes E, Kirilusha A, Marinov GK, Williams BA, Trout D, Amrhein H, Fisher-Aylor K, Antoshechkin I, DeSalvo G, See L-H, Fastuca M, Drenkow J, Zaleski C, Dobin A, Prieto P, Lagarde J, Bussotti G, Tanzer A, Denas O, Li K, Bender MA, Zhang M, Byron R, Groudine MT, McCleary D, Pham L, Ye Z, Kuan S, Edsall L, Wu Y-C, Rasmussen MD, Bansal MS, Kellis M, Keller CA, Morrissey CS, Mishra T, Jain D, Dogan N, Harris RS, Cayting P, Kawli T, Boyle AP, Euskirchen G, Kundaje A, Lin S, Lin Y, Jansen C, Malladi VS, Cline MS, Erickson DT, Kirkup VM, Learned K, Sloan CA, Rosenbloom KR, Lacerda de Sousa B, Beal K, Pignatelli M, Flicek P, Lian J, Kahveci T, Lee D, James Kent W, Ramalho Santos M, Herrero J, Notredame C, Johnson A, Vong S, Lee K, Bates D, Neri F, Diegel M, Canfield T, Sabo PJ, Wilken MS, Reh TA, Giste E, Shafer A, Kutyavin T, Haugen E, Dunn D, Reynolds AP, Neph S, Humbert R, Scott Hansen R, De Bruijn M, Selleri L, Rudensky A, Josefowicz S, Samstein R, Eichler EE, Orkin SH, Levasseur

D, Papayannopoulou T, Chang K-H, Skoultchi A, Gosh S, Disteche C, Treuting P, Wang Y, Weiss MJ, Blobel GA, Cao X, Zhong S, Wang T, Good PJ, Lowdon RF, Adams LB, Zhou X-Q, Pazin MJ, Feingold EA, Wold B, Taylor J, Mortazavi A, Weissman SM, Stamatoyannopoulos JA, Snyder MP, Guigo R, Gingeras TR, Gilbert DM, Hardison RC, Beer MA, Ren B, Mouse ENCODE Consortium (2014) A comparative encyclopedia of DNA elements in the mouse genome. Nature 515:355–364.

91. Belizario JE (2009) Immunodeficient Mouse Models: An Overview. Open Immunol J 2:79–85.

92. Kijima N, Kanemura Y (2017) Mouse Models of Glioblastoma. Glioblastoma. doi: 10.15586/CODON.GLIOBLASTOMA.2017.CH7

93. Wu J, Jordan M, Waxman DJ (2016) Metronomic cyclophosphamide activation of anti-tumor immunity : tumor model , mouse host , and drug schedule dependence of gene responses and their upstream regulators. BMC Cancer 1–17.

94. Oh T, Fakurnejad S, Sayegh ET, Clark AJ, Ivan ME, Sun MZ, Safaee M, Bloch O, James CD, Parsa AT (2014) Immunocompetent murine models for the study of glioblastoma immunotherapy. J Transl Med 12:107.

95. Szatmári T, Lumniczky K, Désaknai S, Trajcevski S, Hídvégi EJ, Hamada H, Sáfrány G (2006) Detailed characterization of the mouse glioma 261 tumor model for experimental glioblastoma therapy. Cancer Sci 97:546–553.

96. Seligman AM, Shear MJ, Alexander L (1939) Studies in Carcinogenesis: VIII. Experimental Production of Brain Tumors in Mice with Methylcholanthrene. Am J Cancer 37:364–395.

97. Scott OC (1991) Tumor transplantation and tumor immunity: a personal view. Cancer Res 51:757–63.

98. Delgado-Goñi T, Ortega-Martorell S, Ciezka M, Olier I, Candiota AP, Julià-Sapé M, Fernández F, Pumarola M, Lisboa PJ, Arús C (2016) MRSI-based molecular imaging of therapy response to temozolomide in preclinical glioblastoma using source analysis. NMR Biomed 29:732–743.

99. Simões RV, Ortega-Martorell S, Delgado-Goñi T, Le Fur Y, Pumarola M, Candiota AP, Martín J, Stoyanova R, Cozzone PJ, Julià-Sapé M, Arús C (2012) Improving the classification of brain tumors in mice with perturbation enhanced (PE)-MRSI. Integr Biol (Camb) 4:183–91.

100. Ciezka M, Acosta M, Herranz C, Canals JM, Pumarola M, Candiota AP, Arús C (2016) Development of a transplantable glioma tumour model from genetically engineered mice: MRI/MRS/MRSI characterisation. J Neurooncol 129:67–76.

101. Kober C, Rohn S, Weibel S, Geissinger U, Chen NG, Szalay AA (2015) Microglia and astrocytes attenuate the replication of the oncolytic vaccinia virus LIVP 1.1.1 in murine GL261 gliomas by acting as vaccinia virus traps. J Transl Med 13:216.

102. Xu M, Yao Y, Hua W, Wu Z, Zhong P, Mao Y, Zhou L, Luo F, Chu Y (2014) Mouse glioma immunotherapy mediated by A2B5+ GL261 cell lysate-pulsed dendritic cells. J Neurooncol 116:497–504.

103. Reardon DA, Gokhale PC, Klein SR, Ligon KL, Rodig SJ, Ramkissoon SH, Jones KL, Conway AS, Liao X, Zhou J, Wen PY, Van Den Abbeele AD, Hodi FS, Qin L, Kohl NE, Sharpe AH, Dranoff G, Freeman GJ (2016) Glioblastoma Eradication Following Immune Checkpoint

Blockade in an Orthotopic, Immunocompetent Model. Cancer Immunol Res 4:124–135.

104. Towner RA, Ihnat M, Saunders D, Bastian A, Smith N, Pavana RK (2015) A new anti-glioma therapy , AG119 : pre-clinical assessment in a mouse GL261 glioma model. BMC Cancer 1–8.

105. Tompa M, Kalovits F, Nagy A, Kalman B (2018) Contribution of the Wnt Pathway to Defining Biology of Glioblastoma. NeuroMolecular Med 20:437–451.

106. West AJ, Tsui V, Stylli SS, Nguyen HPT, Morokoff AP, Kaye AH, Luwor RB (2018) The role of interleukin-6-STAT3 signalling in glioblastoma. Oncol Lett 16:4095–4104.

107. Cattaneo MG, Vanetti C, Samarani M, Aureli M, Bassi R, Sonnino S, Giussani P (2018) Cross-talk between sphingosine-1-phosphate and EGFR signaling pathways enhances human glioblastoma cell invasiveness. FEBS Lett 592:949–961.

108. Salvi M, Sarno S, Cesaro L, Nakamura H, Pinna LA (2009) Extraordinary pleiotropy of protein kinase CK2 revealed by weblogo phosphoproteome analysis. Biochim Biophys Acta - Mol Cell Res 1793:847–859.

109. Brault L, Gasser C, Bracher F, Huber K, Knapp S, Schwaller J (2010) PIM serine/threonine kinases in the pathogenesis and therapy of hematologic malignancies and solid cancers. Haematologica 95:1004–1015.

110. Zheng Y, McFarland BC, Drygin D, Yu H, Bellis SL, Kim H, Bredel M, Benveniste EN (2013) Targeting protein kinase CK2 suppresses prosurvival signaling pathways and growth of glioblastoma. Clin Cancer Res An Off J Am Assoc Cancer Res 19:6484–6494.

111. Herzog S, Fink MA, Weitmann K, Friedel C, Hadlich S, Langner S, Kindermann K, Holm T, Böhm A, Eskilsson E, Miletic H, Hildner M, Fritsch M, Vogelgesang S, Havemann C, Ritter CA, Meyer zu Schwabedissen HE, Rauch B, Hoffmann W, Kroemer HK, Schroeder H, Bien-Möller S (2015) Pim1 kinase is upregulated in glioblastoma multiforme and mediates tumor cell survival. Neuro Oncol 17:223–242.

112. Meggio F, Pinna LA (2003) One-thousand-and-one substrates of protein kinase CK2? FASEB J 17:349–368.

113. Ruzzene M, Pinna LA (2010) Addiction to protein kinase CK2: a common denominator of diverse cancer cells? Biochim Biophys Acta 1804:499–504.

114. Jafari M, Ghadami E, Dadkhah T, Akhavan-Niaki H (2019) PI3k/AKT signaling pathway: Erythropoiesis and beyond. J Cell Physiol 234:2373–2385.

115. Steinhart Z, Angers S (2018) Wnt signaling in development and tissue homeostasis. Development 145:dev146589.

116. Tilborghs S, Corthouts J, Verhoeven Y, Arias D, Rolfo C, Trinh XB, van Dam PA (2017) The role of Nuclear Factor-kappa B signaling in human cervical cancer. Crit Rev Oncol Hematol 120:141–150.

117. Pinna LA (1990) Casein kinase 2: an “eminence grise” in cellular regulation? Biochim Biophys Acta 1054:267–84.

118. Bidwai AP, Reed JC, Glover C V (1993) Phosphorylation of calmodulin by the catalytic subunit of casein kinase II is inhibited by the regulatory subunit. Arch Biochem Biophys

300:265–270.

119. Poletto G, Vilardell J, Marin O, Pagano MA, Cozza G, Sarno S, Falqués A, Itarte E, Pinna LA, Meggio F (2008) The regulatory beta subunit of protein kinase CK2 contributes to the recognition of the substrate consensus sequence. A study with an eIF2 beta-derived peptide. Biochemistry 47:8317–8325.

120. Litchfield DW (2003) Protein kinase CK2: structure, regulation and role in cellular decisions of life and death. Biochem J 369:1–15.

121. Hériché JK, Lebrin F, Rabilloud T, Leroy D, Chambaz EM, Goldberg Y (1997) Regulation of protein phosphatase 2A by direct interaction with casein kinase 2alpha. Science 276:952–955.

122. Lou DY, Dominguez I, Toselli P, Landesman-Bollag E, O'Brien C, Seldin DC (2008) The alpha catalytic subunit of protein kinase CK2 is required for mouse embryonic development. Mol Cell Biol 28:131–139.

123. Xu X, Toselli PA, Russell LD, Seldin DC (1999) Globozoospermia in mice lacking the casein kinase II α ′ catalytic subunit. 23:

124. Faust M, Montenarh M (2000) Subcellular localization of protein kinase CK2. A key to its function? Cell Tissue Res 301:329–340.

125. Guerra B, Siemer S, Boldyreff B, Issinger OG (1999) Protein kinase CK2: evidence for a protein kinase CK2beta subunit fraction, devoid of the catalytic CK2alpha subunit, in mouse brain and testicles. FEBS Lett 462:353–357.

126. Liu Y, Amin EB, Mayo MW, Chudgar NP, Bucciarelli PR, Kadota K, Adusumilli PS, Jones DR (2016) CK2α' Drives Lung Cancer Metastasis by Targeting BRMS1 Nuclear Export and Degradation. Cancer Res 76:2675–2686.

127. Turowec JP, Vilk G, Gabriel M, Litchfield DW (2013) Characterizing the convergence of protein kinase CK2 and caspase-3 reveals isoform-specific phosphorylation of caspase-3 by CK2α': implications for pathological roles of CK2 in promoting cancer cell survival. Oncotarget 4:560–571.

128. Messenger MM, Saulnier RB, Gilchrist AD, Diamond P, Gorbsky GJ, Litchfield DW (2002) Interactions between protein kinase CK2 and Pin1. Evidence for phosphorylation-dependent interactions. J Biol Chem 277:23054–23064.

129. Perez M, Avila J (1999) The expression of casein kinase 2 K P and phosphatase 2A activity. Biochim Biophys Acta 1449:150–156.

130. Miyata Y, Yahara I (1995) Interaction between casein kinase II and the 90-kDa stress protein, HSP90. Biochemistry 34:8123–8129.

131. Olsten MEK, Canton DA, Zhang C, Walton PA, Litchfield DW (2004) The Pleckstrin homology domain of CK2 interacting protein-1 is required for interactions and recruitment of protein kinase CK2 to the plasma membrane. J Biol Chem 279:42114–42127.

132. Di Maira G, Brustolon F, Pinna LA, Ruzzene M (2009) Dephosphorylation and inactivation of Akt/PKB is counteracted by protein kinase CK2 in HEK 293T cells. Cell Mol life Sci C 66:3363–3373.

133. Robitzki A, Bodenbach L, Voss H, Pyerin W (1993) Human casein kinase II. The subunit alpha protein activates transcription of the subunit beta gene. J Biol Chem 268:5694–702.

134. Lupp S, Gumhold C, Ampofo E, Montenarh M, Rother K (2013) CK2 kinase activity but not its binding to CK2 promoter regions is implicated in the regulation of CK2α and CK2β gene expressions. Mol Cell Biochem 384:71–82.

135. Hanna DE, Rethinaswamy A, Glover CVC (1995) Casein Kinase II Is Required for Cell Cycle Progression during G 1 and G 2 / M in Saccharomyces cerevisiae. J Biol Chem 270:25905–25914.

136. Bosc DG, Lüscher B, Litchfield DW (1999) Expression and regulation of protein kinase CK2 during the cell cycle. Mol Cell Biochem 191:213–222.

137. Carroll D, Marshak DR (1989) Serum-stimulated Cell Growth Causes Oscillations in Casein Kinase I1 Activity. J Biol Chem 264:7345–7348.

138. Orlandini M, Semplici F, Ferruzzi R, Meggio F, Pinna LA, Oliviero S (1998) Protein kinase CK2alpha' is induced by serum as a delayed early gene and cooperates with Ha-ras in fibroblast transformation. J Biol Chem 273:21291–21297.

139. Ryu S, Hyung J, Kim Y, Lee Y, Woo J, Bae Y (2006) Downregulation of protein kinase CKII is associated with cellular senescence. FEBS Lett 580:988–994.

140. Kim E-K, Kang J-Y, Rho Y-H, Kim YS, Kim D-S, Bae Y-S (2009) Silencing of the CKII alpha and CKII alpha' genes during cellular senescence is mediated by DNA methylation. Gene 431:55–60.

141. Massagué J (2004) G1 cell-cycle control and cancer. Nature 432:298–306.

142. Stacey DW (2003) Cyclin D1 serves as a cell cycle regulatory switch in actively proliferating cells. Curr Opin Cell Biol 15:158–163.

143. Hwang K-A, Kang N-H, Yi B-R, Lee H-R, Park M-A, Choi K-C (2013) Genistein, a soy phytoestrogen, prevents the growth of BG-1 ovarian cancer cells induced by 17β-estradiol or bisphenol A via the inhibition of cell cycle progression. Int J Oncol 42:733–740.

144. Zuryń A, Litwiniec A, Klimaszewska-Wiśniewska A, Nowak JM, Gackowska L, Myśliwiec BJ, Pawlik A, Grzanka A (2014) Expression of cyclin D1 after treatment with doxorubicin in the HL-60 cell line. Cell Biol Int 38:857–867.

145. Santo L, Siu KT, Raje N (2015) Targeting Cyclin-Dependent Kinases and Cell Cycle Progression in Human Cancers. Semin Oncol 42:788–800.

146. Münstermann U, Fritz G, Seitz G, Lu YP, Schneider HR, Issinger OG (1990) Casein kinase II is elevated in solid human tumours and rapidly proliferating non-neoplastic tissue. Eur J Biochem 189:251–257.

147. Daya-Makin M, Sanghera JS, Mogentale TL, Lipp M, Parchomchuk J, Hogg JC, Pelech SL (1994) Activation of a tumor-associated protein kinase (p40TAK) and casein kinase 2 in human squamous cell carcinomas and adenocarcinomas of the lung. Cancer Res 54:2262–8.

148. Faust RA, Gapany M, Tristani P, Davis A, Adams GL, Ahmed K (1996) Elevated protein

kinase CK2 activity in chromatin of head and neck tumors: association with malignant transformation. Cancer Lett 101:31–35.

149. Ji H, Lu Z (2013) The role of protein kinase CK2 in glioblastoma development. Clin Cancer Res 19:6335–7.

150. Ferrer-Font L, Alcaraz E, Plana M, Candiota AP, Itarte E, Arús C (2016) Protein Kinase CK2 Content in GL261 Mouse Glioblastoma. Pathol Oncol Res POR 22:633–637.

151. Trembley JH, Wang G, Unger G, Slaton J, Ahmed K (2009) Protein kinase CK2 in health and disease: CK2: a key player in cancer biology. Cell Mol life Sci C 66:1858–1867.

152. Sarno S, Papinutto E, Franchin C, Bain J, Elliott M, Meggio F, Kazimierczuk Z, Orzeszko A, Zanotti G, Battistutta R, Pinna LA (2011) ATP site-directed inhibitors of protein kinase CK2: an update. Curr Top Med Chem 11:1340–1351.

153. Winska P, Skierka K, Lukowska-Chojnacka E, Koronkiewicz M, Ciesla J, Bretner M (2018) Effect of Simultaneous Inhibition of Protein Kinase CK2 and Thymidylate Synthase in Leukemia and Breast Cancer Cells. Anticancer Res 38:4617–4627.

154. Aho TLT, Sandholm J, Peltola KJ, Mankonen HP, Lilly M, Koskinen PJ (2004) Pim-1 kinase promotes inactivation of the pro-apoptotic Bad protein by phosphorylating it on the Ser112 gatekeeper site. FEBS Lett 571:43–9.

155. Mochizuki T, Kitanaka C, Noguchi K, Muramatsu T, Asai A, Kuchino Y (1999) Physical and functional interactions between Pim-1 kinase and Cdc25A phosphatase. Implications for the Pim-1-mediated activation of the c-Myc signaling pathway. J Biol Chem 274:18659–66.

156. Bachmann M, Kosan C, Xing PX, Montenarh M, Hoffmann I, Möröy T (2006) The oncogenic serine/threonine kinase Pim-1 directly phosphorylates and activates the G2/M specific phosphatase Cdc25C. Int J Biochem Cell Biol 38:430–43.

157. Wang Z, Bhattacharya N, Mixter PF, Wei W, Sedivy J, Magnuson NS (2002) Phosphorylation of the cell cycle inhibitor p21Cip1/WAF1 by Pim-1 kinase. Biochim Biophys Acta 1593:45–55.

158. Morishita D, Katayama R, Sekimizu K, Tsuruo T, Fujita N (2008) Pim Kinases Promote Cell Cycle Progression by Phosphorylating and Down-regulating p27Kip1 at the Transcriptional and Posttranscriptional Levels. Cancer Res 68:5076–5085.

159. Li S, Xi YU, Zhang H, Wang Y, Wang XIN, Liu H, Chen K (2010) A pivotal role for Pim-1 kinase in esophageal squamous cell carcinoma involving cell apoptosis induced by reducing Akt phosphorylation. 997–1004.

160. Peltola K, Hollmen M, Maula S-M, Rainio E, Ristamäki R, Luukkaa M, Sandholm J, Sundvall M, Elenius K, Koskinen PJ, Grenman R, Jalkanen S (2009) Pim-1 kinase expression predicts radiation response in squamocellular carcinoma of head and neck and is under the control of epidermal growth factor receptor. Neoplasia 11:629–36.

161. Chon HJ, Bae KJ, Lee Y, Kim J (2015) The casein kinase 2 inhibitor, CX-4945, as an anti-cancer drug in treatment of human hematological malignancies. Front Pharmacol 6:70.

162. Zandomeni R, Zandomeni MC, Shugar D, Weinmann R (1986) Casein kinase type II is involved in the inhibition by 5,6-dichloro-1-beta-D-ribofuranosylbenzimidazole of specific

RNA polymerase II transcription. J Biol Chem 261:3414–9.

163. Sarno S, Reddy H, Meggio F, Ruzzene M, Davies SP, Donella-Deana A, Shugar D, Pinna LA (2001) Selectivity of 4,5,6,7-tetrabromobenzotriazole, an ATP site-directed inhibitor of protein kinase CK2 ('casein kinase-2'). FEBS Lett 496:44–8.

164. Pagano MA, Meggio F, Ruzzene M, Andrzejewska M, Kazimierczuk Z, Pinna LA (2004) 2-Dimethylamino-4,5,6,7-tetrabromo-1H-benzimidazole: a novel powerful and selective inhibitor of protein kinase CK2. Biochem Biophys Res Commun 321:1040–1044.

165. Pagano MA, Bain J, Kazimierczuk Z, Sarno S, Ruzzene M, Di Maira G, Elliott M, Orzeszko A, Cozza G, Meggio F, Pinna LA (2008) The selectivity of inhibitors of protein kinase CK2: an update. Biochem J 415:353–365.

166. Janeczko M, Orzeszko A, Kazimierczuk Z, Szyszka R, Baier A (2012) CK2α and CK2α' subunits differ in their sensitivity to 4,5,6,7-tetrabromo- and 4,5,6,7-tetraiodo-1H-benzimidazole derivatives. Eur J Med Chem 47:345–350.

167. Bollacke A, Nienberg C, Le Borgne M, Jose J (2016) Toward selective CK2alpha and CK2alpha' inhibitors: Development of a novel whole-cell kinase assay by Autodisplay of catalytic CK2alpha'. J Pharm Biomed Anal 121:253–260.

168. Bian Y, Han J, Kannabiran V, Mohan S, Cheng H, Friedman J, Zhang L, VanWaes C, Chen Z (2015) MEK Inhibitor PD-0325901 Overcomes Resistance to CK2 Inhibitor CX-4945 and Exhibits Anti-Tumor Activity in Head and Neck Cancer. Int J Biol Sci 11:411–422.

169. Siddiqui-Jain A, Drygin D, Streiner N, Chua P, Pierre F, O'Brien SE, Bliesath J, Omori M, Huser N, Ho C, Proffitt C, Schwaebe MK, Ryckman DM, Rice WG, Anderes K (2010) CX-4945, an orally bioavailable selective inhibitor of protein kinase CK2, inhibits prosurvival and angiogenic signaling and exhibits antitumor efficacy. Cancer Res 70:10288–10298.

170. Hwang DW, So KS, Kim SC, Park K-M, Lee Y-J, Kim S-W, Choi C-M, Rho JK, Choi YJ, Lee JC (2017) Autophagy Induced by CX-4945, a Casein Kinase 2 Inhibitor, Enhances Apoptosis in Pancreatic Cancer Cell Lines. Pancreas 46:575–581.

171. Kohsaka S, Wang L, Yachi K, Mahabir R, Narita T, Itoh T, Tanino M, Kimura T, Nishihara H, Tanaka S (2012) STAT3 inhibition overcomes temozolomide resistance in glioblastoma by downregulating MGMT expression. Mol Cancer Ther 11:1289–99.

172. Pierre F, Chua PC, O'Brien SE, Siddiqui-Jain A, Bourbon P, Haddach M, Michaux J, Nagasawa J, Schwaebe MK, Stefan E, Vialettes A, Whitten JP, Chen TK, Darjania L, Stansfield R, Bliesath J, Drygin D, Ho C, Omori M, Proffitt C, Streiner N, Rice WG, Ryckman DM, Anderes K (2011) Pre-clinical characterization of CX-4945, a potent and selective small molecule inhibitor of CK2 for the treatment of cancer. Mol Cell Biochem 356:37–43.

173. Drygin D, Ho CB, Omori M, Bliesath J, Proffitt C, Rice R, Siddiqui-Jain A, O'Brien S, Padgett C, Lim JKC, Anderes K, Rice WG, Ryckman D (2011) Protein kinase CK2 modulates IL-6 expression in inflammatory breast cancer. Biochem Biophys Res Commun 415:163–7.

174. Drygin D, Ho CB, Omori M, Bliesath J, Proffitt C, Rice R, Siddiqui-Jain A, O'Brien S, Padgett C, Lim JKC, Anderes K, Rice WG, Ryckman D (2011) Protein kinase CK2 modulates IL-6 expression in inflammatory breast cancer. Biochem Biophys Res Commun 415:163–167.

175. Cozza G, Girardi C, Ranchio A, Lolli G, Sarno S, Orzeszko A, Kazimierczuk Z, Battistutta R, Ruzzene M, Pinna LA (2014) Cell-permeable dual inhibitors of protein kinases CK2 and

PIM-1: structural features and pharmacological potential. Cell Mol Life Sci 71:3173–3185.

176. Battistutta R, Cozza G, Pierre F, Papinutto E, Lolli G, Sarno S, O'Brien SE, Siddiqui-Jain A, Haddach M, Anderes K, Ryckman DM, Meggio F, Pinna LA (2011) Unprecedented Selectivity and Structural Determinants of a New Class of Protein Kinase CK2 Inhibitors in Clinical Trials for the Treatment of Cancer. Biochemistry 50:8478–8488.

177. Di Maira G, Salvi M, Arrigoni G, Marin O, Sarno S, Brustolon F, Pinna LA, Ruzzene M (2005) Protein kinase CK2 phosphorylates and upregulates Akt/PKB. Cell Death Differ 12:668–677.

178. Vanhaesebroeck B, Alessi DR (2000) The PI3K-PDK1 connection: more than just a road to PKB. Biochem J 346 Pt 3:561–76.

179. Vadlakonda L, Dash A, Pasupuleti M, Kumar KA (2013) The paradox of Akt-mTOR interactions. 3:1–9.

180. del Peso L, González-García M, Page C, Herrera R, Nuñez G (1997) Interleukin-3-induced phosphorylation of BAD through the protein kinase Akt. Science 278:687–9.

181. Harada H, Becknell B, Wilm M, Mann M, Huang LJ, Taylor SS, Scott JD, Korsmeyer SJ (1999) Phosphorylation and inactivation of BAD by mitochondria-anchored protein kinase A. Mol Cell 3:413–22.

182. Gadian DG (1995) NMR and its applications to living systems, 2^{o} edition. Oxford University Press

183. Vogelbaum MA, Jost S, Aghi MK, Heimberger AB, Sampson JH, Wen PY, Macdonald DR, Van den Bent MJ, Chang SM (2012) Application of novel response/progression measures for surgically delivered therapies for gliomas: Response Assessment in Neuro-Oncology (RANO) Working Group. Neurosurgery 70:234-43; discussion 243–4.

184. De León-Rodríguez LM, Martins AF, Pinho MC, Rofsky NM, Sherry AD (2015) Basic MR relaxation mechanisms and contrast agent design. J Magn Reson Imaging 42:545–65.

185. Vander Heiden MG, Cantley LC, Thompson CB (2009) Understanding the Warburg Effect: The Metabolic Requirements of Cell Proliferation. Science (80-) 324:1029–1033.

186. Zhu H, Barker PB (2011) MR spectroscopy and spectroscopic imaging of the brain. Methods Mol Biol 711:203–26.

187. Soares DP, Law M (2009) Magnetic resonance spectroscopy of the brain: review of metabolites and clinical applications. Clin Radiol 64:12–21.

188. Delgado-Goñi T, Julià-Sapé M, Candiota AP, Pumarola M, Arús C (2014) Molecular imaging coupled to pattern recognition distinguishes response to temozolomide in preclinical glioblastoma. NMR Biomed 27:1333–1345.

189. Segebarth CM, Balériaux DF, Luyten PR, den Hollander JA (1990) Detection of metabolic heterogeneity of human intracranial tumors in vivo by 1H NMR spectroscopic imaging. Magn Reson Med 13:62–76.

190. Ortega-Martorell S, Lisboa PJ, Vellido A, Simões RV, Pumarola M, Julià-Sapé M, Arús C (2012) Convex non-negative matrix factorization for brain tumor delimitation from MRSI data. PLoS One 7:e47824.

191. Ferrer-Font L, Arias-Ramos N, Lope-Piedrafita S, Julià-Sapé M, Pumarola M, Arús C, Candiota AP (2017) Metronomic treatment in immunocompetent preclinical GL261 glioblastoma: effects of cyclophosphamide and temozolomide. NMR Biomed 30:e3748.

192. Simões R V, García-Martín ML, Cerdán S, Arús C (2008) Perturbation of mouse glioma MRS pattern by induced acute hyperglycemia. NMR Biomed 21:251–264.

193. Simões R V, Delgado-Goñi T, Lope-Piedrafita S, Arús C (2010) 1H-MRSI pattern perturbation in a mouse glioma: the effects of acute hyperglycemia and moderate hypothermia. NMR Biomed 23:23–33.

194. Delgado-goñi T, Martín-Sitjar J, Simões R V, Acosta M (2013) Dimethyl sulfoxide (DMSO) as a potential contrast agent for brain tumors. NMR Biomed 173–184.

195. Chou T-C (2010) Drug combination studies and their synergy quantification using the Chou-Talalay method. Cancer Res 70:440–446.

196. Cozza G, Zanin S, Determann R, Ruzzene M, Kunick C, Pinna LA (2014) Synthesis and properties of a selective inhibitor of homeodomain-interacting protein kinase 2 (HIPK2). PLoS One 9:e89176.

197. Boyd-Tressler A, Penuela S, Laird DW, Dubyak GR (2014) Chemotherapeutic drugs induce ATP release via caspase-gated pannexin-1 channels and a caspase/pannexin-1-independent mechanism. J Biol Chem 289:27246–63.

198. Valverde D, Quintero MR, Candiota AP, Badiella L, Cabañas ME, Arús C (2006) Analysis of the changes in the 1H NMR spectral pattern of perchloric acid extracts of C6 cells with growth. NMR Biomed 19:223–230.

199. Eisenhauer EA, Therasse P, Bogaerts J, Schwartz LH, Sargent D, Ford R, Dancey J, Arbuck S, Gwyther S, Mooney M, Rubinstein L, Shankar L, Dodd L, Kaplan R, Lacombe D, Verweij J (2009) New response evaluation criteria in solid tumours: revised RECIST guideline (version 1.1). Eur J Cancer 45:228–47.

200. Chua MMJ, Ortega CE, Sheikh A, Lee M, Abdul-rassoul H, Hartshorn KL, Dominguez I (2017) CK2 in Cancer : Cellular and Biochemical Mechanisms and Potential Therapeutic Target. Pharmaceuticals (Basel) 10:20–22.

201. Medley JC, Kabara MM, Stubenvoll MD, DeMeyer LE, Song MH (2017) Casein kinase II is required for proper cell division and acts as a negative regulator of centrosome duplication in Caenorhabditis elegans embryos. Biol Open 6:17–28.

202. Rusin SF, Adamo ME, Kettenbach AN (2017) Identification of Candidate Casein Kinase 2 Substrates in Mitosis by Quantitative Phosphoproteomics. Front Cell Dev Biol. doi: 10.3389/fcell.2017.00097

203. Lin F, Cao S-B, Ma X-S, Sun H-X (2017) Inhibition of casein kinase 2 blocks G2/M transition in early embryo mitosis but not in oocyte meiosis in mouse. J Reprod Dev 63:319–324.

204. Deshiere A, Spreux E, Ciais D, Combes F, Vandenbrouck Y, Coute Y (2013) Unbalanced expression of CK2 kinase subunits is sufficient to drive epithelial-to-mesenchymal transition by Snail1 induction. Oncogene 32:1373–1383.

205. Kim E, Kang J, Rho Y, Sook Y, Kim D, Bae Y (2009) Silencing of the CKII α and CKII α ' genes during cellular senescence is mediated by DNA methylation. 431:55–60.

206. Nematullah M, Hoda M, Khan F (2017) Protein Phosphatase 2A : a Double-Faced Phosphatase of Cellular System and Its Role in Neurodegenerative Disorders. doi: 10.1007/s12035-017-0444-3

207. Cozza G, Sarno S, Ruzzene M, Girardi C, Orzeszko A, Kazimierczuk Z, Zagotto G, Bonaiuto E, Di Paolo ML, Pinna LA (2013) Exploiting the repertoire of CK2 inhibitors to target DYRK and PIM kinases. Biochim Biophys Acta - Proteins Proteomics 1834:1402–1409.

208. Daina A, Michielin O, Zoete V (2017) SwissADME: a free web tool to evaluate pharmacokinetics, drug-likeness and medicinal chemistry friendliness of small molecules. Sci Rep 7:42717.

209. Daina A, Michielin O, Zoete V (2014) iLOGP: A Simple, Robust, and Efficient Description of *n* -Octanol/Water Partition Coefficient for Drug Design Using the GB/SA Approach. J Chem Inf Model 54:3284–3301.

210. McConnell EL, Basit AW, Murdan S (2008) Measurements of rat and mouse gastrointestinal pH, fluid and lymphoid tissue, and implications for in-vivo experiments. J Pharm Pharmacol 60:63–70.

211. Martin YC (2005) A Bioavailability Score. J Med Chem 48:3164–3170.

212. Lipinski CA, Lombardo F, Dominy BW, Feeney PJ (2001) Experimental and computational approaches to estimate solubility and permeability in drug discovery and development settings. Adv Drug Deliv Rev 46:3–26.

213. Mandapathil M, Szczepanski M, Harasymczuk M, Ren J, Cheng D, Jackson EK, Gorelik E, Johnson J, Lang S, Whiteside TL (2012) CD26 expression and adenosine deaminase activity in regulatory T cells (Treg) and CD4(+) T effector cells in patients with head and neck squamous cell carcinoma. Oncoimmunology 1:659–669.

214. Brenk R, Schipani A, James D, Krasowski A, Gilbert IH, Frearson J, Wyatt PG (2008) Lessons Learnt from Assembling Screening Libraries for Drug Discovery for Neglected Diseases. ChemMedChem 3:435–444.

215. Ferrer Font L (2017) Tuning response to therapy in preclinical GL261 glioblastoma through CK2 targeting and temozolomide metronomic approaches: non-invasive assessment with MRI and MRSI-based molecular imaging strategies. TDX (Tesis Dr. en Xarxa) http//hdl.handle.net/10803/402400

216. Laboratory Animal Science Association, NC3Rs (2009) Guidance on dose level selection for regulatory general toxicology studies for pharmaceuticals. http://www.lasa.co.uk/pdf/lasa-nc3rsdoselevelselection.pdf.

217. Son YH, Song JS, Kim SH, Kim J (2013) Pharmacokinetic characterization of CK2 inhibitor CX-4945. Arch Pharm Res 36:840–845.

218. Hughes JP, Rees S, Kalindjian SB, Philpott KL (2011) Principles of early drug discovery. Br J Pharmacol 162:1239–49.

219. Burger AM, Fiebig H-H (2004) Preclinical Screening for New Anticancer Agents. Handb. Anticancer Pharmacokinet. Pharmacodyn. Humana Press, Totowa, NJ, pp 29–44

220. Sebaugh JL (2011) Guidelines for accurate EC50/IC50 estimation. Pharm Stat 10:128–134.

221. Stepanenko AA, Dmitrenko VV (2015) Pitfalls of the MTT assay: Direct and off-target effects of inhibitors can result in over/underestimation of cell viability. Gene 574:193–203.

222. Liu H-L, Huang C-Y, Chen J-Y, Wang H-YJ, Chen P-Y, Wei K-C (2014) Pharmacodynamic and therapeutic investigation of focused ultrasound-induced blood-brain barrier opening for enhanced temozolomide delivery in glioma treatment. PLoS One 9:e114311.

223. Zhou Q, Guo P, Wang X, Nuthalapati S, Gallo JM (2007) Preclinical pharmacokinetic and pharmacodynamic evaluation of metronomic and conventional temozolomide dosing regimens. J Pharmacol Exp Ther 321:265–75.

224. Luo Y, Chihara Y, Fujimoto K, Sasahira T, Kuwada M, Fujiwara R, Fujii K, Ohmori H, Kuniyasu H (2013) High mobility group box 1 released from necrotic cells enhances regrowth and metastasis of cancer cells that have survived chemotherapy. Eur J Cancer 49:741–751.

225. Kleijn A, van den Bossche W, Haefner ES, Belcaid Z, Burghoorn-Maas C, Kloezeman JJ, Pas SD, Leenstra S, Debets R, de Vrij J, Dirven CMF, Lamfers MLM (2017) The Sequence of Delta24-RGD and TMZ Administration in Malignant Glioma Affects the Role of CD8+T Cell Anti-tumor Activity. Mol Ther oncolytics 5:11–19.

226. De Salvo M, Maresca G, D'agnano I, Marchese R, Stigliano A, Gagliassi R, Brunetti E, Raza GH, De Paula U, Bucci B (2011) Temozolomide induced c-Myc-mediated apoptosis via Akt signalling in MGMT expressing glioblastoma cells. Int J Radiat Biol 87:518–33.

227. Shinsato Y, Furukawa T, Yunoue S, Yonezawa H, Minami K, Nishizawa Y, Ikeda R, Kawahara K, Yamamoto M, Hirano H, Tokimura H, Arita K (2013) Reduction of MLH1 and PMS2 confers temozolomide resistance and is associated with recurrence of glioblastoma. Oncotarget 4:2261–70.

228. Slater TF, Sawyer B, Straeuli U (1963) Studies on succinate-tetrazolium reductase systems. III. Points of coupling of four different tetrazolium salts. Biochim Biophys Acta 77:383–93.

229. Azzalin A, Nato G, Parmigiani E, Garello F, Buffo A, Magrassi L (2017) Inhibitors of GLUT/SLC2A Enhance the Action of BCNU and Temozolomide against High-Grade Gliomas. Neoplasia 19:364–373.

230. Buontempo F, Orsini E, Martins LR, Antunes I, Lonetti A, Chiarini F, Tabellini G, Evangelisti C, Evangelisti C, Melchionda F, Pession A, Bertaina A, Locatelli F, McCubrey JA, Cappellini A, Barata JT, Martelli AM (2014) Cytotoxic activity of the casein kinase 2 inhibitor CX-4945 against T-cell acute lymphoblastic leukemia: targeting the unfolded protein response signaling. Leukemia 28:543–553.

231. Dai C, Zhang B, Liu X, Ma S, Yang Y, Yao Y, Feng M, Bao X, Li G, Wang J, Guo K, Ma W, Xing B, Lian W, Xiao J, Cai F, Zhang H, Wang R (2013) Inhibition of PI3K/AKT/mTOR pathway enhances temozolomide-induced cytotoxicity in pituitary adenoma cell lines in vitro and xenografted pituitary adenoma in female nude mice. Endocrinology 154:1247–59.

232. de Bruyn M, Wiersma VR, Helfrich W, Eggleton P, Bremer E (2015) The ever-expanding immunomodulatory role of calreticulin in cancer immunity. Front Oncol 5:35.

233. Panaretakis T, Joza N, Modjtahedi N, Tesniere A, Vitale I, Durchschlag M, Fimia GM, Kepp O, Piacentini M, Froehlich K-U, van Endert P, Zitvogel L, Madeo F, Kroemer G (2008) The co-translocation of ERp57 and calreticulin determines the immunogenicity of cell death.

Cell Death Differ 15:1499–1509.

234. Intemann J, Saidu NEB, Schwind L, Montenarh M (2014) ER stress signaling in ARPE-19 cells after inhibition of protein kinase CK2 by CX-4945. Cell Signal 26:1567–1575.

235. Lecciso M, Ocadlikova D, Sangaletti S, Trabanelli S, De Marchi E, Orioli E, Pegoraro A, Portararo P, Jandus C, Bontadini A, Redavid A, Salvestrini V, Romero P, Colombo MP, Di Virgilio F, Cavo M, Adinolfi E, Curti A (2017) ATP Release from Chemotherapy-Treated Dying Leukemia Cells Elicits an Immune Suppressive Effect by Increasing Regulatory T Cells and Tolerogenic Dendritic Cells. Front Immunol 8:1918.

236. Martins I, Wang Y, Michaud M, Ma Y, Sukkurwala AQ, Shen S, Kepp O, Métivier D, Galluzzi L, Perfettini J-L, Zitvogel L, Kroemer G (2014) Molecular mechanisms of ATP secretion during immunogenic cell death. Cell Death Differ 21:79–91.

237. Jozsef Karman, Changying Ling, Matyas Sandor and ZF (2004) Initiation of Immune Responses in Brain Is Promoted by Local Dendritic Cells. J Immunol 173(4):2353–61.

238. Schiavoni G, Sistigu A, Valentini M, Mattei F, Sestili P, Spadaro F, Sanchez M, Lorenzi S, Urso MTD, Belardelli F, Gabriele L, Proietti E, Bracci L (2011) Cyclophosphamide Synergizes with Type I Interferons through Systemic Dendritic Cell Reactivation and Induction of Immunogenic Tumor Apoptosis. 71:768–779.

239. Liikanen I, Ahtiainen L, Hirvinen MLM, Bramante S, Cerullo V, Nokisalmi P, Hemminki O, Diaconu I, Pesonen S, Koski A, Kangasniemi L, Pesonen SK, Oksanen M, Laasonen L, Partanen K, Joensuu T, Zhao F, Kanerva A, Hemminki A (2013) Oncolytic adenovirus with temozolomide induces autophagy and antitumor immune responses in cancer patients. Mol Ther 21:1212–23.

240. Dai B, Qi N, Li J, Zhang G (2018) Temozolomide combined with PD-1 Antibody therapy for mouse orthotopic glioma model. Biochem Biophys Res Commun 501:871–876.

241. Sager O, Dincoglan F, Demiral S, Uysal B, Gamsiz H, Dirican B, Beyzadeoglu M (2018) A concise review of immunotherapy for glioblastoma. Neuroimmunol Neuroinflammation 5:25.

242. Jia L, Waxman DJ (2013) Thrombospondin-1 and pigment epithelium-derived factor enhance responsiveness of KM12 colon tumor to metronomic cyclophosphamide but have disparate effects on tumor metastasis. Cancer Lett 330:241–249.

243. Doloff JC, Chen C-S, Waxman DJ (2014) Anti-tumor innate immunity activated by intermittent metronomic cyclophosphamide treatment of 9L brain tumor xenografts is preserved by anti-angiogenic drugs that spare VEGF receptor 2. Mol Cancer 13:158.

244. Doloff JC, Chen C-S, Waxman DJ (2014) Anti-tumor innate immunity activated by intermittent metronomic cyclophosphamide treatment of 9L brain tumor xenografts is preserved by anti-angiogenic drugs that spare VEGF receptor 2. Mol Cancer 13:158.

245. Delgado-Goñi T, Ortega-Martorell S, Ciezka M, Olier I, Candiota AP, Julià-Sapé M, Fernández F, Pumarola M, Lisboa PJ, Arús C (2016) MRSI-based molecular imaging of therapy response to temozolomide in preclinical glioblastoma using source analysis. NMR Biomed 29:732–743.

246. Hwa Y, Jin S, Song S, Hwan S, Kim J (2013) Pharmacokinetic characterization of CK2 inhibitor CX-4945. 840–845.

247. Kim H-R, Kim K, Lee K-H, Kim SJ, Kim J (2008) Inhibition of casein kinase 2 enhances the death ligand- and natural kiler cell-induced hepatocellular carcinoma cell death. Clin Exp Immunol 152:336–344.

248. Chen T, Chen J, Zhu Y, Li Y, Wang Y, Chen H, Wang J, Li X, Liu Y, Li B, Sun X, Ke Y (2018) CD163, a novel therapeutic target, regulates the proliferation and stemness of glioma cells via casein kinase 2. Oncogene. doi: 10.1038/s41388-018-0515-6

249. Shiraishi D, Fujiwara Y, Horlad H, Saito Y, Iriki T, Tsuboki J, Cheng P, Nakagata N, Mizuta H, Bekki H, Nakashima Y, Oda Y, Takeya M, Komohara Y (2018) CD163 Is Required for Protumoral Activation of Macrophages in Human and Murine Sarcoma. Cancer Res 78:3255–3266.

250. Hoarau-Véchot J, Rafii A, Touboul C, Pasquier J (2018) Halfway between 2D and Animal Models: Are 3D Cultures the Ideal Tool to Study Cancer-Microenvironment Interactions? Int J Mol Sci. doi: 10.3390/ijms19010181

251. Erazo T, Lorente M, López-Plana A, Muñoz-Guardiola P, Fernández-Nogueira P, García-Martínez JA, Bragado P, Fuster G, Salazar M, Espadaler J, Hernández-Losa J, Bayascas JR, Cortal M, Vidal L, Gascón P, Gómez-Ferreria M, Alfón J, Velasco G, Domènech C, Lizcano JM (2016) The New Antitumor Drug ABTL0812 Inhibits the Akt/mTORC1 Axis by Upregulating Tribbles-3 Pseudokinase. Clin Cancer Res 22:2508–19.

252. Baell JB, Leaver DJ, Hermans SJ, Kelly GL, Brennan MS, Downer NL, Nguyen N, Wichmann J, McRae HM, Yang Y, Cleary B, Lagiakos HR, Mieruszynski S, Pacini G, Vanyai HK, Bergamasco MI, May RE, Davey BK, Morgan KJ, Sealey AJ, Wang B, Zamudio N, Wilcox S, Garnham AL, Sheikh BN, Aubrey BJ, Doggett K, Chung MC, de Silva M, Bentley J, Pilling P, Hattarki M, Dolezal O, Dennis ML, Falk H, Ren B, Charman SA, White KL, Rautela J, Newbold A, Hawkins ED, Johnstone RW, Huntington ND, Peat TS, Heath JK, Strasser A, Parker MW, Smyth GK, Street IP, Monahan BJ, Voss AK, Thomas T (2018) Inhibitors of histone acetyltransferases KAT6A/B induce senescence and arrest tumour growth. Nature 560:253–257.

253. Chen C-S, Doloff JC, Waxman DJ (2014) Intermittent metronomic drug schedule is essential for activating antitumor innate immunity and tumor xenograft regression. Neoplasia 16:84–96.

254. Ott PA, Hu Z, Keskin DB, Shukla SA, Sun J, Bozym DJ, Zhang W, Luoma A, Giobbie-Hurder A, Peter L, Chen C, Olive O, Carter TA, Li S, Lieb DJ, Eisenhaure T, Gjini E, Stevens J, Lane WJ, Javeri I, Nellaiappan K, Salazar AM, Daley H, Seaman M, Buchbinder EI, Yoon CH, Harden M, Lennon N, Gabriel S, Rodig SJ, Barouch DH, Aster JC, Getz G, Wucherpfennig K, Neuberg D, Ritz J, Lander ES, Fritsch EF, Hacohen N, Wu CJ (2017) An immunogenic personal neoantigen vaccine for patients with melanoma. Nature 547:217–221.

255. Sahin U, Derhovanessian E, Miller M, Kloke B-P, Simon P, Löwer M, Bukur V, Tadmor AD, Luxemburger U, Schrörs B, Omokoko T, Vormehr M, Albrecht C, Paruzynski A, Kuhn AN, Buck J, Heesch S, Schreeb KH, Müller F, Ortseifer I, Vogler I, Godehardt E, Attig S, Rae R, Breitkreuz A, Tolliver C, Suchan M, Martic G, Hohberger A, Sorn P, Diekmann J, Ciesla J, Waksmann O, Brück A-K, Witt M, Zillgen M, Rothermel A, Kasemann B, Langer D, Bolte S, Diken M, Kreiter S, Nemecek R, Gebhardt C, Grabbe S, Höller C, Utikal J, Huber C, Loquai C, Türeci Ö (2017) Personalized RNA mutanome vaccines mobilize poly-specific therapeutic immunity against cancer. Nature 547:222–226.

256. Koks CA, Garg AD, Ehrhardt M, Riva M, Vandenberk L, Boon L, Vleeschouwer S De,

Agostinis P, Graf N, Gool SW Van Newcastle disease virotherapy induces long-term survival and tumor-specific immune memory in orthotopic glioma through the induction of immunogenic cell death. doi: 10.1002/ijc.29202

257. Baricordi OR, Ferrari D, Melchiorri L, Chiozzi P, Hanau S, Chiari E, Rubini M, Di Virgilio F (1996) An ATP-activated channel is involved in mitogenic stimulation of human T lymphocytes. Blood 87:682–90.

258. Curley CT, Sheybani ND, Bullock TN, Price RJ (2017) Focused Ultrasound Immunotherapy for Central Nervous System Pathologies: Challenges and Opportunities. Theranostics 7:3608–3623.

259. Hygino da Cruz LC, Rodriguez I, Domingues RC, Gasparetto EL, Sorensen AG (2011) Pseudoprogression and Pseudoresponse: Imaging Challenges in the Assessment of Posttreatment Glioma. Am J Neuroradiol 32:1978–1985.

260. Shankar GM, Balaj L, Stott SL, Nahed B, Carter BS (2017) Liquid biopsy for brain tumors. Expert Rev Mol Diagn 17:943–947.

261. Li Y, Liu X, Wei F, Sima DM, Van Cauter S, Himmelreich U, Pi Y, Hu G, Yao Y, Van Huffel S (2017) An advanced MRI and MRSI data fusion scheme for enhancing unsupervised brain tumor differentiation. Comput Biol Med 81:121–129.

262. Aquino D, Gioppo A, Finocchiaro G, Bruzzone MG, Cuccarini V (2017) MRI in Glioma Immunotherapy: Evidence, Pitfalls, and Perspectives. J Immunol Res 2017:5813951.

263. Qin L, Li X, Stroiney A, Qu J, Helgager J, Reardon DA, Young GS (2017) Advanced MRI assessment to predict benefit of anti-programmed cell death 1 protein immunotherapy response in patients with recurrent glioblastoma. Neuroradiology 59:135–145.

264. Wick W, Puduvalli VK, Chamberlain MC, van den Bent MJ, Carpentier AF, Cher LM, Mason W, Weller M, Hong S, Musib L, Liepa AM, Thornton DE, Fine HA (2010) Phase III Study of Enzastaurin Compared With Lomustine in the Treatment of Recurrent Intracranial Glioblastoma. J Clin Oncol 28:1168–1174.

ANNEX I

The Chou-Talalay method [195] was used to classify the combined effect of two drugs. This example shows the method applied to the combined treatment of CX-4945 and TMZ in GL261 cells.

GL261 cells were treated with increasing concentrations of CX-4945 and TMZ for 72h (Figure A) and cellular viability was assessed by MTT. Then, results were analyzed by the Chou-Talalay method to determine if the effect of the combined treatment was synergic, additive or antagonistic.

Dose effect curve

The relationship between drug concentration and reduced cellular viability is shown in the dose effect curves (Figure A) for CX-4945, TMZ and CX-4945+TMZ treatments. This method uses the terminology of unaffected fraction (fu) for the fraction of cells that survive after treatment and affected fraction (fa) for the cells that are missing when comparing untreated and treated cells.

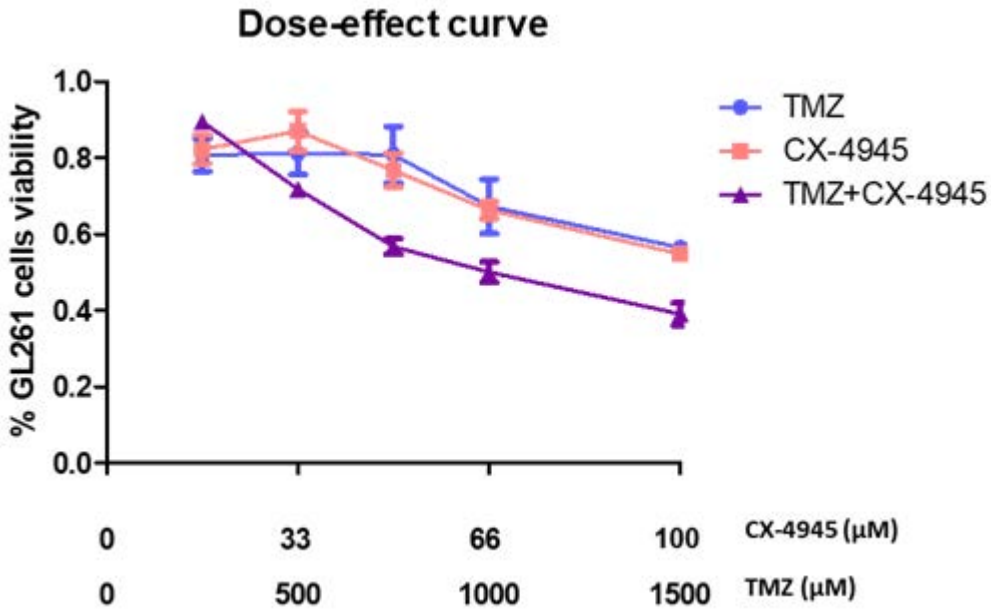

FIGURE A. ***Dose-dependent GL261 viability after 72h of CX-4945, TMZ and CX-4945+TMZ treatment.***
CX-4945 concentrations were 16, 33, 50, 66 and 100µM and TMZ concentrations 250, 500, 750, 1000 and 1500 µM. The value 1 (100% viability) was assigned to control cells treated with vehicle. Experiments were performed with n=4 and mean ± SD values are shown.

Median effect plots

The median effect plots draw the logarithm of the dose of each drug and the logarithm of ((1/SF)-1), being SF the survival fraction of cells. Plotting the median effect for each drug

separately and the combination allowed us to obtain the parameters m (median effect dose) and "D_m" (Hill-type coefficient) for each condition (drug 1, drug 2, drug 1+2). These values were used to calculate the combination index (CI).

The median effect plots (Figure B) of TMZ, CX-4945 and the combination of both were performed in order to obtain the parameters m (median effect dose) and D_m (Hill-type coefficient) (Table 10).

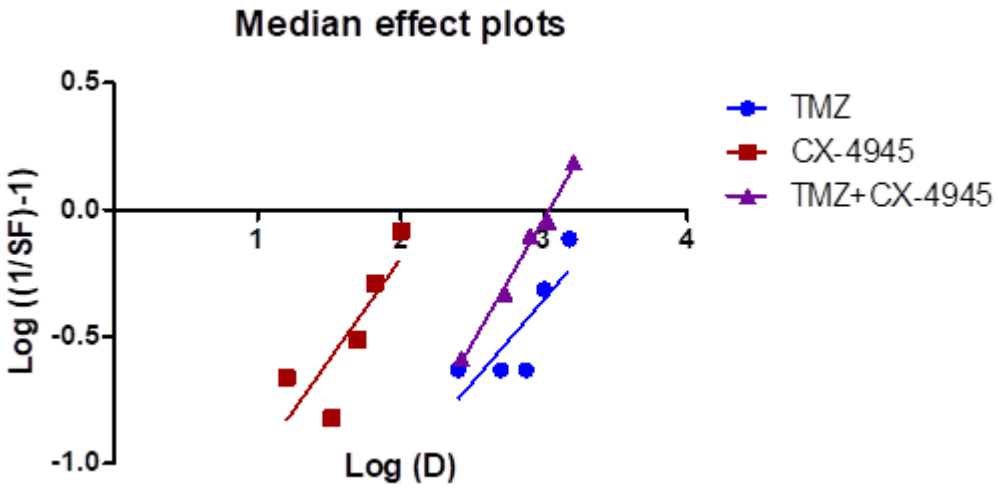

FIGURE B. ***Median effect plots of the 72h treatment of GL261 cells with CX-4945 (red), TMZ (blue) and CX-4945+TMZ (purple).***
The slope of each line (m) is the Hill coefficient and the intersection with the x-axis is Dm, the dose necessary to obtain a Fu (surviving fraction) of 0.5.

Combination index calculation

$(D_x)_{TMZ}$, $(D_x)_{TDB}$ and $(D_x)_{TMZ+TDB}$ were obtained from m and D_m parameters with the equation:

$$D_x = D_m [f_a/(1 - f_a)]^{1/m}$$

Next, it is necessary to calculate the parameters D_{TMZ} and D_{TDB}, that represent the contributions of each drug to the combined treatment, with the equations:

$$(D)_1 = (Dx)_{1,2} \cdot P/(P + Q) \quad \text{and} \quad (D)_2 = (Dx)_{1,2} \cdot Q/(P + Q)$$

In this case the ratio P/Q is 15:1 ([TMZ]/[CX]). The obtained values Dx and D were used to calculate the CI.

CX-4945 (μM)	**TMZ** (μM)	f_a	**CI**	**Result**
16	250	0.21	1.42	Antagonism
33	500	0.32	1.095	Addition
50	750	0.44	0.88	Synergy
66	1000	0.47	0.83	Synergy
100	1500	0.61	0.67	Synergy

***Table** A. Combination index (CI) was calculated for every set of concentrations, fa is the fraction of affected cells after combined treatment compared to control conditions.*

The individual doses for CX-4945 and TMZ are also indicated. The CI for the two lowest concentrations is higher than 1, indicating that at the lowest concentrations the combination is antagonistic. At the three highest concentrations the CI is lower than 1, meaning that the combined effect at these higher concentrations is synergic.

The combination index was calculated for every set of concentrations according to published literature. While increasing the concentrations, the affected fraction of cells (f_a) produced by the combined treatment will also increase. In Table 10 we show that, depending on the concentration, the effect of both drugs can be either synergic, additive or antagonistic. For the lowest concentration the combined effect is antagonistic, since the CI is higher than 1 (1.42). Still, we need to take into account that the viability reduction at the smallest concentrations is very small for all conditions. Moreover, for 500μM of TMZ and 33μM of CX-4945, there is an additive effect, since CI is equal to 1 (1.049). For the remaining, higher concentrations, the combined effect is synergic, since CI is in every case lower than 1 (0.88, 0.83 and 0.67).

ANNEX II
LABORATORY ANIMALS SUPERVISION

Procedure: CEEAH-3665

MONITORING PARAMETERS (scale: 0-3 points):

Wight loss

0) Normal weight
1) Less than 10% loss
2) Between 10 and 15% loss
3) Consistent or rapid, exceeding 20% loss maintained for 72 h.

Physical appearance

0) Normal
1) More than 10% dehydration, body condition 2 (BC; see further for details), skin tenting
2) Erected hair. Cyanosis
3) Hunched back. Loss of muscle mass

Clinical signs

0) None
1) Circular motion of the animal
2) Mucous secretions and/or bleeding form any orifice. Detectable hypertrophy of organs (lymph nodes, spleen, liver).
3) Shortness of breath (particularly if accompanied by nasal discharge and/or cyanosis). Cachexia

Changes in behaviour

0) No
1) Inability to move normally
2) Inability to get to the food/ drink, isolation from the rest of the animals in the cage
3) Unconsciousness or comatose. Lack of response (dying)

Wounds

0) No
1) Scratches
2) Nonhealing wounds. Infection at surgical site
3) Ulcerating, festering wounds. Ulcerating necrotic tumours

The animal condition according to the parameters and overall score:

a) 0 points: Healthy animal
b) 1-2 points: Minor signs, follow stablished protocol
c) 3-11 points: Daily supervision of the animal. Analgesics* or euthanization of the animal**
d) 12-30 points: euthanasia**

*Analgesic: Meloxicam (subcutaneously: 1 mg/kg)

**The *Servei d'Estabulari* veterinary staff will inform a group member as soon as possible to consider halting of the protocol/ experiment.

NOTE: As the tumour grows, it affects in the motor function of the brain. Animals may suffer from: paresis, decreased strength, plegia, paralysis. In these cases, food and water (i.e. hydrogel or water-soaked food) should be placed inside the cage to facilitate access by the animal.

Body Condition (BC):

BC 1

Mouse is emaciated.
- *Skeletal structure extremely prominent; little or no flesh cover.*
- *Vertebrae distinctly segmented.*

BC 2

Mouse is underconditioned.
- *Segmentation of vertebral column evident.*
- *Dorsal pelvic bones are readily palpable.*

BC 3

Mouse is well-conditioned.
- *Vertebrae and dorsal pelvis not prominent; palpable with slight pressure.*

BC 4

Mouse is overconditioned.
- *Spine is a continuous column.*
- *Vertebrae palpable only with firm pressure.*

BC 5

Mouse is obese.
- *Mouse is smooth and bulky.*
- *Bone structure disappears under flesh and subcutaneous fat.*

ANNEX III

High-resolution NMR spectra obtained for TDB standard solution and serum of control and TDB-administered C57BL/6j mice (Figure C).

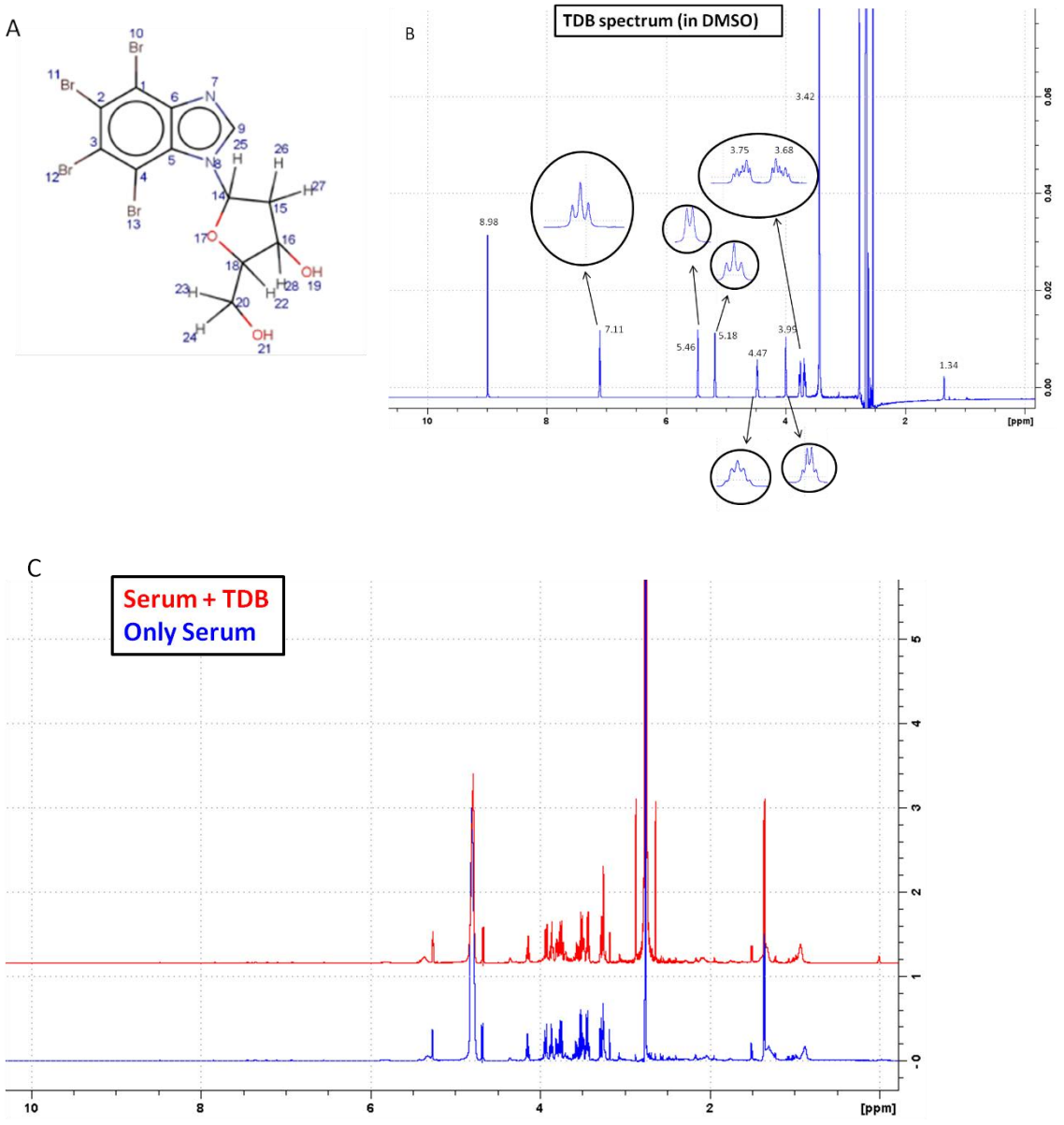

Figure C. High resolution NMR spectrum of TDB in deuterated DMSO and in mice serum obtained at 600Mhz in the SeRMN of UAB. *A)TDB molecule structure. Numbers indicate the hydrogens (^{1}H) atoms of the molecule. B) Standard TDB spectrum in DMSO acquired with the noesypr1d sequence. Signals at 3.68 and 3.76 ppm correspond to H number 23 and 24 in the molecule; 3.99 ppm corresponds to H 22; 4.47ppm to H 28; 5.18 and 5.45 probably to H21 and H19 ; 7.11 probably to H25; 8.9 ppm to H9. B) Spectrum of C57/BL6J serum without drug (in blue) and with TDB added at 14mM (in red) acquired with the "cpmgpr" sequence with an echo time of 0.4ms and a relaxation time interval of 2s. No appreciable differences were found between them.*